Transformation of a membrane protein from the respiratory chain into a sensor for the analysis of its interaction with substrates, inhibitors and lipids

Sébastien Kriegel

Ecole Doctorale des Sciences Chimiques

UMR 7140 – Chimie de la Matière Complexe

Hermann Staudinger Graduiertenschule

Institut für Organische und Biochemie

THÈSE

en cotutelle entre l'Université de Strasbourg et l'Albert-Ludwigs Universität Freiburg

présentée par :

Sébastien Kriegel

soutenue le 11 décembre 2013

Pour l'obtention conjointe du grade de **Docteur de l'Université de Strasbourg** et de **Doktor der Albert-Ludwigs Universität**

Discipline : Chimie

Transformation d'une protéine membranaire de la chaîne respiratoire en une sonde pour l'analyse de substrats, inhibiteurs et lipides

Transformation of a membrane protein from the respiratory chain into a sensor for the analysis of its interaction with substrates, inhibitors and lipids

THÈSE dirigée par :

Dr. Petra Hellwig	Prof. - Université de Strasbourg
Dr. Thorsten Friedrich	Prof. - Albert-Ludwigs Universität Freiburg

RAPPORTEURS :

Dr. Alain Walcarius	DR - Université de Lorraine, Nancy
Dr. Oliver Einsle	Prof. - Albert-Ludwigs Universität Freibug

AUTRES MEMBRES DU JURY :

Dr. Burkhard Bechinger	Prof. - Université de Strasbourg

This study was carried out in the following research laboratories :

Laboratoire de Bioélectrochimie et Spectroscopie (group of Pr. Dr. Petra Hellwig)
UMR 7140 Chimie de la Matière Complexe, Université de Strasbourg - CNRS
1 rue Blaise Pascal, 67070 Strasbourg, France

Institut für Biochemie (group of Pr. Dr. Thorsten Friedrich)
Albert-Ludwigs Universität
Albertstraße 21, 79104 Freiburg i. Br., Germany

Section of Interfacial Spectrochemistry (group of Pr. Dr. Masatoshi Osawa)
Catalysis Research Center, Hokkaido University
Kita21, Nishi10, Kita-ku, Sapporo, Hokkaido, Japan, 001-0021

Science is wonderfully equipped to answer the question " How ? " but it gets terribly confused when you ask the question " Why ? "

Erwin Chargaff (1905-2002)

Table of contents

TABLE OF CONTENTS I

LIST OF FIGURES III

LIST OF TABLES VI

ACKNOWLEDGEMENTS VII

ABBREVIATIONS IX

THE TWENTY AMINO ACIDS X

RESUME XI

ZUSAMMENFASSUNG XVI

ABSTRACT XVII

1 INTRODUCTION 1

1.1 THE LIVING CELL AND HOW IT HARVESTS ENERGY 1
1.2 THE RESPIRATORY CHAIN 4
1.3 THE NADH:UBIQUINONE OXIDOREDUCTASE (COMPLEX I) 17
1.4 THE PHOSPHOLIPID BILAYER MEMBRANE AND ITS INTERACTIONS WITH THE RESPIRATORY CHAIN COMPLEXES 32
1.5 Zn^{2+} AND THE RESPIRATORY CHAIN 36
1.6 SPECTROELECTROCHEMICAL METHODS APPLIED TO PROTEINS 37
1.6.1 GENERALITIES 37
1.6.2 UV-VISIBLE ABSORPTION SPECTROSCOPY 40
1.6.3 INFRARED ABSORPTION SPECTROSCOPY 42
1.6.4 CYCLIC VOLTAMMETRY 55
1.7 ELECTRODE SURFACE-IMMOBILIZATION OF REDOX ENZYMES 58
1.7.1 GENERAL STRATEGIES 58
1.7.2 STRATEGIES TO IMMOBILIZE MEMBRANE PROTEINS ON A GOLD SURFACE 58
1.7.3 STRATEGY TO IMMOBILIZE COMPLEX I 59
1.8 AIM OF THE WORK 62

2 EXPERIMENTAL PROCEDURES 63

2.1 SAMPLE PREPARATION 63
2.1.1 PREPARATION OF *NUOF*$_{HIS}$ NADH:UBIQUINONE OXIDOREDUCTASE (COMPLEX I) FROM *ESCHERICHIA COLI* 63
2.1.2 PREPARATION OF *NUOF*$_{HIS}$ COMPLEX I FROM *E. COLI* WITH REDUCED LIPID CONTENT 65
2.1.3 PREPARATION OF WILD TYPE COMPLEX I FROM *E. COLI* 65
2.1.4 PREPARATION OF *E. COLI* COMPLEX I *NUOF* Y178 MUTANTS 65
2.1.5 PREPARATION OF NADH-DEHYDROGENASE FRAGMENT (NDF) FROM *E. COLI* 66
2.1.6 PREPARATION OF *NUOEF* SUBCOMPLEX FROM *AQUIFEX AEOLICUS* 67

2.1.7 NADH/K_3[Fe(CN)$_6$] oxidoreductase activity measurements 67
2.1.8 Determination of Complex I concentration through UV-Visible spectroscopy 68
2.1.9 Determination of total protein content by biuret reaction 68
2.1.10 SDS-PolyAcrylamid Gel Electrophoresis (SDS-PAGE) 69
2.1.11 Protein sample buffer exchange 69
2.1.12 Other preparations 69
2.2 Potential induced differential FTIR measures 71
2.2.1 The optically transparent thin layer electrochemical cell 71
2.2.2 Interaction of Complex I with phospholipids 73
2.2.3 Interaction of Complex I with Zinc(II) 74
2.3 Hydrogen-deuterium exchange kinetics followed by FTIR spectroscopy 75
2.3.1 Experimental 75
2.3.2 Calculation of the exchange fractions and rates 76
2.4 UV-Vis redox titrations 77
2.4.1 Experimental 77
2.4.2 Estimation of the midpoint potentials from the obtained spectra 78
2.5 SEIRAS and CV measurements of Complex I, NDF and *nuoEF* adsorbed on a gold surface 79
2.5.1 Electroless deposition of the Gold Film on the ATR prism : 81
2.5.2 Surface modifications : 82
2.5.3 Immobilization of Complex I/NDF/*nuoEF* and reconstitution into a lipid bilayer : 83
2.5.4 Potential induced difference spectroscopy of the immobilized enzymes 83
2.6 Cyclic Voltammetry 84

3 RESULTS AND DISCUSSION 85

3.1 Immobilization and functional probing of Complex I 85
3.1.1 Introduction 85
3.1.2 Creation and chemical modification of the Gold surface 86
3.1.3 Immobilization of Complex I and insertion into a lipid bilayer 91
3.1.4 Probing the electrochemically-induced reaction of the immobilized Complex I through SEIRAS and CV 93
3.1.5 Conclusion 103
3.2 Role of *nuoF* Tyr^{178} in the NADH binding site and inhibition of Complex I by NADH-OH 104
3.2.1 Introduction 104
3.2.2 $_F$Tyr^{178} mutants characterization 105
3.2.3 NADH-OH inhibition 113
3.2.4 Conclusion 115
3.3 Interaction of Complex I with Phospholipids 118
3.3.1 Introduction 118
3.3.2 FTIR difference spectroscopy of Complex I in the presence of lipids 119
3.3.3 Hydrogen-Deuterium Exchange kinetics in the presence of lipids 129
3.3.4 Conclusion 132
3.4 Zn^{2+} inhibition of Complex I 136
3.4.1 Introduction 136
3.4.2 FTIR Difference spectroscopy of Complex I in the presence and absence of Zn^{2+} 136
3.4.3 Conclusion 150
3.5 Proton pumping and coupling with UQ reduction - A model for the function of Complex I 151
3.5.1 Structural analysis of the coupling elements 151
3.5.2 Coupling mechanism between electron transfer and proton pumping 168

4 SUMMARY 176

5 APPENDIX 179

5.1 EXPERIMENTAL PROCEDURES APPENDIX 179
5.1.1 *NUOF*$_{HIS}$ COMPLEX I PREPARATION 179
5.1.2 PREPARATION OF *NUOF*$_{HIS}$ COMPLEX I WITH REDUCED LIPID CONTENT 181
5.1.3 PREPARATIONS OF COMPLEX I *NUOF*$_{HIS}$ TYR^{178} MUTANTS 182
5.1.4 PREPARATIONS OF WILD TYPE COMPLEX I, NDF AND *NUOEF* FRAGMENT 182
5.2 RESULTS AND DISCUSSION APPENDIX 183

REFERENCES 188

List of Figures

Figure 1.1.1 : Schematic representation of A. the bacterial-, B. the animal- and C. the plant-cell and summary of their similarities and differences. 2
Figure 1.2.1 : Structure of the mitochondrion, structure, organization and functioning of the respiratory chain. 6
Figure 1.2.2 : Representation of the Complex II mechanism and its cofactors. 7
Figure 1.2.3 : Schematic representation of the Complex III mechanism. 7
Figure 1.2.4 : Catalytic cycle of the cytochrome c oxidase 8
Figure 1.2.5 : Mechanism of the F1Fo ATP synthase 9
Figure 1.2.6 : Structure of ubiquinones. 10
Figure 1.2.7 : Macromolecular organization of the mitochondrial cristæ. 12
Figure 1.2.8 : Representation of the mitochondrial respirasome (supercomplex I/III$_2$/IV). 13
Figure 1.2.9 : Evolution of E'$_0$ and of free energy per electron in the respiratory chain. 14
Figure 1.3.1 : Schematic subunit repartition of the human mitochondrial Complex I. 17
Figure 1.3.2 : Crystallographic structure of the entire Complex I from T. thermophilus and correspondence to homologuous core subunits from E. coli and H. sapiens. 19
Figure 1.3.3 : A. Spatial arrangement of the FeS clusters in the T. thermophilus Complex I. B. Midpoint potential profile of the FeS clusters from E. coli Complex I. 21
Figure 1.3.4 : A. Potential energy profile and B. Thermodynamic reversibility of Complex I from B. taurus. 22
Figure 1.3.5 : Structures of FMN at three oxidation states occurring in Complex I. 23
Figure 1.3.6 : Representation of the NADH and FMN binding pocket of Complex I. PDB ID : 4HEA. 24
Figure 1.3.7 : View of the NADH binding site of Complex I in the reduced and in the oxidized state. 25
Figure 1.3.8 : Bound Piericidin A and decylubiquinone (A., B.) and representation of the Q binding pocket (C.). .26

Figure 1.3.9 : Putative proton channels of the T. thermophilus Complex I, ...27
Figure 1.3.10 : Representation of the coupling elements and of modelized water molecules in the T. thermophilus Complex I. 28
Figure 1.3.11 : Structures of different NADH and Q competitive inhibitors. 31
Figure 1.4.1 : The fluid-mosaic model and different types of lipids and membrane proteins. 33
Figure 1.4.2 : Structures of the major phospholipids of the E. coli inner membrane. 34
Figure 1.4.3 : Charge distribution map of the membrane domain from Complex I. 35
Figure 1.6.1 : A. : The electromagnetic spectrum. B. Energy states in matter. 38
Figure 1.6.2 : A. : The eletrochemical cell based on three electrode. B. : Schematic representation of a three electrode potentiostat. 40
Figure 1.6.3 : Normal mode vibrations commonly seen in IR spectroscopy. 43
Figure 1.6.4 : Typical MIR spectrum of a protein in solution. 44
Figure 1.6.5 : Example of a difference spectrum between the fully oxidized and the fully oxidized state of an enzyme, Complex I. 46
Figure 1.6.6 : Representations of a conventional FTIR spectrometer, an interferogram and the corresponding absorbance spectrum obtained by Fourier transform. 48
Figure 1.6.7 : Schematic representation of the ATR principle. 50
Figure 1.6.8 : A. AFM image of a chemically deposited Au layer. B. SEIRA EM enhancement mechanism. 53
Figure 1.6.9 : A. Potential vs. time for a cyclic voltammetric experiment. B. Typical CV of a reversible redox reaction. 56
Figure 1.7.1 : Representation of Complex I immobilized on a NiNTA SAM at a SEIRA-active gold surface. 60
Figure 1.7.2 : Adsorption of Complex I on a NADH SAM. 61
Figure 1.7.3 : Immobilized Complex I before (A.) and after (B.) insertion into a lipid bilayer. 61
Figure 2.2.1 : The thin layer electrochemical cell during (A.) and after (B.) assembly. 71
Figure 2.2.2 : 3-MPA - Cyst SAM formed on the gold grid 72
Figure 2.3.1 : Representation of the perfusion ATR cell. 75
Figure 2.3.2 : Example of the fraction of exchanged protein "Amide-H" vs. time. 77
Figure 2.4.1 : Example of the electrochemically-induced UV-Vis absorption change of a redox enzyme. 78
Figure 2.4.2 : Example of the E_m estimation from multiple curve fitting to δΔAbs vs. E. 79
Figure 2.5.1 : Representation of the ATR electrochemical cell. 80
Figure 2.5.2 : Photographs of the whole setup (lef) and zoom on the mirror configuration (right). 81
Figure 3.1.1 : Oxidized minus reduced FTIR difference spectrum and cyclovoltammogram of Cyt_c in the ATR-Electrochemical cell. 87
Figure 3.1.2 : Reaction steps for the NiNTA SAM formation. Step 4 represents the attachment of the Complex I His-tag 88
Figure 3.1.3 : Creation of the NiNTA SAM followed by FTIR difference spectroscopy. 88
Figure 3.1.4 : Reaction steps for the NADH SAM formation. 89
Figure 3.1.5 : Creation of the NADH SAM followed by FTIR difference spectroscopy. 90

Figure 3.1.6 : Adsorption of Complex I on the NiNTA and NADH SAMs. 91
Figure 3.1.7 : Insertion of the adsorbed Complex I into a lipid bilayer. 92
Figure 3.1.8 : Redox induced behavior of the Au layer in different conditions probed by FTIR. 94
Figure 3.1.9 : CV of the bare Au layer (A.) and the NADH and NiNTA SAMs (B.). 95
Figure 3.1.10 : Oxidized minus reduced spectra of FMN in solution and of adsorbed Complex I, both with the NADH SAM. 96
Figure 3.1.11 : Comparison of ox-red spectra (A.) and CVs (B.) of NuoEF fragment, NDF and Complex I adsorbed on a NADH SAM. 98
Figure 3.1.12 : Comparison of the ox-red spectra of Complex I adsorbed on the NiNTA and NADH SAMs. 99
Figure 3.1.13 : Comparison of the ox-red spectra and CV of Complex I adsorbed on the NiNTA and NADH SAMs before and after reconstitution into a lipid bilayer. 100
Figure 3.1.14 : Effect of the addition of Decylubiquinone and Rotenone on the adsorbed Complex I. 101
Figure 3.1.15 : Effects of Zn^{2+} on Complex I adsorbed on the NADH SAM and of NADH-OH on Complex I adsorbed on the NiNTA SAM. 102
Figure 3.2.1 : UV-Vis titration of the midpoints potentials from the Wild-Type Complex I. 107
Figure 3.2.2 : Estimation of the E_m of FMN in the $nuoF_{HIS}$ Tyr^{178} mutants from their UV-Vis redox titration curves. 108
Figure 3.2.3 : Stabilization of oxidized FMN in a quinoid state through interaction with $_FCys^{178}$ 110
Figure 3.2.4 : Electrochemically induced FTIR difference spectra of Complex I and the $_FTyr^{178}$ mutants and of FMN. 112
Figure 3.2.5 : Estimation of Em FMN and of the FeS clusters in the NADH-OH inhibited Complex I. 114
Figure 3.3.1 : Evolution of Complex I NADH/DQ oxidoreductase activity in function of the addition of phospholipids. 118
Figure 3.3.2 : Oxidized minus reduced FTIR spectra of Complex I with (black line) and without (blue line) lipids. 119
Figure 3.3.3 : Double difference spectrum of delipidated Complex I minus WT Complex I. 120
Figure 3.3.4 : Double difference spectra of delipidated Complex I minus Complex I in the presence of PG, CL and PE. 123
Figure 3.3.5 : Comparison between the effect of native lipids, added E. coli lipid extract and PE, PG and CL added individually. 125
Figure 3.3.6 : Double difference spectra of delipidated Complex I minus delipidated Complex I in the presence of PE, PG and CL in ^2H_2O buffer. 126
Figure 3.3.7 : ^1H-^2H exchange kinetic curves of delipidated Complex I alone and in the presence of PE and PG. 130
Figure 3.3.8 : Representations of the membrane domain of Complex I. 134
Figure 3.4.1 : Oxidized minus reduced FTIR difference spectra of Complex I with (red line) and without Zn^{2+} (black line). 137
Figure 3.4.2 : Double-difference spectra of Complex I minus Complex I with Zn^{2+} in the spectral region from 1800 to 1200 cm^{-1}. 138

Figure 3.4.3 : Evolution of the oxidized minus reduced FTIR spectra of Zn^{2+} inhibited Complex I in function of the number of redox cycles. 145
Figure 3.4.4 : Evolution of the oxidized minus reduced spectra of Zn^{2+} inhibited Complex I over time. 145
Figure 3.4.5 : Evolution of the oxidized minus reduced FTIR spectra of uninhibited Complex I in function of the number of redox cycles. 146
Figure 3.5.1 : Localization of the putative Zinc binding sites in the membrane domain of Complex I from E. coli. 152
Figure 3.5.2 : HL helix and β-element induced internal proton flow regulating mechanism. 154
Figure 3.5.3 : Ubiquinone oxidoreduction reactions with intermediate species. 156
Figure 3.5.4 : Representation of the proposed $_4His^{38}$ channel and its opening mechanism. 157
Figure 3.5.5 : Directional proton transfer mechanism in the antiporter modules. 159
Figure 3.5.6 : Conformational movements inducing distal proton intake. 161
Figure 3.5.7 : Nqo7 loop and proposed transmission to HL helix and β-elements. 164
Figure 3.5.8 : Representation of the Q binding cavity. 167
Figure 3.5.9 : Proposed coupling mechanism of Complex I. 169
Figure 3.5.10 : Different positions of Ubiquinone in its binding pocket. 171
Figure 3.5.11 : Sequence alignment for Nqo6 homologues from different organisms. 174

List of tables

Table 1.2.1 : Estimation of Δp in three systems at equilibrium. 16
Table 1.6.1 : Amide contributions of the polypeptide backbone in the MIR range. 44
Table 1.6.2 : Amide I frequency range for protein secondary structures in ^1H_2O and ^2H_2O. 45
Table 2.2.1 : List of the mediators used in spectroelectrochemical experiments. 73
Table 3.2.1 : Kinetic parameters and ROS production of $_FTyr^{178}$ mutants compared to the WT enzyme. 105
Table 3.2.2 : Estimated E_m FMN in the $_FTyr^{178}$ mutants. 109
Table 3.2.3 : ROS production in the NADH-OH inhibited Complex I. 113
Table 3.3.1 : ^1H-^2H exchange rates and times for delipidated Complex I alone and in the presence of PE and PG. 130
Table 3.4.1 : Tentative assignments for the peaks from Figure 3.4.2. 139
Table 3.4.2 : Tentative attributions and direction of variation for the peaks from Figure 3.4.3. 147
Table 3.5.1 : Residue conservation in cytoplasmic loops of interest for different organisms. 152

Acknowledgements

This study was carried out at the Laboratoire de Spectroscopie Vibrationnelle et Electrochimie des Biomolecules at the Université de Strasbourg (FR), at the Institut für Organische und Biochemie at the Albert Ludwigs Universität in Freiburg (DE) and at the Catalysis Research Center at the University of Hokkaido in Sapporo (JPN) ; funding was provided by the Region Alsace, the DFH-UFA, the JSPS, the Université de Strasbourg and the CNRS and is gratefully acknowledged.

First, I would like to thank my supervisors Pr. Petra Hellwig and Pr. Thorsten Friedrich, who gave me the opportunity to realize this thesis and provided invaluable support and scientific guidance during these four years. Their patience, kindness and helpful advices helped me to make the transition from my initial field of research, organic synthesis, to the world of biochemistry and biophysics. I am also grateful to Pr. Masatoshi Osawa, who welcomed me for two months in Japan and allowed me to discover this fabulous country. I would like to thank my collaborators, Dr. Myriam Seemann and Dr. Jean-Jacques Lacapère for giving me the opportunity to work on other proteins than Complex I, Dr. Martin Holzer for help with the preparation of liposomes, as well as my reviewers and jury members, Pr. Oliver Einsle, Dr. Alain Walcarius and Pr. Burkhard Bechinger for taking the time to critically read this work, for constructive comments and suggestions.

My gratitude goes to all my past and present colleagues in these different groups. Thank you Yashvin, Thomas, Frédéric, Youssef, Julien, Michelle, Mireille, Maddy, Batoul, Ruth, Aurélien, Nesrine, Léa, Alicia, the interns who stayed in our lab and our secretaries, Christiane and Sandra. You taught me a lot about the practical aspects of spectroscopy and biochemistry but above all, the moments we shared went far beyond the context of work ; every single one of you was always keen to share a laughter, a good advice, a cheer-up during hard times or simply a coffee-break. I am also thankful to the members of Pr. Friedrich's group for welcoming me and for showing me how to purify proteins. Thank you Marius, Klaudia and Emmanuel for your collaboration on different projects. My warmest

thanks also go to the members of Pr. Osawa's group for their hospitality in such a culturally different country and for their help with the SEIRAS project.

My deepest thanks go to my fellow PhD student or former BSc. / MSc. friends, for their support and countless hours of discussions that helped to put some aspects of the long road to graduation into perspective. Thanks Bi, Tri, Eric, Fiou, Jamel, Béné, Paco, Schnee, Kern, Popo, Gregès', Tomtom, Piou, Faboutch, Keupon, Vivès, David, Grand Tom, Seb², Tim, Sandra, Karl, Lydie and many others. I would also like to thank all my friends and family for their unconditional friendship, support and of course for all those good moments during these years. It would probably take another thesis to list each one of you together with the reasons why I am thankful to you. I would especially thank Bart, Matheus, Will, Flo, Billy, JN, Sushi, Marie, Cindy, Manu, Julie, Isa, JB, Aurèl, Philippe, Mélo, Uni, Gridou, JN le grand, Fob, Meg, Nanoushka, Jo, Emma, Bruno, Fanny, Nicole, Tiffany, Erica, Seth, to name just a few of you.

Finally, I dedicate this thesis to my parents, Marianne and Francis, and to my significant other, my beloved girlfriend Aurélie. Thank you for enduring my mood jumps, for helping me in the battle against procrastination and for believing in me, especially while I was writing this manuscript. Without your love and care, none of this would have been possible.

Strasbourg, September 2013 Sébastien Kriegel

Abbreviations

Abs	Absorbance
ADP	Adenonsine Diphosphate
ANTA	N_α,N_α-Bis(carboxymethyl)-L-lysine hydrate
ATP	Adenonsine Triphosphate
ATR	Attenuated Total Reflection
B. taurus	*Bos taurus*
CE	Counter Electrode
CL	Cardiolipin
CV	Cyclic Voltammetry / voltammogram
Cyst	Cysteamine
Da	Dalton
DDM	*n*-Dodecyl β-D-Maltoside
DMSO	Dimethyl Sulfoxide
DNA	Desoxyribonucleic Acid
DTGS	Deuterated Triglycine Sulfate
DTSP	Dithioscuccinimide
DTT	DL-Dithiothreitol
E. coli	*Escherichia coli*
EDC	1-Ethyl-3-(3-dimethylaminopropyl)-carbodiimide
E_m	Midpoint Potential
EPR	Electronic Paramagnetic Resonance
ETC	Electron Transfer Chain
FeS	Iron-sulfur Cluster
FMN	Flavin Mononucleotide
FTIR	Fourier Transform Infrared
H. sapiens	*Homo sapiens*
HDX	Hydrogen Deuterium Exchange
IRE	Internal Reflection Element
K_m	Michaelis Constant
MCT	Mercury Cadmium Telluride
MES	2-(*N*-morpholino)ethanesulfonic Acid
MIR	Mid Infrared
MPA	3-Mercaptopropionic Acid
mtDNA	Mitochondrial DNA
MUA	11-mercaptoundecanoic Acid
NAD(P)H	Nicotinamide Adenine Dinucleotide Phosphate, reduced
NAD^+	Nicotinamide Adenine Dinucleotide, oxidized
NADH	Nicotinamide Adenine Dinucleotide, reduced
ND	NADH-Dehydrogenase
NDF	NADH-Dehydrogenase Fragment
nDNA	Nuclear DNA
NiNTA	Nickel-nitrilotriacetic Acid
Nqo	NADH Quinone Oxidoreductase
Nuo	NADH Ubiquinone Oxidoreductase
ox	Oxidized
OXPHOS	Oxidative Phosphorylation
PC	Phosphatidylcholine
PDB	Protein Data Base
PE	Phosphatidylethanolamine
PG	Phosphatidylglycerol
P_i	Inorganic Phosphate
pmf	Proton Motive Force
PMSF	Phenylmethanesulfonyl Fluoride
Q	Quinone
QH_2	Reduced Quinone
RE	Reference Electrode
red	Reduced
RNA	Ribonucleic Acid
ROS	Reactive Oxygen Species
SAM	Self-Assembled Monolayer
SDS-PAGE	Sodium Dodecyl Sulfate Polyacrylamide Gel Electrophoresis
SEIRA(S)	Surface Enhance Infrared Absorption (Spectroscopy)
SMP	Submitochondrial Particle
SQ	Semiquinone
T. thermophilus	*Thermus thermophilus*
TM	Transmembrane (helix)
UQ	Ubiquinone
UV-Vis	Ultraviolet-visible
WE	Working Electrode

The twenty amino acids

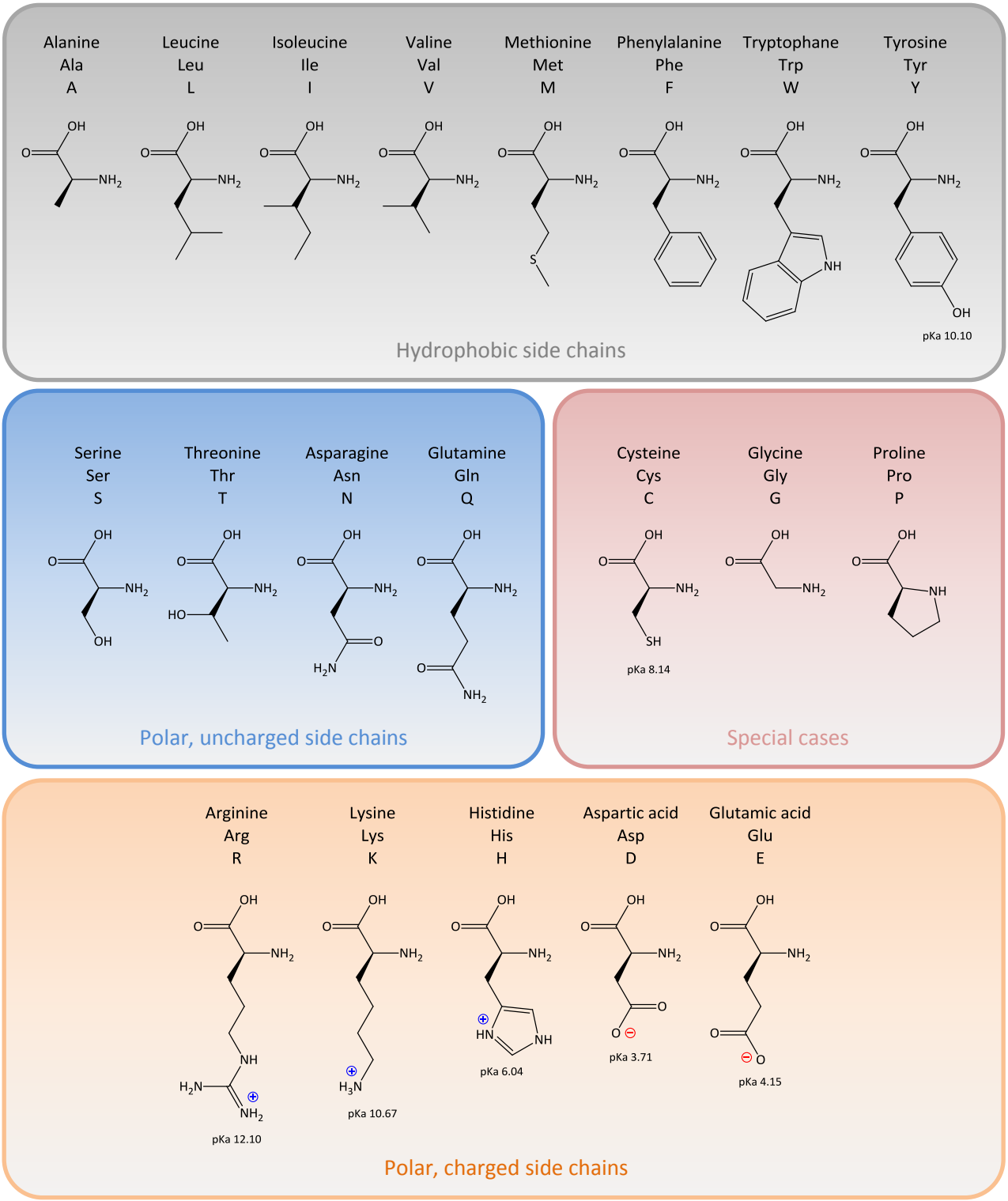

Side chain charges at a physiological pH of 7.4.

Résumé

Transformation d'une protéine membranaire de la chaîne respiratoire en une sonde pour l'analyse de substrats, inhibiteurs et lipides.

La chaîne respiratoire est constituée d'une série de cinq complexes enzymatiques membranaires insérés dans la bicouche lipidique interne des mitochondries. Le premier de ces complexes, la NADH:ubiquinone oxidoreductase (également appelé Complexe I) catalyse le transfert d'électrons à partir d'un coenzyme issu du catabolisme des nutriments (notamment du cycle de Krebs), le NADH, vers le pool de coenzyme Q (ubiquinone) présent dans la bicouche lipidique. Ce processus est accompagné par la translocation de quatre protons au travers de la membrane. Les électrons stockés sur le coenzyme Q sont ensuite transférés vers le complexe cytochrome bc_1 (Complexe III) qui catalyse leur transfert vers un autre porteur d'électrons, le cytochrome *c*. Ce dernier les achemine vers la cytochrome *c* oxidase (Complexe IV) où ils sont utilisés pour réduire l'oxygène en eau. Ces transferts sont également couplés à la translocation de protons au travers de la membrane, ce qui conduit à la formation d'un gradient de protons. L'énergie stockée par le biais de ce gradient permet finalement à l'ATPsynthase (Complexe V) de catalyser la production d'adénosine triphosphate (ATP) à partir d'adénosine diphosphate (ADP) et de phosphate inorganique (Pi). Cet ATP est l'une des majeures sources d'énergie métabolique.

Dans le cadre du travail de cette thèse, nous étudions plus particulièrement le Complexe I. Ce complexe enzymatique de 500 kDa est à la fois le plus grand et le moins bien connu des complexes de la chaîne respiratoire. En dépit de récentes avancées structurales, le mécanisme de couplage de l'oxydation de NADH à la translocation de protons reste sujet à discussion. Il est suspecté que des modifications de la fonction ou de la structure de cet enzyme mènent à une variété de pathologies humaines courantes, telles que les maladies de Parkinson et d'Alzheimer ou encore la neuropathie optique héréditaire de Leber. Le Complexe I est également impliqué dans la génération de radicaux libres, générateurs de stress oxydant dans les cellules. Cette protéine est aussi la cible de certains pesticides. Afin d'étayer les informations concernant le fonctionnement détaillé du Complexe I et son

interaction avec l'environnement, nous avons choisi une approche technique combinant les spectroscopies infrarouge et UV-Visible, l'électrochimie et la biochimie. Le but principal de ce travail est de créer, à partir de cette combinaison de techniques, une sonde moléculaire dans laquelle la NADH:ubiquinone oxidoreductase est immobilisée sur un support de façon à pouvoir déceler des interactions avec son environnement.

Purification du Complexe I, de ses sous-fragments et production de mutants

Afin d'avoir à disposition des quantités de protéines suffisantes, celles-ci ont été produites dans le laboratoire du Pr. Friedrich à l'Albert-Ludwigs Universität Freiburg dans le cadre d'une cotutelle de thèse. Une première partie de ce travail traite donc de la production et de la purification du Complexe I et de ses variantes. Toutes les études ont été menées sur le Complexe I d'*E. coli*, dont la fonction et la structure servent de modèles pour l'étude du complexe mitochondrial. Les techniques employées pour obtenir cette protéine membranaire purifiée sont exposées et brièvement discutées.

Création d'une sonde moléculaire à partir du Complexe I

Afin de créer une méthode permettant une analyse du Complexe I différente des méthodes habituelles utilisées au laboratoire, la spectroscopie infrarouge en mode de réflexion totale atténuée (ATR-IR) a été utilisée comme base de départ. L'ATR-IR permet d'effectuer des mesures sur des molécules déposées à la surface d'un cristal, en silicium ici. Afin d'amplifier les signaux obtenus, une fine couche d'or (de 20 Å à 50 Å) est déposée à la surface du cristal avant les molécules à étudier, technique appelée SEIRAS. Lorsqu'on la connecte à un potentiostat cette couche d'or sert également d'électrode de travail dans un montage d'électrochimie classique (avec une électrode de travail et une électrode de référence), ce qui permet d'induire un changement dans les molécules absorbées en fonction du potentiel électrochimique appliqué.

Dans un premier temps, la manière de déposition de l'or sur le silicium a été étudiée, menant au choix de la déposition dite electroless impliquant la réduction d'Au(IV) en or métallique. La couche ainsi créé possède les propriétés voulues pour le SEIRAS en termes

d'épaisseur et de granulosité. Secundo, pour mesurer efficacement les changements ayant lieu au sein du Complexe I, deux voies d'immobilisation de l'enzyme sur la couche d'or ont été explorées. L'une tire parti de l'affinité naturelle du Complexe pour son substrat, le NADH. Ce dernier est fixé de manière covalente *via* un couplage peptidique à un alkylthiol précédemment adsorbé sur l'or. La protéine vient ensuite positionner son site de liaison du NADH face à la couche d'or. L'autre méthode d'immobilisation se base sur l'affinité d'un tag hexahistidine introduit près du site de liaison du NADH envers le Ni(II) chélaté par trois carboxylates. Ce complexe métallique est également immobilisé sur l'or grâce à un thiol. Le processus détaillé d'adsorption des modifiants puis de la protéine est suivi par ATR-IR. Une partie de ces travaux ont étés effectués au sein du laboratoire du Pr. Osawa à l'Université d'Hokkaido.

Le Complexe I ainsi immobilisé présente son côté d'entrée des électrons à la couche d'or (figure 1). En appliquant un potentiel électrochimique, l'état redox de l'enzyme peut être contrôlé. Dans le montage créé ici, des mesures de voltammétrie cyclique et d'ATR-IR différentiel peuvent ainsi être effectuées et combinées. Une partie de ce travail traite donc de l'analyse des résultats obtenus par ces biais. Des expériences sur des fragments du Complexe I (le fragment NADH dehydrogenase et le sous-complexe *nuoEF*) ont aussi été menées, de façon à pouvoir attribuer avec plus de certitude certains signaux observés.

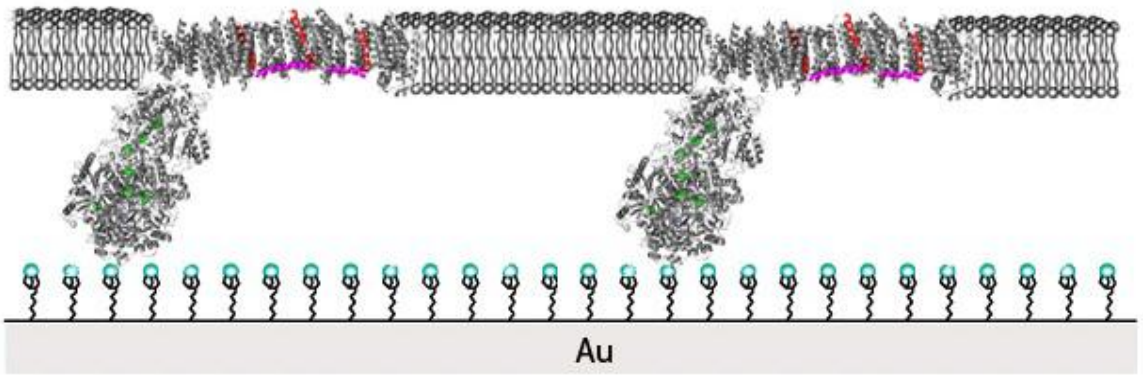

Représentation du Complexe I immobilisé sur une surface d'or modifiée

Afin de créer des conditions expérimentales biomimétiques, le Complexe I ainsi immobilisé a été reconstitué dans une bicouche lipidique par l'addition de liposomes

préformés suivi de la soustraction du détergent (figure 1). Grâce à cela, l'interaction avec le substrat ubiquinone a pu être caractérisée. De même, l'effet de différents inhibiteurs a été étudié : la roténone au niveau site de fixation de l'ubiquinone, le NADH-OH pour le site de fixation du NADH et l'ion Zn(II), au niveau du pompage de protons. Cela a permis de mettre en application la sonde moléculaire ainsi créée, et d'en discuter les tenants et les aboutissants.

Interaction entre Complexe I et phospholipides

Toujours dans l'optique d'une meilleure caractérisation du Complexe I, l'influence de différents types de phospholipides a été étudiée. Pour ce faire, l'enzyme purifiée préalablement délipidée a été mélangée avec trois lipides naturellement présents dans la membrane d'*E. coli.* Deux techniques ont été utilisées pour sonder l'interaction entre protéine et lipides : la spectroscopie infrarouge différentielle induite par électrochimie (cellule spectroelectrochimique) et l'échange Hydrogène-Deuterium suivi par ATR-IR. Les expériences en cellule spectroelectrochimique ont montrées que les phospholipides ont un effet sur les changements conformationnels associés au fonctionnement de la protéine et que l'interaction semble perturber certains résidus acides, probablement ceux situés dans la région de fixation de la tête polaire des lipides. L'échange ^{1}H-^{2}H permet de recueillir des informations quant à l'accessibilité au solvant des différentes parties de la protéine. Cela a dévoilé une diminution de la région d'échange rapide (hydrophile) accompagnée d'une augmentation de la région d'échange lente (hydrophobe), ce qui traduit le fait que le cœur hydrophobe est davantage protégé du solvant en présence de lipides.

Interaction entre Complexe I et Zinc

L'ion Zn^{2+} est un inhibiteur du pompage de protons par l'enzyme, ce qui devrait se traduire par des changements dans la signature en FTIR de certains acides aminés connus pour participer au transfert de protons. Afin d'éviter des interactions parasites entre un tag hexahistidine présent sur le Complexe I utilisé pour les autres mesures et l'ion Zinc, l'étude a eu lieu sur l'enzyme de type sauvage préalablement purifiiée. Les mesures effectuées en spectroscopie infrarouge différentielle induite par électrochimie ont permis de conclure que le fait de bloquer le pompage de protons avait une influence sur les changements conformationnels lors du fonctionnement de la protéine.

Influence sur le potentiel redox du cofacteur FMN de mutations de Tyr178 de *nuoF*

Toujours en rapport avec le Complexe I et dans le cadre d'une cotutelle avec l'Albert-Ludwigs Universität Freiburg, une tyrosine proche du site de fixation du cofacteur FMN a été remplacée par quatre acides aminés différents (Ala, Cys, Phe et Leu). La mutation de ce résidu est connue pour être impliquée dans certaines pathologies. Les conséquences de cette mutation sur le potentiel redox de ce cofacteur ont été suivies par titration UV-Visible en cellule spectroelectrochimique. Cela a mis à jour une baisse plus ou moins importante du potentiel redox du FMN en fonction de la nature de la mutation. La baisse de potentiel la plus importante a été observée lorsque la tyrosine a été remplacée par une cystéine, expliquant ainsi que lorsqu'elle a lieu in vivo cette mutation est la plus pathogène.

La même technique a été utilisée pour déterminer si la liaison de l'inhibiteur NADH-OH au Complexe I entraînait aussi des changements du potentiel du FMN, ce qui a montré qu'il s'abaissait 100 mV en présence de NADH-OH. Les implications en termes de contrôle de la productions de radicaux libres sont discutées.

Zusammenfassung

Umwandlung eines Proteins der Atmungskette in einen Sensor für die Analyse von Substraten, Inhibitoren und Lipiden.

Die Atmungskette besteht aus fünf in die innere Mitochondrienmembran eingebetteten enzymatischen Komplexen. Ihr Hauptzweck besteht darin, die chemische Energie, die aus der Zellatmung resultiert, in Form von ATP zu speichern. Der erste dieser fünf Komplexe ist die NADH: Ubichinon Oxidoreduktase (Komplex I), die den Transfer von zwei Elektronen von NADH zu Ubichinon mit der Translokation von vier Protonen durch die Membran verbindet. Der Informationsmangel über die genaue Funktionsweise dieses Enzyms und dessen Beteiligung in Krankheiten und in den Alterungsprozess haben ein starken Fokus in dem Gebiet der Mitochondrienatmung auf Komplex I gebracht.

Um mehr über Komplex I zu erfahren wird hier die Gestaltung eines Sensors vorgestellt. Das Enzym wird auf einer Goldoberfläche immobilisiert und durch eine Kombination aus Oberflächen-verstärkter Infrarotabsorptionsspektroskopie (SEIRAS) und Elektrochemie erprobt. Nach der Immobilisierung von Komplex I durch zwei verschiedene auf Affinität basierenden Verfahren wird das Enzym in eine Lipiddoppelschicht rekonstituiert, wodurch eine biomimetische Umgeben erzeugt wird. Dieser Sensor wird dann gegen verschiedene Substrate, Hemmer oder Lipide getestet, und die Ergebnisse werden diskutiert.

Neben der Konzeption des Sensors wird auch das Zusammenspiel von Komplex I mit Lipiden und mit Zn(II) durch elektrochemisch induzierte FT-IR Differenzspektroskopie und durch ^{1}H-^{2}H Austausch untersucht. Es wird gezeigt, dass beide einen Effekt auf die Konformativen Bewegungen des Proteins während des Redox-Zykluses hervorrufen.

Der Einfluß der Mutation von *nuoF* Y178 auf das Mittelpunkt Potential des FMN‘s wird mittels UV-Vis-Titration untersucht. Die Mutation Y178C, die bei manchen Formen von Leigh-Syndrom gefunden wird, verursacht eine -80mV Verschiebung des FMN Potentials. Inhibition von Komplex I durch NADH-OH ergibt eine -100 mV Verschiebung.

Abstract

The field of bioenergetics deals with the flow and transformation of energy within and between living organisms and their environment. Numerous cellular processes, such as photosynthesis and cellular respiration participate to these energetic transfers. Their detailed study from the macroscopic to the molecular level aims to explain and understand the basis of life.

The respiratory chain consists of five enzymatic complexes embedded in the inner mitochondrial membrane. Its main purpose is to store the chemical energy originating from nutrient catabolism by converting ADP to ATP. The first of these five complexes is the NADH:ubiquinone oxidoreductase (Complex I) which couples the transfer of two electrons from NADH to ubiquinone to the translocation of four protons across the membrane. Recent structural advances allowed further insight in the mechanism of Complex I, but its detailed functioning at the molecular level is still unclear. Since Complex I function is essential for life and as its dysfunction is involved in disease and aging, the necessity to fully understand its mechanism created a strong focus on this enzyme in the field of mitochondrial respiration.

The work presented in this thesis report is articulated around two main axes, both aiming to clarify the function of Complex I. First, the creation of a sensor involving the biomimetically immobilized enzyme is presented and probed through a combination of surface enhanced infrared absorption spectroscopy (SEIRAS) and electrochemistry. This sensor is then tested against different substrates and inhibitors.

In a second part, the interaction of Complex I with lipids, inhibitors (Zn^{2+} and NADH-OH) and the role of a Tyrosine situated in the NADH binding pocket are investigated through electrochemically induced UV-Vis and FTIR difference spectroscopies and ^{1}H-^{2}H exchange kinetics. The results gathered through these experiments are then explored under a structural perspective and a coupling mechanism between quinone reduction and proton translocation is proposed.

1 Introduction

1.1 The living cell and how it harvests energy

The cell is the smallest structural and functional unit of living organisms. Depending on its ribosomal RNA, a cell is classified as prokaryotic (Achaea, Bacteria) or eukaryotic (Protists, Fungi, Plants and Animals). Most prokaryotic cells correspond to unicellular organisms and most eukaryotic cells are at the basis of pluricellular organisms. In eukaryotes, specific metabolic activities are compartmentalized in organelles separated from the cytosol by phospholipid membranes, whereas in prokaryotes these functions are localized in the cytosol or in the cytoplasmic membrane. Figure 1.1.1 summarizes the differences between the generalized bacterial, animal and plant cells.

All cells need to harvest and transform the energy from their environment to grow, survive and reproduce. This energy is transiently stored by all cells in the form of Adenosine triphosphate (ATP). The two major cellular energy converting processes are photosynthesis and cellular respiration :

Photosynthesis, mainly performed by plants and some bacteria, transforms the energy of light into the formation of ATP from Adenosine diphosphate (ADP) and inorganic phosphate (P_i), as well as the reductions of Nicotinamide Adenine Dinucleotide Phophate ($NADP^+$) to NADPH and of H_2O to O_2. This is achieved through a chain of pigments (chlorophylls) and membrane embedded enzymes (photosystems I[1, 2] and II[3, 4], cytochrome b_6f[5], ATP synthase[6-10], ferredoxin-$NADP^+$ reductase[11]) located in the plants' chloroplasts. The energy stored on ATP and NADPH is then used in the Calvin cycle[12] to fixate CO_2 in the form of glyceraldehyde-3-phosphate (G3P), a building stone for the synthesis of saccharides (as glucose), amino- or fatty-acids.

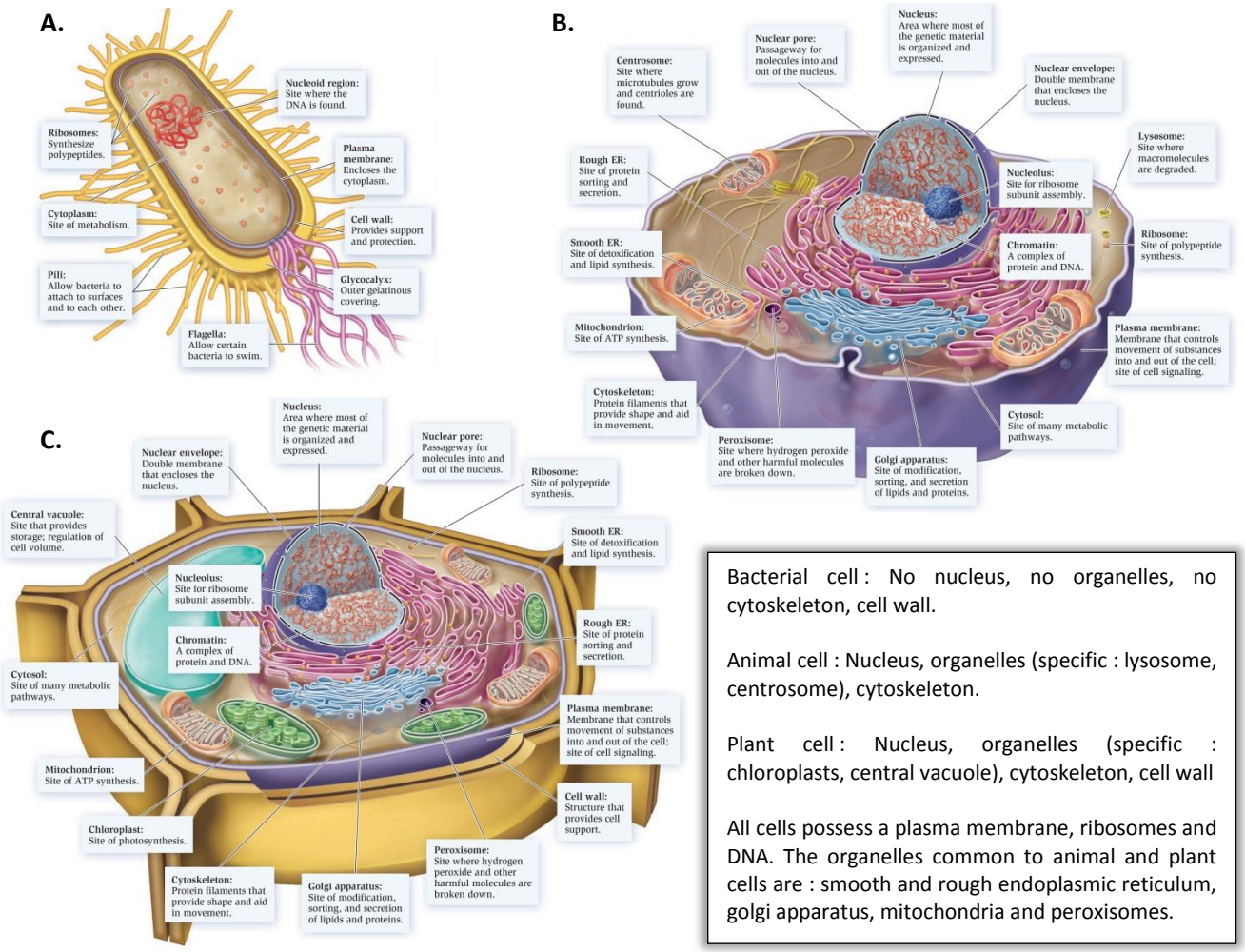

Figure 1.1.1 : Schematic representation of A. the bacterial-, B. the animal- and C. the plant-cell and summary of their similarities and differences. Adapted from ref[13]. The pictures are not to scale, as the general volume of a eukaryotic cell is ca. 1000x larger than for a prokaryotic cell.

Cellular respiration is the process which couples the exergonic oxidation of nutrients (mainly carbohydrates) produced through photosynthesis to the endergonic formation of ATP from ADP and P_i. Organisms unable to photosynthesize first have to absorb these nutrients from their environment. At the beginning of cellular respiration, metabolic processes (principally glycolysis) break down the nutrients to smaller fragments (catabolism) which then enter the Krebs cycle[14], *via* pyruvate and acetyl coenzyme A. Within this cycle, succinate is formed and Nicotinamide Adenine Dinucleotide (NAD^+) is reduced to NADH. The electrons hereby stored are finally transferred through a network of membrane embedded enzymes (respiratory complexes I - IV - see chapter 1.2 for further details) and mobile electron carriers to the almost universal electron acceptor in aerobic respiration, oxygen.

The free energy hereby liberated is used by ATP synthase (also termed Complex V) to drive the synthesis of ATP from ADP. The network of enzymes and electron carriers underlying the last steps of cellular respiration is referred to as the respiratory chain or electron transfer chain (ETC) and the process is termed oxidative phosphorylation (OXPHOS). In eukaryotes, the Krebs cycle occurs in the mitochondrial matrix and the ETC is embedded in the inner mitochondrial membrane, whereas in respiring bacteria they are located in the cytosol/cytoplasmic membrane. Anaerobic respiration also uses an ETC (although with different enzymes than for aerobic respiration) and the final electron acceptors are other oxidizing substances, such as sulfates, nitrates or fumarate.

Cellular respiration coupled to oxidative phosphorylation is responsible for the production of about 90 % of ATP in respiring organisms and is therefore the major source of energy for the metabolism. For the oxidation of one mole of glucose in mammalian mitochondria, 10 NADH and 2 succinates are formed. Classical textbook values indicate that up to 34 moles of ATP can be produced through aerobic oxidative phosphorylation of these 12 substrates[13, 15], in addition to the 2 moles of ATP produced by glycolysis (36 ATP in total). A more recent reevaluation of this stoichiometry estimated the total ATP production from one mole of glucose closer to 30[16]. In respiring bacteria, the situation can be different and depends on the nature of the enzymes catalyzing parts of this process. Besides energy in a cell-usable form (ATP), aerobic respiration also generates CO_2 and H_2O as waste products, closing the energetic cycle of life.

In the absence of a respiratory chain or if no external terminal electron acceptor is available, some cells can rely on glycolysis to gain ATP from nutrients. The reducing equivalents and substrates produced through glycolysis are then transformed into other small molecules, for example ethanol in yeasts or lactic acid in muscle cells. This process is called fermentation and is much less efficient than cellular respiration, as it produces only 2 ATP per glucose.

1.2 The respiratory chain

In the early twentieth century, the works of Keilin[17] on cytochromes and of Warburg[18] and Wieland[19] on respiratory hydrogen carriers had led to the first concept of the respiratory chain : a water-insoluble complex of redox carriers, operating between the reducing substrates or coenzymes and molecular oxygen. This concept however failed to explain the mechanism linking the energy-generating electron transfer to the production of ATP by ATPase ; hypothetical stable high-energy intermediates were thought to play a role in the process[20]. The lack of experimental evidence for such intermediates and the work of Mitchell on the biochemical concepts of chemiosmotic group-translocation reactions and vectorial metabolism led him to propose another theory in 1961[21]: the energy from electron transfer is accumulated into a transmembrane electrochemical gradient (termed proton-motive force) through ion (H^+) pumps within the respiratory complexes. The protons then flow back along their gradient and through the ATP synthase, which uses this energy to drive ATP production. After initial rejection of this theory by the scientific community, increasing experimental evidence of ion pumping by the respiratory enzymes could not anymore be ignored - the chemiosmotic hypothesis was born. Eventually, it was summarized in four simple postulates[22] :

1. ATPase systems are hydro-dehydration proteins specific to water and ATP that couple the reversible flow of H^+ across the membrane to the synthesis of ATP from ADP and P_i.
2. The respiratory chain located in the membrane couples electron-flow between substrates of different redox potentials to H^+-translocation across the membrane. These membrane bound enzymes contribute to the H^+-gradient across the membrane that is then used by the ATP synthase.
3. Exchange proteins transport anions against an OH^- gradient and cations against an H^+ gradient in order to maintain the osmotic difference across the membrane. These proteins also allow the entrance of metabolites without collapsing the membrane potential.
4. The enzymes involved in postulates 1, 2 and 3 are located in membranes with low permeability to H^+ and ions in general.

Following the consecration of the chemiosmotic theory by the awarding of a Nobel prize to Mitchell in 1978[23], significant efforts were made to get structural insights into the enzymes composing the respiratory chain. From the beginning of the 1990's to the present

date, all respiratory complexes have been crystallized and their structure determined through X-ray diffraction at sufficiently high resolutions to discern single amino acids (higher than ca. 3.5 Å). Except for the first complex, NADH:ubiquinone oxidoreductase, the available structures include the eukaryotic (mitochondrial) enzymes. Figure 1.2.1 summarizes the structure of the mitochondrial respiratory chain and its chemiosmotic coupling mechanism, followed by a brief description of each respiratory enzyme. Please note that in prokaryotes the nature and function of these enzymes can be different : for example, in the aerobic respiratory chain from *Escherichia coli* no cytochrome bc_1 complex is present and the terminal oxidase (cytochrome bo_3 ubiquinol oxidase[24]) directly uses the electrons from ubiquinol to reduce O_2[25]. The variety of reduced substrates and terminal electron acceptors that can be used by prokaryotes also contributes to a higher enzymatic diversity than in eukaryotes. Transmembrane F_1F_o ATP synthases on the other hand all share a common structure and function, be it in cellular respiration or photosynthesis.

In the mitochondrion, the inner membrane forms folds called cristæ, which harbor the respiratory chain (Figure 1.2.1 A.). The proton gradient created by the ETC is thus spatially concentrated in these structures, which is important for increasing the overall efficiency of oxidative phosphorylation. This will be described in further details on page 12. The respiratory complexes I-V from Figure 1.2.1 B. (left to right) have the following characteristics and function :

Complex I (NADH:ubiquinone oxidoreductase) is the first entry point of electrons in the respiratory chain. It couples the oxidation of NADH in its soluble part to the reduction of ubiquinone, a soluble electron carrier (see page 10), in its membrane part. The free energy released by this process is transformed into the translocation of four H^+ (current consensus value) across the membrane, by a mechanism that is yet to be defined precisely. As Complex I is the main enzyme studied in the present work, it will be described in further details in chapter 1.3. The net reaction catalyzed by Complex I is as follows :

$$NADH + Q + 4\ H^+_{in} \rightarrow NAD^+ + H^+ + QH_2 + 4\ H^+_{out}$$

(in = mitochondrial matrix ; out = intermembrane space)

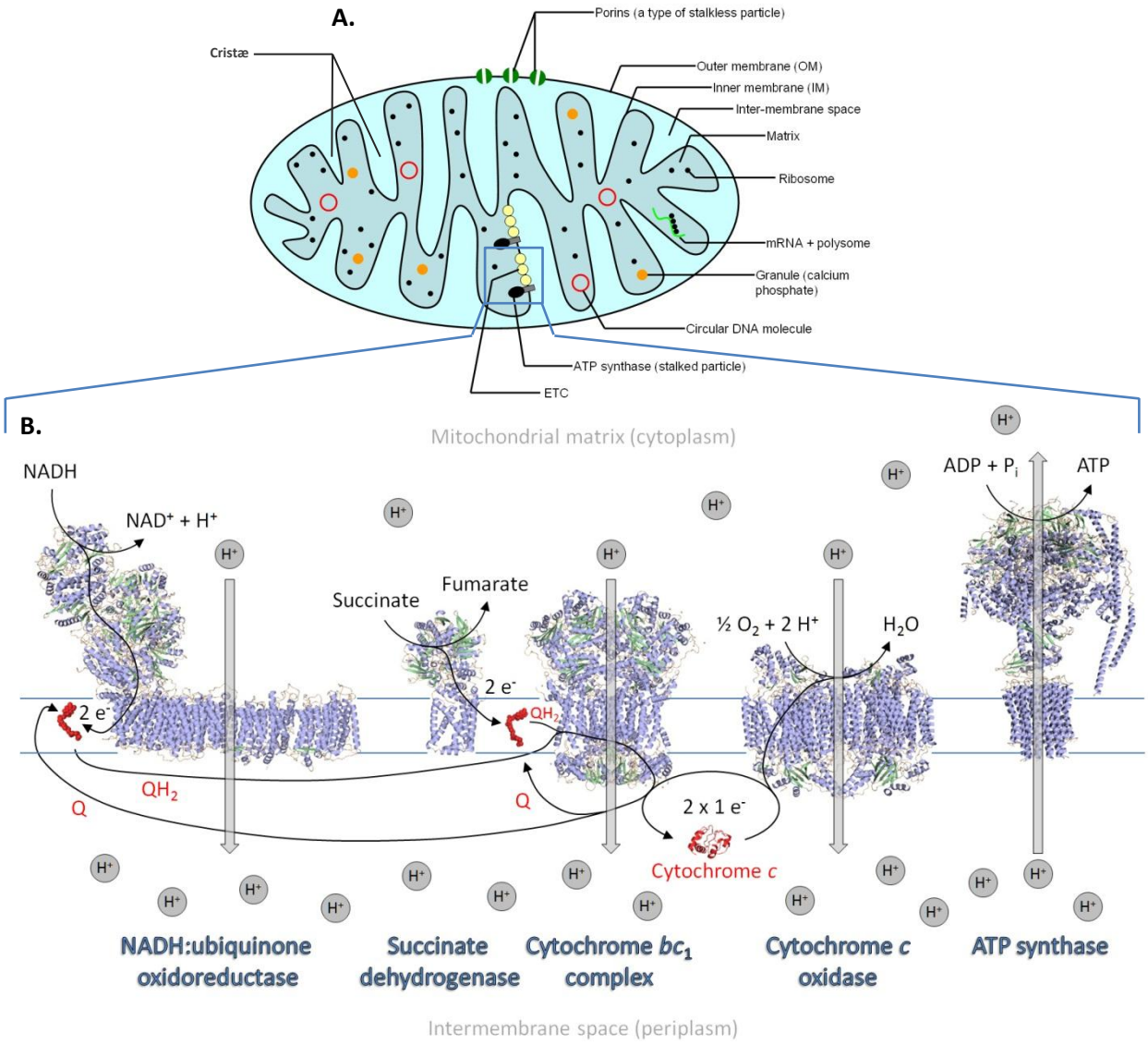

Figure 1.2.1 : Structure of the mitochondrion, structure, organization and functioning of the respiratory chain. A. The structure of the mitochondrion (sliced view) was adapted from ref[26]. **B.** The inner mitochondrial membrane is schematized by two parallel blue lines. The respiratory chain enzymes were represented using PyMOL. Only the protein backbone is shown and colored by secondary structure : α-helices in blue, β-sheets in pale green and β-turns in wheat. The mobile electron carriers ubiquinone 10 and cytochrome *c* are colored in red. The following crystal structures were used (with PDB accession ID given in brackets) : NADH:ubiquinone oxidoreductase from *Thermus thermophilus* (4HEA) ; Succinate dehydrogenase (quinone) from *Sus scrofa* (3AEF) ; Cytochrome bc_1 complex from *Bos taurus* (2A06) ; Cytochrome *c* oxidase from *Bos taurus* (2DYR) ; ATP synthase - Central stalk from *Saccharomyces cerevisiae* (2WPD) and stator from *Bos taurus* (2CLY) ; Cytochrome *c* from *Bos taurus* (2B4Z).

Complex II (succinate dehydrogenase [SDH] or succinate:quinone oxidoreductase [SQR])[27, 28] is the second entry point of electrons in the ETC. It oxidizes succinate to fumarate and transfers the released electrons to drive ubiquinol formation *via* a chain of redox cofactors : typically a Flavin Adenine Dinucleotide (FAD), three FeS clusters and a *b*-type heme (Figure 1.2.2 from ref[29]). It is the only enzyme of the respiratory chain that also participates in the Krebs cycle and that does not pump protons, the latter being due to the insufficient amount of free energy liberated by the electron transfer from succinate to Q ($\Delta E'_0$ = 15 mV, $\Delta G'_0$ = -2.9 kJ.mol^{-1}) compared to the cost of moving a proton across the membrane (>15 kJ.mol^{-1}). The family of Complex II-type enzymes also comprises fumarate reductase (FRD) and quinol:fumarate oxidoreductase (QFR), which catalyze the reverse reaction of SDH / SQR in the anaerobic respiration of some organisms[30]. The reaction catalyzed by SQR is as follows :

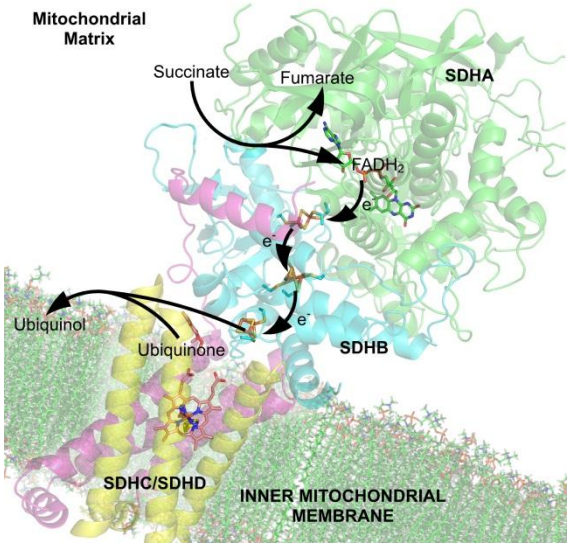

Figure 1.2.2 : Representation of the Complex II mechanism and its cofactors.

$$\text{Succinate} + Q \rightarrow \text{Fumarate} + QH_2$$

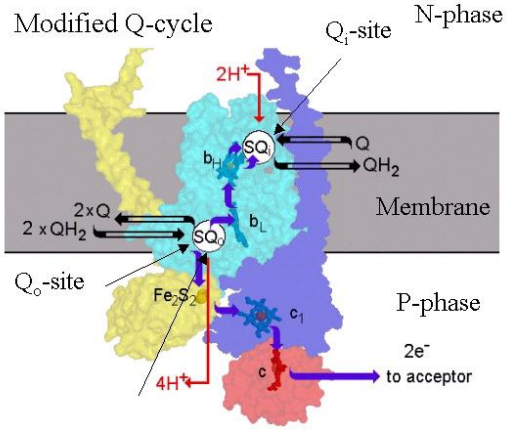

Figure 1.2.3 : Schematic representation of the Complex III mechanism.

Complex III (cytochrome bc$_1$ *complex)*[31] transfers the electrons from the previously reduced ubiquinol to another soluble electron carrier, cytochrome *c* (see page 11). This is accompanied by a release of free energy which is transformed into indirect proton pumping across the membrane. Complex III is a hetero-dimer[32] in which proton and electron transfers occur through the Q-cycle[33, 34], supported by the cofactors heme b_{Low}, heme b_{High}, heme c_1 and an FeS cluster (in the Rieske protein) and

summarized in Figure 1.2.3 (from ref[35]). Two quinone sites are present : Q_0, located near the intermembrane space (p side) and Q_i, located near the mitochondrial matrix (n side). Oxidation of ubiquinol at Q_0 results in the release of two protons at the p side. Simultaneously, the 2 e^- from the reduction of ubiquinol are split to reduce the FeS cluster and heme b_L. Heme b_L then gives its electron to the Q_i site via heme b_H. A ubiquinone bound here is reduced to ubiquinol in a two-step mechanism, together with an uptake of 2 H^+ from the n side. The reduced FeS center delivers its electron to heme c_1 by a large conformational movement (> 20 Å) of the Rieske protein[36]. Electrons are donated to cytochrome *c*. Overall, 2 H^+ are taken in from the n side and 4 H^+ are released on the p side, while two electrons are donated one at a time to cytochrome *c.* The cytochrome bc_1 complex is closely related to the cytochrome b_6f complex from photosynthesis[5], which also function through a Q cycle and builds up an transmembrane electrochemical H^+ gradient. The reaction catalyzed by Complex III is the following :

$$QH_2 + 2 \text{ cytochrome } c\ (Fe^{III}) + 2\ H^+_{in} \rightarrow Q + 2 \text{ cytochrome } c\ (Fe^{II}) + 4\ H^+_{out}$$

Complex IV (cytochrome c *oxidase)*[37, 38] receives electrons from cytochrome *c* and uses them to reduce O_2 to H_2O. As in complexes I and III, the energy released from this reaction is used to pump H^+ across the membrane. The cofactors underlying electron transfer are Cu_A, heme *a*, and the bimetallic heme a_3 - Cu_B center where oxygen reduction occurs[39]. In the X-ray structure shown in Figure 1.2.1, Complex IV is a homodimer, but this is not a requirement for its function[40]. Crystallographic studies of cytochrome *c* oxidase showed that a post-translational modification links the C6 of a tyrosine to the ε-N of a histidine located in the vicinity of the dinuclear center, enabling the latter to accept four electrons when reducing O_2 to H_2O[41]. The mechanism of oxygen reduction is highly complex (Figure 1.2.4 from ref[42]) : first, two electrons are donated by two

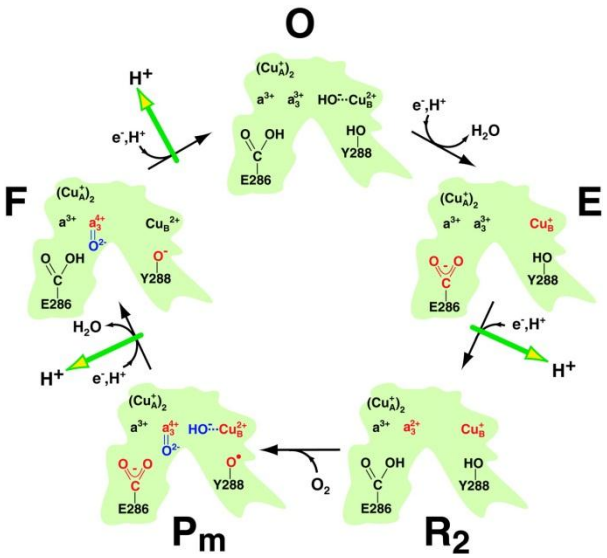

Figure 1.2.4 : Catalytic cycle of the cytochrome c oxidase

cytochrome *c* molecules, via Cu_A and heme *a* to the Fe^{3+} - Cu^{2+} binuclear center, reducing it to the Fe^{2+} - Cu^{+} form. An OH^- ligand bound here is protonated, lost as H_2O and replaced by O_2. The oxygen is rapidly reduced (the O=O bond is broken) by two electrons coming from heme a_3's Fe^{2+}, forming a ferryl-oxo moiety (Fe^{4+}=O). The oxygen atom facing Cu_B^{+} picks up one electron from the copper and a second electron as well as a proton from the hydroxyl of the neighboring tyrosine, yielding a tyrosyl radical. A third electron delivered by another cytochrome *c* is used, together with two protons, to restore the tyrosine and to convert the OH^- bound to Cu_B^{2+} to H_2O. The fourth and last electron from another cytochrome *c* finally reduces the ferryl oxo species to Fe^{3+}, while a proton regenerates the hydroxide ion coordinated in the middle of the dinuclear center, thus closing the enzymatic cycle. Protons are pumped through the membrane at different steps of the cycle (as shown be the green arrows on Figure 1.2.4) through three proton channels - D, K and H - but the exact mechanism linking the two is still unclear. The reaction catalyzed by Complex IV is the following (note that it requires 4 reducing equivalents, i.e. the oxidation of two NADH or succinates) :

$$4 \text{ cytochrome } c\ (Fe^{II}) + 8\ H^+_{in} + O_2 \rightarrow 4 \text{ cytochrome } c\ (Fe^{III}) + 2\ H_2O + 4\ H^+_{out}$$

Complex V (F_1F_0 - ATP synthase)[9, 10], often described as the smallest known molecular rotor, converts the electromotive force (electrochemical gradient) into a rotary torque that is used to promote substrate binding and to liberate ATP[7, 8] (Figure 1.2.5 from ref[43]). F_o represents the membrane part of the enzyme (subunits a, b and c), while F_1 is the soluble domain (α, β, γ, δ and ε subunits). The rotor consists of subunits $\gamma\varepsilon c_n$ (where *n* = 8-15, forming a c-ring) and the stator comprises subunits $\alpha_3\beta_3\delta b_2 a$[6]. Protons enter the enzyme through a half-channel facing the intermembrane space in subunit a and are subsequently transferred to a c subunit. Here, a conformational change by the protonation of acidic residues causes the rotor to turn clockwise (when viewed from the intermembrane space). The proton is then released through the matrix-facing half-channel in subunit a. Each time the γ shaft turns by 120°, its interaction-

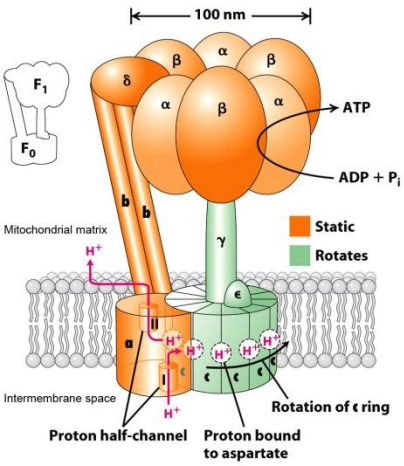

Figure 1.2.5 : Mechanism of the F1Fo ATP synthase

pattern with the three β subunits changes, causing a succession of three different conformations in these subunits for a complete rotation of the shaft (360°). In the first conformation, ADP and P_i bind with high affinity ; in the second ADP and P_i bind so tightly that ATP is made ; in the third ATP (and ADP and P_i) bind weakly and ATP is released. The number of protons required for a complete rotation depends on the number of c subunits (*n*) in the c-ring. In the F_1F_o ATP synthase of vertebrates and probably inverterbrates also, 8 H^+ are thus required for the synthesis of 3 ATP molecules, to which an additional H^+/ATP should be added to import ADP into the mitochondrion through the ADP/ATP translocase. Thus, the synthesis of one ATP requires 11/3 = 3.7 H^+. The reaction catalyzed by ATP synthase is as follows :

$$3\ ADP + 3\ Pi + n\ H^+_{out} \rightarrow 3\ ATP + + 3\ H_2O + n\ H^+_{in}$$

In addition to the membrane embedded enzymes, where electron transfer is mediated by electron-tunneling[44, 45], soluble electron carriers also play an essential role in the respiratory chain, as they allow diffusion-based long-range electron transfer from one complex to another :

Ubiquinone-10 (Q, UQ or CoQ_{10})[46] is a lipid soluble small molecule comprising a polar 2,3-dimethoxy-5-methylpara-p-benzoquinone ring attached to an apolar tail of ten isoprenoid at ring position 6 (Figure 1.2.6). Its 2 e^-, 2 H^+ reduction (E'_0 = 65 mV[47] although sometimes 45 mV is used) forms ubiquinol (UQH_2). In a controlled, hydrophobic environment such as the interior of a protein, semiquinones (radicals) can also be formed[48]. The midpoint potential associated to the formation of these species can vary significantly from E'_0 UQ/UQH_2[49, 50], a feature of mechanistic importance for the enzymes from the respiratory chain. The quinone pool is the population of UQ/UQH_2 molecules in the lipid bilayer. In general, they are considered as diffusing freely in the membrane, mediating electron transfer

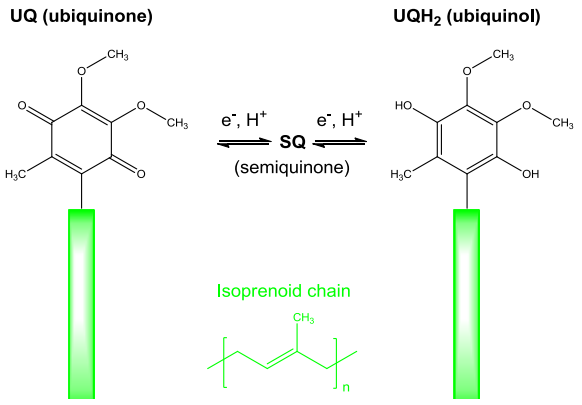

Figure 1.2.6 : Structure of ubiquinones.

through random collisions with enzymatic complexes. This model is called “simple Q pool behavior” or “fluid model”[51], but only partially reflects the reality of electron transfer through Q. Non-random distribution of proteins throughout the membrane, for example by the formation of supercomplexes (see page 12) can regulate interenzymatic electron transfer[52]. Quinones bind to their enzymatic oxidoreduction sites through polar interactions with their headgroup and hydrophobic interactions with their isoprenoid. No specific “strong” Q binding motives have been identified in the respiratory or photosynthetic complexes, only a “weak” motif is known[53]. Quinones with different headgroups (and thus different E'_0) and/or isoprenoid chain length can also be used in the respiratory chains of some organisms, for example menaquinone-8 in many bacteria. In photosynthesis, plastoquinone-9 is used to carry reducing equivalents from Photosystem II to the cytochrome b_6f Complex[5].

Cytochrome c is a small water soluble protein bearing a single *c*-type heme, which can accept one electron : $Fe^{3+} + e^- \rightarrow Fe^{2+}$, E'_0 = +235 mV. It consists mainly of α-helices and random structures[54]. Other types of cytochrome *c* with different E'_0 exist, often named after the position of their α-band absorption, e.g. cytochrome c_{552}. As for Q, cytochrome *c*-mediated electron takes place through random encounters of the freely diffusing protein with its redox partners (Complexes III and IV)[55] and can be promoted by supercomplex formation. Cytochrome *c* - enzyme interactions occur through the formation of an encounter complex steered by long range electrostatic forces, followed by the formation of a bound state mainly through apolar interactions[56]. Cytochrome *c* was also reported to have role in apoptosis, where it initiates a major caspase activating pathway by leaving the mitochondrion [57, 58]. This is triggered by the production of reactive oxygen species (ROS) in the respiratory chain, which leads to the cytochrome *c*-mediated peroxidation of a mitochondria specific phospholipid, cardiolipin (CL), in turn leading to membrane permeabilization to facilitate cytochrome *c* escape[59, 60].

Spatial and supramolecular organization of the respiratory chain : Figure 1.2.1 showed that the respiratory chain is located in the mitochondrial cristae. The volume of the intermembrane space is thus restrained, facilitating its rapid acidification by the respiratory H^+ pumps. The formation of ATP synthase supercomplexes (dimers) contribute to shaping the edges of these cristæ[61], as shown in Figure 1.2.7 (from ref[62]). The other respiratory

complexes are distributed over the flat regions of the membrane[62], creating a chimney-like system where the consumption of protons by ATP synthases creates a proton gradient parallel to the membrane surface[63], thus enhancing the overall efficiency of the respiratory chain by channeling of the proton diffusion. In addition to this repartition through the membrane, Complexes I to IV can also organize in supercomplexes. Although the existence of such assemblies was predicted over 50 years ago[64], it was unambiguously experimentally proven only in the last decade[65]. The most well-documented supercomplexes in mitochondria are Complex I/III$_n$, Complex I/III$_n$/IV$_n$ (also termed "respirasome" - Figure 1.2.8) and Complex III/IV$_n$. Complex II seems less prone to supercomplexes association, although small fractions were shown to form a complex with respirasomes. The proportions of respiratory enzymes associated in supercomplexes is dynamic : these associations define dedicated Q and cytochrome *c* pools, organizing electron flux to optimize the use of available substrates[52]. Diverse factors promoting supercomplex assembly were identified[65], including proteins (Rcf-1 and 2, AAC1 and 2) and lipids[66, 67] (phosphatidylethanolamine [PE] and cardiolipin [CL]).

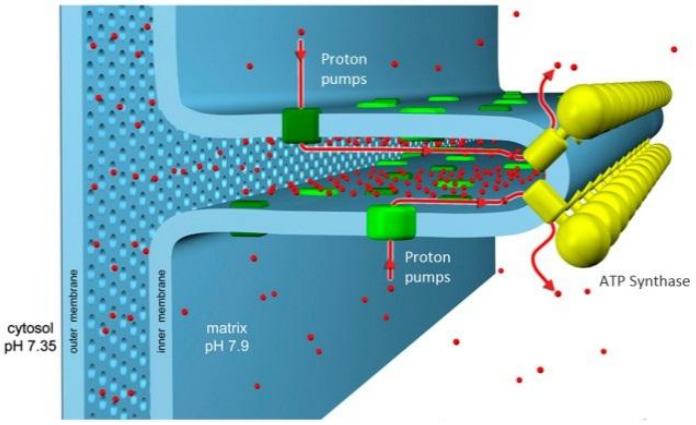

Figure 1.2.7 : Macromolecular organization of the mitochondrial cristæ.

Indications that supercomplexes in turn assemble into megacomplexes, as for example a string of ATP synthase dimers, were also reported[68]. In bacteria, supercomplexes also exist[69] but their composition and repartition are less clear, owing to a higher diversity of respiratory chains.

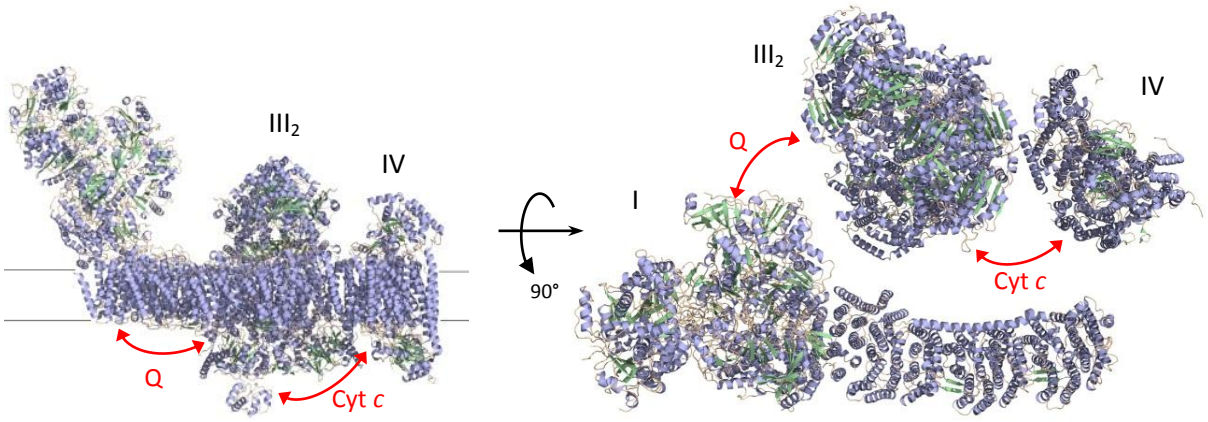

Figure 1.2.8 : Representation of the mitochondrial respirasome (supercomplex I/III$_2$/IV). The structure of the bovine mitochondrial respirasome obtained by cryo-EM) was used (PDB 2YBB), in which Complex I was manually replaced by the X-ray structure of the entire enzyme from *T. thermophilus* (PDB 4HEA). The approximate pathways of Q and cytochrome c are shown by the red arrows.

Thermodynamics in the respiratory chain : Equation *(1)* represents the change in Gibbs free energy ΔG associated to the transportation of one mole of ion X carrying a charge Z down an electrochemical gradient. F is the Faraday constant, $\Delta\Psi$ the membrane potential, R the ideal gas constant, T the temperature (in Kelvin), *A* and *B* the two phases separated by the membrane. When the ion is the proton, equation *(1)* can be simplified to equation *(2)*, which represents the proton electrochemical gradient. Note that some bacteria can also power their oxidative phosphorylation through a sodium motive force, based on the sodium electrochemical gradient $\Delta\tilde{\mu}_{Na^+}$.

$$\Delta G\ (kJ.mol^{-1}) = -ZF\Delta\Psi + 2.3\ RT\ log_{10}\left(\frac{[X^Z]_B}{[X^Z]_A}\right) \qquad (1)$$

$$\Delta\tilde{\mu}_{H^+} = -F\Delta\Psi + 2.3\ RT\Delta pH \qquad \text{where } \Delta pH = pH_B - pH_A \qquad (2)$$

Mitchell defined the proton-motive force Δp or *pmf* as the opposite of $\Delta\tilde{\mu}_{H^+}$ and related it to a potential by introducing the Faraday constant (equation *(3)*). Besides facilitating the comparison with redox potential differences in the electron transfer chain complexes generating the proton gradient, this also shows that there is a potential driving an

H^+ circuit, which would be pretty useless if there weren't molecular machines able to use it. Under physiological conditions and at 37°C, equation *(3)* becomes equation *(4)*.

$$\Delta p\ (mV) = -\frac{\Delta\tilde{\mu}_{H^+}}{F} \qquad (3)$$

$$\Delta p\ (mV) = \Delta\Psi - 60\ \Delta pH \qquad (4)$$

$\Delta\Psi$ and ΔpH are defined as the difference of the P phase (intermembrane space) *minus* the N phase (mitochondrial matrix). In mammalian mitochondria, $\Delta\Psi$ is in general around 170 mV and ΔpHca. -0.5, thus generating a Δp of 200 mV.

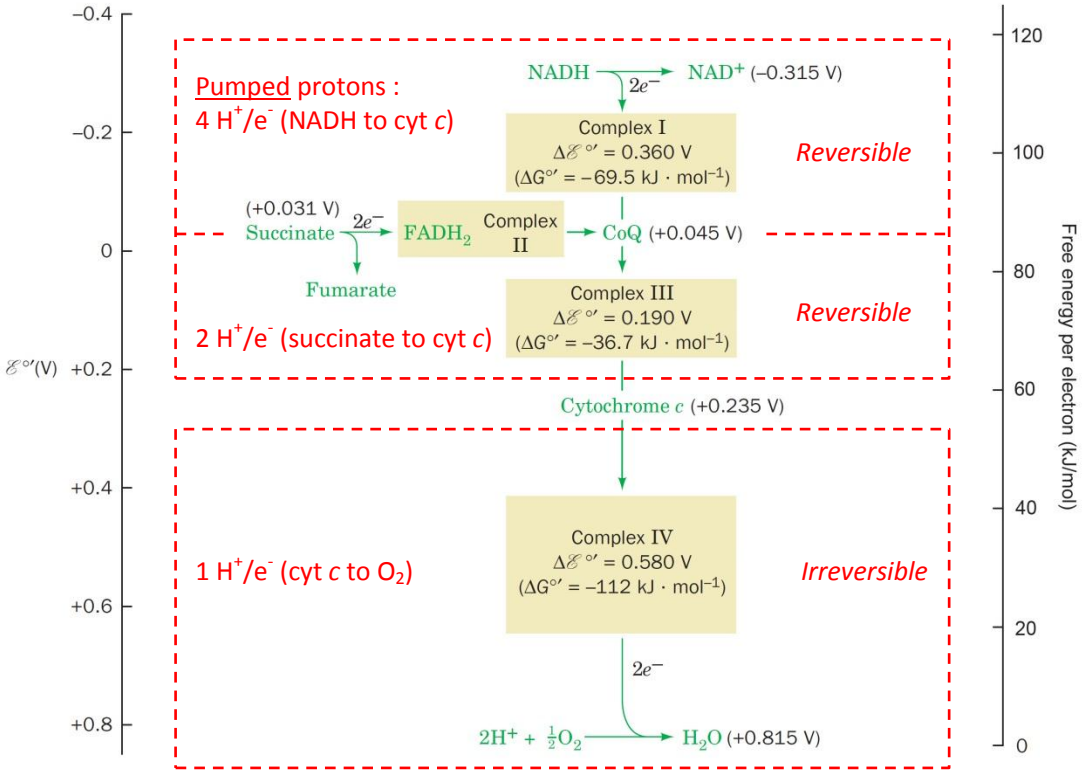

Figure 1.2.9 : Evolution of E'$_0$ and of free energy per electron in the respiratory chain. Adapted from ref[70]. For the sake of simplification, only vectorial ("pumped") protons were considered here. Additional Δp is generated through charge cancellation by O_2 reduction.

The successive electron transfer steps in the respiratory chain and the release of free energy transformed into the proton motive force and ATP formation can be correlated to

the differences between the standard redox potentials of the substrates of each respiratory complex through the following equation : $\Delta G'_0 = -nF\Delta E'_0$ (Figure 1.2.9).

For the oxidation of NADH or succinate by ½ O_2, the $\Delta E'_0$ is ca. 1.13 V ($\Delta G'_0 \approx -220$ kJ.mol^{-1}) and 0.78 V ($\Delta G'_0 \approx -150$ kJ.mol^{-1}), respectively. This results in the translocation of 10 and 6 H^+. If we assume that the Δp is 200 mV, the energy conserved in this proton gradient is thus 10 x 200 x *F* = 200 kJ for NADH and 120 kJ for succinate, showing that the energy efficiencies of these steps are high - about 80 to 90 %. As the synthesis of one ATP in mammalian mitochondria requires 3.7 H^+[71], the theoretical number of ATPs produced per reduction of ½ O_2 by NADH or succinate (termed P/O ratio) is 10/3.7 = 2.7 and 6/3.7 = 1.6, respectively. This is close to the experimentally measured values of 2.5 (NADH) and 1.5 (succinate), although these values can differ depending on the organism, the cell-type and external conditions[72]. Proton leakage due to defects in the membrane impermeability, "slips" in proton pumps (no H^+ is pumped during the enzymatic cycle) and numerous other factors can account for the small differences between theory and reality [72]. In addition, mitochondria can modulate the efficiency of their respiration in response to changes in the metabolism[73], up to complete uncoupling of the electrochemical gradient from ATP synthesis. This is for example used by the newborn or by hibernating animals to generate heat, and is achieved through uncoupling proteins (UCPs) present in the brown adipose tissue[74].

An important observation concerning the catalytic equilibria of the different sections in the respiratory chain can be made by comparing the pumped H^+/e^- ratio (*n*), Δp and the redox span ΔE_h accompanying an electron transfer. When the equilibrium (ΔG = 0) is reached, these factors can be related through equation *(5)* for a one electron transfer that crosses the membrane. The term $\Delta\Psi$ is thus introduced as it affects this transfer. The lower the value obtained for Δp, the closer the system is to equilibrium.

$$n\Delta_p = (\Delta E_h + \Delta\Psi) \qquad (5)$$

In the respiratory chain, three equilibria were assessed through this equation (Figure 1.2.9 and Table 1.2.1). The individual enzymes can also be assessed, as will be shown for Complex I in chapter 1.3.

Reaction	n (H^+/e^-)	ΔE_h(mV)	$\Delta\Psi$	$\Delta_{p,eq}$ (mV)
NADH + 2 cyt $c^{3+} \rightleftharpoons NAD^+ + H^+ + 2$ cyt c^{2+} (Complex I + Complex III)	4	550	-170	95
succinate + 2 cyt $c^{3+} \rightleftharpoons$ fumarate + 2 cyt c^{2+} (Complex II + Complex III)	2	205	-170	17.5
2 cyt c^{2+} + ½ O_2 + 2 $H^+ \rightleftharpoons$ 2 cyt c^{3+} + H_2O (Complex IV)	1	580	170	750

Table 1.2.1 : Estimation of Δp in three systems at equilibrium.

From the calculated values of Δp,eq, it is evident that Complex I, II and III are operating relatively close to the thermodynamic equilibrium between ΔE_h and Δp, at least compared to Complex IV. Consequently, the first three respiratory complexes can catalyze reverse electron transfer under specific conditions, whereas the reaction catalyzed by Complex IV is irreversible - it would require a 750 mV proton-motive force incompatible with membrane integrity. There are other reasons why catalysis by Complex IV is irreversible, but this is beyond the scope of this part. As the ATP synthase is also readily reversible, ATP hydrolysis can generate a sufficiently high Δp used to drive the reverse electron transfer. This process is used by some bacteria to convert the energy of ATP into high energy reducing equivalents (NADH or NADPH) that they can't obtain through the rest of their metabolism. Selective supply of oxidized or reduced substrates and/or inhibition of other members of the respiratory chain can also reverse the electron flow through Complexes I, II and III. These processes were and are still widely used to determine certain mechanistic details of these enzymes, for example through study of submitochondrial particles where the respiratory chain is artificially turned inside-out and thus easily experimentally accessible[75, 76].

1.3 The NADH:ubiquinone oxidoreductase (Complex I)

Complex I is the first entry point of electrons into the respiratory chain, catalyzing the oxidation of NADH, the reduction Q and coupling this electron transfer to the translocation of 4 protons across the membrane. From its first isolation by Hatefi in 1961[77] to nowadays, considerable progress has been made in elucidating the structure and functional details of Complex I[78-81]. It is an L-shaped protein with a mass of~1 MDa for the mammalian enzyme and comprises several cofactors and up to 45 different subunits, from which 14 form the functional core of the enzyme (Figure 1.3.1). Conserved homologues of these core subunits are found in all organisms that possess Complex I. They can be subdivided in two groups of 7 subunits, whether they are situated in the membrane arm or in the soluble arm, also called NADH-Dehydrogenase fragment (NDF). The proteins that do not belong to the functional core are termed supernumerary subunits and their number varies between organisms. With a few exceptions as in the Complex I from plants[82], their function is largely unknown and they were thus associated with generic roles in regulation, protection against reactive oxygen species (ROS), assembly and stability[83].

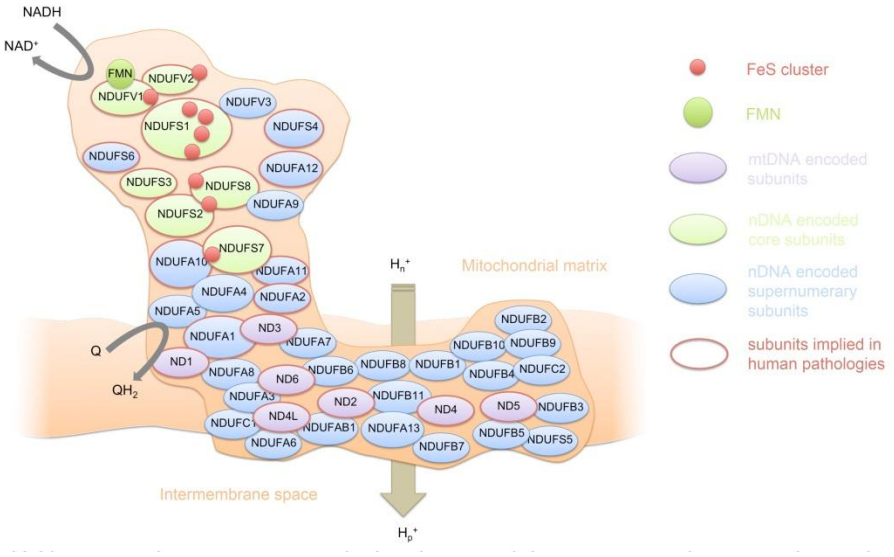

Figure 1.3.1 : Schematic subunit repartition of the human mitochondrial Complex I. Adapted from ref[84]. The catalytic sites and the redox cofactors are also indicated together with subunits known to be implied in human pathologies.

In eukaryotes, the 7 core subunits composing the membrane arm are encoded by the mitochondrial DNA, whereas the remaining subunits are encoded by nuclear DNA, synthesized in the cytosol and subsequently imported into the mitochondrion. Here, the assembly of the complete enzyme takes place through a process that remains yet to be completely understood, although considerable progress has been made in this field[85-87]. It was for example shown that prior to complete assembly, a 830 kDa fragment of Human Complex I assembles with the respirasome (supercomplex $I/III_n/IV_n$)[65, 88].

In prokaryotes which have Complex I, the enzyme is in general stripped down to its 14 core subunits for a total mass of a 530 kDa. Its function however is preserved. The two most studied prokaryotic NADH:quinone oxidoreductases are from *Escherichia coli* (where it is sometimes called NDH-1) and *Thermus thermophilus*. The crystal structure of the entire enzyme from the latter was recently solved at 3.3 Å resolution[89] (Figure 1.3.2), revealing key elements that were not evident from previous crystallographic studies[90, 91]. Structures of the membrane arm of *E. coli* Complex I at 3.0 Å resolution[92] and of the entire mitochondrial enzyme from *B. taurus* at 6.3 Å resolution[93] were also reported. Figure 1.3.2 also shows the correspondence between the subunits from *T. thermophilus* (termed Nqo since they are coded by the NADH:quinone oxidoreductase operon), *E. coli* (termed Nuo as they are coded by the NADH:ubiquinone oxidoreductase operon) and *H. sapiens* Complex I (called ND for NADH Dehydrogenase). The eukaryotic enzyme uses only ubiquinone-10 while the two prokaryotic enzymes use shorter chain derivatives : menaquinone-8 in *T. thermophilus* and both ubiquinone-8 and menaquinone-8 in aerobically grown *E. coli* cells[94].

In the context of this work the NADH:ubiquinone oxidoreductase from *E. coli*[95] was studied as it can readily be purified at high quantity and purity[96, 97], be genetically modified[97-99] and also because *E. coli* is the most well-known prokaryotic model organism. If not specified, the subunit nomenclature used hereafter thus refers to the *E. coli* enzyme.

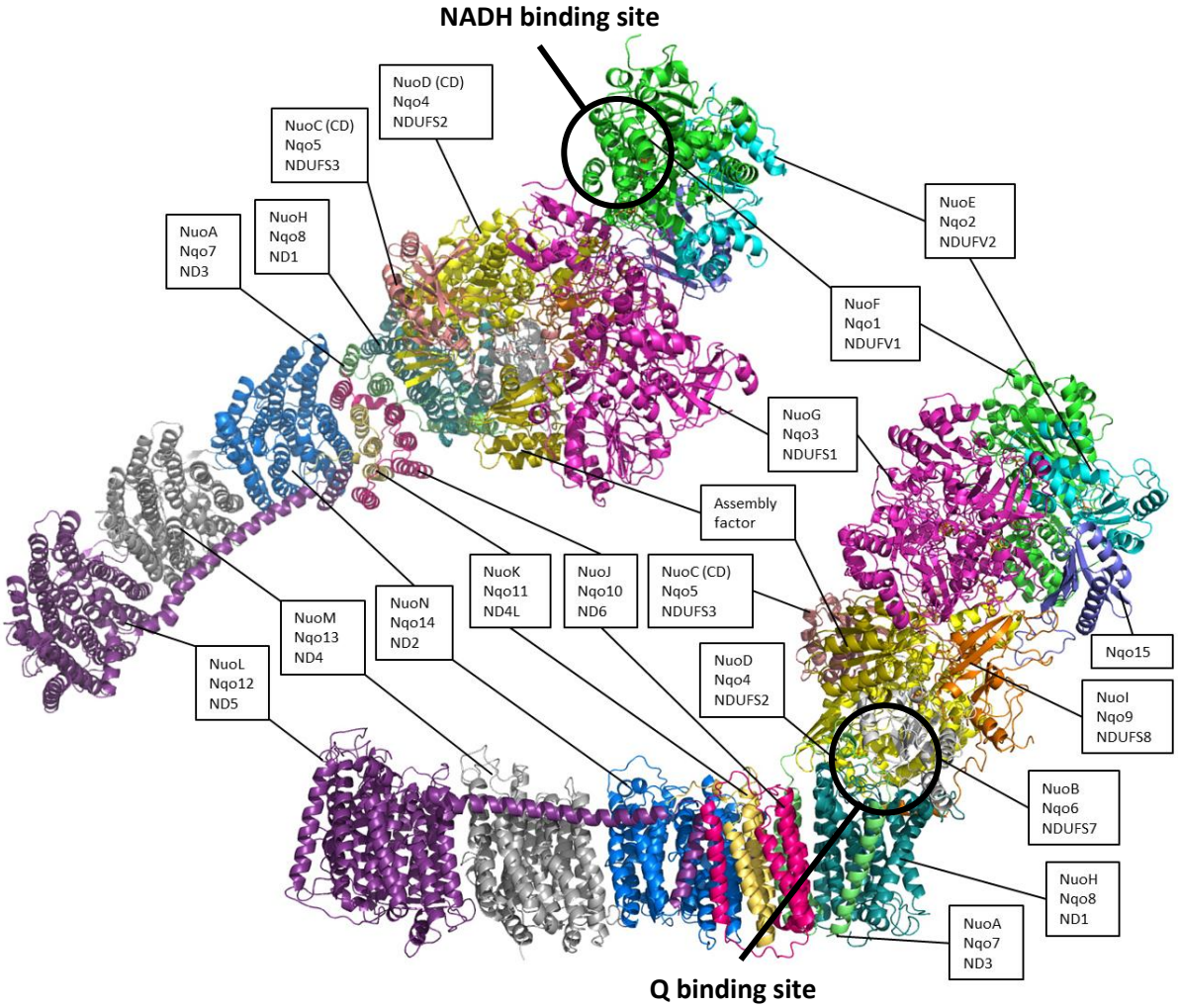

Figure 1.3.2 : Crystallographic structure of the entire Complex I from *T. thermophilus* and correspondence to homologuous core subunits from *E. coli* and *H. sapiens*. PDB ID : 4HEA. The Nqo15 subunit as well as the co-crystallized assembly factor are specific to the *T. thermophilus* Complex I.

The structures of the different core subunits of Complex I are homologous to smaller enzymes which assembled modularly during evolution to form the whole enzyme[49, 100]. Subunits NuoEFG, also termed the N-module since they harbor the NADH oxidase activity, are homologous to group-3 bidirectional soluble NiFe hydrogenases, which use soluble cofactors like F_{420}, NADH or NADPH to reversibly oxidize hydrogen. Subunits NuoBCDI, the so-called Q-module because it is the site of Q reduction, are related to another class of water-soluble as well as membrane bound NiFe-hydrogenases. Subunits NuoAJKLMN, referred to as the P-module since they hosts the Proton-pumping activity, are close to the class of membrane-potential driven Na^+/H^+ Mrp antiporters[101, 102]. Until recently, subunit

NuoH could not be traced back to any known ancestor solely on the basis of its amino acid sequence. Now it was shown that its structure is also related to those of Mrp antiporters[89]. The attachment of the soluble domain to the membrane arm thus probably originated in the capacity of the former to mimic a membrane potential to drive one or more antiporter modules. Some of the supernumerary subunits were also shown to be related to diverse enzymes, although their function seems to have been lost[103]. The evolutionary study of Complex I holds the key to numerous details about its function.

Redox cofactors and electron transfer : a chain of redox active cofactors located in the NDF fragment supports the transfer of electrons between NADH and Q in their respective binding sites, separated by a distance of approximately 80 Å. The NADH binding site is located in a pocket formed by subunits NuoEF (Figure 1.3.2) and comprises the first cofactor, the two electron-acceptor Flavin Mononucleotide (FMN). NADH gives these two electrons to FMN in one step in the form of an hydride[104]. The morphology and composition of this binding site will be described in details on page 23. The Q binding site is located in a cavity at the interface of subunits NuoBCDH (Figure 1.3.2) where the terminal cofactor N2, an obligatory one electron donating 4Fe-4S cluster, is found. This site is further detailed in page 27. Between the two, a chain of one 2Fe-2S and seven 4Fe-4S clusters[105] named N1 to N7 transfer the electrons through electron tunneling[106]. Their arrangement for the *T. thermophilus* Complex I is shown in Figure 1.3.3 A. All clusters are within efficient electron tunneling distance (< 14 Å) to their neighbor. An additional iron sulfur cluster (N7), found only in the Complex I from certain organisms, does not participate in the electron transfer but was shown to be essential for stability[107].

As the iron sulfur clusters from Complex I are obligatory one electron acceptors/donors, this raises the question how the two electrons from the reduced FMN ($FMNH^-$) are transferred through the chain. The probable answer resides in the presence of an additional 2Fe-2S cluster situated off the main electron path, N1a. Upon reduction of FMN, one electron is transferred to the first cluster of the main chain (N3) while the other is donated to N1a[91]. When the first electron tunnels further towards N2, the second passes again through FMN to N3. This is proposed to minimize the lifetime of the reactive FMN radical, also called flavosemiquinone ($FMN^{\bullet -}$ or $FMNH^{\bullet}$) and thus the production of reactive

oxygen species (see page 29). However the measurement of the intrinsic midpoint potential of N1a showed that its values vary significantly (from -400 to -150 mV) from one species to another[80], giving rise to the debate whether all Complex Is use the same mechanism. It is possible that the E_m of N1a can be modulated by conformational changes that occur in this part at different redox states of the enzyme[108].

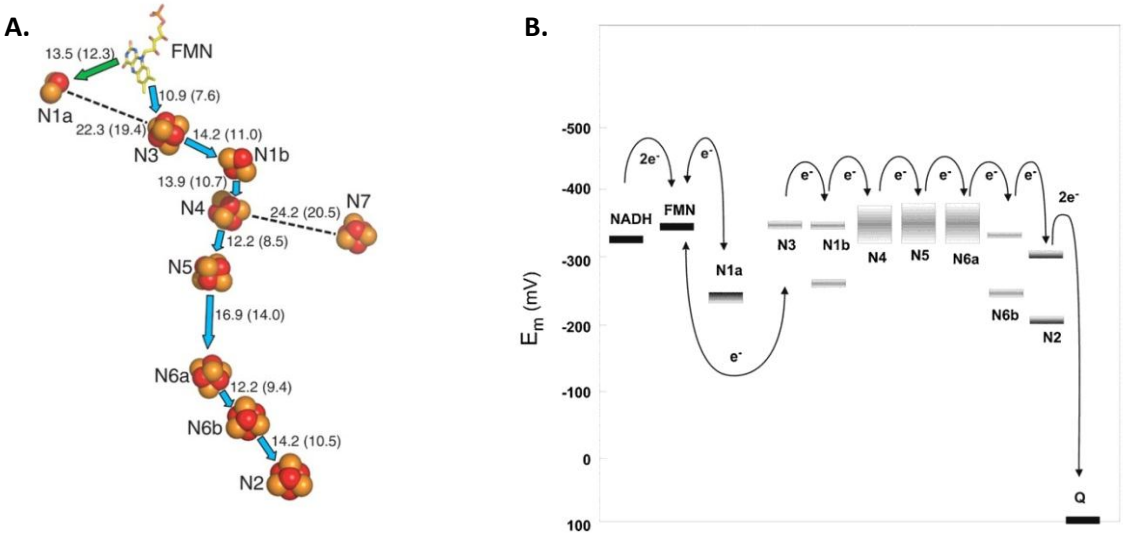

Figure 1.3.3 : A. Spatial arrangement of the FeS clusters in the *T. thermophilus* Complex I. B. Midpoint potential profile of the FeS clusters from *E. coli* Complex I. From refs[80, 91]. **A.** : the center to center and edge to edge distances between adjacent clusters are given in Å. The main electron path is shown by the blue arrows and the side path to N1a by a green arrow **B.** : The potentials are represented by bars. Large bars indicate uncertain values. Split bars indicate redox potentials redox for clusters thermodynamically interacting with their neighbors - high E_m's represent intrinsic values, low E_m's include interaction.

The midpoint potentials of the FeS clusters are arranged as shown in Figure 1.3.3 B. Clusters N3, N1b, N4, N5 and N6a are considered as almost equipotential to the FMN (-300 to -350 mV), which is useful to promote rapid electron tunneling. N6b and N2 have a less negative E_m, creating a potential gradient which attracts the electrons down the chain to N2. The intrinsic E_m values reported in the literature differ between species and from those shown here[109, 110]. It was however shown that these values could be harmonized to a certain degree when electrostatic interactions between the clusters were taken into account by calculation[79], as shown both in Figure 1.3.3 B. and in Figure 1.3.4 A. The E_m of Q is also

uncertain : its reduction occurs in a strictly controlled environment and involves the formation of semiquinone radicals, it is thought that the E_m of some steps could be as low as -300 mV and depend on the quinone's reduction and protonation states[49]. Such a low E_m for Q would also be compatible with the ability of Complex I to catalyze reverse electron transfer at a sufficiently high Δp, as it would facilitate the oxidation of QH_2 (or, to be more specific, of QH^- or Q^{2-}) by N2. The contribution of Δp to the E_m of Q was taken into account in Figure 1.3.4 A. The electron transfer process from FMN to Q can be described as a "tug-of-war" between their reduced, semiquinone and oxidized states where the rope would be the electrons[111]. The rate limiting step in the overall NADH to Q electron transfer is the reduction of Q by cluster N2[104]. The catalytic activity of Complex I is reversible and its rate and direction are controlled by Δp and by the redox states ([ox]/[red] ratio) of the NADH and Q pools[112]. The equilibrium is attained when $4\Delta p = -2\Delta E$, i.e when $\Delta p = -\Delta E/2$ ($\Delta\Psi$ does not affect this rate since the electron transfer does not cross the membrane). This equilibrium was experimentally determined to be attained when Δp reaches 157 mV[113] (Figure 1.3.4 B.).

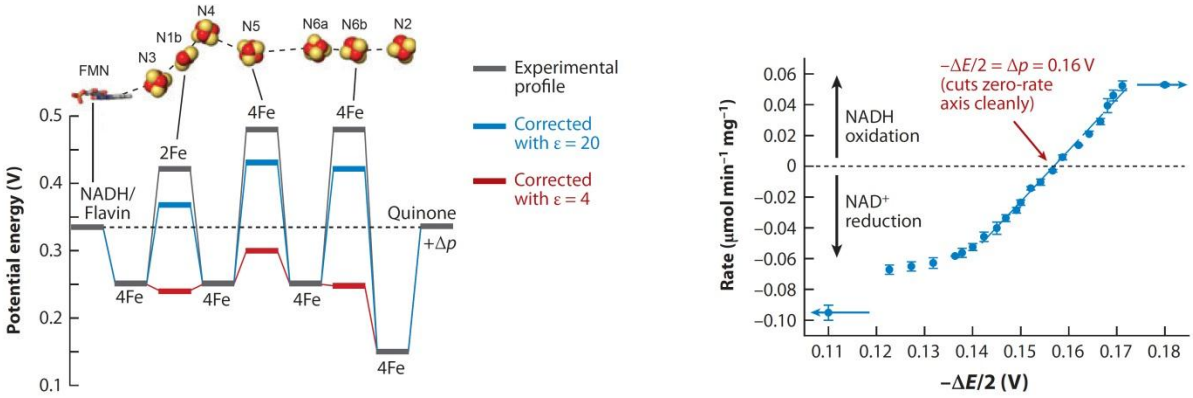

Figure 1.3.4 : A. Potential energy profile and B. Thermodynamic reversibility of Complex I from *B. taurus.* Adapted from ref[79]. **A.** The experimentally determined values for each cluster are shown in grey, the values in red include high electrostatic interactions and the values in blue include low interaction. The potential of the Q was corrected with Δp to enforce the equilibrium. **B.** Rate of NADH:fumarate oxidoreduction by submitochondrial particles (with KCN to inhibit cytochrome *c* oxidase and Δp generated by ATP hydrolysis) in function of ΔE (the potential for NADH:fumarate oxidoreduction, set by the NADH, NAD^+, fumarate, and succinate concentrations).

The NADH binding site and FMN : The cofactor FMN (Figure 1.3.5) is tightly (although non-covalently) bound in a specific pocket part of the NADH binding site, whose nature and structure determine the redox midpoint potentials of the flavin[114]. Free FMN in solution has an E_m of ca. -210 mV[115] for the two electron reaction at pH 7, whereas in Complex I it is lower : values from -330 to -350 mV were reported for the *E. coli* enzyme[80, 116], and -360 to -380 mV for the bovine Complex I. The one electron reactions in the bovine enzyme have an E_m of -414 and -336 mV for the $FMN^{1/0}$ and $FMN^{2/1}$ couples at pH 7.5, respectively[117]. Modifications of the FMN binding pocket, for example by genetic mutations of specific residues, will shift the midpoint potential[118, 119] and thereby impact the NADH oxidase activity of the enzyme. In addition, production of ROS and electron tunneling to N3 and N1a might be affected by the mutations without any noticeable shifts of E_m FMN. Strong modifications induced by harsh reducing conditions may also lead to the reversible loss of the cofactor[120].

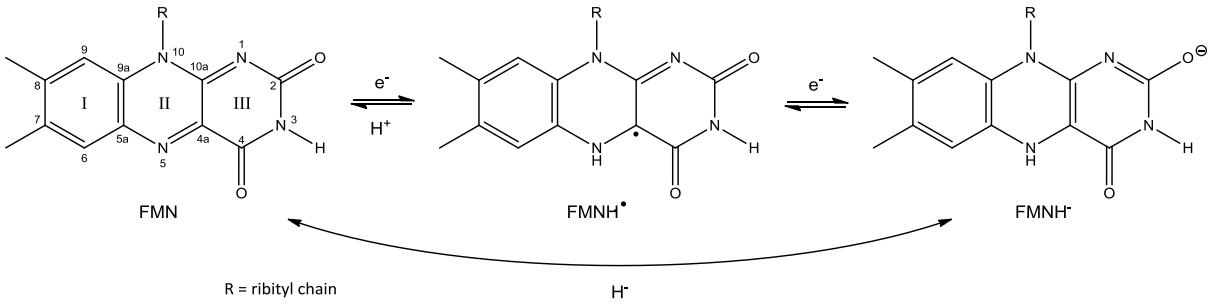

Figure 1.3.5 : Structures of FMN at three oxidation states occurring in Complex I. Atom and ring numbering are shown on the fully oxidized state of the cofactor. In Complex I, N1 and O(C2) are not accessible to protonation, thus $FMNH_2$ is not formed. The intermediate semiquinone state can also be $FMN^{\bullet -}$ if the deprotonation occurs before the $FMN^{1/0}$ transition. The hydride transfer from NADH is symbolized by the arrow connecting FMN to $FMNH^-$.

When compared to other NADH dehydrogenases, the NADH/FMN binding site of Complex I is constituted of an unusual Rossman nucleotide-binding fold created by an arrangement of four parallel β-sheets flanked by α-helices[91], instead of six parallel β-sheets as in the usual Rossman fold[81]. Differences in number and positions of Glycine rich loops also contribute to the creation of a unique nucleotide binding motif. As shown on Figure 1.3.6, the FMN (represented as sticks) is buried at the end of a solvent-accessible cavity

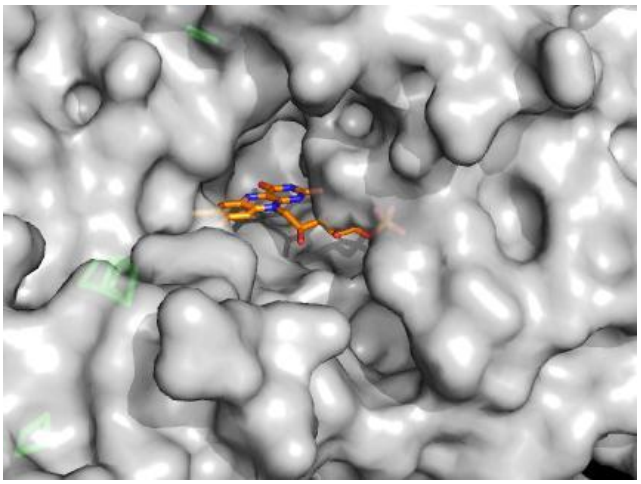

Figure 1.3.6 : Representation of the NADH and FMN binding pocket of Complex I. PDB ID : 4HEA.

(shown as a grey surface) where it is non-covalently immobilized through an array of conserved residues. This cavity can accommodate NADH. It was shown that the nicotinamide moiety of NADH is not essential for nucleotide binding, as the main interactions are made with the ribose, the phosphates and the adenine[104]. Nevertheless, the X-ray structures of the oxidized and NADH reduced hydrophilic arm of Complex I showed that NADH binding (or FMN reduction) induces conformational shifts in the vicinity of the nicotamide ring[108] : the positions of a conserved tyrosine ($_1$Tyr^{180} in the *T. thermophilus* nomenclature, $_F$Tyr^{178} in *E. coli*) and a conserved glutamic acid ($_1$Glu^{97} or $_F$Glu^{95}, whose backbone nitrogen interacts with the amide of the nicotinamide ring) are shifted (Figure 1.3.7). The hydrogen bonding motives in this region are thus redox dependent, affecting the stabilization of FMN. Notably, $_F$Glu^{95} makes stronger hydrogen bonds to $_F$Tyr^{178} and to the backbone of residues situated on a loop shifted upon reduction of the enzyme ($_1$Ser^{295} and $_1$Ser^{296} - not conserved in *E. coli*). This is even more evident in the X-ray structures of the oxidized and NADH reduced NuoEF subcomplex from *Aquifex Aeolicus* (E. Gnandt, personal communication).

$_F$Glu^{95} was shown to contribute to the stabilization of FMN *via* its negatively charged side chain[119]. When it was replaced by a neutral glutamine, the midpoint potential of FMN exhibited a 40 mV positive shift, from -350 to -310 mV *vs.* SHE (pH 7.5), consistent with the co-reported reduced NADH oxidase activities. In addition, this mutation caused a lower K_m of NADH as well as lower K_i for NAD^+ and ADP-ribose (see page 31 for further details about Complex I inhibition), indicating that the upshift of E_m FMN was not the only factor affecting the NADH oxidase activities. From the crystal structure, it appears that $_F$Glu^{95} interacts with the nicotamide ring and potentially with the ribose, as the latter is situated at *ca.* 5 Å from the glutamate. $_F$Glu^{95} might thus play roles in various processes : stabilization of FMN and prevention of ROS, binding of NADH/NAD^+, hydride transfer, transmission of conformational

movements and electron tunneling to N3 and N1a as it is situated between these clusters and FMN. These processes might be interconnected.

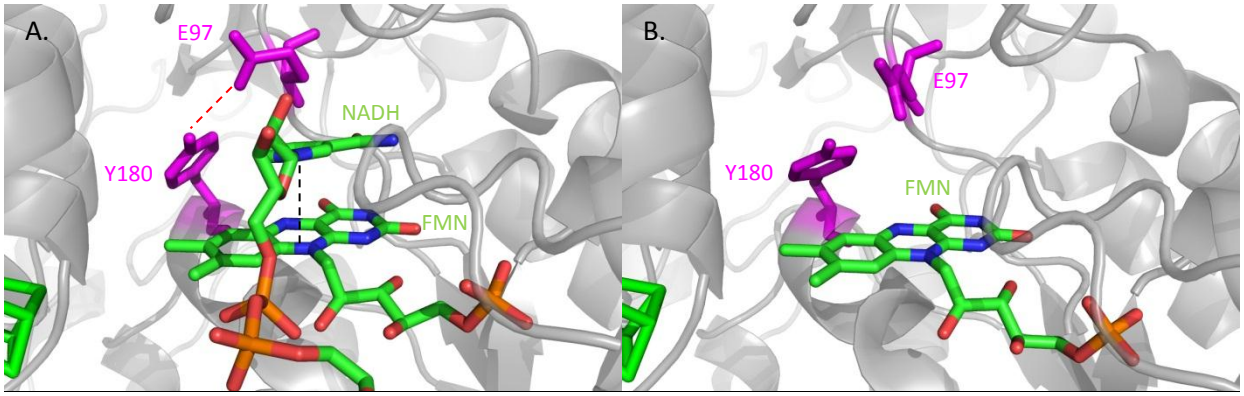

Figure 1.3.7 : View of the NADH binding site of Complex I in the reduced and in the oxidized state. Structures from the *T. thermophilus* Complex I. **A.** : Reduced state. PDB ID : 3I9V. FMN and NADH are colored in correspondence of their elements. $_{1}$Tyr^{180} and $_{1}$Glu^{97} are shown in magenta, with the hydrogen bond between the two marked by a dashed red line. The π-interaction between the isoalloxazine and the nicotamide ring is shown by a dashed black line. This also the location of the hydride transfer. **B.** : Oxidized state. PDB ID :3IAM. Colors are the same as in A). Iron sulfur cluster N3 can be seen in green on the bottom-left edge in both pictures. N1a mentioned in the text is out of frame, on top and behind $_{1}$Tyr^{180} and $_{1}$Glu^{97}.

As mentioned above, $_{F}$Tyr^{178} is a hydrogen bond partner of $_{F}$Glu^{95}. It was demonstrated that the mutation of this tyrosine ($_{NDUFV1}$Tyr^{204} in the human mitochondrial Complex I) to Cysteine is involved in some cases of Leigh- and Leigh-like disease (see page 30), together with the mutation of $_{NDUFV1}$Cys^{206} to Glycine[121, 122]. The latter might play a role in transducing conformational movements since the Cys side chain is involved in hydrogen bonds to residues from other moving loops, but as these movements are difficult to quantify and their role here is unclear, no further consideration will be given to this mutation. Due to its ability to hydrogen bond the functionally important $_{F}$Glu^{95}, the proximity of its aromatic ring to the FMN and its position between N3 / N1a and FMN, the Tyrosine mutation is more likely to be the main cause of the symptoms associated to Leigh syndrome and thus received our attention. Complex I dysfunction at the electron input level is mainly linked to disease through three processes : ROS production, modification of affinity to NADH/NAD^{+} or inhibitors, or modification of E_m FMN and subsequent electron transfer. To address these

options, a series of $_F$Tyr^{178} mutants in the *E. coli* Complex I was prepared by E. Gnandt at the laboratory of Pr. Friedrich. Their characterization in terms of E_m FMN, affinity to NADH and ROS production will be described in chapter 3.2.

The Quinone binding site : the Q site of Complex I is a narrow cavity with FeS cluster N2 located at its end, nearly 25 Å above the membrane plane. It is lined by a mixture of polar and apolar residues that form an access ramp[89], allowing the quinone headgroup to diffuse by more than 15 Å out of the membrane plane to its binding site. Crystallographic studies with decylubiquinone and Piericidin A showed that the Q ring binds 10 Å away from N2 and interacts mainly with two conserved residues, a tyrosine and a histidine.

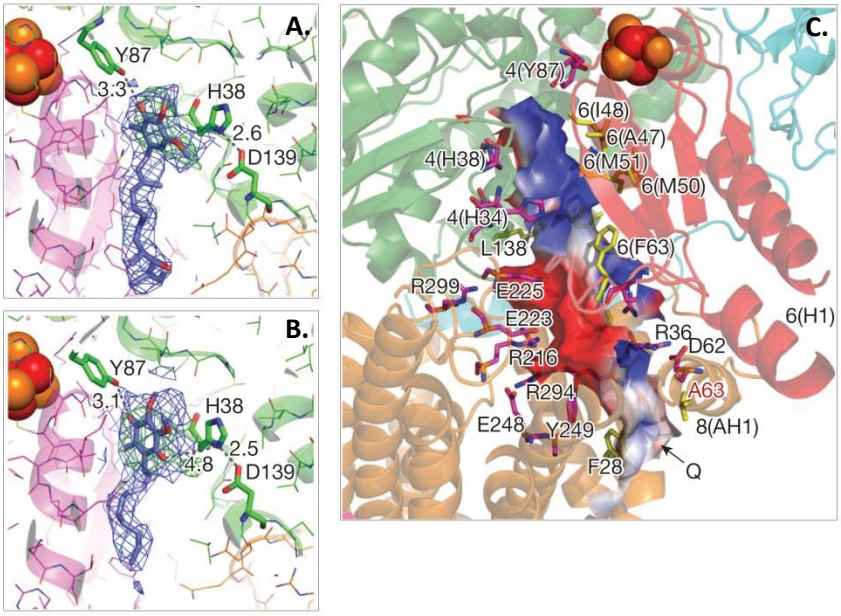

Figure 1.3.8 : Bound Piericidin A and decylubiquinone (A., B.) and representation of the Q binding pocket (C.). Structures and residue numbering for the *T. thermophilus* Complex I from ref[89]. **A.**, **B.** : Experimental electron density ($2mF_o–DF_c$ in blue, contoured at 1σ, and $mF_o–DF_c$ in green, contoured at 3 σ) and models obtained from crystals with bound piericidin A and decylubiquinone. **C.** : Quinone-reaction chamber, with its internal solvent-accessible surface coloured red for negative, white for neutral and blue for positive surface charges. Charged residues lining the cavity are shown with carbon in magenta and hydrophobic residues in yellow.

When Q-8 to 10 is bound, its last one-to-three isoprenoid units protrude from the cavity entrance, thus sealing the reaction chamber by blocking solvent access. Conformational rearrangements are probably necessary to let the quinone in and out. In the middle of the reaction chamber, several negatively charged residues form a connection (called "E-channel") to the central hydrophilic axis in the membrane arm (see page 28). Post-translational modifications of two arginines situated next to N2 and to the E-channel were evidenced in the bovine Complex I[123], but their role is unclear.

Proton pumping : in the membrane arm, 4 H^+ (current consensus value[79, 124]) are transferred through the membrane per enzymatic cycle. From the structures of the entire Complex I from *T. thermophilus* and of the membrane arm from *E. coli*, four putative proton channels were proposed[89] (Figure 1.3.9).

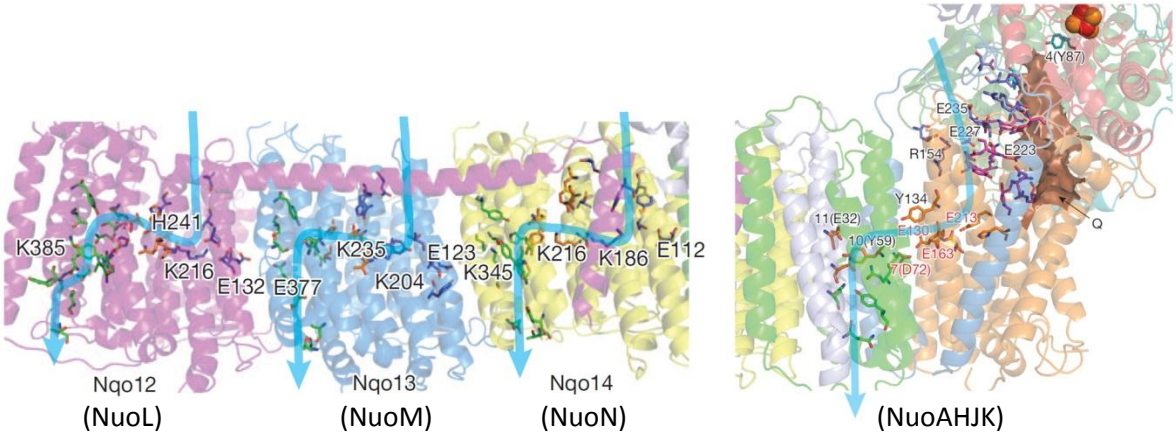

Figure 1.3.9 : Putative proton channels of the *T. thermophilus* Complex I, as proposed in ref[89]. The proton pathways are shown by the blue arrows. Proposed key residues are shown as sticks. In the right panel, the Q binding pocket is modellized by a brown surface and iron sulfur cluster N2 is shown as spheres.

Three of them are located in the antiporter-like subunits NuoL, M and N and one goes through subunits NuoAHJK. All are articulated around a structural particularity of Complex I : a chain of hydrophilic residues situated in the middle of the hydrophobic domain and running from the Q binding site through the E-channel to the distal tip of NuoL. The calculated pKa of the majority of these residues is around 7, indicating that they are competent for H^+ transfer. Gaps between the chain members are filled with water molecules

that can also transfer protons by the Grotthus mechanism[125-127] (Figure 1.3.10). While this part is well-defined and highly conserved, the proton intake and output half-channels could not be located with certainty as no apparent channel of hydrophilic residues leads continuously from the central hydrophilic axis to the surface, except for the exit half-channels in NuoL and NuoKJ. In addition, no conserved gating residue at the entry or exit could be identified. To enforce directional proton transfer, the proton channels should include such a gating mechanism and it should be controlled by the redox reaction[127].

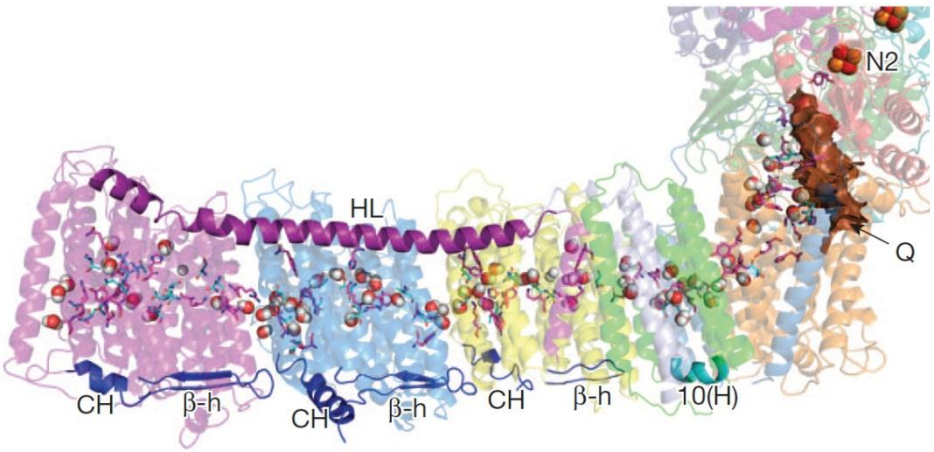

Figure 1.3.10 : Representation of the coupling elements and of modelized water molecules in the *T. thermophilus* Complex I. From ref[89]. Helix HL and the the β- and C-terminal elements are shown as cartoon. Residues from the central hydrophilic axis are shown as sticks, modelized water molecules as shperes and the Q binding pocket in brown.

Coupling between redox and proton pumping activities : the mechanism by which these two activities are linked is currently not known, although the puzzle begins to take form. From the potential profile of the cofactors involved in the electron transfer, it is clear that most of the energy is released upon Q reduction. A small part is also released when N2 is reduced. Thus the Q binding site is the coupling site. The first crystallographic studies of the membrane arm revealed how the proton pumps might be controlled : by conformational changes mediated through an unusual amphipatic α-helix (helix HL) and a repeating motif of β-elements and C-terminal domains, both parallel to the membrane surface (Figure 1.3.10). Helix HL stretches from the tip of NuoL to the the interface between NuoN and NuoK on the cytoplasmic side, whereas the β- and C-terminal elements connect both ends of the membrane arm (NuoL to NuoH) and face the periplasm. In addition, discontinuous

transmembrane α-helices where revealed by the x-ray structures. These kind of helices are often found in other ion-translocating enzymes and could be part of the proton gating mechanism[127]. These features are also found in the eukaryotic enzyme. As the Q reduction goes through the formation of negatively charged species, it was speculated that these species drive the conformational changes and the distal proton pumping through electrostatic attraction or repulsion. This prompted the creativity of the scientific community : the putative mechanism of Complex I was for example compared to the functioning of a piston[128], a steam engine[129], a wave-spring[80] and a semi-automatic shotgun[130]. Various other mechanisms were also proposed. Some favored a single-stroke mechanism (4 H^+ pumped through 4 different channels) and others a two stroke mechanism (2 x 2 H^+ through 2 different channels), with further variations including direct pumping through the quinone[131-133]. An ongoing debate about the H^+/e^- stoichiometry, sometimes estimated to be $3H^+/2e^-$, led to even more propositions[134]. The presence of two quinone molecules was also discussed, with one being tightly bound to the enzyme and the other being readily exchangeable with the Q pool[135]. Each mechanism has its pros and contras and probably encompasses a part of the reality. Both the proton channels and the coupling mechanism will be further detailed in chapter 3.5.

Production of Reactive Oxygen Species (ROS) by Complex I : in the cell, the reaction of the hydrophobic, triplet state molecular oxygen with radicals produces ROS, mainly $O_2^{\bullet-}$, H_2O_2 and $HO^{\bullet}$. Excessive ROS production can lead to oxidation of macromolecules and has been implicated in DNA mutations, aging, and cell death through apoptosis[136-138]. Cells thus possess an enzymatic defense system against ROS, which might be overwhelmed by excess ROS production. Mitochondria are responsible for ca. 15 % of the total cellular ROS production and Complex I was estimated to produce ca. 35 % of this fraction[139]. Both ends of the cofactor chain have been proposed to participate in the process, producing a mixture of H_2O_2 and $O_2^{\bullet-}$[139, 140]. While at the NADH binding site, strong evidence point to FMN-mediated H_2O_2 production, it is not clear if cluster N2, Q or another unknown cofactor produce $O_2^{\bullet-}$ at the Q binding site. It was shown that ROS production at the Q site of the *E. coli* and *T. thermophilus* enzymes can cause oxidative damage in the form of covalent crosslinks between subunits in this area[141]. To generate ROS, certain imperatives have to be met : the lifetime of the reactive electron donor has to be long enough for oxygen to

encounter it and the binding site has to be accessible and apolar enough to not repulse O_2. Their production rate is thus ruled by a combination of different factors : the concentration of the substrates and O_2, their K_m and K_i (which dictate occupancy of the binding site) and the time of residence of the reactive electrons on the production sites. In Complex I, it was shown that these factors are well orchestrated to minimize ROS production rates[104]. Thus, both ROS generation and prevention mechanisms where proposed[113]. However, the measured rates and ratios of $H_2O_2/O_2^{\bullet-}$ production differ between the species and between forward and reverse electron transfer, thus complicating the analysis of these mechanisms[116]. Genetic modifications in the vicinity of the binding site or inhibition can affect the equilibrium between the rate-controlling factors and lead to increased, unmanageable levels of ROS in the mitochondria. The consequences of genetic mutations and inhibition at the FMN site on the ROS production by Complex I will be assessed in chapter 3.2.

Complex I in health and disease : numerous pathologies, aging and cell death have been related to Complex I dysfunction or deficiency[142, 143]. Point mutations of the nDNA or mtDNA can lead to mutation of key residues[121, 122] and therefore affect its function or assembly[85] and oxidative phosphorylation in general. The subunits of human Complex I where such mutations could be related to pathologies[84] are shown in Figure 1.3.1. Often presenting at birth or in early childhood, Complex I deficiency is usually a progressive neurodegenerative disorder and is responsible for a variety of clinical symptoms, particularly in organs and tissues that require high energy levels[144]. Specific mitochondrial disorders that have been associated with Complex I deficiency include Leber's hereditary optic neuropathy (LHON), lactic acidosis (MELAS), and Leigh Syndrome (LS). A mutation in the FMN binding site was shown to be involved in LS and will be studied in chapter 3.2. Environmental or pathological factors can also affect Complex I function. Parkinson's disease and metastatic properties of cancerous cells have for example been linked to it[145-148], but in many cases the cause-effect relationships are unclear. Increased ROS production by Complex I is thought to play a central role in numerous diseases[138].

Inhibitors of Complex I activity : both the redox and the proton pumping activities of Complex I can be inhibited. As both are tied, the inhibition of one will inhibit the other. It is not known if they can be selectively uncoupled. For now and to the best of our knowledge, only one direct inhibitor of proton-pumping is known : Zn^{2+} (ref[149] and M. Schulte, manuscript in preparation). The role of $Zinc^{II}$ ions in cell metabolism and its interaction with the respiratory chain will be discussed in chapter 1.5. Concerning the redox activity, inhibitors both for NADH and Q binding are known. Adenosine and all its nucleotide-derivatives are, to different degrees, NADH competitive inhibitors[104]. NAD^+, ADP-ribose, Adenosine di- and mono-phophate (ADP and AMP) and Adenosine are all present in the mitochondrion, but either their K_i is high and their concentration also, or vice-versa, so that in reality only NAD^+ can be considered to "inhibit" Complex I during normal respiration, in the sense that its dissociation precludes the binding of a new NADH molecule. Nevertheless, these nucleotides are useful to probe the NADH redox mechanism under artificial conditions, often in combination with artificial electron acceptors as Hexaammineruthenium (HAR) or $[Fe(CN)_6]^{3-}$.

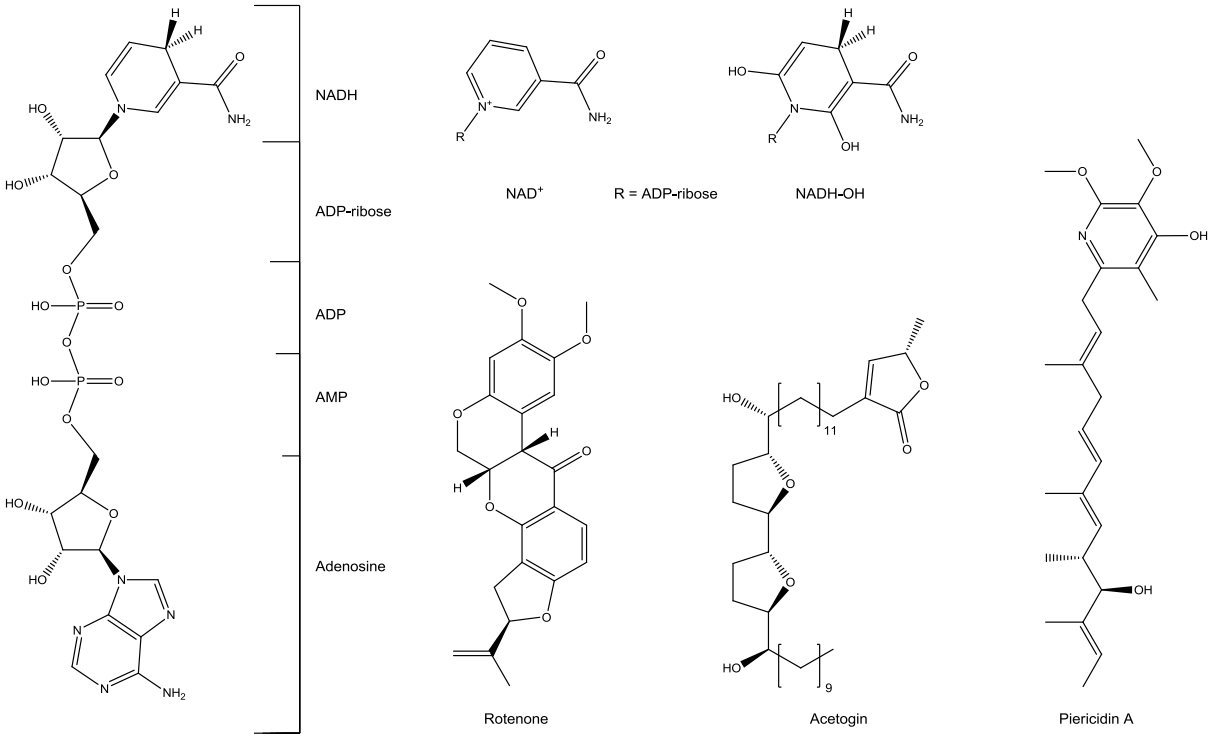

Figure 1.3.11 : Structures of different NADH and Q competitive inhibitors.

Another NADH competitive inhibitor, NADH-OH, results from the exposure of NADH to O_2 in a highly alkaline environment[150], yielding a compound whose proposed structure is shown in Figure 1.3.11. NADH-OH exhibits a low K_i (1.2×10^{-8} M) with respect to K_m NADH (NADH:HAR activity), making it the most NADH competitive inhibitor known for Complex I, with an affinity more than 3 orders of magnitude higher than ADP-ribose and 5 than NAD^+ ($K_i = 1.10^{-3}$ M). Moreover, it seems to be specific to Complex I. Until now its presence *in vivo* has not been reported but an enzymatic generation by mitochondria to regulate Complex I activity is conceivable. In addition to competing with NADH binding it was proposed to block electron transfer from the FMN to the Iron-Sulfur clusters. Some aspects of its mode of action will be studied in chapter 3.2. For the Q site, a plethora of inhibitors is known[151-155], the most widely used being rotenone, which is based on a steroid skeleton, piericidin A, a quinone analogue and derivatives of acetogenin. Among the quinone analogues, some are amidst the rare compounds that showed a certain success in the treatment of mitochondrial diseases[156].

1.4 The phospholipid bilayer membrane and its interactions with the respiratory chain complexes

Biological membranes are essential for life, as they provide specialized barriers used to compartmentalize cellular functions. They are mainly composed of lipids and proteins with different structures and functions which shape the membrane-specific permeability. Among the different types of lipids, phospholipids are a major component of biological membranes. They comprise a polar headgroup, a hydrophobic chain and can assemble in bilayers. Membrane proteins can be attached to the bilayer in different fashions, as they may completely cross the lipid bilayer, be partially inserted into it or just interact with the polar lipid headgroup region. In general, integral membrane proteins are constituted of α-helices which are hydrophobic in their middle and polar at the edges, in order to match the bilayer properties. In the context of the respiratory chain, we will focus on the interactions between phospholipids and integral membrane (transmembrane) proteins. As respiratory complexes and quinones, lipids diffuse more or less freely in the membrane. This is known as the fluid-mosaic model[157]. Increasing evidence shows that in reality the membrane is more mosaic than fluid, as the cell can organize the membrane in rafts of functional relevance[158]. This is

well illustrated by the fact that phospholipid and membrane protein biogenesis are closely linked together[159].

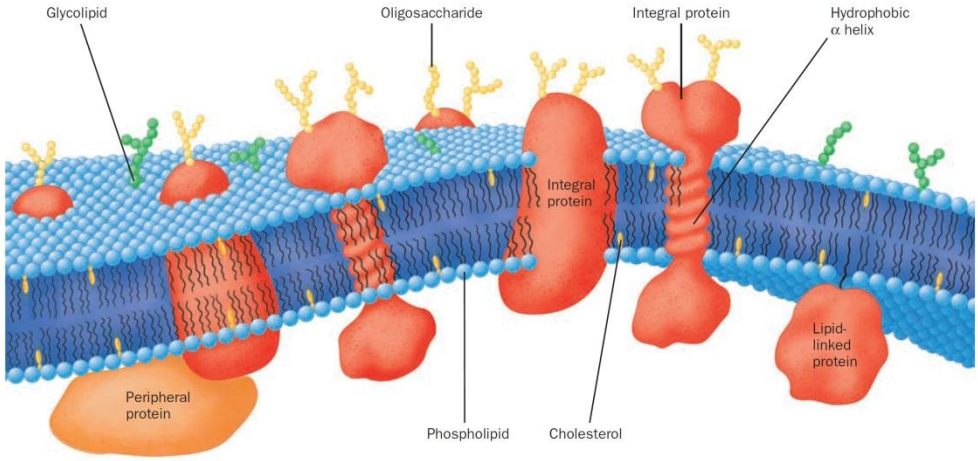

Figure 1.4.1 : The fluid-mosaic model and different types of lipids and membrane proteins. From ref[70].

A first layer of motionally restricted lipids, called annular lipids, surrounds each transmembrane protein[160]. Its radius depends on the physicochemical properties of the protein and the lipid bilayer. In general, only the lipids within 1 to 2 nm of the protein surface are considered as annular[161]. Non-annular- or tightly-bound- lipids are located in crevices between α-helices[160]. Their motion is strongly restrained, so that they almost never exchange with the annular lipids. They are often retained during purification and some even co-crystallize with proteins. It was shown that both annular and tightly-bound lipids can control protein function through various mechanisms, which are often more straightforward for tightly-bound than for annular lipids[162-165]. The amino acid composition of binding sites for non-annular lipids is highly variable, thus no consensus motif is known[166].

As mitochondria are thought to be ancient prokaryotes incorporated into eukaryotic cells during an endosymbiotic event, their phospholipid composition shares some similarities. For example, the plasma membrane from *E. coli* or *T. thermophilus* and the inner mitochondrial membrane all include phosphatidylethanolamine (PE), phosphatidylglycerol (PG) and cardiolipin (CL), although in different proportions[167-169] (Figure 1.4.2). This

facilitates inter-species comparisons of lipid-protein interactions in the respiratory complexes. Numerous examples of such interactions are found in the literature, mainly involving PE, CL and Complexes I, III and IV. CL was co-crystallized in the structures of Complex III and IV[39, 56], and in both it was independently shown to be essential for proton pumping[170, 171]. CL and PE were also shown to promote supercomplex assembly[65]. The pro-apoptotic activity of cytochrome *c* is also linked to CL[59].

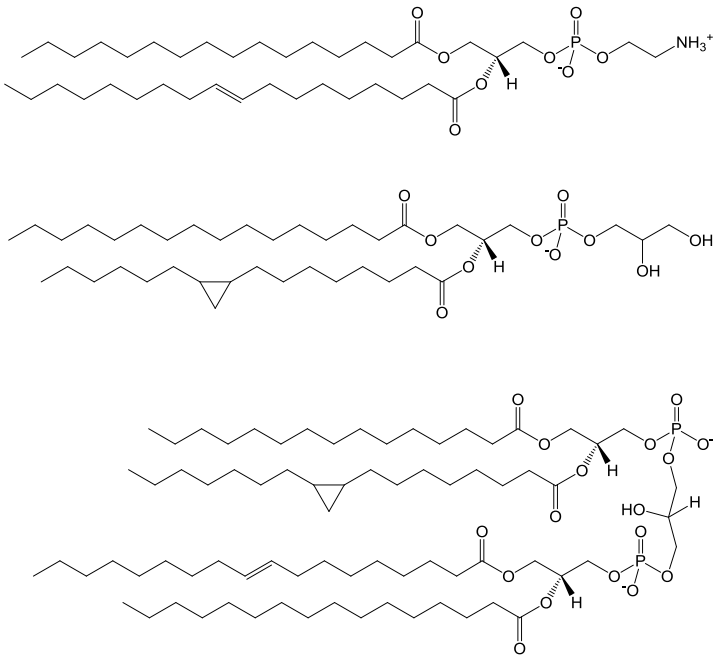

Phosphatidyethanolamine :
ca. 70 %, zwitterionic

Phosphatidylglycerol :
ca. 20-25 %, anionic

Cardiolipin :
ca. 5-10 %, anionic. Contains two phosphate groups and four acyl chains.

Figure 1.4.2 : Structures of the major phospholipids of the *E. coli* inner membrane. Structures of the predominant species. The nature, positions and number of the double bonds/cyclopropyls might vary in minor species.

Lipids and Complex I : the addition of lipids to a delipidated sample of the enzyme restores native activity of the enzyme[172] and lipids play a crucial role in stabilization and thus crystallization of the protein[173]. Previous studies performed in our laboratory with *E. coli* polar lipid extract suggested that some lipids bind specifically to Complex I[174, 175]. Another study made by Shinzawa-Itoh *et al.*[176] on the mitochondrial enzyme from bovine heart estimated that its fully functional form contained 8 phosphatidylcholines (PC - not present in *E. coli*), 16 CL, 23 PE and 8 PG per molecule of Complex I. Further removal of the lipid content by purification concomitantly decreased the enzymatic activity. These findings

were in line with those made by Sharpley *et al.*[177], who stated that ~10 CL are tightly bound to the Complex and that while PC and PE are essential for activity, they can substitute for one another. As the bacterial enzyme is smaller it is probable that the number of lipids required for optimal activity is lowered as well, but their nature should remain the same, due to the bacterial reminiscence of mitochondria. Cardiolipin seems to play a particular role, in the sense that it is more tightly bound and that the addition of excess CL in ref[177] did not significantly affect the enzymatic activity compared to the other lipids.

Due to the different nature of their headgroups and acyl chains, each lipid will have a different influence on Complex I. The hydrophilic headgroups of the phospholipids present in the *E. coli* or *T. thermophilus* membrane are either zwitterions (PE) or anions (PG and CL), which means that they will preferentially interact with positively charged areas located on the surface of the membrane domain of the protein. The hydrophobic tails interact with the nonpolar patches on this surface. To tentatively locate the lipid binding sites the charge distribution map of the membrane domain was calculated (Figure 1.4.3) .Numerous positively charged patches can be identified together with the hydrophobic parts and some negatively charged areas. The charged areas form two rims along the membrane domain, where the lipid headgroups are expected to bind. The interaction of Complex I with lipids will be studied in chapter 3.3.

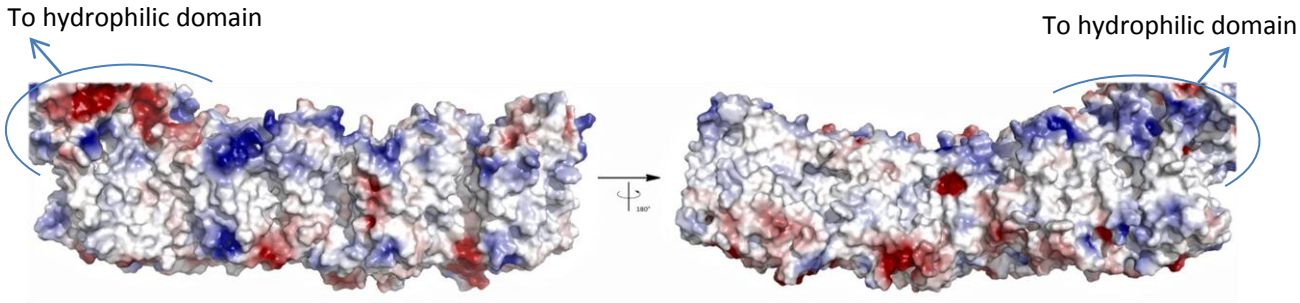

Figure 1.4.3 : Charge distribution map of the membrane domain from Complex I. Solvent accessible surface is colored red for negative, white for neutral and blue for positive surface charges. PDB ID : 4HEA.

1.5 Zn^{2+} and the respiratory chain

Zinc is an essential micronutrient, as it is incorporated as a structural feature in many proteins (e.g. “Zinc fingers”) and it plays a role in neuronal signaling in specific, so called “gluzinergic” neurons[178]. Besides special zinc receptors, it affects $GABA_{A\&B,}$ serotonin, dopamine and acetylcholine receptors as well as Ca^{2+}, Na^{+}, K^{+} channels and many more[179]. The regulation of the Zn^{2+} concentration in the cytoplasm is ruled out by metallothionein which is a cysteine−rich protein and can coordinate up to seven Zn^{2+} cations. The tightly bound Zn^{2+} can be released by the oxidation of the cysteines. Free ionic zinc levels are toxic and lead to the death of neurons. Zinc toxicity is not limited to neurons, as it is known to inhibit the cell energy production by affecting the GAP dehydrogenase during glycolysis, the α-ketoglutarate dehydrogenase complex in the Krebs cycle and the respiratory complexes I[149], III[180, 181] and IV[182, 183]. The $[IC]_{50}$ values for the inhibition of the respiratory complexes were estimated to be in the mid-micromolar range for Complexes I and IV and in the mid nanomolar range for Complex III. Under normal physiological conditions, the levels of free Zn^{2+} in the mitochondria are close to zero. However, pathologies can increase it, thus inhibiting oxidative phosphorylation principally at the third site[184]. It is not clear if the inhibition of Complexes I and IV are of physiological relevance. As in the case of complex IV it was shown that zinc inhibits the proton translocation and causes selective uncoupling from electron transfer[185], it can however be used as a tool to investigate proton pumping. This will be used in chapter 3.4 to gather new information about the proton-pumping and coupling mechanisms of Complex I.

Zinc and Complex I : both Shinzawa-Itoh *et al.*[176] and Giachini *et al.*[186] revealed the presence of one tightly bound Zn atom in the bovine heart Complex I, but this was not confirmed in the structure of the entire bacterial enzyme[89]. Hence, this specific Zn binding site is probably located in one of the supernumerary subunits and its function has yet to be explored. The study conducted by Sharpley *et al.*[149] suggested Zn^{2+} ions to act as an irreversible inhibitor of proton pumping by the mitochondrial Complex I. The $[IC]_{50}$ was estimated to be ~10-50 µM and dependent on the preincubation time. In addition, the strength and kinetics of the inhibition depended on the state of the enzyme : during the catalysis, Zinc only binds slowly and progressively, whereas the resting state is affected

faster. At the time, no high resolution structure of the membrane domain was available, thus no detailed suggestions about the inhibition mechanism were made. It was however made clear that Zn^{2+} does not inhibit the catalysis at the levels of the NADH oxidation or the electron transfer, but rather interferes either by blocking one or more of the proton channels and/or the quinone reduction site.

1.6 Spectroelectrochemical methods applied to proteins

1.6.1 Generalities

Spectroscopy is the study of the interactions between matter and electromagnetic (EM) radiations, which is described as a particle (the photon) and by Maxwell's laws as two oscillating fields perpendicular to each other on a unique plane. These oscillating fields are represented by sinusoidal functions that propagate at a constant velocity, c - the speed of light. The relation between the energy associated to these radiations (E) and their frequency (ν) is described by the Planck relation (equation *(6)*), where h is the Planck's constant (6.626 x 10^{-34} J.s). This relation is expressed through different forms, as the frequency is related to the wavelength of a radiation by c ($\nu = c/\lambda$) and the wavenumber $\bar{\nu}$ is the inverse of the wavelength ($\bar{\nu} = 1/\lambda$).

$$E = h\nu \qquad E = {}^{hc}/_{\lambda} \qquad E = hc\bar{\nu} \qquad (6)$$

Electromagnetic radiation exists as a broad and continuous spectrum, which is subdivided into seven regions according to their energy level (Figure 1.6.1 A). Matter only exists as a discrete succession of energetic states depending on its atomic and electronic composition (Figure 1.6.1 B). In order to interact with matter, the energy of a photon has to match the difference between two of these energetic states ($\Delta E = E_2 - E_1 = h\nu$). In the case of absorption spectroscopy, the transition from an initial state (i) to a final state (f) of higher energy (equation *(7)*) gives rise to an absorption signal specific to each system.

$$\Delta E = hc\left(\frac{1}{\lambda_i} - \frac{1}{\lambda_f}\right) \qquad (7)$$

Each type of EM radiation interacts with matter through different processes (Figure 1.6.1). Low energy radio waves will for example only change the spin orientation, whereas gamma rays will change the nuclear configuration of matter. In the present study, the two spectral regions of interest are the UV-Visible and the infrared spectral domains, related to valence-electron transitions and to changes in molecular vibrational levels, respectively (Figure 1.6.1 B). Both are used in absorption spectroscopies.

A.

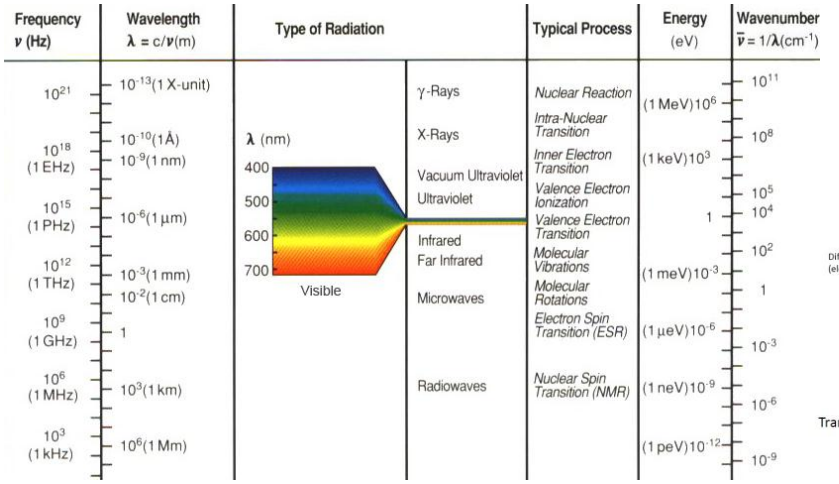

B.

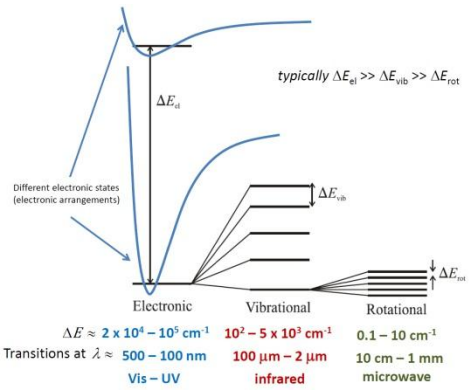

Figure 1.6.1 : A. : The electromagnetic spectrum. B. Energy states in matter. Adapted From ref[187]. **A.** : Classification in terms of energy, frequency, wavelength and wavenumber. Typical processes linked to each type of radiation are listed. **B.** : Example of a discrete succession of energy states in matter in the UV-Visible, infrared and microwave domains.

To gain experimental access to ΔE of a particular sample, spectrophotometers are used. They comprise a light source emitting within the desired spectral range and a corresponding photosensitive detector. The experimental sample is placed between the two and the energetic flux of the incident light beam (ϕ_0, set by the source) is compared to that of the beam transmitted (or reflected) through the sample (ϕ , measured by the detector). The physical property hereby measured is the transmittance, defined as $T = \phi / \phi_0$. For practical reasons, the transmittance is in general converted into the absorbance (or Optical Density, O.D.), defined as $A_\lambda = \log_{10}(\phi_0 / \phi)$. The Beer-Lambert law[188] (equation *(8)*) defines absorbance at each wavelength (A_λ) as being proportional to the sample-specific molar extinction coefficient at this wavelength (ε_λ in $mol^{-1}.cm^{-1}.L$), the concentration of the sample (C in $mol.L^{-1}$) and the optical path length of the sample (l in cm).

$$A_\lambda = \varepsilon_\lambda . l . C \qquad (8)$$

When A_λ is plotted against the wavelength, this gives the absorption spectrum in which each peak is characterized by its position λ and intensity A_λ.

Electrochemistry studies chemical reactions which take place in a solution at the interface of an electron conductor (the electrode) and an ionic conductor (the electrolyte). These reactions involve electron transfer between the electrode and the electrolyte or species in solution. Here, a simple electrochemical cell comprising three electrodes connected to a variable current supply (Figure 1.6.2 A.) is used to apply an external voltage to drive redox reactions of enzymes or substrates in solution. The first of the three electrodes is the working electrode, at which the electrochemical redox reactions take place. The second functional electrode is the reference electrode, whose potential is constant and thus acts as the reference standard against which the potentials of the other electrodes present in the cell are applied. The third functional electrode is the counter electrode, which serves as an electron source or sink so that a current can be passed from the external circuit through the cell. In the present study, the WE was always a gold electrode, in the form of a gold mesh (chapter 1.6.3.4) or a nano-structured thin gold layer (chapters 1.6.3.6 and 1.7). The RE was always the Ag/AgCl electrode at 3M KCl (E^0 = 208 mV) and the CE was a piece of Platinum. The actual device used to deliver, control and measure the current and the voltage is a potentiostat, whose function is described in Figure 1.6.2 B. and the corresponding figure caption.

The Nernst equation is used to describe the equilibrium reduction potential of an electrochemical half-cell (E_h) in function of the standard potential (E^0) and the chemical activities of the two redox states of the species in solution (a_{ox} and a_{red}) as shown in equation *(9)* (where R is the ideal gas constant, T the absolute temperature, n the number of electrons participating in the reaction and F the Faraday constant).

$$E_h = E^0 + \frac{RT}{nF} \ln\left(\frac{a_{ox}}{a_{red}}\right) \qquad (9)$$

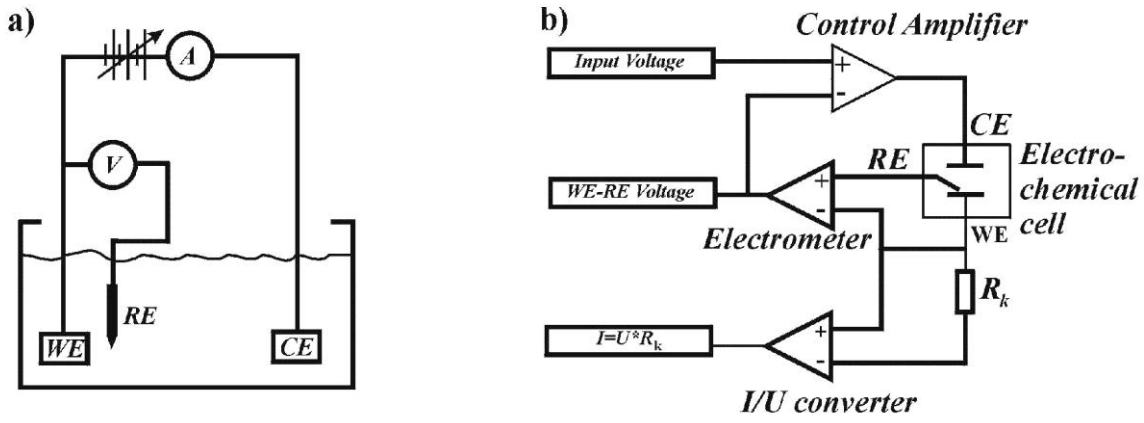

Figure 1.6.2 : A. : The eletrochemical cell based on three electrode. B. : Schematic representation of a three electrode potentiostat. Adapted from ref[189]. **A.** : WE : Working Electrode ; RE : Reference Electrode ; CE : Counter Electrode. The cuvette is filled with the electrolyte solution. The RE is used to control and to measure the WE potential, while the CE passes all the current needed to balance the current observed at the working electrode. **B.** : The voltage intended to be applied between the reference electrode and the sample is delivered as the input voltage for the potentiostat. The real WE-RE voltage is measured by a differential amplifier (Electrometer) and is compared with the input voltage by a second differential amplifier (Control Amplifier). If a difference between the two voltages is detected, the controlling amplifier will adapt the input voltage until both are equal. The I/U converter measures the cell current and forces it to flow through the resistor R_k. The voltage drop across R_k is thus a measure of the cell current through Ohm's law (U = RI).

The other half-cell in the electrochemical cell here is the RE. With all other factors kept constant, the application of an external potential will change the equilibrium between the chemical activities of the oxidized and reduced species. Such electrochemically-induced variations can be probed, among others, by spectroscopy, as will be described in the following chapters.

1.6.2 UV-Visible absorption spectroscopy

The absorption of electromagnetic radiation in the UV-Visible spectral domain leads to electronic transitions, i.e. the promotion of an electron from a ground state to an excited electronic state. Easily excited electrons absorb at longer wavelengths than their less excitable counterparts. Transitions of π-electrons or non-bonding η-electrons to higher anti-

bonding molecular orbitals (σ* or π*) are commonly seen, while transitions from σ-electrons are less common as they require more energy. UV-Visible spectroscopy is a common tool for the study of proteins, mainly in the spectral range from 200 to 800 nm as numerous amino acids and cofactors have high extinction coefficients in this range and are thus easily detectable, even at the low concentrations often used in protein studies. Among a myriad of applications, it is for example used to estimate the concentration of a protein sample by measuring A_{280nm}, as ε_{280nm} can be calculated from the primary amino acid sequence of a protein[190]. The study of the respiratory enzymes has its roots in UV-Visible spectroscopy, as it was related to their discovery by Keilin, who coined the appellation "cytochrome" after observing a characteristic four-band visible spectrum of the respiratory chain enzymes[17]. These cytochromes were later shown to correspond to the absorption bands of the hemes present in Complexes II, III and IV and cytochrome *c*. The cofactors and substrates from Complex I have also been extensively studied by UV-Visible spectroscopy, as NADH, FMN, iron sulfur clusters and quinones absorb in the spectral region from ~200 to ~600 nm[191, 192]. Moreover, their extinction coefficients depend on their redox state, so that UV-Visible spectroscopy is often used to follow the corresponding redox reactions. For example, the NADH oxidase activity of Complex I can be followed by the progressive diminution of the NADH-characteristic peak at 340 nm[193]. The redox state of the cofactors or substrates can be controlled through an electrochemical cell, giving access to thermodynamic properties such as their midpoint potential[119, 194]. This is done through an adaptation of the Nernst equation, by assuming that the chemical activities of the redox species are proportional to the absorption changes observed (ΔA_λ) (equation *(10)*).

$$\Delta A_\lambda = A_{red,\lambda} + \frac{A_{ox,\lambda} + A_{red,\lambda}}{1 + exp^{(p - E_m)\frac{nF}{RT}}} \qquad (10)$$

$A_{ox,\lambda}$ and $A_{red,\lambda}$ are the absorbances for the fully oxidized and fully reduced species linked by their midpoint potential E_m and p is the applied potential. The combination of electrochemistry and UV-Visible spectroscopy will be used in chapter 3.2 to determine the E_m of FMN in Complex I in different $_F$Tyr^{178} mutants and in presence of the inhibitor NADH-OH, as the oxidized FMN absorbs at 456 nm (ε_{450nm} = 12800 mol^{-1}.cm^{-1}.L) while the reduced FMNH$^-$ does not[194].

UV-Visible spectrometers are generally dispersion spectrometers ; the light beam from the UV-Vis source is sent through a sample and a reference path. It is focused into a diffraction grating, which is comparable to a prism. This grating separates the wavelengths of light and guides each wavelength separately through a slit to the detector. Each wavelength is measured one at a time, with the slit monitoring the spectral bandwidth and the grating moving to select the wavelength being measured.

1.6.3 Infrared absorption spectroscopy

The infrared (IR) domain covers electromagnetic radiation of wavenumbers from 10 to 12500 cm^{-1} (see Figure 1.6.1 for correlation with frequencies, wavelengths or energies). In general, it is divided into three additional domains : Near Infrared (NIR) from 4000 to 12500 cm^{-1}, Mid Infrared (MIR) from 400 to 4000 cm^{-1} and Far Infrared (FIR) from 10 to 400 cm^{-1}. The absorption of IR radiation results in changes of the vibrational or rotational modes of molecules. For a linear or a non-linear molecule of N atoms, 3N-5 or 3N-6 normal vibrational modes exist, respectively. These normal vibrational modes are infrared active only if the dipole moment of a molecule changes during the course of the vibration. For a molecule composed of two atoms, the vibrational frequencies can be predicted by comparing it to a harmonic oscillator. The atoms, of mass m_1 and m_2, are considered as point-like and the chemical bond is equated to a spring. The wavenumber of the stretching vibration can be described by equation *(11)*, which is derived from Hooke's law[195, 196].

$$\bar{\nu} = \frac{1}{2\pi c}\sqrt{\frac{k}{\mu}} \qquad \text{where } \mu = \frac{m_1 m_2}{m_1 + m_2} \qquad (11)$$

The force constant k represents the strength of the chemical bond and μ is the reduced mass of the atoms. From equation 11, it can be seen that if k increases or μ decreases, the wavenumber shifts to higher frequencies, and vice-versa. Both the bond-strength and the mass of atoms can be modified experimentally to induce variations of the vibrational mode in a sample, which is useful to attribute certain vibrations to a particular absorption peak. Isotopic labeling is one of the methods used to influence these parameters.

The diatomic stretching mode is only one of several vibrational modes that can be observed by infrared spectroscopy. Figure 1.6.3 summarizes the other types of vibrations that are commonly seen in IR. Their mathematical descriptions are more complicated as 3 dimensions need to be considered and is based on the group theory. In general, the IR absorption bands correspond to the fundamental bands, i.e. the transition from the vibrational ground state (v = 0) to the first excited state (v = 1) of a molecule. However, so-called overtone bands can appear for transitions to the second excited state (v = 2) or beyond (v = n). The intensities of these overtone bands are relatively low compared to those of the fundamental bands.

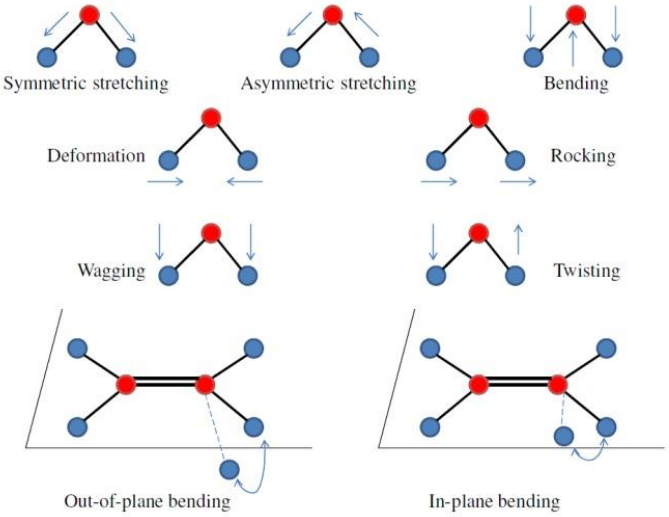

Figure 1.6.3 : Normal mode vibrations commonly seen in IR spectroscopy. From ref[197].

1.6.3.1 IR absorption of proteins

Proteins are macromolecules constituted of amino acid residues linked through peptide bonds and of cofactors. The IR absorption of proteins is mainly characterized by the vibrational modes of their backbone amides, with smaller, overlapping, contributions from the amino acid side chains and possible cofactors[198]. The most studied spectral region in protein IR spectroscopy is the MIR, as it contains many indications of structural and functional relevance and is well-mastered from the technical point-of-view. The typical MIR absorption spectrum of a protein in solution is shown on Figure 1.6.4 and the assignments of the different amide modes (or bands) is summarized in Table 1.6.1.

Designation	Position (cm^{-1})	Vibrational modes
Amide A	ca. 3300	ν(N-H)
Amide B	ca. 3100	ν(N-H) in resonance with the first Amide II overtone
Amide I	1700-1600	ν(C=O) 80 % ; ν(C-N) 10 % ; δ(N-H) 10 %
Amide II	1580-1510	Coupled ; δ(N-H) 60 % ; ν(C-N) 40 %
Amide IIII	1400-1200	Coupled ; δ(C-N) 30 % ; δ(N-H) 30 % ; ν(C=O) 10 ; δ (N-C=O) 10 % ; overlap with other modes

Table 1.6.1 : Amide contributions of the polypeptide backbone in the MIR range. From ref[199].

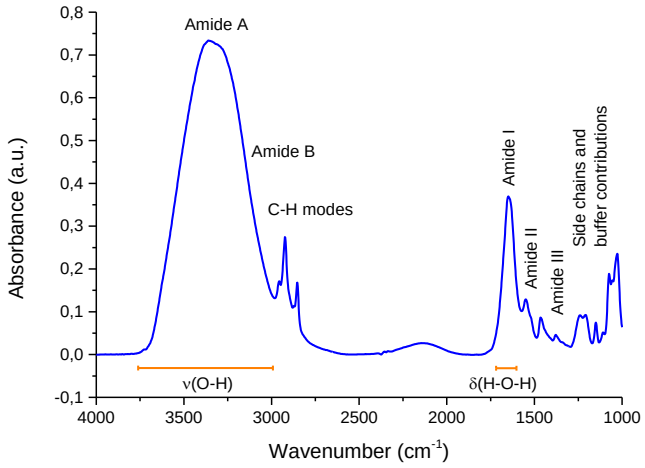

Figure 1.6.4 : Typical MIR spectrum of a protein in solution.

The main advantage of protein IR spectroscopy is that almost every chemical bond in the protein is IR active. Thus, a wealth of information about structure and environment of the protein backbone, amino acid side-chains and bound ligands or cofactors can be gathered from the spectral parameters : band position, bandwidth and absorption coefficient[200]. However, its main advantage is also its major inconvenience : rare are the signals from a protein that do not overlap with other signals, making their assignment anything but trivial. This can for example be seen in Figure 1.6.4, where the Amide A and Amide I modes overlap with the stretching and bending modes from water. Different technical approaches, such as the use of differential spectroscopy (chapter 1.6.3.2), allow to partially circumvent this handicap to access the information of interest. The literature abounds with descriptions of model compounds to which this information can be compared.

This is for example used to identify the vibrational modes of specific side chains[201, 202] or to estimate the secondary structure of a protein[203, 204], as described hereafter.

The amide I mode of a protein is particularly well suited for secondary structure analysis, as the C=O vibration is sensitive to the differences in hydrogen-bonding characteristic to each substructure. Table 1.6.2 summarizes the positions of the different components of Amide I for different structures. As most of the proteins contain more than one secondary structure, their signals overlap and it is often necessary to deconvolute the Amide I band to estimate in which proportions they are present.

$^{1}H_2O$ (cm^{-1})	$^{2}H_2O$ (cm^{-1})	Type of structure
1623-1641	1615-1638	β-sheets
1642-1657	1639-1654	Random coils
1648-1657	1642-1660	α-helices
1662-1686	1653-1691	β-turns
1674-1695	1672-1694	β-sheets

Table 1.6.2 : Amide I frequency range for protein secondary structures in $^{1}H_2O$ and $^{2}H_2O$. From ref[198].

The replacement of H_2O by D_2O is frequently used in protein IR spectroscopy, as it can disambiguate the assignment of certain vibrational modes by shifting their frequency. Whereas the amide I mode is only slightly sensitive towards the exchange (see Table 1.6.2), the amide II mode is extremely sensitive to N-deuteration, as its main component, the δ(N-H) mode, shifts several hundred cm^{-1} to lower frequencies upon deuteration. The now uncoupled (C-N) mode is seen in the so-called Amide II' band between 1420 and 1490 cm^{-1}. This can be for example exploited in ^{1}H-^{2}H exchange kinetics to estimate which parts of the protein are solvent accessible (chapter 1.6.3.7). The vibrational modes of (de)protonable or hydrogen-bond capable amino acid side chains also respond differently to the replacement of H_2O by D_2O, facilitating their assignment. The Amide A, B and III modes are rarely used in protein IR spectroscopy.

1.6.3.2 Differential IR spectroscopy

The principle of differential spectroscopy is to record a spectrum of a system in a particular state (generally called the background or reference spectrum), to perturb this state and to record a second spectrum from which the background is subtracted. Only the vibrational modes that changed, appeared or disappeared are thus seen in a differential IR spectrum. The system can be perturbed through many ways and various techniques are used. Here, the two main methods used to displace proteins from an equilibrium are electrochemically-induced variations of the redox states of species in solution and addition, replacement or removal of external chemical compounds such as the solvent, protein ligands or enzymatic substrates.

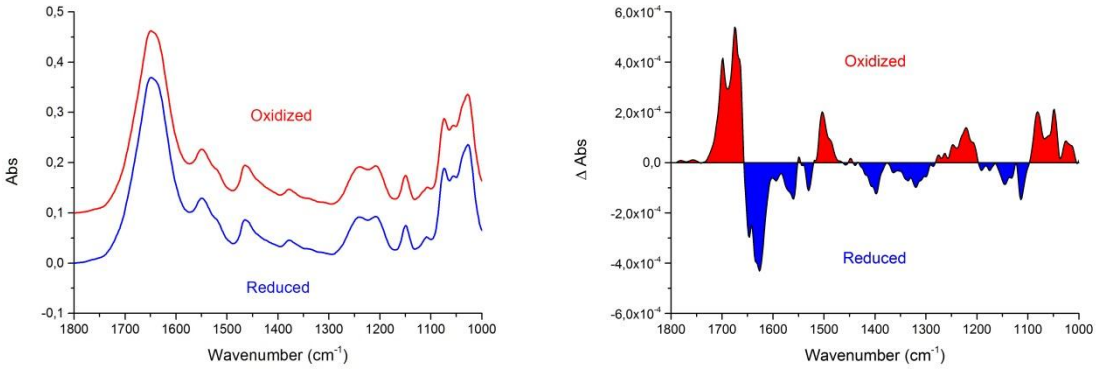

Figure 1.6.5 : Example of a difference spectrum between the fully oxidized and the fully oxidized state of an enzyme, Complex I.

Figure 1.6.5 illustrates the IR difference spectrum of a protein. The left panel shows the spectra of a protein in two different states (fully oxidized and fully reduced), which comprise the contributions of all the vibrational modes from the protein, thus overlapping the changes that occurred. In the right panel, the spectrum of the reduced form was subtracted from the oxidized form, revealing the numerous changes that actually occurred. The positive signals (blue) in Figure 1.6.5 correlate with the oxidized form, while the negative signals (red) correspond to the reduced form.

The signals highlighted through this method may allow direct attribution of certain signals to specific structural or environmental changes. If a conformational change occurs in the course of the studied reaction, it might be related to a particular type of structures through the position of the signals in the amide I range. Certain changes in the vibrations of amino acids can also directly be assigned to different events. For example the (de)protonation of acidic residues can be detected through spectral changes in between 1700 and 1800 cm^{-1}. However, the majority of the signals from the protein backbone and the side chains still overlap below 1700 cm^{-1}, and further experiments are necessary. These experiments include for example measures in D_2O, comparison of the difference spectra of a protein in presence and absence of ligands, site-directed mutagenesis to replace residues of interest or isotopic labeling..

1.6.3.3 Fourier-transform infrared spectroscopy

The first IR spectrometers were dispersive spectrometers operating along the same process as described for UV-Vis spectrometers in chapter 1.6.2. Nowadays, a much faster process is used, based on an optical setup comprising a polychromatic source, a detector and a Michelson interferometer[196, 205]. The latter is composed of two perpendicularly plane mirrors, one of which is mobile in the direction perpendicular to the plane. A semi-reflecting film termed beamsplitter cuts the planes of the two mirrors. If a monochromatic beam passes an ideal beamsplitter, 50% of the incident radiation will be reflected to one of the mirrors while 50% will be conveyed to the other mirror. The two beams are reflected from these mirrors, back to the beamsplitter where they recombine and interfere. Again, the beam is split to 50 % but this time beam one half goes through the sample to the detector (transmitted beam) while the other half is reflected back in the direction of the source (reflected beam).

The moving mirror creates an optical path difference between the two branches of the interferometer. For path differences of $(n + ½)\lambda$, the two beams interfere destructively in the case of the transmitted beam and constructively in the case of the reflected beam. The resulting interferogram is shown in Figure 1.6.6 for a source of polychromatic radiation, which contains all the spectral information of the radiation captured by the detector. This

information belongs to the length domain (δ), which needs to be inverted into the easily interpretable reciprocal length domain ($\bar{\nu}$), i.e. the absorbance spectrum. This is done by applying a Fourier-transform which relates the intensity falling on the detector $I(\delta)$ to the spectral power density $B(\bar{\nu})$ through equations *(12)* and *(13)*.

$$I(\delta) = \int_0^{+\infty} B(\bar{\nu}) \cos\ (2\pi\bar{\nu}\delta) d\bar{\nu} \qquad (12)$$

$$B(\bar{\nu}) = \int_{-\infty}^{+\infty} I(\delta) \cos\ (2\pi\bar{\nu}\delta) d\delta \qquad (13)$$

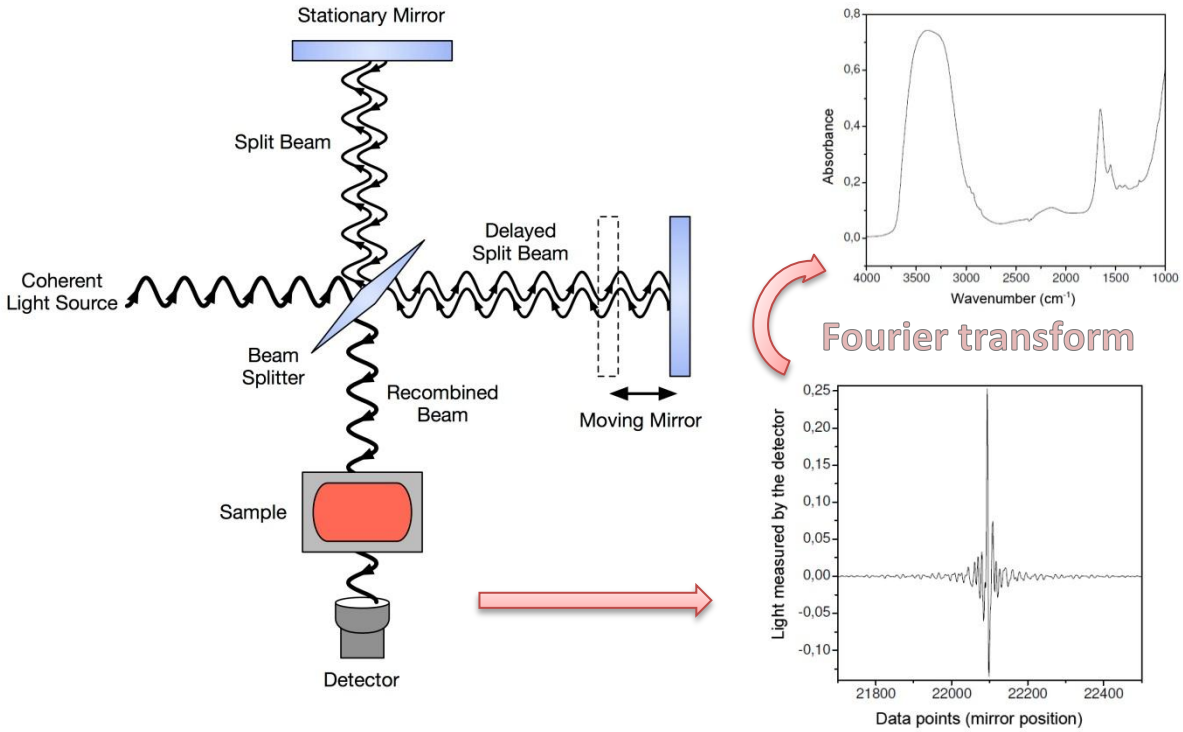

Figure 1.6.6 : Representations of a conventional FTIR spectrometer, an interferogram and the corresponding absorbance spectrum obtained by Fourier transform. These equations are interconvertible and are solved with the help of computers by an algorithm known as fast Fourier-transform (FFT). The movement amplitude of the mobile mirror determines the spectral resolution, whereas its frequency determines the maximum signal intensity of the interferogram. The three main advantages of FTIR over dispersive IR spectroscopy are as follows[196, 205] :

- The Fellget, or multiplex advantage is that all the spectral elements can be measured simultaneously, thus allowing a rapid acquisition of the spectrum. In a same time period, more scans can thus be accumulated with FTIR than with dispersive IR, improving the signal-to-noise ratio (S/N) of the final spectrum.
- The Jacquinot, or throughput advantage arises because unlike dispersive spectrometers, FTIR spectrometers have no monochromator slits which attenuate the optical throughput of IR radiation, also increasing the S/N ratio.
- The Connes', or registration advantage is that the wavelength is known very accurately, so that mathematical operations such as the averaging or subtraction of multiple spectra can be carried out without a significant error margin.

Some minor disadvantages are also inherent to the technique, as for example its sensitivity to changes in atmospheric conditions during the course of the experiment, as the spectrum is compared to a reference spectrum recorded at the beginning of the experience. Hence, most of the modern FTIR spectrometers are purged with a dry gas, mainly to minimize the rotational-vibrational absorption of gas-phase water molecules. The temporal resolution limit of FTIR at a given wavelength is less than in dispersive IR, although significant advances were made in this domain, extending the limit to ~1.10^{-9} s[205].

In an FTIR spectrometer, different sources, beamsplitters and detectors can be used, depending on which frequency range needs to be studied. In the context of this study, all experiments were done in the MIR range. The source used was always a globar and the beamsplitter a KBr film. A liquid nitrogen cooled Mercury-Cadmium- Telluride (LN-MCT) detector was used for experiments requiring less than 8-10 hours while a Deuterated Triglycerine Sulfate (DTGS) detector was used for longer experiments, such as ^{1}H-^{2}H exchange kinetics.

1.6.3.4 The transmission mode

The simplest manner to direct a beam through a sample is by placing it in the optical path of the spectrometer on a support that is transparent at the desired spectral range. It is sometimes useful to have a small path-length and a high concentration, for example to limit

the IR contribution of water in a protein sample without using large protein quantities. Here, the sample is pressed between two windows, as will be shown in chapter 2.2.1. The path-length in the setup used here is ca. 5 to 10 µm. To be able to induce electrochemical changes in the sample, a gold grid used as a WE is placed between the two windows and the cell is filled with buffer solution in contact with a RE and a CE. This setup can be used in both in IR and UV-Visible spectroscopies if for example CaF_2 windows are chosen. The use of this type of cell contributed to the general understanding of the respiratory chain's functioning[180, 206-210]. In particular, Complex I has been extensively studied through this method[175, 191, 192, 211, 212], providing numerous points of comparison for the results in the present work.

1.6.3.5 Attenuated Total Reflection (ATR) mode

Another experiment IR method is called Attenuated Total Reflection (ATR), which is a variation of total internal reflection[195]. The incident IR beam is directed into an IR-transparent crystal of refractive index n_1 called the internal reflection element (IRE). The sample is placed on the surface of the IRE in a medium of refractive index n_2 (Figure 1.6.7) If $n_1 > n_2$, the total internal reflection will occur at the interface of the two media, if the angle of incidence θ of the beam exceeds the critical angle θ_c.

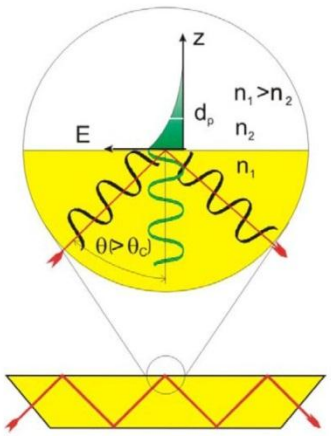

Figure 1.6.7 : Schematic representation of the ATR principle. From ref[195]. The IRE is represent by the yellow trapezoid and the reflected IR beam by the red arrow. The evanescent wave's decreasing intensity is represent by the green curve.

The critical angle can be defined as a function of the refractive indices of two media (equation *(14)*). The IRE can be shaped to allow multiple internal reflections before leaving the IRE.

$$\theta_c = sin^{-1}\left(\frac{n_2}{n_1}\right) \qquad (14)$$

At each internal reflection, an evanescent field extends into the sample. This field can be described as a standing electric wave perpendicular to the surface resulting from the overlap of the electric fields of the incident and reflected waves. Its amplitude E decays exponentially with the distance from the surface, as described by equation *(15)*, where E_0 is the amplitude of the electric field at the interface, z is the distance from the surface and d_p is the penetration depth.

$$E = E_0 exp^{-\left(\frac{z}{d_p}\right)} \qquad (15)$$

$$d_p = \frac{\lambda}{2\pi\sqrt{n_1^2\, sin^2\theta - n_2^2}} \qquad (16)$$

d_p in turn is defined as the distance where the amplitude of the electric field is $1/e$ of E_0, which is a function of n_1, n_2, θ and the wavelength of the radiation, λ (equation *(16)*). In the MIR range, d_p is ~1 µm[213].

The IR absorption of the sample attenuates the amplitude of the total reflection, hence the name ATR. The amplitude of the absorption is proportional to the number of internal reflections. In this study, the ATR crystals (the IREs) were made of silicon, ZnSe or diamond, and both single and multiple internal reflections were used. It is important to notice that the crystal itself has a polarizing effect on the IR radiation, which might lead to spectral differences when compared to other methods. Anisotropic adsorption of the sample may cause additional spectral differences, which might however be used to determine the orientation of the adsorbed molecule.

ATR-IR spectroscopy of proteins presents some advantages over the transmission mode[203, 213]. The sample quantity needed to obtain a spectrum of the same intensity is ca. 5-fold diminished and the sample and the crystal surface are easily accessible during the course of the experiment, allowing the addition or removal of chemical compounds to make differential spectroscopy. The sample compartment can also be closed and connected to a perfusion circuit, as will be shown in chapter 2.3.1. However, the prerequisite for these experiments is that the studied protein remains adsorbed within the d_p of the evanescent wave. To achieve this, a protein sample can be dried at the surface of an ATR crystal, forming a pellet that remains stably attached to the surface through hydrophobic interactions[214]. The pellet is then rehydrated with buffer solution. This method has a number of shortcomings as the removal of the solvent can denature the structure of the protein or the protein surface might be too polar to form hydrophobic interactions with the surface. It is thus preferable to use other methods in solution, as for example the chemical modification of the crystal surface to tailor its affinity towards the protein[215, 216].

1.6.3.6 Surface Enhanced IR Absorption Spectroscopy (SEIRAS)

The so-called SEIRA effect is the enhancement of the IR absorption of molecules adsorbed on a nano-structured metal thin film placed on a surface (Figure 1.6.8 A), as compared to the absorption of the same molecules on the surface alone[217]. This can be for example achieved by a densely crowded gold metal island thin layer. It has a strong enhancement effect in the MIR range (up to three orders of magnitude), and the surface in question is a single internal reflection Silicon ATR crystal.

Both, an electromagnetic (EM) and a chemical mechanism contribute to the observed enhancement. The EM mechanism is based on the polarization of the metal islands by the incident photon field through the excitation of collective electron resonance (or localized plasmon) modes. The dipole p induced in an island generates a local EM field stronger than the incident photon field around the island, which excites the molecular vibration ν_{mn}. As the enhanced EM field is polarized along the surface-normal at each point of the metal particles, surface selection rules apply ; only vibrations that have dipole moment derivative components perpendicular to the particles surface are IR-active[218]. In addition, this local EM

field decays sharply when the distance to the surface increases, explaining why the SEIRA effect is generally considered to apply only to molecules situated within ~10 nm of the metal surface. This part of the EM mechanism explains only an enhancement by about one order of magnitude. Another explanation of the EM effect is that the vibrations of absorbed molecules induce an additional dipole δp in the metal, thus perturbing its optical properties. Since the perturbation is larger at frequencies of molecular vibrations than at other frequencies, the molecular vibrations can be observed through the change in the absorbance of the metal island film. Absorptivities of metals are larger than those of molecules in the MIR region. Furthermore, the relative volume fraction of the metal is considerably larger than that of adsorbates and the change in optical properties of the metal island film will dominate the spectrum. This film thus functions as an amplifier of the IR absorption, with an enhancement of up to two orders of magnitude in addition to the near field effect. The nano-structure of the metal film determines the enhancement that can be obtained. In general, an islet size of 30 to 80 nm and a film thickness of 10 to 50 nm produce the best enhancement.

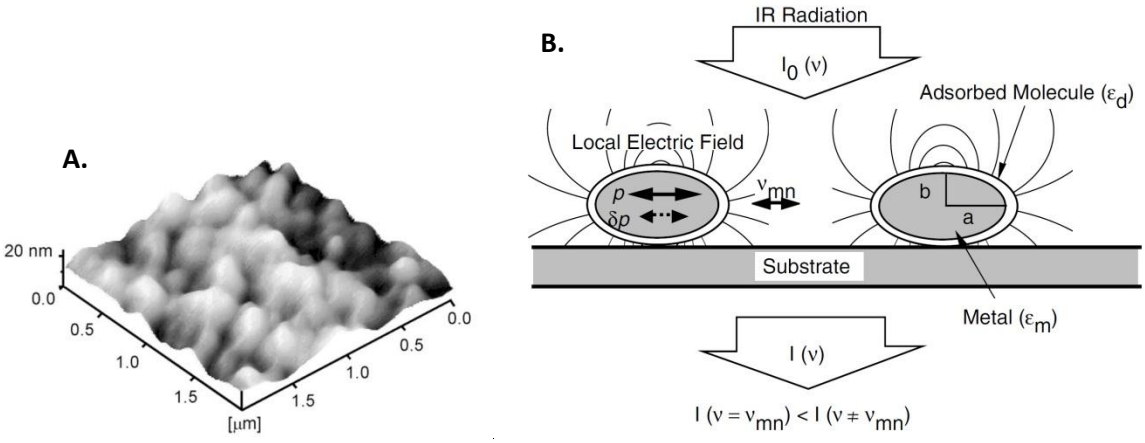

Figure 1.6.8 : A. AFM image of a chemically deposited Au layer. B. SEIRA EM enhancement mechanism. From refs[217, 219]. In B, the local electric field is represented by the lines originating from the Au ellipsoids. ν_{mn} are the vibrations of the adsorbed molecules.

The chemical enhancement mechanism is also discussed, as in general the IR absorption of chemisorbed molecules is more enhanced than that of physisorbed molecules. This may involve charge oscillations between molecular orbitals and the metal surface,

increasing the absorption coefficients of adsorbates by 'intensity borrowing' from the charge-oscillations. Other mechanisms may also contribute to the enhancement, but their nature is unclear.

When compared to "simple" ATR IR spectroscopy, SEIRAS has a number of advantages. First, the gold film can be used as a working electrode in an electrochemical cell in order to make difference SEIRAS. Another advantage of gold is its affinity towards chalcogens, especially sulfur. This allows the creation of self-assembled monolayers (SAM) of thiol derivatives, principally thioalkanes. The properties of the surface can thus be adapted to the needs of the experiment, for example by choosing a thioalkane containing another functional group. The initial formation of a SAM is fast (less than 5 minutes in general) and can be followed by a longer phase of molecular reorganization. The formation of these SAMs can be monitored with high accuracy, since the molecules are chemisorbed on the gold surface. Moreover, the relatively small enhancement distance of SEIRA is advantageous to minimize solvent absorption. Subsequent chemical modifications of the SAM and adsorption of biomolecules are reported in much detail, provided they occur within the enhancement distance[216, 220, 221]. The strategies to adsorb proteins on a gold surface will be detailed in chapter 1.7. The main disadvantages of SEIRAS applied to proteins is that the surface selection rules occult the absorption of vibrational modes with dipole moment derivative components parallel to the surface. Consequently, if the exact orientation of the protein is unknown it is virtually impossible to estimate it, given the important number of residues[216].

1.6.3.7 ^{1}H-^{2}H exchange kinetics of proteins followed by FTIR.

When the $^{1}H_2O$ solvent of a protein sample is exchanged to $^{2}H_2O$, the absorption bands of exchangeable X-H bonds modes shift in position and intensity, which is for example used to attribute the vibrational modes of specific side chains. In practice, X corresponds to sulfur, oxygen or nitrogen as C-H bonds are much more stable and thus not exchangeable at the timescale of the experiments performed in this study. In large proteins such as transmembrane proteins, the interior is shielded from the solvent, so that the exchange is slower or not possible at all. Thus, if the ^{1}H-^{2}H exchange (HDX) is monitored over time, it provides an information about the solvent accessibility of different parts of a protein. In

general, three parts are distinguished : the fast exchanging, or readily solvent-accessible part comprises residues at the surface of the protein ; the intermediate part encompasses residues located just beneath the surface or in specific transport channels, such as proton translocation channels ; the slow, or constant part contains the residues from the hydrophobic core of the protein. With HDX kinetics, it is possible to monitor flexibility, hydrogen bonding as well as conformational changes of proteins in addition to their solvent accessibility[222].

The experimental procedure used for HDX kinetics in the MIR region is detailed in chapter 2.3. It is based on the changes occurring in the Amide I and II modes when a buffer solution in $^{2}H_2O$ is perfused to a protein sample immobilized on a hydrophobic ATR crystal. As upon HDX the Amide II mode splits into the Amide II' and the ν(N-^{2}H) modes at lower frequencies, the diminution of its area (estimated through integration of the Amide II band) is a good indicator to see which fraction of the backbone amide ^{1}H was already exchanged. The Amide I mode, mainly composed of ν(C=O) vibrations, shifts only by ~10 cm^{-1} to lower frequencies so that its area is conserved. It can thus serve is an internal reference to monitor eventual protein desorption from crystal. If, in two different experiments, a protein is in a different conformation or if ligands block solvent access to certain parts, the exchange rates and/or the respective percentages of the fast, intermediate and slow parts can vary. HDX kinetics will be used in chapter 3.3.3 to study the effect of phospholipids on Complex I.

1.6.4 Cyclic voltammetry

Cyclic voltammetry allows to monitor the redox events occurring in a system[223, 224]. A potential linearly ramped against time is applied to an electrochemical cell. When the potential reaches a set value, the potential ramp is inverted and returns back to its initial value (Figure 1.6.9 A.). The process can be repeated infinitely. The number of $V.s^{-1}$ is known as the scan rate, υ. During the potential sweeps, the current is measured, and when plotted against the potential this gives the cyclic voltammogram (CV). If a redox reaction occurs in the scanned potential range, a current peak will appear since the reaction consumes or liberates electrons. When the potential approaches the reduction potential of the studied reaction, the peak will increase, and decrease again when the concentration of the active

species close to the working electrode surface is depleted (this supposes that the solution is not stirred). If the reaction is reversible, a peak will appear both during forward and backward scans (Figure 1.6.9 B.).

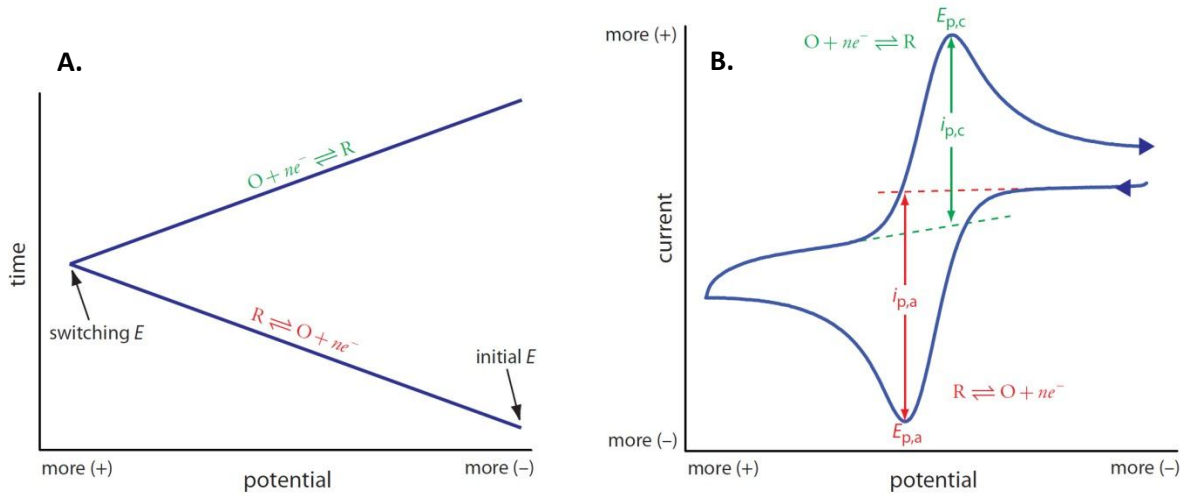

Figure 1.6.9 : A. Potential vs. time for a cyclic voltammetric experiment. B. Typical CV of a reversible redox reaction. From ref[223]. R = Reducing agent, O = Oxydizing agent. In B., the anodic peak corresponds to the oxidation of an analyte and is defined by its potential $E_{p,a}$ and its intensity $i_{p,a}$. The cathodic peak corresponds to the reduction of an analyte and is defined by its potential $E_{p,c}$ and its intensity $i_{p,c}$.

The separation between the anodic and cathodic peaks of a reversible redox reaction in an ideal system ($|i_{p,a}|$ = $|i_{p,c}|$) is inversely proportional to the number of electrons transferred (equation *(17)*). This hysteresis is due to polarization overpotentials. The E'_0 of the redox couple can be easily estimated according to equation *(18)*.

$$\Delta E_p = \left|E_{p,c} - E_{p,a}\right| = \frac{59}{n}\, mV \qquad (17)$$

$$E'_0 = \frac{E_{p,c} + E_{p,a}}{2} \qquad (18)$$

The peak current i_p is described by the Randles-Sevcik equation, which at 25°C can be written :

$$i_p = 269.000\, n^{3/2}\, AD^{1/2} C v^{1/2} \qquad (19)$$

where A is the area of the electrode, D the diffusion coefficient and C the concentration. A two-electron transfer, as expected for NADH for example, will thus yield a higher current. All these properties can be estimated from a CV - in the ideal case. When semi- or non-reversible reactions are involved, the interpretation of the CVs is more complicated.

Cyclic voltammetry has been employed to resolve electron transfer and coupled chemistries within redox enzymes, which represent ca. 30 % of all known enzymes[225]. This is mainly done by investigating kinetic and voltage dependence of proteins films adsorbed on the electrode's surface. This abolishes the limitation of protein diffusion in solution and allows direct measures of the redox chemistry in an active site, provided that the latter is oriented in a manner to allow electron transfer with the electrode surface (see chapter 1.7). Cyclic voltammetry of protein films is used to measure the intrinsic properties of the redox centers, or, if a substrate is added, to measure the catalytic power of the enzymes. The dynamics of electron transfer to and within enzymes depend on the rate-limiting step ; this can be the transfer of electrons from the electrode surface to the enzyme, the reaction of a cofactor or unfavorable substrate binding. This 'control-point' will determine which potential is actually seen in the CV of a redox enzyme. For example, a film of the NDF from mitochondrial Complex I (subfragment Iλ) was adsorbed on a spinning pyrolitic graphite edge electrode in presence of NADH and NAD^+ [226]. While the signals of the individual cofactors were not seen in the resulting CV due to low surface coverage, the catalytic interconversion of the substrates by the fragment was observed. This allowed to conclude that the control-point is a one electron transfer, most-likely the second one-electron reoxidation of FMN or the electron transfer to or from N1a. Furthermore, no overpotential was needed for the NADH/NAD^+ electrochemical conversion, which otherwise requires an overpotential of up to 1 V[227].

1.7 Electrode surface-immobilization of redox enzymes

1.7.1 General strategies

Numerous strategies to adsorb proteins on an electrode surface are found in the literature[218, 220, 221, 225, 228]. Here, we will focus on the adsorption of proteins on a gold surface, which can subsequently be used in SEIRAS and CV experiments. To avoid protein denaturation, the metal surface has to be coated with a layer of organic molecules. This is achieved through the formation of a thiol-based SAM. Depending on the desired orientation of a protein, the polarity and the morphology of the SAM/surface can be modulated by choosing different thiol-containing compounds and by adapting the nano-structure of the gold film. Once a SAM is formed, it can be further modified through chemical reactions. The number of possible surfaces hereby created is virtually unlimited. To determine the influences of the SAM and the surface on the properties of a redox enzyme, numerous studies used the soluble electron carrier cytochrome *c* as a model[229], as this enzyme is small (~13 kDa) and its only redox cofactor (the heme *c*) readily transfers electrons to and from the protein surface. For example, when the thioalkane used to create the SAM contains less than~10 methylene groups, electron tunneling from the electrode to the enzyme is rapid and not rate limiting. Also, the electrostatic properties of the SAM are important ; a SAM of 11-mercaptoundecanoic acid (MUA) on a typical SEIRA active gold surface allowed to immobilize cytochrome *c* through electrostatic interaction between the negatively charged MUA (at pH 7) and the positively charged protein surface[230]. This allowed to obtain both a CV showing the reversible redox reaction of the heme and a differential SEIRAS spectrum revealing the changes in the vibrational modes of the protein backbone, certain amino acid side chains and the heme. The electrode area was also increased by adding gold nanoparticles, so that the current measured in a CV experiment was increased[231].

1.7.2 Strategies to immobilize membrane proteins on a gold surface

Different strategies have been employed to immobilize detergent solubilized membrane proteins on electrodes[220]. For example, a hydrophobic SAM of chemically modified thioalkanes can be used to adsorb the protein through its membrane domain[232]. Thiol-containing lipids were also used to create a lipid bilayer directly on the electrode, and

the subsequent protein insertion into this bilayer is promoted by dialysis-based detergent removal. Other methods employed covalent attachment of the protein to SAM through peptide coupling between carboxylic acid and amine, *via* a chemical coupling agent. Affinity-based immobilization of tagged proteins was also used, e.g. by using the streptavidin-biotin couple.

Concerning the respiratory chain enzymes, mainly the adsorption of Complex IV on a gold electrode was studied[233-235]. One method was based on the affinity of a genetically introduced histidine-tag on the enzyme towards a Nickel Nitrilotriacetic acid (NiNTA) containing SAM. Once the protein was adsorbed, preformed liposomes were added and the detergent was removed through biobeads, reconstituting the native lipid bilayer.

1.7.3 Strategy to immobilize Complex I

Until now, the adsorption of Complex I on a gold electrode was not reported. Here, we propose two strategies to achieve this immobilization, in order to probe the immobilized enzyme through SEIRAS and CV. The first method is based on the same strategy as for Complex IV, i.e. the affinity-based adsorption of a histagged Complex I on a NiNTA SAM. The histag is genetically inserted at the N-terminus of subunit NuoF for purification purposes[97], so that the enzyme would be immobilized through the tip of the NDF fragment. The NiNTA SAM would be prepared as in ref , i.e. through the creation of a SAM containing a O-succinimide ester, which can be coupled to Nitrilotriacetic acid and chelated with Ni^{2+} (see chapter 2.5 for experimental procedure). However, in this approach the NADH binding site of Complex I (and the first electron acceptor, FMN) might be too far away from the electrode surface to allow rapid electron transfer between the two (Figure 1.7.1).

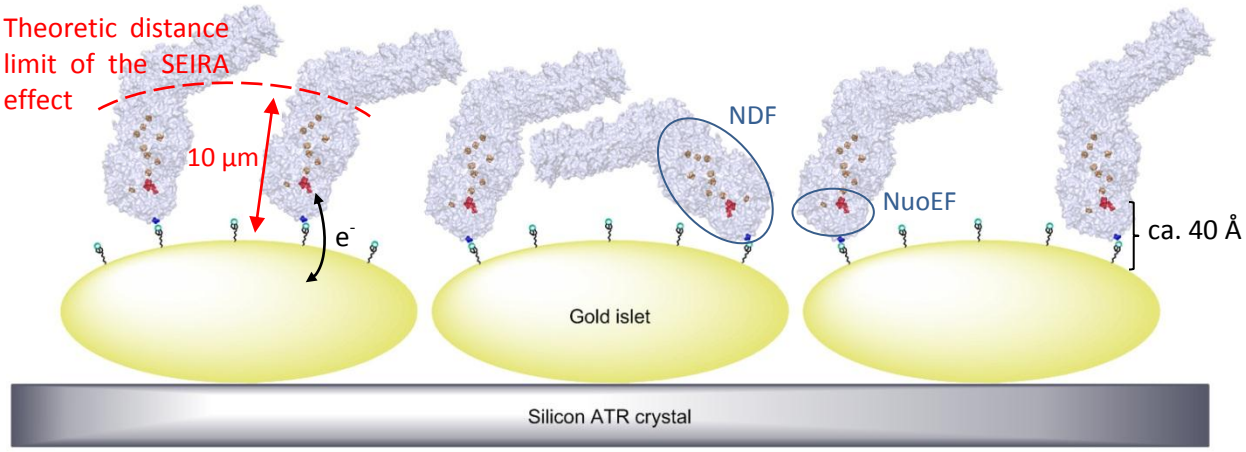

Figure 1.7.1 : Representation of Complex I immobilized on a NiNTA SAM at a SEIRA-active gold surface. The cofactors of Complex I are shown as colored dots, with FMN in red. The location of the Histag is indicated by the blue dots. The distance between FMN and the gold surface is at least 40 Å.

Since the SEIRA effect is limited to the first~10 µm from the gold surface, it is possible that the IR absorption of some parts of Complex I is not enhanced. The adsorption of smaller fragments such as the NDF and the NuoEF subcomplex will also be studied, as they might allow to attribute certain parts of the IR spectra of the whole Complex I (Figure 1.7.1).

A second approach was imagined to reduce the distance between the gold surface and the FMN : if it was possible to covalently attach the NADH substrate to a preformed SAM, direct and rapid electron input to the FMN could be possible. The covalent immobilization of NADH can be afforded through a rather simple process ; the alkanethiols used to create the SAM should contain a carboxylic acid which can form a peptide bond with the NADH Adenine-Amine when a crosslinking agent is added (see chapter 2.5 and 3.1). To avoid steric hindrance for the correct insertion of NADH into the binding pocket, a mixed SAM composed of a longer chain acid and short-chain alcohols should be used (Figure 1.7.2).

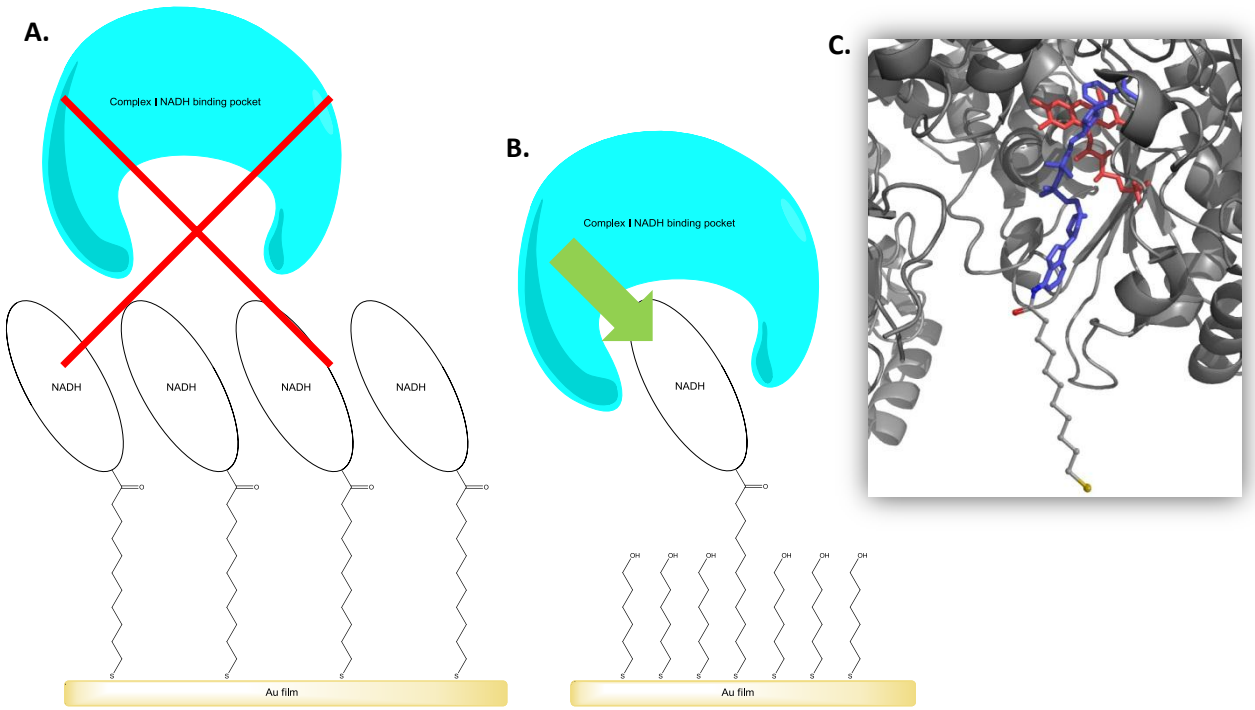

Figure 1.7.2 : Adsorption of Complex I on a NADH SAM. A. If a densely packed monolayer of NADH is present, they might induce a sterical hindrance for the adsorption of the protein through its NADH binding site. **B.** When the SAM is diluted with shorter-chain thioalkanes, adsorption should be possible. **C.** Representation of bound NADH (blue sticks) attached to MUA (grey sticks) in the NADH binding pocket. FMN is shown as red sticks.

The electrode surface coverage expected for the large Complex I is probably too low to obtain CVs where the individual cofactor reactions can be seen. However, the catalytic interconversion of quinones might be seen. As quinones are hydrophobic, their reaction would be favored in a lipid bilayer. Therefore, the immobilized Complex I should be reconstituted in a lipid bilayer (Figure 1.7.3). As for Complex IV, this can be achieved through addition of preformed liposomes and subsequent detergent removal through biobeads-based dialysis. The addition of quinone and inhibitors will be probed in chapter 3.1.

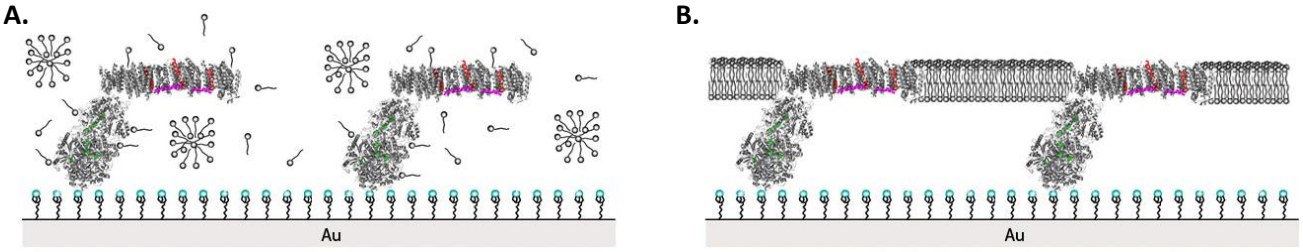

Figure 1.7.3 : Immobilized Complex I before (A.) and after (B.) insertion into a lipid bilayer.

1.8 Aim of the work

The main objectives of this study are the following :

i. Create an experimental setup which allows combined SEIRAS and electrochemical measurements of proteins. Test it for a model redox enzyme, cytochrome *c*. Once the setup operational, immobilize Complex I in a biomimetic fashion and probe it against substrates and inhibitors through electrochemically-induced differential SEIRAS and CV.

ii. Investigate the effect of $_{F}Tyr^{178}$ and NADH-OH inhibition on the FMN through UV-Vis spectroscopy. Combine these results to measures of NADH binding constants and ROS production.

iii. Obtain detailed information about the Complex I - lipid interaction through electrochemically-induced difference FTIR spectroscopy and ^{1}H-^{2}H exchange kinetics.

iv. Probe the inhibition of Complex I by Zn^{2+} through electrochemically-induced difference FTIR spectroscopy

v. Explore the results of (iii) and (iv) in the light of the crystal structure of the entire Complex I and propose new possibilities for the proton pumping and coupling mechanisms of Complex I.

2 Experimental procedures

2.1 Sample preparation

The preparations of Complex I were realized in Pr. Dr. T. Friedrich's group at the Albert-Ludwigs University Freiburg. Further details concerning the purification and biochemical characterization methods are given in Appendix chapter 5.1.

2.1.1 Preparation of *NuoF*$_{HIS}$ NADH:ubiquinone oxidoreductase (Complex I) from *Escherichia coli*

The *E. coli* cells from Strain BW25113Δnuo[236] (derivative of *E. coli* K-12 strain BD792) were transformed with pBAD*nuo*/*nuoF*$_{HIS}$. Large volumes were obtained in a 200 L fermenter in YP medium (containing 0.5% w/v yeast extract and 1% w/v peptone). The medium was composed of 10 L 0.3 M Na_3PO_4, 0.2 M Na_2HPO_4, 0.5 M KH_2PO_4, 1 M NH_4Cl, 0.25 M Na_2SO_4, 400 mL of 1 M $MgSO_4$, 15 mg/mL ferric ammonium citrate, 10 g riboflavin and 100 mL of 1 M L-cysteine. Cells were grown aerobically at 37°C. After 1 h, the expression of the *nuo*-operon was induced with 0.2% w/v L-arabinose. The cells were then harvested until they entered the stationary growth phase by continuous flow centrifugation at 17000 *g* at 4 °C, shock frozen in liquid nitrogen and stored at -80 °C for further use.

For isolation of Complex I, each step was carried out at 4°C. First, approx. 30 g of the previously grown frozen *E. coli* cells were added to 150 mL of buffer containing 50 mM MES, 50 mM NaCl and 100 µM phenylmethylsulfonyl fluoride (PMSF) at pH 6.3. One spatula tip of DNAse I was added to the solution which was then homogenized in a mixer. The foam resulting from this step was removed with Antifoam 204 (Sigma-Aldrich). The suspended cells were then disrupted by a single pass through a French Press (SLM-Aminco) at 110 MPa. After removal of cell debris by centrifugation (RC-5 SR Centrifuge, Sorvall Instruments) at 9500 *g* for 20 min, the cytoplasmic membranes were collected through ultracentrifugation (L8-M Ultracentrifuge, Beckmann Coulter) at 250000 *g* for 1 h 10 min. To extract the membrane proteins, detergent extraction was used. For this, the membranes were resuspended in 50 mM MES, 50 mM NaCl, 5 mM $MgCl_2$, 30 µM PMSF, pH 6.3 at 1 g per mL of

suspension and the solution was carefully homogenized in a glass-teflon homogenizer. 100 µL were sampled from this solution for purification yield estimation (see 2.1.7 and 2.1.9). *n*-dodecyl β-D-maltoside (DDM, Sigma) was then added to a final concentration of 3 % w/v. The mixture was incubated on ice for 15 min with occasional gentle stirring. The unsolubilized material was removed through a 15 min step of ultracentrifugation at 250000 *g* and the supernatant was collected into a graduated cylinder kept on ice. 150 µL were collected from this solution for yield estimation.

The solution was then pumped (flow-rate : 6 mL/min) *via* an ÄKTA Prime Plus chromatography system (GE Healthcare) onto a 50 mL anion exchange chromatography column (Fractogel EMD TMAE Hicap M, Merck) previously equilibrated with a 50 mM MES, 50 mM NaCl, 0.1 % w/v DDM, 5 mM MgCl2, pH 6.3 buffer. The column was then washed with the same buffer until the Absorbance at 280 nm decreased significantly (see Appendix 1), indicating that non-bound proteins were eluted. The concentration of NaCl was then increased to 150 mM and a first fraction of bound protein was washed away, as indicated by a peak of A_{280nm}. After the second decrease of A_{280nm}, a 75 mL linear gradient from 150 mM to 350 mM NaCl was applied, and the eluate was collected in 4 mL fractions. The fractions exhibiting the highest NADH/ferricyanide activity (see 2.1.7 for details) were pooled together and 400 µL of this solution were sampled for yield estimation. Imidazole was then added to a final concentration of 20 mM. The solution was pumped (flow rate : 1.3 mL/min) onto a 20 mL ProBond Ni^{2+}-IDA affinity column (Invitrogen) previously equilibrated with a 50 mM MES, 500 mM NaCl, 0.1 % DDM, 5 mM $MgCl_2$, 20 mM imidazole, pH 6.3 buffer. Non-bound proteins were again washed off by elution with the same buffer used for equilibration. Elution of Complex I was started once A_{280nm} again reached its initial value by increasing the imidazole concentration stepwise from 20 mM to 500 mM (see Appendix 1). The eluate was collected in 2 mL fractions, and the ones exhibiting NADH/ferricyanate activity were pooled together. To remove the imidazole, the solution was concentrated, diluted 10 fold with 50 mM MES, 50 mM NaCl, 0.1 % DDM, 5 mM $MgCl_2$, pH 6.3 buffer and these two steps were repeated 2 times. Finally, the sample was concentrated to at least 50 mg/mL (as measured by UV-Vis, see 2.1.8) by ultrafiltration (Amicon 100 kDa cut-off membrane, Millipore), aliquoted, shock-frozen in liquid nitrogen and stored at -80°C for further use.

2.1.2 Preparation of *NuoF*$_{HIS}$ Complex I from *E. coli* with reduced lipid content

To remove a higher quantity of lipids from the protein during the purification, the protocol described in 2.1.1 was slightly modified. Each step before the affinity chromatography column was rigorously the same. The sole difference was that after A_{280nm} returned to its initial value during the elution with the 50 mM MES, 500 mM NaCl, 0.1 % DDM, 5 mM $MgCl_2$, 20 mM imidazole, pH 6.3 buffer, the imidazole concentration was not increased before 150 mL of this buffer were washed over the column (see Appendix 4).

2.1.3 Preparation of wild type Complex I from *E. coli*

This preparation was done in cooperation with Marius Schulte in Pr. Dr. T. Friedrich's laboratory as described in ref.[107]. Briefly, the Complex I overexpressing cells were disrupted through a French pressure cell, the membranes were collected *via* ultracentrifugation and the proteins were extracted through DDM extraction. The untagged Complex I was then purified using two anion exchange columns (Fractogel EMD TMAE Hicap M, Merck and Source 15Q, GE Healthcare) and one size-exclusion chromatography column (Sephacryl S-300 HR, GE Healthcare) before being concentrated and stored at -80°C for further use.

2.1.4 Preparation of *E. coli* Complex I *nuoF* Y178 mutants

All the *nuoF* Y178 mutants were prepared in Pr. Dr. T. Friedrich's laboratory by Emmanuel Gnandt and Klaudia Morina. Since the plasmid used for Complex I homolog overexpression in *E. coli* (pBAD*nuo nuoF*$_{His}$) is too long for site-directed mutagenensis, λ-Red mediated recombination[97] was used to swap Y178 for Ala, Cys, Phe and Leu. This was done the following way : electrocompetent cells from *E. coli* strain DH5αΔnuo/pKD46 (50 µL, OD_{600} = 40) were cotransformed with the plasmid pBAD*nuo nuoF*$_{HIS}$*::nptI-sacRB* (50 ng) and linear DNA fragment lin_*nuoF* Y178A/C/L/F (250-350 ng) *via* electroporation. Upon transformation the cells were incubated for 24 h at 30°C on chloramphenicol containing YP saccharose agar plates to ensure that only the cells were the *nptI-sacRB* cassette was replaced by lin_*nuoF* survived. Single colonies were then transferred to chloramphenicol-LB

medium, incubated and their plasmids were extracted with the help of a commercially available Wizard® Plus SV Minipreps DNA Purification kit.

After analysis of the correct insertion of the mutations into the plasmid through restriction mapping, electrocompetent cells of *E. coli* strain BW25113Δ*nuo* (50 µL) were transformed with the isolated plasmid pBAD*nuo* *nuoF*$_{HIS}$ Y178A/C/L/F (10 ng) by electroporation. The cells were then pre-cultivated in 400 mL chloramphenicol-LB medium for 14 h at 37°C and the culture was scaled-up to 10 L in a fermenter containing an auto-induction medium. They were grown aerobically at 37°C, and once the stationary phase was reached (as indicated by OD_{600}) they were harvested *via* centrifugation (10 min, 5750 *g* and 2 min, 3600 *g*). The resulting cell sediment was then shock frozen and stored at -80°C.

The purifications of all the *nuoF* Y178 mutants were identical to those described in chapter 2.1.1.

2.1.5 Preparation of NADH-Dehydrogenase Fragment (NDF) from *E. coli*

The NDF was prepared with the help of Dr. Ruth Hielscher and Michelle Yegrès (Université de Strasbourg). The NADH dehydrogenase was overexpressed in *E. coli* strain BL21(DE3)/pET11a as described in ref.[237]. The purification was slightly modified from ref.[237]. The cells were broken by a single pass through a French pressure cell at 110 MPa. Cell debris were removed by ultracentrifugation at 250000 *g* for 60 min. The supernatant was applied to a 50 mL anion exchange chromatography column (Fractogel, EMD, Merck) equilibrated with 50 mM MES, 50 mM NaCl, pH 6.0, 30 µM PMSF and 5 mM DTT. The column was washed with the same buffer until the absorbance at 280 nm decreased. Proteins were eluted with a 300 mL linear salt gradient from 50 to 300 mM NaCl in 50 mM MES, pH 6. Fractions exhibiting NADH/ferricyanide oxidoreductase activity were combined and adjusted to pH 6.6 with 200 mM NaOH. The solution was then applied to a 10 mL Strep−Tactin Sepharose column (IBA) previously equilibrated with 50 mM MES/NaOH, 50 mM NaCl, pH 6.6, 30 µM PMSF and 5 mM DTT. The NADH dehydrogenase fragment was eluted with 2.5 mM D−desthiobiotine in 50 mM MES, 50 mM NaCl, pH 6.0. The fractions with

NADH/ferricyanide oxidoreductase activity were pooled, concentrated by ultrafiltration (100 kDa MWCO Amicon, Millipore), shock frozen in liquid nitrogen and stored at -80 °C for further use.

2.1.6 Preparation of *nuoEF* subcomplex from *Aquifex aeolicus*

The *nuoEF* fragment was prepared by Michelle Yegrès. The protocol used was adapted from ref.[238]. *E. coli* cells were used to overexpress the *Aquifex aelicus nuoEF* fragment. All steps were performed at 4°C. 10 g Rosetta(DE3)/pLacI/pETBlue-1*nuoEF*$_{HIS}$ cells were suspended in 40 mL buffer containing 50 mM MOPS, 200 mM NaCl, 20 mM imidazole, 100 µM PMSF and a spatula tip of DNAse I at pH 7. After homogenization the cells were lysed by two passes through a French Pressure Cell at 110 MPa. Cell debris were removed by ultracentrifugation (160 000 *g* for 70 min) and the supernatant was loaded onto a 10 mL ProBond Ni^{2+}-IDA affinity column (Invitrogen) previously equilibrated with the same buffer. After decrease of A_{280} weakly bound proteins were eluted from the column by increasing the imidazole concentration to 100 mM. The proteins of interest were then eluted with a 40 mL gradient from 100 to 500 mM imidazole. Fractions exhibiting peak NADH/ferricyanide oxidoreductase activity were pooled together and concentrated to 500 µL by ultrafiltration (Amicon ultra 15, 30 kDa MWCO, 4000 *g*). The solution was applied to a 120 mL Superdex 200 size exclusion column equilibrated with a 50 mM MOPS, 50 mM NaCl, pH 7 buffer. After elution of the proteins with the same buffer, the fractions that exhibited NADH/$K_3[Fe(CN)_6]$ activity were reassembled and subjected to ion exchange chromatography on a 5 mL Source 15Q column (Amersham Bioscience) equilibrated in the same buffer as before. After a washing step, proteins were eluted with 25 mL gradient from 50 to 350 mM NaCl. Again, fractions with NADH/ferricyanide activity were combined and applied onto the same Superdex 200 size exclusion column. Finally, fractions of interest were concentrated to approx. 5 $mg.mL^{-1}$, shock frozen and stored at -80°C.

2.1.7 NADH/$K_3[Fe(CN)_6]$ oxidoreductase activity measurements

The oxidoreductase activity of the Complex I samples was measured by following the reduction of ferricyanide by NADH[193]. This was done by measuring the Absorbance at

410 nm[239] in a cuvette with 1 cm path length at room temperature. The cuvette contained 1 mL of 50 mM MES, 50 mM NaCl, 1 mM $K_3[Fe(CN_6)]$, 0.2 mM NADH, pH 6.3 buffer. To calculate the NADH/$K_3[Fe(CN_6)]$ oxidoreductase activity (in $\mu mol.min^{-1}.mL^{-1}$ or $U.mL^{-1}$) the Beer-Lambert Law was used (chapter 1.6.1) and the extinction coefficient of $K_3[Fe(CN_6)]$ at 410 nm was 1 $mM^{-1}.cm^{-1}$.

2.1.8 Determination of Complex I concentration through UV-Visible spectroscopy

To quantify the concentration of the Complex I, an UV-Vis spectrum of 5 µL sample diluted in 245 µL buffer (MES 50 mM, NaCl 50 mM, 5 mM $MgCl_2$, 0.1 % DDM) was recorded in a 1 cm path length quartz cuvette *via* a Diode-Array UV-Vis Spectrophotometer (TIDAS II, J&M). The spectrum of the buffer was previously recorded and subtracted from the sample spectrum. To account for absorption by lipids or detergents, the absorbance value at 310 nm, where no protein absorption should be present, was subtracted from the absorbance value at 280 nm. The concentration was then calculated according to the Beer Lambert Law using a molar extinction coefficient for Complex I (MW 535.4 kDa) of ε_{280nm} = 781 $mM^{-1}.cm^{-1}$ (calculated according to ref.[190]).

2.1.9 Determination of total protein content by biuret reaction

To evaluate the yield of the Complex I purification, the total protein content after the four main purification steps (Membrane Collection, Detergent Extraction and Anion Exchange Chromatography and Affinity Chromatography - see 2.1.1) was determined by means of biuret reaction[240]. In 10 to 40 µL of the sample solutions, 1 mL 6% w/v trichloroacetic acid (TCA) was added. The mixtures were then centrifuged for 1 min at 15700 g. The supernatant was discarded and the pellets were briefly dried before being resuspended in 1 mL Biuret-reagent. They were then shaken for 30 min at 1400 rpm at 37°C (Thermomixer Compact, Eppendorf). The absorbance of each sample was measured at 546 nm, which corresponds to the absorption maximum of the created Protein-Cu(II) complexes. After addition of a spatula tip of potassium cyanide in order to mask the Protein-Cu(II) complexes, the absorbance was again measured at 546 nm. These second absorbance values

serve as a background by taking the absorption of lipids and detergents into account. The calculated difference between the two absorbance values was then used to estimate the protein concentration by comparison to a calibration line of 0.1 to 10 mg/mL Bovine Serum Albumin solution.

2.1.10 SDS-PolyAcrylamid Gel Electrophoresis (SDS-PAGE)

To analyse the purity and integrity of the purified proteins, a SDS PAGE[241] was run on each sample. The gel was constituted of two sections, the first to sample the protein (3.9 % of [acrylamid - bisacrylamid 30%]) and the second to separate the subunits (10 % of [acrylamid - bisacrylamid 30%]). Prior to the electrophoresis, 50 to 80 µg of each sample was completed with 5 µL Millipore water and 2 µL Schägger sample buffer[241] and shaken at 800 rpm for 30 min at 37°C (Thermomixer Compact, Eppendorf). The sample was then applied on the gel together with a molecular weight marker (PageRuler Unstained Broad Range Protein Ladder, Fermentas). The electrophoresis was then started by the application of a 40 mA current (500 mV, 100 W) and stopped once the first marker band reached the end of the plate. The protein spots were stained with hot Coomassie blue solution followed by decoloration of the gel with an acetic acid/ethanol solution.

2.1.11 Protein sample buffer exchange

Whenever a different buffer than the one of the final purification step was needed, the sample to be exchanged was diluted at least 20 times with the new buffer and re-concentrated by ultrafiltration (Amicon, Eppendorf, 100 kDa MWCO for Complex I or NDF, 30 kDa for *nuoEF*) at 3800 *g* and 4°C for 20 min. The whole step was repeated at least 3 times. If not needed right-away the sample was shock-frozen in liquid N_2 and stored at -80°C.

2.1.12 Other preparations

2.1.12.1 EPE 79 % : CL 11 % : EPG 9 % : SPS : 1 % Liposomes

Liposomes were prepared together with Dr. Martin Holzer in Pr. Schubert's laboratory at the Albert-Ludwigs Universität Freiburg. Their composition was chosen to be as close as

possible to the natural composition of the *E. coli* membrane[167-169]. All lipids were purchased from Avanti polar lipids. 15.8 mg Egg Phosphatidylethanolamine (EPE), 2.2 mg Cardiolipine from Bovine Heart (CL), 1.8 mg Egg Phosphatidylglycerol and 0.2 mg Soy Phosphatidylserine (SPS) were dissolved in chloroform and/or methanol in a round bottom flask. The flask was set up in a rotary evaporator at 30°C and the solvents were slowly removed at 90 rpm under a 300 mbar depression for 10 min, then 90 mbar. To completely remove solvent, the flask was hooked onto a high vacuum pump for 1 hour. 1 mL of buffer (50 mM MES, 50 mM NaCl, pH 6.3) was added to the dried lipids and the flask was swiveled by hand until the colloidal suspension was formed, as judged by the complete disappearance of solids from the flask walls. The resulting liposomes were then extruded (Avanti mini-extruder kit) 21 times through a 200 nm membrane and 51 times through a 100 nm membrane. The size distribution of the liposomes was controlled by Dynamic Light Scattering and their Zeta potential by electrophoretic mobility (Zetamaster S for both, Malvern).

2.1.12.2 NADH-OH

NADH-OH was prepared by a protocol adapted from ref [150]. 100 mM KOH were added to a 20 mM NADH solution at 4°C. Pure O_2 was then bubbled through the solution for 30 min and the solution was left at RT for two days during which the O_2 treatment was repeated twice a day. 40 mL of this solution were then applied to a 5 mL Q-Sepharose column (Amersham Bioscience) previously equilibrated with 5 mM KPi at pH 12. Elution of NADH-OH was done with a linear KPi gradient from 5 to 500 mM. The fractions containing NADH-OH were eluted from the column at approx. 350–400 mM K-Pi and after NADH. To monitor the fractions containing NADH-OH, their inhibitory effect was tested on a Complex I sample by following its NADH/ferricyanide activity (2.1.7). The NADH-OH containing fractions were pooled, adjusted to pH 4.5 with HCl and applied to a Bakerbond Octadecyl 40 µM flash chromatography column equilibrated with 0.5 M KPi pH 4.5. NADH-OH elution was done with water. The NADH-OH containing fractions were united, yielding a 300 µM solution.

2.2 Potential induced differential FTIR measures

2.2.1 The optically transparent thin layer electrochemical cell

The optically transparent thin layer electrochemical cell[210], briefly introduced in chapter 1.6.3.4, consists of a solid PVC cell body with four inlets, three serving to connect a three electrode system and one used to fill the cell with buffer solution.

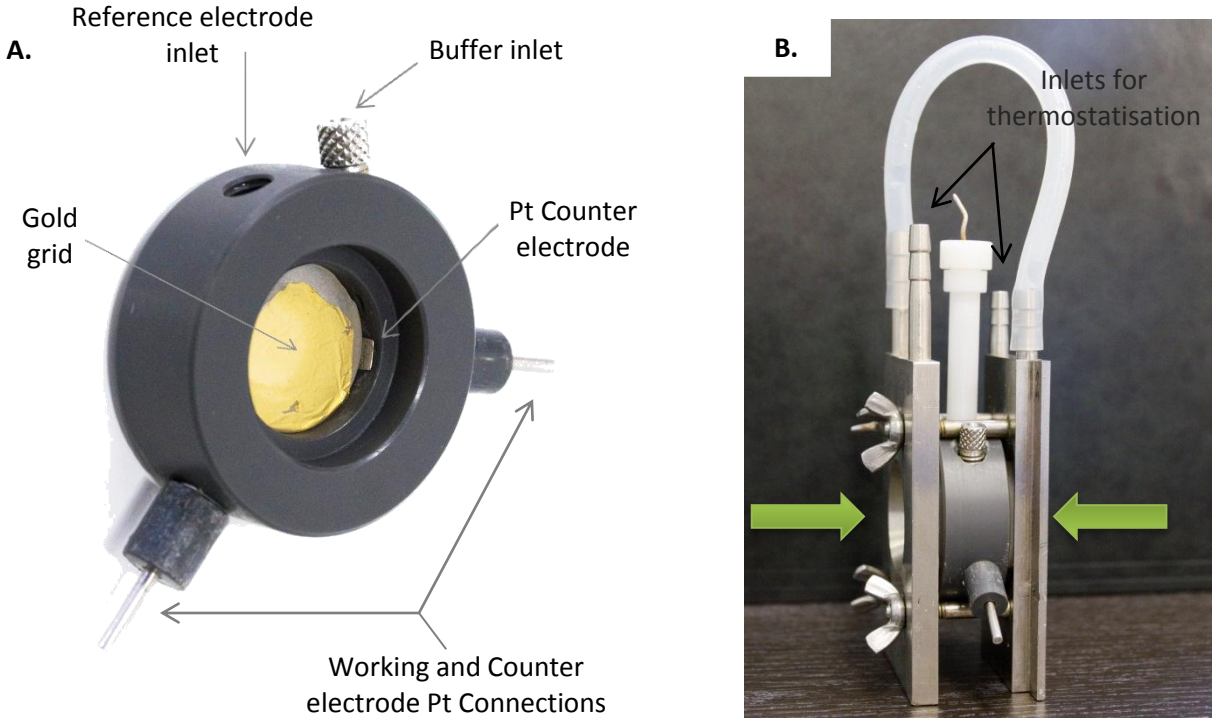

Figure 2.2.1 : The thin layer electrochemical cell during (A.) and after (B.) assembly. The green arrows represent the optical pathway.

To set the cell up, a thiol-modified gold grid used as a working electrode is placed on a UV-Vis- and IR-transparent CaF_2 window, connected to a platinum wire in one of the inlets, and a second Pt wire is connected to a piece of Pt to compose the counter electrode (Figure A.). The sample to be analyzed is then deposited in the middle of the gold grid and a second CaF_2 window is placed on top of it. The whole cell is then fit between two steel plates which can be squeezed together, thus jamming the gold grid between the CaF_2 windows and thereby creating a very short optical path-length, below 15 µm (Figure 2.2.1 B.). To complete

the setup, the cell is filled with the adequate buffer through inlet 1 figure x and a Ag/AgCl 3M KCl reference electrode (+208 mV *vs.* SHE) is screwed into the inlet represented on Figure 2.2.1 A). The cell is then transferred in the desired spectrometer, connected to a homemade potentiostat *via* the three electrodes and also to a thermostat through the inlets pictured in Figure 2.2.1 B).

The gold grid is modified by thioalkane derivatives. The mixture used here (1 mM cysteamine, Cyst, and 1 mM 3-mercaptopropionic acid, MPA) prevents protein denaturation that occurs on bare gold surfaces by forming a self-assembled monolayer (SAM) (Figure 2.2.2).

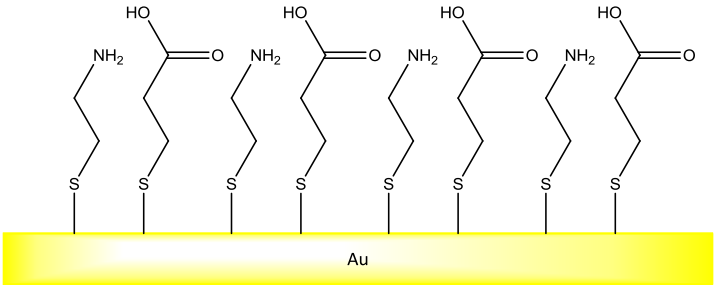

Figure 2.2.2 : 3-MPA - Cyst SAM formed on the gold grid

Since the enzymes studied here have numerous cofactors buried deep inside their structure, the electron transfer rates between the cofactors and the working electrode are quite slow. To promote electron transfer, the proteins studied by this method were pre-incubated on a mixture of 19 electrochemical mediators (Table 2.2.1). Their midpoint potentials were chosen to cover the range from -600 to +600 mV *vs.* Ag/AgCl 3 M KCl, and their final concentrations in the samples were less than 25 µM in order to prevent any contribution to the FTIR or UV-Vis spectra.

Substance	E'_0 (mV) *vs.* Ag/AgCl	Purchased from	Solvent
Ferrocenylmethyltrimethylammoniumiodide	607	Strem chemicals	Ethanol
1,1'−ferrocenedicarboxylic acid	436	Fluka	Ethanol
Potassiumhexacyanoferrate(II) trihydrate	212	Riedel−de−Haën	Water
1,1'−dimethylferrocene	133	Aldrich	Ethanol
Quinhydrone	70	Fluka	Ethanol
Tetrachloro−1,4−benzoquinone (*p*−Chloranil)	72	Aldrich	Acetone
N,N,N',N'−tetramethyl−*p*−phenylenediamine dihydrochloride	62	Fluka	Water
2,6−dichlorophenolindophenol sodium salt hydrate	9	Biochemika	Ethanol
Hexaammineruthenium(III)chloride	-8	Aldrich	Water
Anthraquinone−2−sulfonic acid sodium salt	-23	Aldrich	Water
1,4 naphthoquinone hydrate	-63	Aldrich	Ethanol
Anthraquinone	-108	Aldrich	Ethanol
5−hydroxy−1,4−naphtoquinone	-158	Aldrich	Ethanol
Duroquinone	-198	Sigma	Ethanol
Menadione	-220	Sigma	Acetone
2−hydroxyl−1,4 naphthoquinone	-333	Sigma	Ethanol
9,10−antraquinone−2,6−disulfonic acid disodium salt	-433	Sigma	Ethanol
Neutral Red	-515	Sigma-Aldrich	Ethanol
Methyl viologen dichloride hydrate	-628	Aldrich	Water

Table 2.2.1 : List of the mediators used in spectroelectrochemical experiments.

The mediators were mixed together in their respective solvents and a small amount of that mixture was deposited in 500 µL Eppendorfs. They were then left open to dry overnight, closed and stored at -20°C until use.

2.2.2 Interaction of Complex I with phospholipids

6 to 8 µL of 100 mg.mL^{-1} *nuoF*$_{HIS}$ Complex I with reduced lipid content (purified as described in 2.1.2) in 50 mM KH_2PO_4, 100 mM NaCl, 0.005 % DDM, pH 7 buffer were mixed for 3 hours at 4°C (Thermomixer Compact, Eppendorf) with 1 µL EPE, EPG, CL (Avanti polar lipids or Sigma-Aldrich) or *E. coli* lipid extract (provided by Pr. Blanca Barquera, Rensselaer

Polytechnic Institute) dissolved in the same buffer. The concentrations of the phospholipids were adapted to each sample in order to obtain a Complex I : lipid ratio of 1 : 50. When the lipid was not soluble enough, DDM was added until the solution was homogenous. The mixture was then incubated on one dose of mediator cocktail (Table 2.2.1) and mixed for another hour. The sample was transferred into a thinlayer electrochemical cell (chapter 2.2.1) which was connected to a homemade potentiostat, a thermostat (5°C) and set up in a Bruker Vertex 70 FTIR spectrometer (Globar source, KBr Beamsplitter, Liquid-N_2 cooled MCT detector) where a background spectrum was previously taken. A series of spectra was recorded (average of 256 scans) to ensure that the cell was correctly set up and that no leak or air bubble was present. After approx. 30 min, the temperature was stabilized and the atmospheric conditions did not vary anymore. The potentiostat was switched on and the potential was manually cycled a few times from -700 mV to +200 mV *vs.* Ag/AgCl 3 M KCl. The current was monitored during these cycles to ensure the right electrical contact between each part of the setup ; typically it was between -100 µA and -20 µA right after the potential switch. Then, the redox state of the enzyme was cycled *n* times between reduced state (-700 mV) and oxidized state (+200 mV). At each point, 2 spectra averaging 256 scans were taken and the program (Opus, Bruker) automatically calculated the oxidized *minus* reduced and vice-versa average spectra. The equilibration times between each cycle were 5 min for the reduced state and 4 min for the oxidized state. To obtain a reliable average spectrum, the number of redox cycles was at least 20 and ≥ 60 in most cases.

For control, Complex I with reduced lipid content as well as regular *nuoF*$_{HIS}$ Complex I (purified according to 2.1.1) were measured in the same conditions, except that no phospholipids were added.

2.2.3 Interaction of Complex I with Zinc(II)

6-8 µL 80 of 100 mg.mL^{-1} *nuoF*$_{HIS}$ Complex I (2.1.1) or wild type Complex I (2.1.3) in 50 mM MES, 50 mM NaCl, 0.01 % DDM, pH 6.3 were mixed for 3 h at 4°C (Thermomixer Compact, Eppendorf) with 1 µL of $ZnSO_4$ dissolved in the same buffer. The $ZnSO_4$ concentration was adjusted for each sample in order to obtain a 1 : 100 Complex I : $ZnSO_4$ ratio. The mixture was then incubated on one dose of mediator cocktail (2.2.1) and mixed

for another hour. The rest of the procedure was identical to 2.2.2, except that the equilibration times were extended to 10 min for the reduced state and 9 min for the oxidized state.

2.3 Hydrogen-deuterium exchange kinetics followed by FTIR spectroscopy

2.3.1 Experimental

The *nuoF*$_{HIS}$ Complex I sample with reduced lipid content was mixed with phospholipids as described in 2.2.2. The sample was then deposited on a Si/ZnSe ATR-crystal (BioATR2, Bruker) coupled to a Bruker IFS 28 FTIR spectrometer (globar source, KBr beamsplitter, DTGS detector). The ATR setup is constituted of two compartments (Figure 2.3.1) separated by a semi-permeable membrane (MWCO 3 kDa, manufacturer).

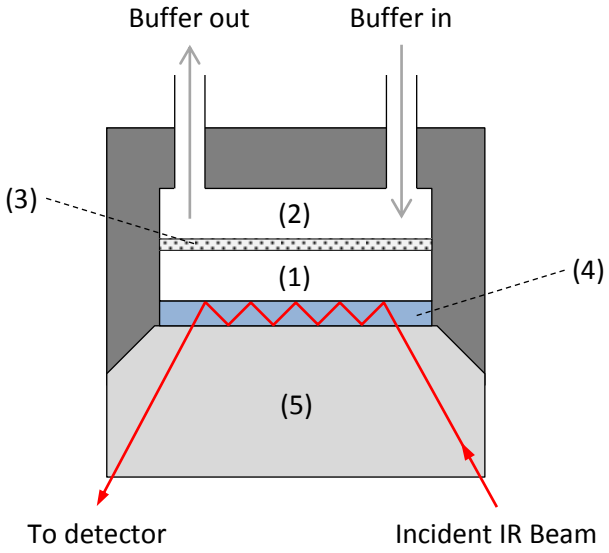

Figure 2.3.1 : Representation of the perfusion ATR cell.(1) : sample compartment ; (2) : perfusion compartment ; (3) semi-permeable membrane ; (4) Silicon crystal (Internal reflection element) ; (5) ZnSe optical element.

The sample was left to dry on air (30 to 60 min), rehydrated with 15 µL 50 mM KPi, 100 mM NaCl, 0.005 % DDM, pH 7 buffer and the compartment was closed. D_2O buffer of same

composition was then perfused at 0.2 mL.min^{-1} flow rate. 16 spectra blocks were recorded during the perfusion, with no time interval between them. Each spectrum from the first block averaged 16 scans, 32 scans for the ones from the second block, 64 and 256 for the third and fourth blocks. At the end of these series, approx. 10 mL of deuterated buffer had been washed over the sample and a closed circuit was set up since most of the H_2O had been removed. A series of 72 spectra averaging 256 scans was finally recorded at 20 min intervals.

2.3.2 Calculation of the exchange fractions and rates

The exchange fractions and rates were calculated according to references[197, 242]. All operations on the spectra were done with the Opus software from Bruker and standard calculations were done with Microsoft Excel and Origin (OriginLab). Briefly, a reference spectrum of the H_2O buffer used in this experiment was interactively subtracted from each spectrum. The coefficient for this subtraction was previously calculated from the quantities of H_2O, D_2O and HOD present in the sample at each time as determined by the integration of their respective signals. To account for small variations of sample quantity in the vicinity of the ATR surface, the spectra were then normalized with respect to the Amide I band. The fraction of exchanged protein (i.e., of "Amide-H") at each point was calculated by integration of the Amide I and II bands (equation *(20)*). By plotting this fraction against time the rate of exchange can be followed (Figure 2.3.2).

$$\frac{\left(\frac{\int_{1525}^{1575} Amide\ II}{\int_{1600}^{1710} Amide\ I}\right)_t}{\left(\frac{\int_{1525}^{1575} Amide\ II}{\int_{1600}^{1710} Amide\ I}\right)_0} = Fraction\ of\ Amide\ H \qquad (20)$$

$$Fraction\ of\ Amide\ H = C_f . e^{\left(-t/\tau_f\right)} + C_s . e^{\left(-t/\tau_s\right)} + C_c . e^{\left(-t/\tau_c\right)} \qquad (21)$$

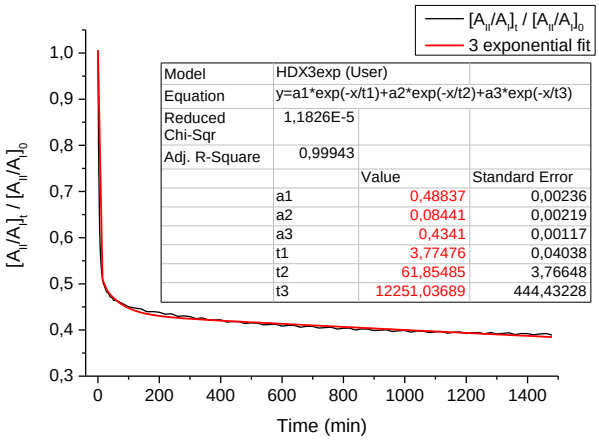

Figure 2.3.2 : Example of the fraction of exchanged protein "Amide-H" *vs.* time.The black line represents the experimental curve and the red line the fitted curve.

This curve is then fitted with equation *(21)* to represent the three main parts of the exchange, i.e. the fast, intermediate and slow part that were defined in chapter 1.6.3.7. Depending on the shape of the curve, the exponential embodying the slow part could sometimes be replaced by a constant.

2.4 UV-Vis redox titrations

2.4.1 Experimental

All potentials given here are *vs.* a 3M Ag/AgCl reference electrode, and each titration was performed at least two times to ensure reproducibility of the results.

For all these titrations, the thin layer electrochemical cell described in 2.2.1 was used, excepted that two gold grids instead of one were mounted in the cell to increase the optical path-length. 7-8 µL of 150 µM Complex I sample were incubated on a mixture of mediators for 1 hour to promote electron transfer. The sample was deposited between the two gold grids in the thin layer electrochemical cell which was then closed with the CaF_2 windows and filled with buffer (50 mM MES, 50 mM NaCl, 0.01 % DDM, pH 6). The Ag/AgCl reference electrode was mounted and the cell was sealed before being connected to a thermostat set to 10°C and set up in the UV-Vis spectrometer (Varian Carry 300). The good functioning of

the resulting experimental setup was done by taking a fully oxidized *minus* fully reduced spectrum and vice-versa. The two spectra should be mirror images of each other. The applied potential was then set to -300 mV and spectra were taken until no more changes in the absorbance spectrum of the protein could be observed. A baseline was taken and subsequent spectra were all plotted with this baseline subtracted. The potential was changed in -50 mV steps from -300 mV to -450 mV and in -25 mV steps from -450 mV to -700 mV. For each step, spectra were taken at 5 minute intervals until no more changes could be observed. The typical equilibration time was 15 min, with slight variations whether the applied potential was far or near the cofactor midpoint potential.

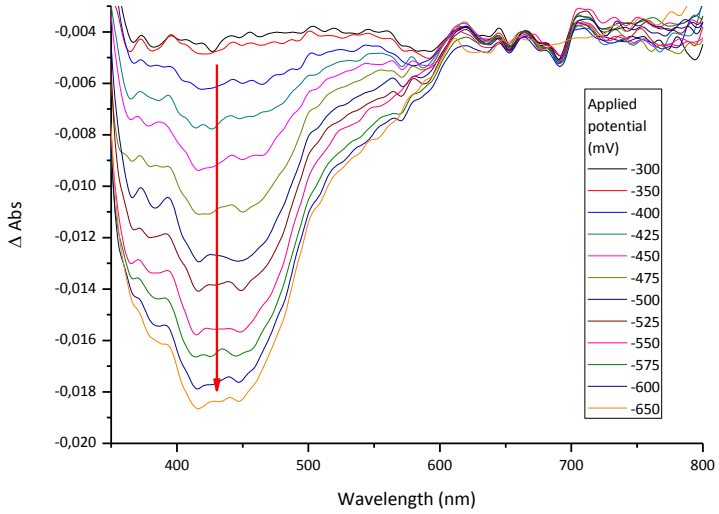

Figure 2.4.1 : Example of the electrochemically-induced UV-Vis absorption change of a redox enzyme.

2.4.2 Estimation of the midpoint potentials from the obtained spectra

To calculate the E_m of the cofactors, the absorbance was plotted against the applied potential. This results in a Nernst-like curve. When multiple cofactors absorb at the same wavelength, the direct fitting of the Nernst curves yields inaccurate results. To enhance the precision of the estimated E_m, the Nernst curve was derived to the first order. This produces a curve showing peaks corresponding to the electronic transitions of the cofactors. To obtain

the best estimation of each E_m, a curve constituted of a combination from multiple Gaussian equations is fitted to the experimental results *via* Origin. The height of each Gaussian is proportional to the extinction coefficient of each species, and the width at half-height of the peak is inversely proportional to the number of electrons transferred, as illustrated in Figure 2.4.2. In the ideal case, the half-height width is 90 mV for a one electron transition and 45 mV for a two electron transition.

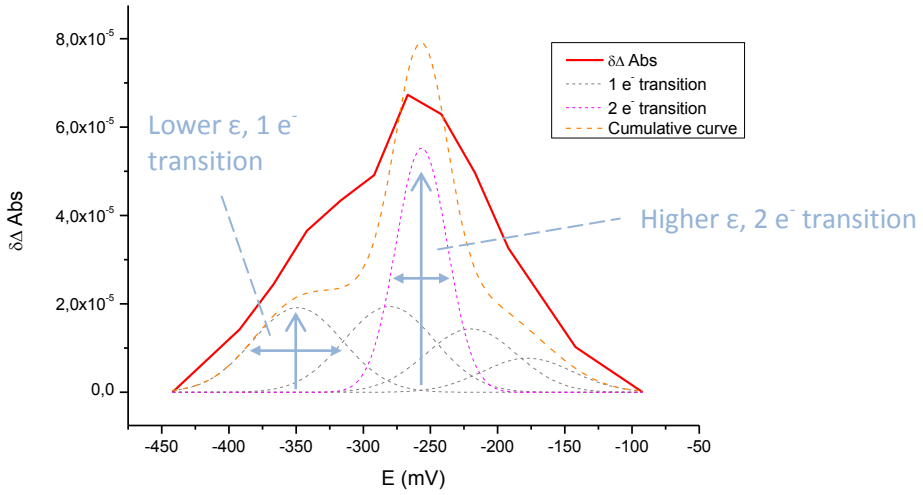

Figure 2.4.2 : Example of the E_m estimation from multiple curve fitting to δΔAbs vs. E. Red line : Experimental curve. Orange line : Fitted curve. Magenta and grey lines : Components of the fitted curve.

2.5 SEIRAS and CV measurements of Complex I, NDF and *nuoEF* adsorbed on a gold surface

A configuration allowing the simultaneous acquisition of FTIR spectra in the attenuated total reflection (ATR) mode and the application of an electrochemical potential was built. The ATR electrochemical cell was made of a hemi-cylindrical “float zone” graded Silicon prism (r = 1cm, h = 2.5cm, Korth Krystalle) on which a glass cell was mounted (Figure 2.5.1). The glass cell (courtesy of Pr. Masatoshi Osawa, Hokkaido University) had 4 inlets, from which 2 were used to fit a Pt counter electrode and an Ag/AgCl reference electrode. A gold film deposited on the ATR crystal (2.5.1) was used as working electrode.

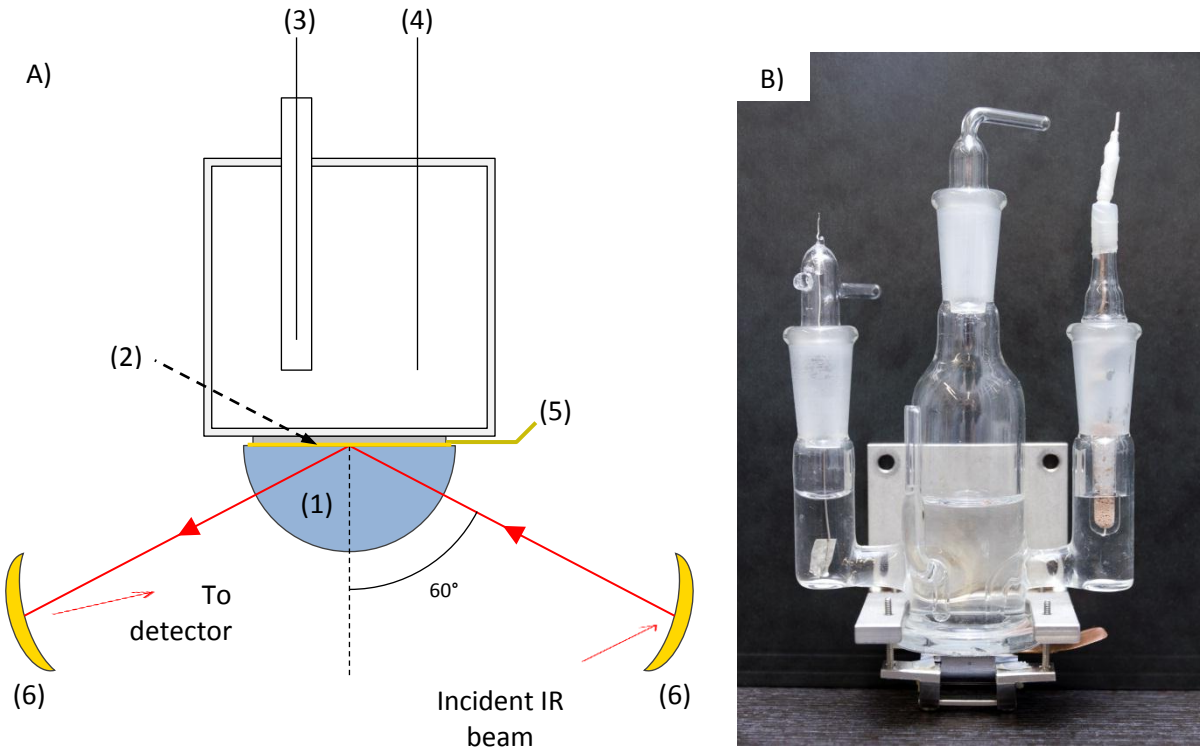

Figure 2.5.1 : Representation of the ATR electrochemical cell.A) (1) : Silicon ATR crystal ; (2) : Gold film on the surface of the crystal ; (3) Ag/AgCl 3 M KCl reference electrode ; (4) Pt counter electrode (4) : Cu wire in contact with the goldfilm ; (6) Gold-coated mirrors ; B) Photography of the assembled cell.

Upon assembly, the ATR crystal was coupled into the IR beam at an incident angle of 60° through a set of 2 gold coated mirrors (Thorlabs) and a laboratory glass slide that was manually coated with gold. The mirrors were arranged as shown on (Figure 2.5.2). The optical path could be fine-tuned through micrometric adjustments of the mirrors and the crystal positions to maximize the signal amplitude. All the measures were made within a Bruker Vertex 70 FTIR spectrometer (Globar source, KBr Beamsplitter, LN-MCT detector) at 6 mm aperture and 20 kHz scanner velocity.

Figure 2.5.2 : Photographs of the whole setup (lef) and zoom on the mirror configuration (right). The gold-coated lab slide in the middle is used to guide the IR beam from the source and to the detector at 90° angles.

Although precautions were taken to evacuate the humidity from the installation, variations of its quantity were ineluctable. The automatic humidity compensation from Opus proved to be inadequate for this particular situation, so a spectrum of the water vapor was recorded before each series of spectra and subtracted interactively in Opus.

2.5.1 Electroless deposition of the Gold Film on the ATR prism :

Adapted from ref[219]. Prior to the deposition of the gold film, the ATR silicon prism was polished with 0.3 µm alumina, rinsed with copious amounts of Millipore water and then sonicated for 4x5 min in water (twice), acetone (once) and water (once), each step being followed by rinsing with water. The prism was then dried under an Argon stream and immersed in 40% w/v NH_4F for 1 min 30 sec, rinsed and dried again. It was then allowed to heat up to 65°C for 10 min, together with the plating solution. This solution was constituted of a 1:1:1 v/v/v mix of A) 15 mM $NaAuCl_4$, B) 150 mM Na_2SO_3, 50 mM $Na_2S_2O_3$ and 50 mM NH_4Cl and C) HF 2% w/v (total mix volume : 1 mL). Once the plating temperature reached, the prism was covered with the solution for 40 sec and the reaction was stopped by copiously washing the plating solution off with water, followed by Ar-stream drying. The resulting gold film was then tested for its electric conductance with a multimeter, the typical electric resistance of the layer as measured from one corner to another of the crystal should be around 15 Ω for a thickness of 50 nm.

2.5.2 Surface modifications :

2.5.2.1 NADH-mercaptoundecanoic acid SAM

Once mounted in the electrochemical cell, the prism was covered with 500 µL ethanol and a background spectrum was recorded. Then, a 1:10 mixture of 11-mercaptoundecanoic acid and 6-mercaptohexanol was added to a final concentration of respectively 0.1 and 1 mM. The monolayer was allowed to self-assemble for 1 hour and the process was followed by a series of spectra. The prism was then rinsed with 3x ethanol and dried with an Argon stream. It was covered with 1 mL Millipore water and a background spectrum was taken. N-(3-Dimethylaminopropyl)-N'-ethylcarbodiimide hydrochloride (EDC) was added to a final concentration of 0.2 mM. After 5 min, 0.2 mM of NADH were added. The formation of the amide bond between NADH and the mercaptoundecanoic acid was followed by IR overnight at RT. After completion, the prism was rinsed with 5x Millipore water.

2.5.2.2 Ni-NTA SAM

This experimental procedure was adapted from ref[233]. Once mounted in the electrochemical cell, the prism was covered with dry dimethylsulfoxide and a background spectrum was recorded. 3,3'-Dithiodipropionic acid di(N-hydroxysuccinimide ester) was added to a final concentration of 1 $mg.mL^{-1}$ and the formation of the monolayer was followed for 1 hour by FTIR . The excess DTSP was then washed away with 3x dry DMSO and the prism was dried under an Argon stream. Once mounted in the measurement cell, it was then covered with 1 mL 0.5 M K_2CO_3 at pH 9.8 and a background was recorded. $N_{\alpha'},N_{\alpha''}$-bis(carboxymethyl)-L-lysine was then added to a final concentration of 100 mM and the reaction was followed by a series of spectra for 3 hours. Upon completion, the prism was rinsed 3x with water, 1 mL water was added and a background was taken. Finally, $NiSO_4$ was added to a final concentration of 50 mM and the complexation of the Ni(II) was followed by FTIR for 1 hour before being washed one last time with water.

2.5.3 Immobilization of Complex I/NDF/*nuoEF* and reconstitution into a lipid bilayer :

The NADH or Ni-NTA modified gold layer was covered with 245 µL of MES buffer (50 mM MES, 50 mM NaCl, pH 6.3) and a reference spectrum was recorded. 5 µL of 50 $mg.mL^{-1}$ purified protein (*nuoF*$_{HIS}$ Complex I, NDF or *nuoEF*) were added to a final concentration of 1.9 µM. After 2 hours, 100 µL of 79:11:9:1 EPE:CL:EPG:SPS liposomes (2.1.12.1) were added to the mixture, and after 5 min previously activated Bio-rad SM-2 Bio-beads stored in MES buffer were deposited on the prism. The lipid bilayer was then allowed to form overnight, and the biobeads and excess lipids were carefully washed off with MES buffer. The electrochemical cell was then filled with 20 mL MES buffer. At each step a background was recorded first and the immobilization/insertion into the bilayer followed by FTIR.

2.5.4 Potential induced difference spectroscopy of the immobilized enzymes

With the proteins adsorbed on the gold surface, the ATR electrochemical cell was connected to a homemade potentiostat and the potential was cycled a few times between -700 mV and +200 mV *vs.* Ag/AgCl 3 M KCl to ensure the correct functioning of the setup. The same macro as used in 2.2.2 was used to generate oxidized *minus* reduced spectra and vice-versa. Equilibration times for the oxidized and reduced states were set to 6 and 5 min respectively. 20 to 30 redox cycles were typically averaged to obtain the final spectrum.

To study the effect of ubiquinone, 0.5 mg of decylubiquinone in 10 µL DMSO were added, yielding a final concentration of 78 µM.

To determine the inhibitory effect of rotenone, 1 mg of it in 10 µL DMSO were added to a final concentration of 127µM. The inhibitory effect of Zn2+ on the immobilized enzyme was also probed by adding $ZnSO_4$ to a final concentration of 100 µM.

2.6 Cyclic Voltammetry

In parallel to the FTIR measures on the immobilized enzymes described in chapter 2.5, cyclic voltammetry experiments were conducted. The ATR electrochemical cell was connected to a Princeton applied research VersaSTAT4 potentiostat, and the potential was linearly swept from +300 mV to -650 mV and back at 0.1 and 0.02 $V.sec^{-1}$ scan rates. The experimental conditions were identical to those described in chapter 2.5.

Prior to the measures in the ATR electrochemical cell, Complex I immobilization methods based on various thioalkane SAMs were tested on gold electrodes covered with Au nanoparticles as described in refs[231, 243]. The protein quantities used in chapter 2.5 were adapted to the smaller size of the electrode.

3 Results and Discussion

3.1 Immobilization and functional probing of Complex I

3.1.1 Introduction

The aim here was to immobilize Complex I in a biomimetic fashion on a gold layer deposited on an ATR-crystal in order to functionally probe the enzyme against substrates and inhibitors *via* Surface-Enhanced IR Absorption Spectroscopy (SEIRAS) and Cyclic Voltammetry (CV). To achieve this immobilization, two methods were employed, both based on the creation of a high affinity Self-Assembled Monolayer (SAM) : the first made use of the affinity of NiNTA towards a hexahistidine tag that was genetically engineered into Complex I for purification purposes[97] ; the second exploited the affinity of the enzyme towards its natural substrate, NADH (see also chapter 1.7).

The combination of SEIRAS and electrochemistry was hereby newly introduced into the technical know-how of our laboratory. This was made possible by a JSPS-funded collaboration with Pr. M. Osawa (Hokkaido University) and his team, who provided the Si ATR crystal, the glass cell used for the experiments and the technical guidance to build a SEIRAS-setup in our laboratory. The creation of the experimental setup is detailed in chapter 2.5, together with further details about the methods employed to afford the SAMs and to immobilize Complex I. In the first part of this chapter here, the step by step results underlying this immobilization are described. Then, a few model compounds were probed to obtain reference data, to which the immobilized Complex I was then compared. Finally, the adsorbed enzyme was inserted in a lipid bilayer and put in presence of substrates and inhibitors.

3.1.2 Creation and chemical modification of the Gold surface

Gold surface : The Au layer was cast on the surface of the Si ATR crystal by etching of the Si with HF and reduction of $AuCl_4^-$ (according to the oxidoreduction equation hereafter[219]) as described in chapter 2.5.1.

$$3\ Si\ (s) + 18\ F^-\ (aq) + 4\ AuCl_4^-\ (aq) \rightarrow 3\ SiF_6^{2-}\ (aq) + 4\ Au\ (s) + 16\ Cl^-\ (aq)$$

The thickness of the gold layer for a deposition time of 60 sec was estimated to 50 nm, with an average size of the gold islets estimated to 300 nm[219]. The measures of the electric resistance done after each deposition however varied from the ideal value of 15 Ω, showing that in spite of identical deposition conditions the thickness and islet-size of the Au layer varied from one experiment to another. This was also evident from differences in the visual aspect (color, brilliance) of the layer. Since the SEIRA effect (see chapter 1.6.3.6) depends on these properties, their variation can impact the IR signals seen later on[244, 245]. To tentatively circumvent these disparities, gold deposition through Argon sputtering[246] accompanied by monitoring of the layer thickness *via* QCM was used. While this yielded gold films with highly reproducible physicochemical properties, their stability was not adapted to routine use, as the layer peeled off most of the time after creation of the initial SAM. Thus, the chemical deposition was privileged, since it produced stable films. Their variable properties were kept in mind when comparing spectra from different experiments.

Validation of the experimental setup : To validate our experimental setup (i.e. correct mirror alignement, Au layer thickness and electric connection) a small soluble protein from the respiratory chain, Cytochrome *c*, was probed by electrochemically induced IR difference spectroscopy and cyclic voltammetry. This experiment and its results were already reported by Jiang *et al.* in ref[230] and therefore provided a good point of comparison. Briefly, a SAM of 11-mercaptoundecanoic acid (MUA) was created in ethanol for 90 min on the gold coated ATR crystal, then the surface was dried under an N_2 stream, immersed in phosphate buffer and Cyt_c was added to a final concentration of 2 µM. The resulting FTIR difference spectrum and the cyclovoltammogram are shown on Figure 3.1.1.

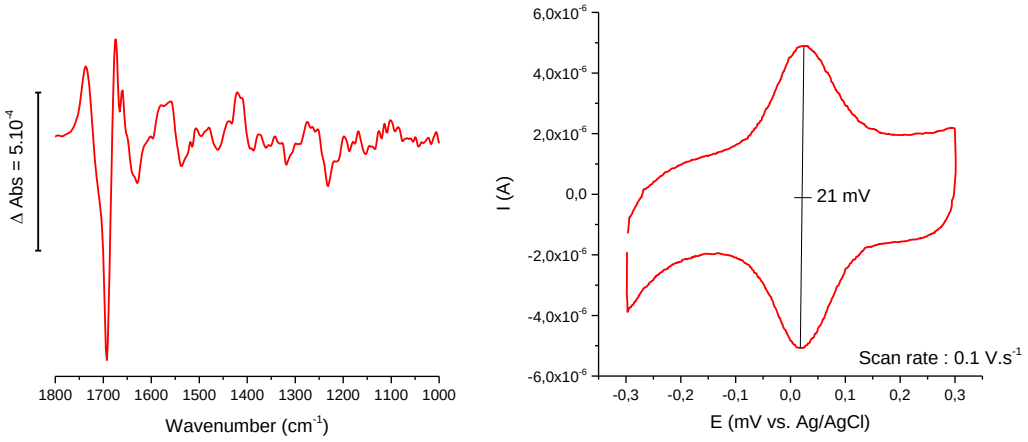

Figure 3.1.1 : Oxidized *minus* reduced FTIR difference spectrum and cyclovoltammogram of Cyt$_c$ in the ATR-Electrochemical cell.

The fully oxidized *minus* fully reduced spectrum and the cyclovoltammogram of adsorbed Cyt$_c$ were virtually identical to those from ref[230], indicating that the gold layer had approximately the right thickness, that the IR beam incidence angle on the prism was correct and that the current was effectively transferred from the electrodes through the gold to the protein. The setup was thus ready for exploration of immobilization methods for Complex I.

Ni-NTA SAM : The step by step formation of the NiNTA SAM (Figure 3.1.2) followed by FTIR is shown in Figure 3.1.3. This method has been reported previously[233] and the described FTIR spectra differed only slightly from the obtained results : in step 1 and 2, the signals from the DMSO solvent at 1436 and 1409 cm^{-1} overlap signals from DTSP and ANTA around these positions, but the marker bands of DTSP (ν(C=O)$_{succinimide}$ and ν(C=O)$_{ester}$ at 1812/1780 and 1733 cm^{-1}, respectively) and ANTA (ν_s(COO$^-$) at 1388 cm^{-1}) are still seen. The amide bond formation between the two in step 2 is seen from the arising peptide's amide I and II modes at ~1650 and 1564 cm^{-1}. In step 3 the Nickel chelation changed not only the ν_{as}(COO$^-$) and ν_s(COO$^-$) modes of ANTA (1589/1569 and 1436/1420 cm^{-1}, respectively) but also two bands at 1706 and 1664 cm^{-1} which could represent parasite Ni^{2+} chelation by the amide. The signal at 1284 cm^{-1} might represent the ν(C-N) mode of the tertiary amine, which is also involved in the chelation. The formation of the NiNTA SAM was relatively fast (2 hours in total) and highly reproducible.

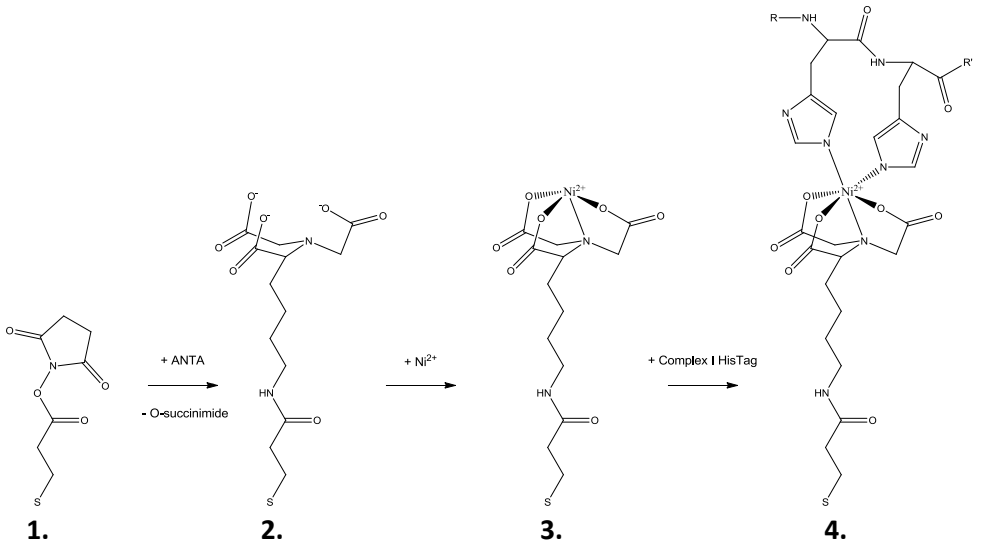

Figure 3.1.2 : Reaction steps for the NiNTA SAM formation. Step 4 represents the attachment of the Complex I His-tag . The corresponding FTIR spectra are shown on Figure 3.1.3 and Figure 3.1.6.

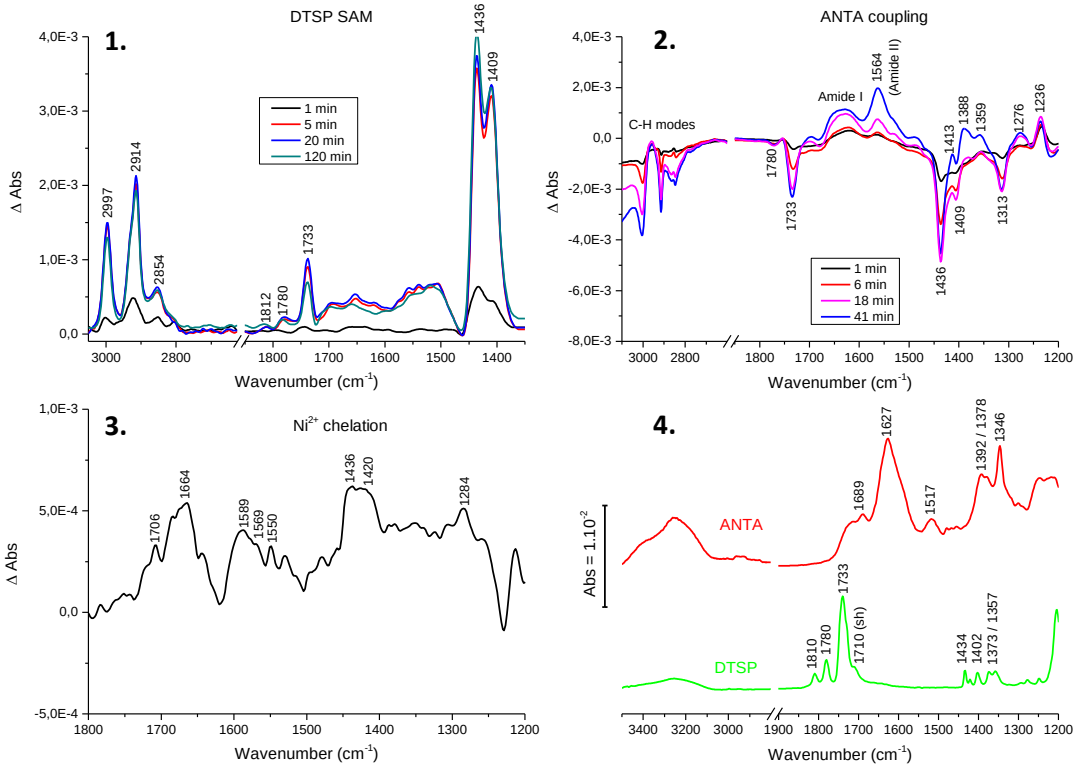

Figure 3.1.3 : Creation of the NiNTA SAM followed by FTIR difference spectroscopy. 1. Temporal evolution of DTSP SAM adsorption on Au layer. Reference spectrum : bare gold layer covered with DMSO - **2.** Peptide coupling of DTSP with ANTA. Reference spectrum : DTSP SAM in K_2CO_3 0.5 M, pH 9.8 - **3.** Chelation of Ni^{2+}. Reference spectrum : 50 mM K_2SO_4. **4.** : Spectra of dry DTSP and ANTA recorded on a Si ATR.

NADH-SAM : In Figure 3.1.4, the steps for the assembly of the NADH SAM are shown. The corresponding reaction were followed by FTIR difference spectroscopy, as shown in Figure 3.1.5. The first step, i.e. the self-assembly of a MUA:6-mercaptohexanol 1:10 monolayer, is rapid (5min) and the signals at 1708 cm^{-1} ($\nu(C=O)_{COOH}$), 1599 and 1415/1378 cm^{-1} ($\nu_s(COO^-)$ and $\nu_{as}(COO^-)$) indicate that the acid is present in a mixture of protonated and deprotonated forms. The adsorption of the 6-mercaptohexanol can't be specifically seen here since the reference spectrum was taken in ethanol, which overlaps the alcohol group vibrations. The increase of the number of alkyl groups near the surface is shown by the bands at 2973, 2931, 2873 and 1458 cm^{-1}.

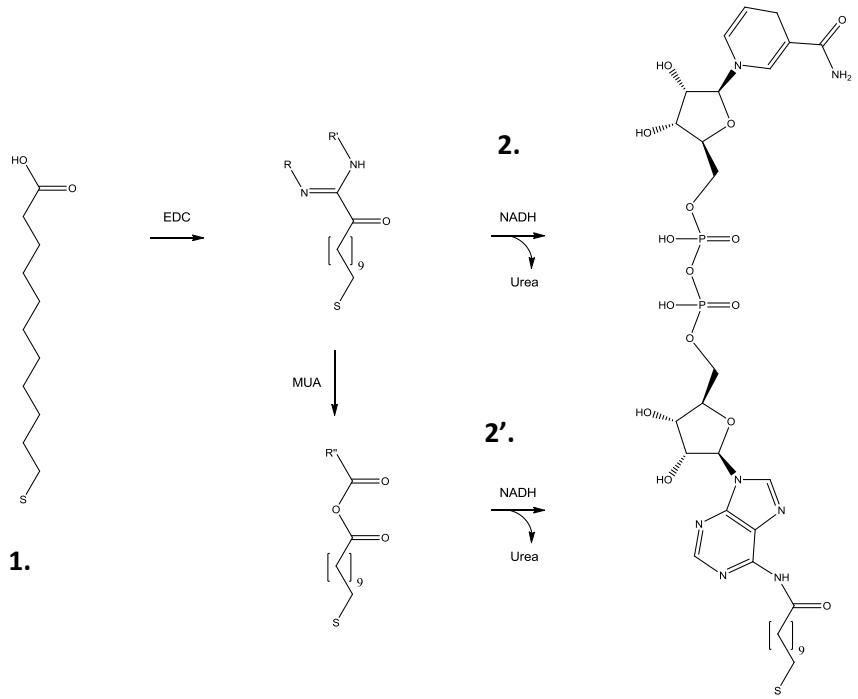

Figure 3.1.4 : Reaction steps for the NADH SAM formation. The corresponding FTIR spectra are shown in Figure 3.1.5.

The coupling of NADH with MUA in step 2 produced complex spectra due to the number of reactants, intermediates and products involved here. For example, water (buffer), NADH, urea and the created NADH-MUA amide all show broad IR absorption around 1650 ± 30 cm^{-1} and overlap, so that no direct conclusion can be drawn for the formation of the amide. By recording a reference spectrum in presence of EDC and immediately after addition

of NADH, the evolution of the reaction could nevertheless be followed. A signal at 1812 cm^{-1} was tentatively attributed to the reaction intermediate from step 2. This signal might also represent the anhydride from step 2', but this is less likely since anhydrides are unstable in water. The band rises quickly (10 min) and then diminishes slowly before disappearing after 10 hours. Concomitantly, two peaks appear at 1697 and 1535 cm^{-1}, which could represent the amide I and II modes of the MUA-NADH peptide. Thus, we suggest that the coupling was complete after 10 h. These slow reaction kinetics are consistent with the low reactivity of the amine from the NADH's adenine moiety due to the delocalization of its lone pair over the aromatic ring. Side reactions might also happen during the peptide coupling, as suggested by the negative peak below 1250 cm^{-1}. This signal could represent reaction of the phosphate from NADH (or simply, its protonation), but could also be due to baseline instabilities that were sometimes observed in this spectral region.

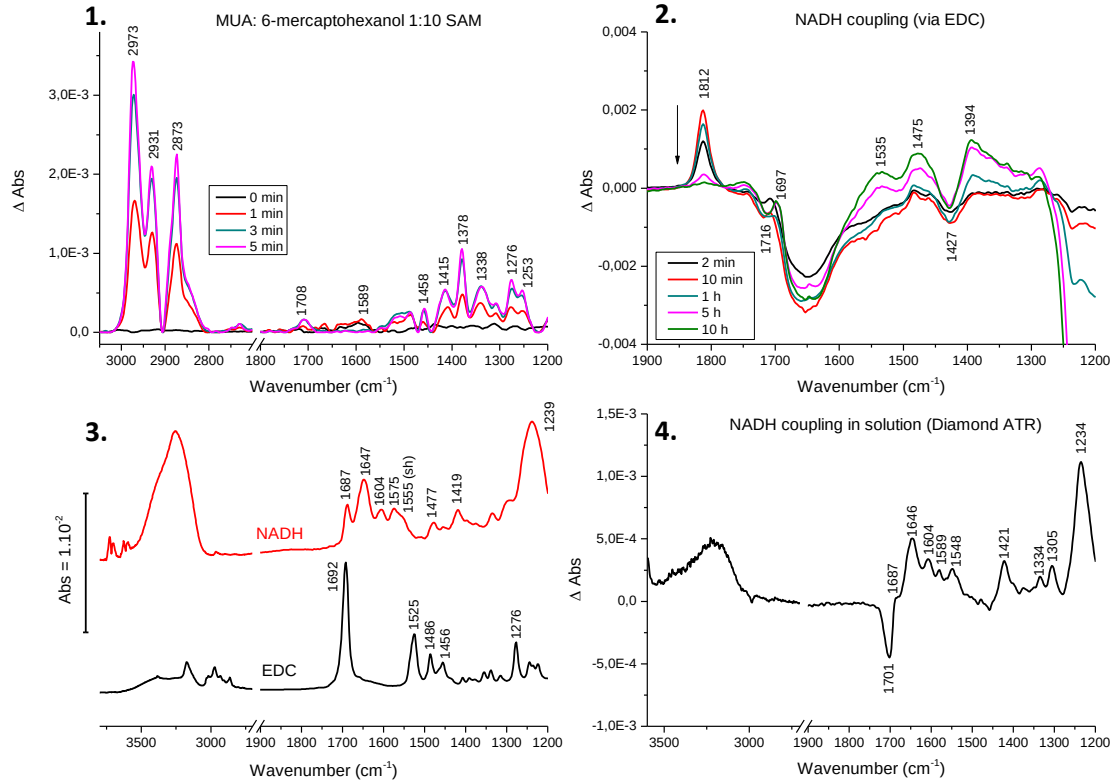

Figure 3.1.5 : Creation of the NADH SAM followed by FTIR difference spectroscopy. 1. Temporal evolution of MUA:6-mercaptohexanol SAM adsorption on the Au layer. Reference spectrum : bare gold layer covered with Ethanol - **2.** Peptide coupling of NADH with MUA through EDC. Reference

spectrum : Thiol SAM in H_2O with 0.2 mM NADH and 0.2 mM EDC - **3.** : Spectra of dry NADH and EDC recorded on a Si ATR **4.** NADH coupling to 3-mercaptopropionic acid in solution (H_2O) recorded on a Diamond ATR.

To identify the coupling of NADH and an acid, the same experiment was performed in solution on a Diamond ATR crystal and by replacing the water insoluble MUA by its shorter alkyl chain counterpart 3-mercaptopropionic acid (MPA) (Figure 3.1.5 D.). This experiment shows clearly the consumption of MPA (negative peak at 1701 cm^{-1}) but the peak at 1812 cm^{-1} was not visible here. It is possible that the thiol from MPA (which is free in solution) can react with the activated acid to form a thioester. The rest of the spectrum is dominated by the absorption spectrum of NADH and thus no further conclusions could be drawn from this experiment.

3.1.3 Immobilization of Complex I and insertion into a lipid bilayer

After the creation of the SAMs, Complex I was adsorbed at their surface. The process was followed by FTIR as shown on Figure 3.1.6.

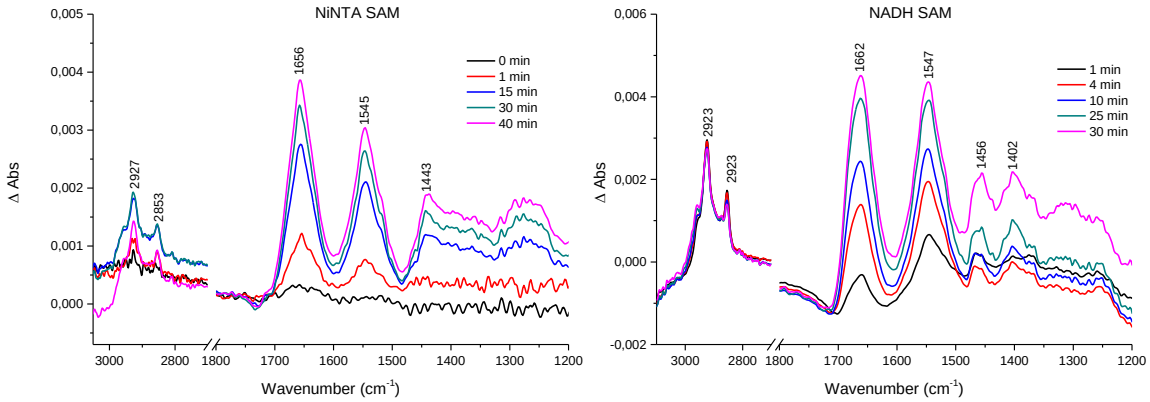

Figure 3.1.6 : Adsorption of Complex I on the NiNTA and NADH SAMs. Reference spectra : SAM covered with MES buffer. t 0 corresponds to the addition of 2 µM Complex I to the milieu.

On both SAMs, the amide I and II modes of Complex I were clearly visible, but their shape, position and intensity ratio varied. This might be due to a different orientation of the protein with respect to the surface. However, as mentioned earlier, the physical properties

of the Au layer did also vary from one experiment to another (as did the Amide I and II bands) so that these differences could not be exploited. The intensity of the amide bands progressively increased before being stabilized after ca. 2 hours, indicating that during this period a certain organization of the protein layer occurs. For both SAMs, Complex I is quite tightly adsorbed on the surface, as the amide signals persisted after (gentle) rinsing of the crystal with buffer to remove excess protein (not shown).

The adsorbed Complex I was then reconstituted into a lipid bilayer by addition of preformed PE:PG:CL liposomes and subsequent detergent removal with Biobeads. Figure 3.1.7 shows the evolution of this step. The removal of the detergent is shown by the diminution of the signals from alkyl chains between 2800 and 3000 cm^{-1}, the presence of lipids is seen by the increase of the signals at 1729 (NADH SAM) and 1725 (NiNTA SAM) cm^{-1}. The $\nu_{as}(PO^{2-})$ mode of the phospholipids, expected at 1230 cm^{-1} (see Appendix 6 for spectra of dry lipids), was not seen as a positive peak here. This could be due to overlap with buffer absorption or to a specific orientation of the lipid bilayer with respect to the Au surface.

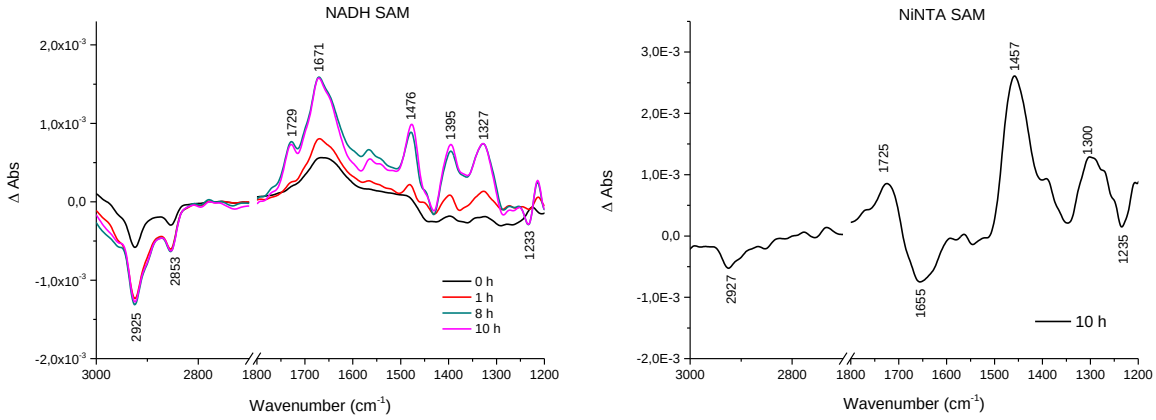

Figure 3.1.7 : Insertion of the adsorbed Complex I into a lipid bilayer. Reference spectrum : SAM + Complex I + liposomes + buffer. t = 0 corresponds to the addition of Biobeads SM2 to the reaction.

For both SAMs, the insertion of Complex I into a lipid bilayer also caused variations within the amide I region (+1671 cm^{-1} in the NADH SAM, -1655 cm^{-1} in the NiNTA SAM) which might reflect the structural (re)organization of the protein layer.

3.1.4 Probing the electrochemically-induced reaction of the immobilized Complex I through SEIRAS and CV

The behavior of the Au layer alone in presence of MES buffer was probed through electrochemically induced FTIR spectroscopy (Figure 3.1.8) and through cyclic voltammetry (Figure 3.1.9). The oxidized *minus* reduced spectrum showed an intense negative peak at 1611 cm^{-1} which might be due to the reorganization of water molecules in the vicinity of the surface. Three smaller positive signals at 1701, 1673 and 1488 cm^{-1} are of unknown origin. The reduced *minus* oxidized showed only limited reversibility with only an intense positive peak at 1638 cm^{-1} (not shown). In the CV, a reductive peak at -320 mV that was strongly diminished in the second cycle was seen. The MES buffer was not at its origin, since the same phenomenon was also observed in phosphate buffer (not shown). It might represent the Au-catalyzed reduction of H^+ to gaseous H_2, which is supported by the fact that in many experiments small gas bubbles were seen after several redox cycles. Other gold-catalyzed reactions involving adsorbed O_2, H_2O or Cl^- can't be excluded. Upon creation of a SAM, as seen for example in the CV of the NADH SAM prior to redox cycles (Figure 3.1.9 B. - black trace), this reductive peak disappeared. This signifies that coverage of the gold surface with a thioalkane hindered the adsorption of the species producing this peak. This was seen regardless of the nature of the SAM. The presence of a SAM also had an effect on the reversibility of the redox-induced FTIR spectra : they were all fully reversible, be it for the SAM alone or in presence of Complex I.

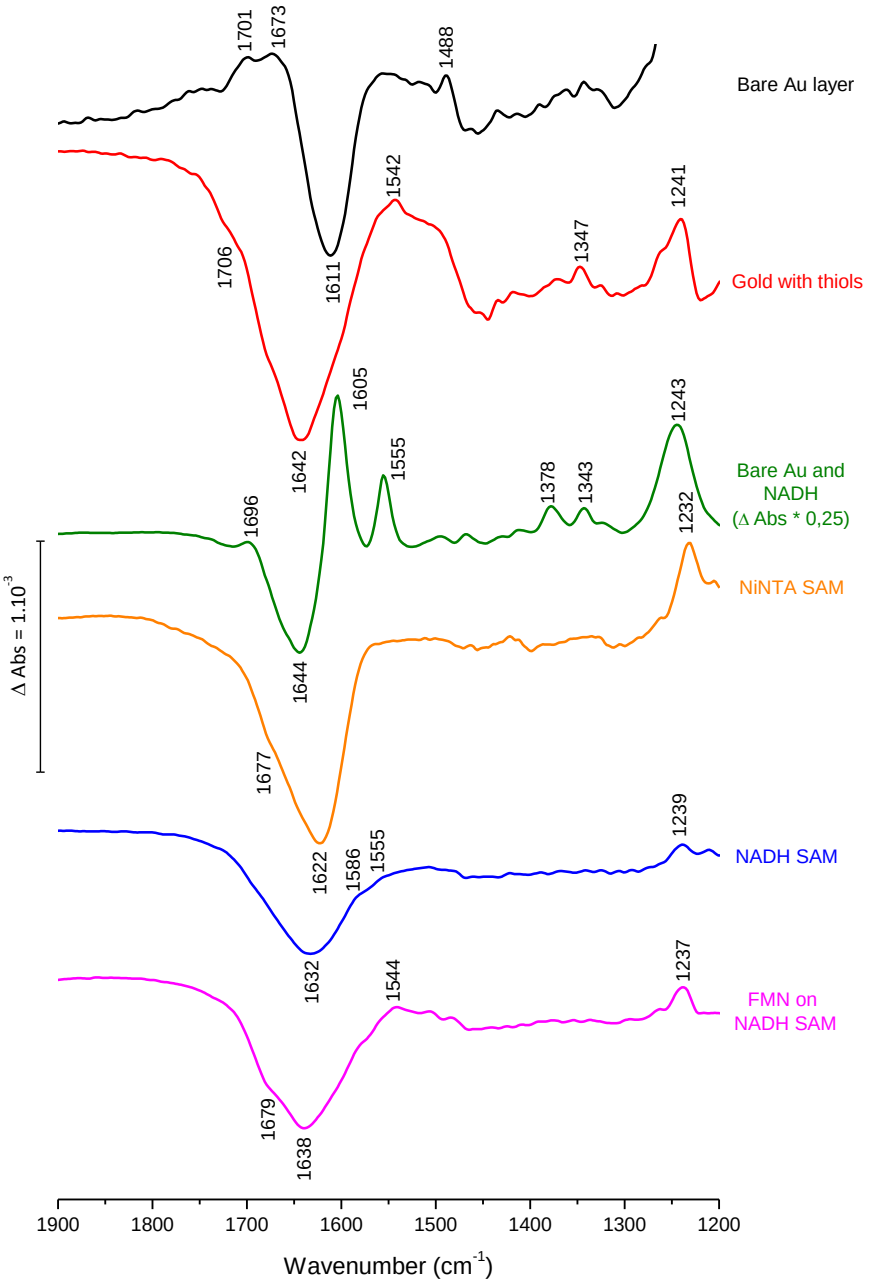

Figure 3.1.8 : Redox induced behavior of the Au layer in different conditions probed by FTIR. Oxidized (+300 mV) *minus* reduced (-650 mV) FTIR difference spectra. Equilibration times : 5 min (ox) and 6 min (red).

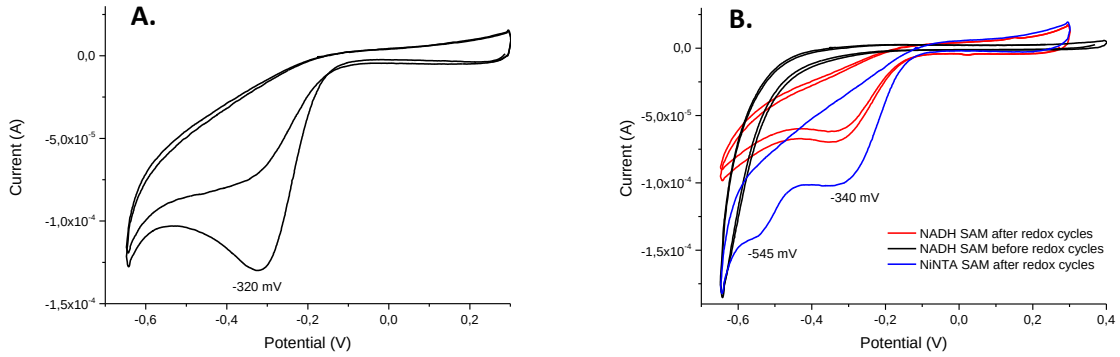

Figure 3.1.9 : CV of the bare Au layer (A.) and the NADH and NiNTA SAMs (B.). The CVs were recorded in MES buffer (50 mM MES, 50 mM NaCl, pH 6.3) at a scan rate of 0.02 $V.s^{-1}$. In **B.**, the CVs of the NADH and NiNTA SAMs are shown before and after several redox cycles.

The ox-red spectrum of a simple SAM (MUA:6-mercaptohexanol 1:10 here) before further chemical modification is shown in Figure 3.1.8. A large negative peak at 1642 cm^{-1} attributed to interfacial water molecule reorganization dominates the spectrum. This peak was also present in all other ox-red spectra and constituted a major hurdle for a precise interpretation of the redox induced difference spectra. Smaller signals at 1706 and 1542 cm^{-1} represent redox-induced variations of the carboxylic acid from MUA.

The redox reaction of NADH in solution was also probed on the bare gold layer. The CV did not show any significant change from that of the bare gold and is thus not shown. The ox-red FTIR spectrum however revealed that NADH was effectively oxidized (and NAD^+ reduced back again) as judged from the two intense peaks at 1605 and 1555 cm^{-1}, that can be attributed to the variations of the ν(C-C) and ν(C-N) modes of the nicotinamide ring upon its aromatization. When NADH was introduced in the SAM, these peaks are still present (albeit downshifted from 1605 to 1586 cm^{-1} for the first one) but strongly diminished. This is a probable consequence of the lower NADH concentration or its inability to react directly with the gold surface.

Both the NADH and NiNTA SAM boasted a similar, almost featureless (excepted for the water band at 1632/1622 cm^{-1}) ox-red FTIR spectrum. In the NiNTA SAM, a shoulder

probably representing a carbonyl mode is seen at 1677 cm^{-1}. Their CV was also identical at first, showing that the SAM isolated the Au layer. However, it appeared that after a few redox-cycles, the CV evolved. For the NADH-SAM, it reverted almost to that of bare gold, while for the NiNTA SAM an additional reductive peak was seen at -545 mV. This probably represents partial desorption of the SAM when exposed to reducing potentials and reduction of Ni^{2+} to Ni^{0} (E^{0} = -250 mV vs. SHE), which complicated analysis of the CV from further experiments. On the other hand, the redox-induced difference spectra did not show any evidence of SAM or protein desorption during the course of the experiments.

Before examining the behavior of the adsorbed Complex I, the reaction of FMN in presence of the NADH SAM was also probed, principally because of its well-known spectroscopic and electrochemical properties and the fact that it is expected to be in direct interaction with the SAM in the enzyme. As the resulting ox-red FTIR spectrum (Figure 3.1.8) differed only slightly from that of the SAM alone, the latter was interactively subtracted from the former to yield the spectrum shown in Figure 3.1.10. This was the only way to remove the large signal in the 1600's cm^{-1} corresponding to redox-induced solvent reorganization near the surface.

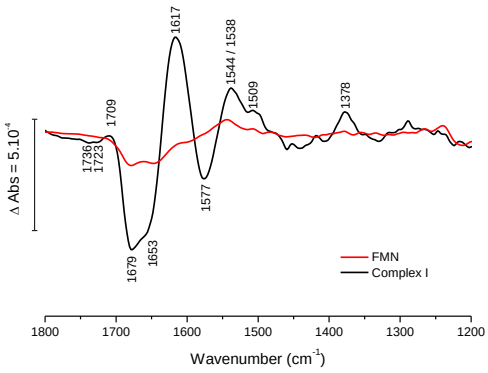

Figure 3.1.10 : Oxidized *minus* reduced spectra of FMN in solution and of adsorbed Complex I, both with the NADH SAM. The oxidized *minus* reduced spectrum of the SAM in presence of MES buffer was subtracted from both spectra. [FMN] was 100 µM.

The reaction of FMN in solution gives rise to a peak at 1544 cm^{-1} which was attributed to the ν(C=C) mode of the isoalloxazine ring (see also Figure 3.2.4). Another, smaller peak at 1509 cm^{-1} could also represent a ν(C=C) mode of the flavin. Above 1600 cm^{-1}, two negative peaks at 1679 / 1648 cm^{-1} and a shoulder at 1615 cm^{-1} can be seen that probably represent a different behavior of the bulk solvent rather than signals from the FMN itself. The CV of the NADH SAM with FMN (Figure 3.1.11 B.) shows both the oxidative and reductive peaks of FMN, with a midpoint potential measured at -390 mV vs. Ag/AgCl (pH 6.3) and therefore in agreement with the E_m of free FMN[247].

The ox-red spectrum of Complex I immobilized on the NADH SAM was then compared to that of FMN (Figure 3.1.10). The peak at 1538 cm^{-1} can be partially attributed to ν(C=C) mode of FMN in Complex I, although its higher intensity (compared to a diminished concentration within the enzyme) suggests that other vibrational modes from Complex I (e.g. Amide II) also contribute to the IR absorption at this wavenumber. The intense bands at 1679 and 1615 cm^{-1} might represent redox-induced conformational movements of β-sheets/turns and the signal at 1653 cm^{-1} could represent those of α-helices or randomly structured amide backbones.

Owing to the considerable size of Complex I (ca. 180 x 170 x 60 Å) and the decay of the SEIRA effect with increasing distance to the surface (chapter 1.6.3.6), it was not clear to which extent the parts of the adsorbed enzyme further away from the surface (that is, the membrane part if the enzyme was effectively attached through the tip of its soluble domain) contributed to the spectrum (Figure 1.7.1). To probe this, smaller fragments of Complex I were adsorbed through the same process on the NADH SAM and their ox-red spectra were compared to the entire enzyme (Figure 3.1.11). The NADH Dehydrogenase Fragment (NDF) from *E. coli* corresponds to the soluble domain of Complex I (NuoB, CD, E, F, G and I, with FMN and all the FeS clusters) and NuoEF from *Aquifex aeolicus* to the subcomplex harboring FMN and FeS cluster N1a and N3.

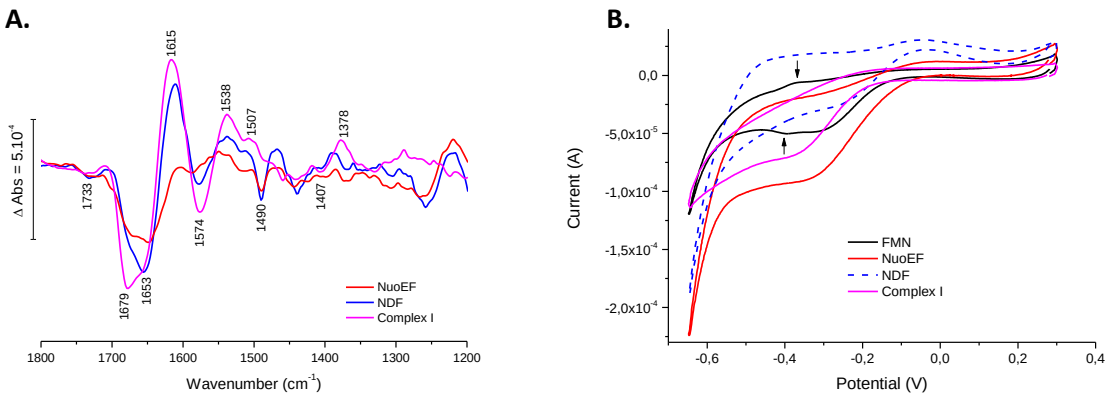

Figure 3.1.11 : Comparison of ox-red spectra (A.) and CVs (B.) of NuoEF fragment, NDF and Complex I adsorbed on a NADH SAM. The spectrum of NADH-SAM alone in MES buffer was subtracted from the enzyme's ox-red spectra. Experimental conditions were the same as in Figure 3.1.10, with an identical protein concentration for the different enzymes (2 µM). The CVs were recorded after the redox cycles for the FTIR experiment and compared to that of 100 µM FMN in MES buffer.

The ox-red FTIR spectra of the fragments show signals at similar positions as for the entire Complex I, but their intensity is diminished, in the order Complex I > NDF > NuoEF fragment. The major part of the Complex I spectrum seems to arise from the NDF (as seen in for Complex I in solution in the thin-layer electrochemical cell[192] - see chapters 3.3 and 3.4), with additional absorptions at 1679 and 1615 that might reflect the conformational movements in the membrane domain. However, the variations of the Au layer properties or a different orientation of the enzyme might also cause this differences. The signals at 1733, 1574 and 1407 cm^{-1} might represent the reaction of carboxylic acids from Complex I. The CVs of the different enzymes show a similar shape as for the NADH SAM alone. The current intensities however differed, indicating that the surface induced more or less capacity. As the intrinsic redox potentials of the Complex I cofactors range from ca. -150 to -400 mV vs. SHE, the observed potential may be within this range but may shift on the surface. Its signal is thus overlapped by those from the redox reaction of the SAM. Even if a densely packed protein monolayer was formed, the surface coverage of Complex I would be quite low due to its size (1.6 x 10^{-12} mol / cm^2 in the best case scenario), which might also explain the absence of any stronger signal in the presence of Complex I.

Complex I on the NiNTA SAM was also probed and compared to the NADH SAM, as shown in Figure 3.1.12. Above 1500 cm^{-1}, the signals observed were similar, although less intense for the NiNTA SAM. Below 1500 cm^{-1}, an apparent shift of the baseline occurred. The corresponding CV shown in Figure 3.1.13 was similar to the others.

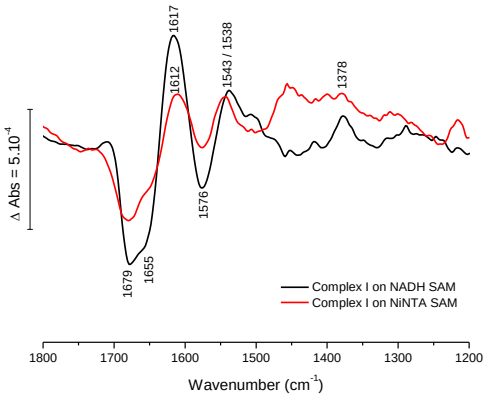

Figure 3.1.12 : Comparison of the ox-red spectra of Complex I adsorbed on the NiNTA and NADH SAMs. Except for the SAM itself, the experimental conditions were identical and the SAM in MES buffer difference spectrum was subtracted from the ox-red spectra.

Now that the behavior of detergent-solubilized adsorbed Complex I was probed, we proceeded investigating its properties when it was inserted in a phospholipid bilayer (Figure 3.1.13). The ox-red spectra showed an overall diminution of the signals of Complex I when the enzyme was reconstituted in the bilayer on a NADH SAM, whereas the contrary occurred on a NiNTA SAM. The main differences are seen below 1500 cm^{-1}. No conclusion could thus be drawn from this. The CV showed a slight diminution of the reductive peak in the NADH SAM, which was less pronounced in the NiNTA SAM. The effect was smaller than expected, since the presence of lipids (see chapter 3.3) influence the catalytic properties of the enzyme.

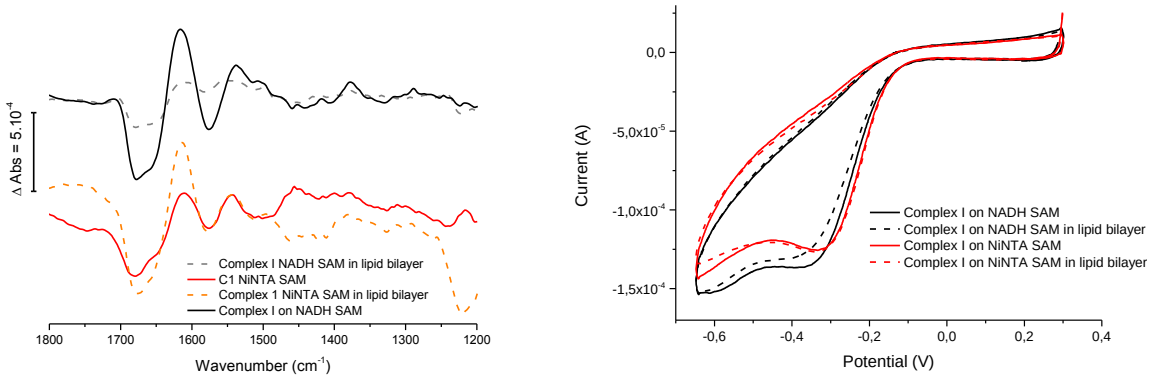

Figure 3.1.13 : Comparison of the ox-red spectra and CV of Complex I adsorbed on the NiNTA and NADH SAMs before and after reconstitution into a lipid bilayer.

This may be due to a partial removal of the protein from the surface upon Biobeads addition or simply to protein degradation during this insertion. The creation of the bilayer was also probed through Electrochemical Impedance Spectroscopy but this gave contradictory and not reproducible results, most likely for the same reason.

Finally, the adsorbed Complex I was probed against its substrate, quinone (decylubiquinone) and against inhibitors : rotenone as a Q site inhibitor, NADH-OH as a NADH site inhibitor and Zn^{2+} as a proton-pumping inhibitor. Figure 3.1.14 shows the consequences of successive additions of a ~50 fold excess of DQ and Rotenone on the adsorbed Complex I alone on the NADH SAM and of Complex I in lipid bilayer on the NiNTA SAM. The effect was also probed on the Complex I alone on NiNTA SAM and Complex I in bilayer on NADH SAM but as the results were identical they are not shown here. The ox-red spectra of Complex I in the presence of DQ are dominated by the signals of the quinone's reaction[208, 248], i.e. the modification of the ν(C=O) and ν(C=C) modes at 1664/1654 and 1610 cm^{-1}, the ring reorganization between 1591 and 1387 cm^{-1} and the ν(C-O) mode of the methoxy group at 1266 cm^{-1}. The addition of rotenone did not change the spectra, except for an additional peak at 1513 cm^{-1} which might represent the oxidation of rotenone to rotenolone. These results might might be due to the excess of quinone and rotenone.

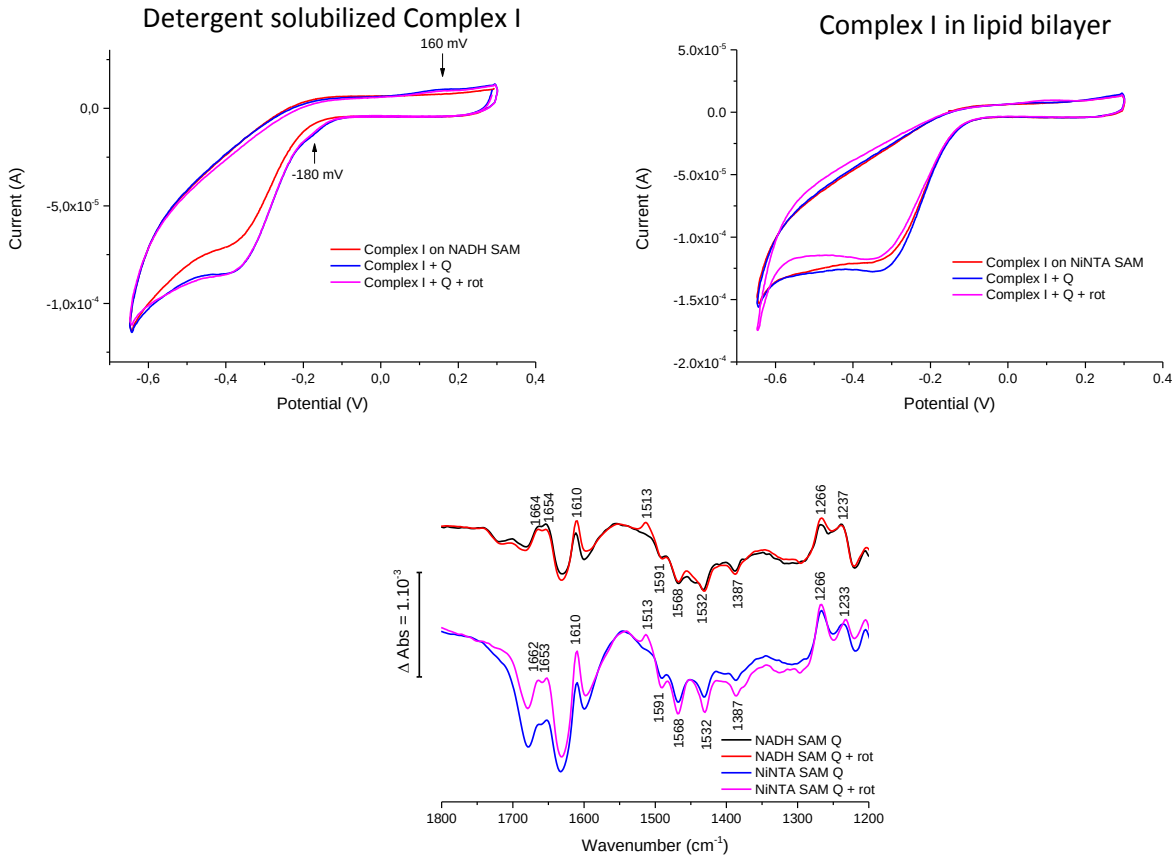

Figure 3.1.14 : Effect of the addition of Decylubiquinone and Rotenone on the adsorbed Complex I.

Both the CV of the Complex I alone and in the bilayer show an increase of the reductive peak upon addition of DQ, but only the enzyme in the bilayer was responsive to subsequent addition of rotenone. When no lipid bilayer was present, the reduction (-180 mV) and reoxidation (+160 mV) of DQ was seen, thus representing the reaction of free (not bound to Complex I) DQ at the electrode surface (E'_0 = 60 mV vs. SHE). The increase of the reductive peak around -380 mV could represent the catalytic reduction of DQ by Complex I (lower E_m of Q in the binding pocket[49, 132]). The insensitivity to rotenone in the absence of a lipid bilayer might be explained by the poor solubility of rotenone in water, so that it is uncertain if it actually inhibits the enzyme, whereas it is more likely to dissolve in the lipid bilayer.

To further investigate the properties of the adsorbed Complex I, it was also probed against Zn^{2+} and NADH-OH. The ox-red spectra did not reveal a change in presence of these inhibitors, while the CVs did (Figure 3.1.15).

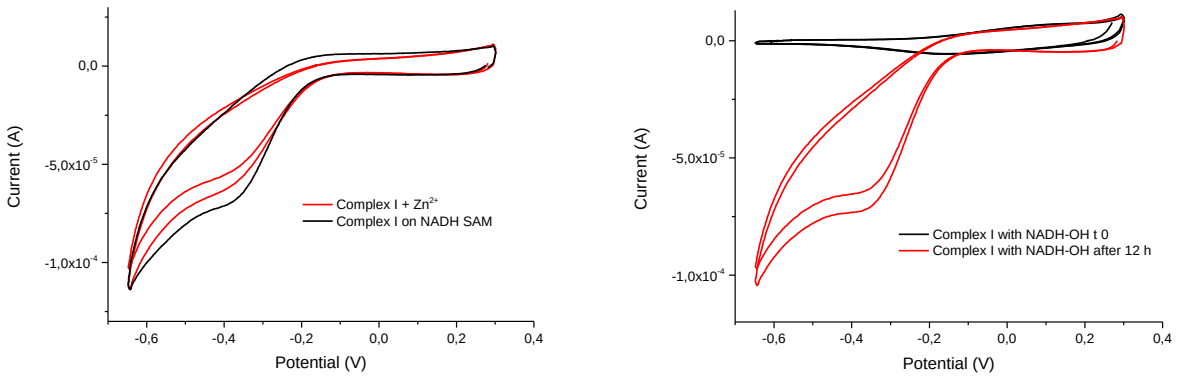

Figure 3.1.15 : Effects of Zn^{2+} on Complex I adsorbed on the NADH SAM and of NADH-OH on Complex I adsorbed on the NiNTA SAM.

100 µM of Zn^{2+} were added to an already immobilized enzyme. The CV shows a gradual decrease of the reductive wave, consistent with the progressive nature of zinc inhibition and showing that the system was sensitive to it. 300 µM NADH-OH were incubated with Complex I prior to its adsorption on a NiNTA SAM since it would have interfered with binding to its NADH counterpart. The CV recorded after this adsorption showed no reduction wave at all, indicating that no catalytic electron transfer happened and that the layer formed isolated the electrode. After 12 h however, the CV returned to normal, probably because NADH-OH eventually dissociated from the enzyme. It was unfortunately not possible to add the inhibitor to the preadsorbed Complex I due to insufficient sample quantity to add to the 20 mL of buffer volume used in this setup.

3.1.5 Conclusion

An experimental setup allowing combined SEIRAS and CV experiments on protein films was successfully created here. This powerful tool can thus be used for the exploration of catalytic mechanisms of redox enzymes. When applied to the study of immobilized Complex I, ambivalent results were obtained ; on the one hand, a stable (against mechanical forces as rinsing) layer of the adsorbed enzyme was formed, but on the other hand its functional probing through SEIRAS and CV was complicated by various factors. For example, the stability over time of the thiol SAM when exposed to reducing potentials below -500 mV is uncertain. Further control over the physical properties of the gold layer is also needed. While the exact orientation of Complex I with respect to the surface is unknown, the experiments with the NDF and the NuoEF fragment indicated that the major part of the FTIR signals seen for the whole Complex I arise from the NDF. However, signals from the membrane domain are also seen, indicating that the size of Complex I is not a barrier to its study by SEIRAS. The addition of quinone and inhibitors produced results showing that at least a part of the system is as it was imagined in chapter 1.7 and that the immobilized Complex I can catalyze the reversible reduction of quinone.

To create a more reliable and performing system, another gold deposition method could be used, or the existing method could be modified for example by creating a thinner film on which Au nanoparticles are deposed to increase the electrode surface area[231], which could allow direct observation of cofactor-signals by CV. Another metal could also be used, as Ag or Pt also show SEIRA properties. This might also open the way to Far-Infrared studies, a spectral domain that we hoped to reach with the present setup but a yet unexplained effect hindered the acquisition of any spectrum in this domain. A SAM stable at the relatively strong reducing potentials needed to address the Complex I cofactors is also required for further investigations, for example a Selenol or Tellurol SAM.

3.2 Role of *nuoF* Tyr^{178} in the NADH binding site and inhibition of Complex I by NADH-OH

3.2.1 Introduction

In this chapter, the role of $_{F}$Tyr^{178} in the NADH binding pocket will be studied. This mutation was shown to be involved in Leigh-like syndrome (see chapter 1.3). At the electron input level, Complex I dysfunction is mainly linked to disease through three processes : ROS production, modification of affinity to NADH/NAD^+ or inhibitors, or modification of E_m FMN and subsequent electron transfer. To address these options, a series of $_{F}$Tyr^{178} mutants in the *E. coli* Complex I was prepared by E. Gnandt at the laboratory of Pr. Friedrich (chapter 2.1.4). The substitution of $_{F}$Tyr^{178} to Phe was made to probe the role of the phenolic hydrogen bond and the aromatic ring, its replacement by Leu and Ala to probe the importance of steric hindrance and hydrophobicity and the mutation to Cys to probe hydrogen bonding with the thiol and why it is causing the disease. ROS production *via* Amplex-Red Assay[249] (sensitive to H_2O_2), activity and affinity measurements (for NADH:DQ activity) of the mutants were done by E. Gnandt. The estimation of their E_m FMN was done through UV-Vis titration as described in chapter 2.4. The $_{F}$Ala^{178} and $_{F}$Cys^{178} variants were also probed by electrochemically induced FTIR difference spectroscopy.

In a second part of this chapter, the effects of the NADH competitive inhibitor NADH-OH were considered. To get further insight into the NADH-OH mode of action, the E_m FMN of the NADH-OH inhibited Complex I from *E. coli* was measured by UV-Vis titration, the global effect was probed through electrochemically induced FTIR difference spectroscopy and the ROS production was measured (by M. Schulte - group of Pr. T. Friedrich).

3.2.2 $_F$Tyr^{178} mutants characterization

3.2.2.1 Kinetic parameters and ROS production

The mutations of $_F$Tyr^{178} were well incorporated and lead to full assembly of Complex I (see appendix chapter 5.1.3). To make certain that the FMN was not lost in the mutants, the FMN content of the preparations was estimated through UV-Vis spectroscopy. No significant variations of the FMN content compared to the WT were seen and the FMN:Complex I ratio was close to unity (not shown). The estimations of V_{max}, of the apparent K_m NADH and of ROS production in each mutant and the WT are summarized in Table 3.2.1.

Protein	V_{max} (μmol.mg^{-1}.min^{-1})	K_m NADH (μM)	% H_2O_2 / NADH	% H_2O_2 / NADH + Fenazaquin
WT ($_F$Tyr^{178})	3.07 ± 0.05	8.4 ± 0.3	1.1 ± 2	19 ± 2
$_F$Ala^{178}	1.10 ± 0.04	10 ± 0.9	8.1 ± 0.9	75 ± 14
$_F$Cys^{178}	1.09 ± 0.04	11.8 ± 1.2	5.4 ± 0.6	65 ± 8
$_F$Phe^{178}	2.26 ± 0.06	23.0 ± 2.4	13 ± 1.0	52 ± 12
$_F$Leu^{178}	0.80 ± 0.03	11.5 ± 2.0	6.5 ± 0.5	73 ± 23

Table 3.2.1 : Kinetic parameters and ROS production of $_F$Tyr^{178} mutants compared to the WT enzyme. All values are for NADH:DQ activity. The production of ROS is given in absence and presence of Fenazaquin (Q site inhibitor). The measurements were made by E. Gnandt.

V_{max} was roughly 1/3rd of V_{max} WT in the Ala, Cys and Leu mutants and 2/3^{rds} in the Phe mutant, indicating that the aromatic ring of $_F$Tyr^{178} is important for turnover. In this mutant, the K_m NADH was also two times higher than for the WT, whereas it was almost unaffected in the Ala mutant and only slightly higher in the Cys and Leu mutations. This indicates that polarity, steric hindrance and hydrogen bonding capacity of $_F$Tyr^{178} all contribute to shaping the K_m NADH. ROS production in all the mutants was higher than in the WT : 5 to 10 times higher for uninhibited NADH:DQ activity, 3 to 4 times higher for Fenazaquin inhibited NADH:DQ activity. The Amplex red assay used here allows the detection of H_2O_2, which in Complex I from *E. coli* is produced in the NADH oxidase region[116], most likely through the $FMNH^-$ or flavosemiquinone intermediates[113]. The increased H_2O_2 production in all the $_F$Tyr^{178} mutants furthers confirms the implication of the FMN in this process. The highest ROS production was seen in the $_F$Phe^{178} variant. Thus, $_F$Tyr^{178} plays an important antioxidant role

via its phenol rather than through its aromatic ring. The $_{F}Cys^{178}$ variant did not show the highest increase in ROS production *per se*, but it had the highest sensitivity to Q site inhibition, with a ca. 12-fold increase of ROS production in presence of Fenazaquin. This could reflect the stabilization of $FMNH^{-}$ or $FMN(H)^{\bullet(-)}$ by the sulfhydryl when downstream electron transfer to Q is blocked, a factor that might contribute to the symptoms of Leigh disease. Electron tunneling to and from N1a and to N3 could also be affected when no Tyr is present at position $_{F}178$, process in which the aromatic ring of the Tyr might play a role as judged by lowest increase of ROS production in $_{F}Phe^{178}$ in presence of Fenazaquin (4 fold compared to the uninhibited $_{F}Phe^{178}$).

3.2.2.2 UV-Vis titration of E_m FMN

The method to estimate the midpoint potentials of FMN in Complex I was described in chapter 2.4. At 450 nm, both FMN and FeS clusters absorb[194] so that a precise analysis of the E_m FMN from the direct fitting of Nernst curves to ΔAbs_{450nm} *vs.* the applied potential (E) is not possible. To get an estimation of the contributions from FeS centers, the first derivative of the absorption at 520 nm (where only FeS centers contribute[194]) *vs.* E was calculated for the WT Complex I (Figure 3.2.1). The redox reactions FeS clusters take place over a broad range of potentials, from below -150 to over -400 mV. Most centers have an pH independent E_m between -250 and -300 mV[110, 194], consistent with the broad n=1 electronic transitions centered around this potential. Some centers have a higher, pH dependent potential, as N2 and N1a ($E_{m,7}$ = -150 and -235 mV in *E. coli*, respectively[110, 194]), explaining the transitions seen above -250 mV here. From the data one or more clusters also seem to exhibit a lower, more negative E_m, as judged by the broad peak centered around -350 mV. This might represent the reduction of N3, N5 or the reduction of the peripheral cluster N7, which is not involved in electron transfer from NADH to Q but can be electrochemically reduced[110]. Next, $\delta\Delta Abs_{450nm}$ was calculated and compared to $\delta\Delta Abs_{520nm}$ (Figure 3.2.1). In $\delta\Delta Abs_{450nm}$, the contributions from the FeS clusters clearly underlie a more intense, sharp (n = 2) electronic transition around -475 mV. This corresponds to the 2 e^{-} redox reaction of FMN, the higher intensity being explained by the higher molar extinction coefficient of this transition (ε_{450nm} = 12.800 $M^{-1}.cm^{-1}$) compared to that of the FeS clusters (ε_{450nm} = 4.100 $M^{-1}.cm^{-1}$). To estimate E_m FMN, a Gaussian curve for a n = 2 electron transition was fitted to the

data, which in the case of the WT resulted in E_m FMN = -262 mV. Compared to the reported values (-340 / -350 mV) this value seems more positive but the measures were made at pH 6 (vs. 7.5 in ref[194]). FMN in solution shows a pH dependency of -52 mV / pH unit, but in protein-bound flavins the effect of pH on E_m is more complex and not always linear. When adjusting E_m FMN to pH 7.5 with the solution value, we obtain -262 - 52 x 1.5 = -340 mV, which is consistent with the reported values. If a lower value for pH dependency is used, the obtained E_m FMN would be less negative. The error margin of the experiments (± 15 mV), differences in the preparations or simply the use of a different buffer (MES in our case, KPi in ref[194]) might cause this difference. To tentatively increase the accuracy of the E_m FMN estimation, the transitions of the FeS clusters were co-fitted in form of Gaussians with the curve representing FMN.

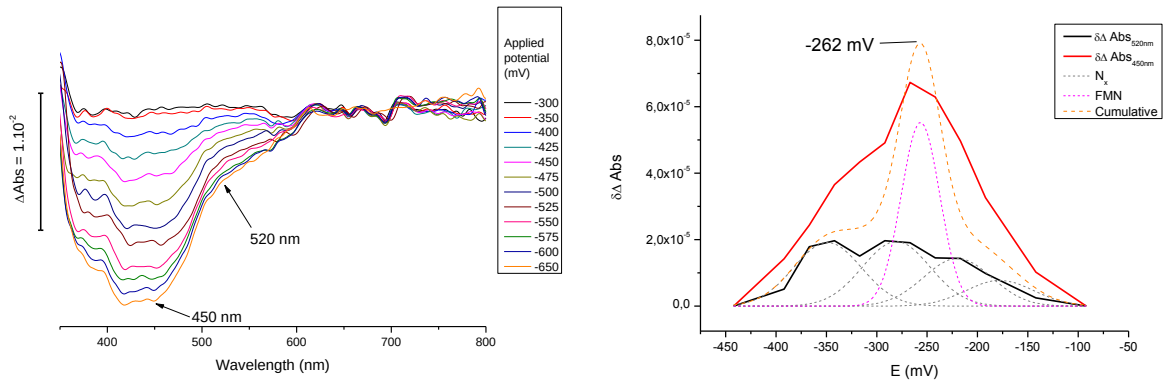

Figure 3.2.1 : UV-Vis titration of the midpoints potentials from the Wild-Type Complex I. Left panel : Potential induced difference spectra. E is given vs. Ag/AgCl 3 M KCl. Right panel : First derivatives of the absorption difference at 450 (red line) and 520 nm (black line) and fitted curves representing the redox transitions of FeS clusters, (termed N_x here - dashed grey lines), FMN (dashed magenta line) and the resulting cumulative curve (dashed orange line). E is given vs. SHE.

For the $_F$Tyr^{178} mutants, the same method as described for the WT was applied. The UV-Vis spectra at different potentials for each mutant and the corresponding δΔ Abs_{450nm} and δΔ Abs_{520nm} are shown in Figure 3.2.2. The estimated E_m FMN of the mutants are summarized in Table 3.2.2.

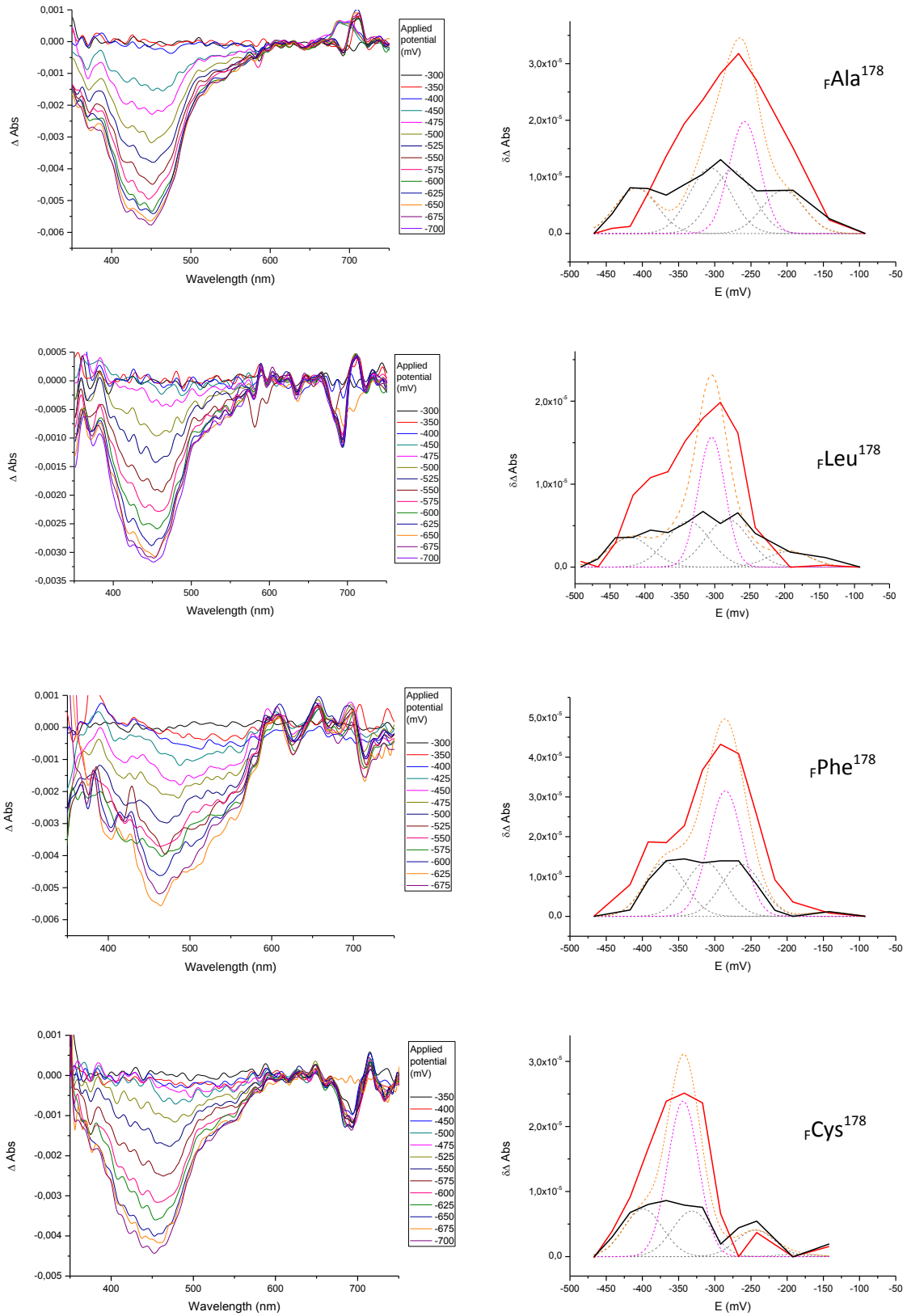

Figure 3.2.2 : Estimation of the E_m of FMN in the *nuoF*$_{HIS}$ Tyr^{178} mutants from their UV-Vis redox titration curves. The applied potentials are given vs. Ag/AgCl 3 M KCl in the left column and vs. SHE in the right column. Colors are as in Figure 3.2.1. Each titration was performed at least two times.

	WT ($_F$Tyr^{178})	$_F$Ala^{178}	$_F$Leu^{178}	$_F$Phe^{178}	$_F$Cys^{178}
E_m FMN (mV)	-262	-259	-304	-285	-343

Table 3.2.2 : Estimated E_m FMN in the $_F$Tyr^{178} mutants. E_m is given vs. SHE at pH 6 (see text for details). The standard deviation was estimated to ± 15 mV.

Since the conditions used for the WT and the mutants were rigorously identical, the values can be compared. Note that the $\lambda_{Abs\ max}$ for the FMN transition did not significantly shift in the mutants compared to the WT, except in the $_F$Phe^{178} variant, where a 10 to 12 nm redshift indicated a small alteration of the electronic transition. Also, the fully reduced *minus* fully oxidized and vice-versa spectra were reversible both at the beginning and at the end of the experiments (not shown), thus the enzyme remained functional over the course of the experiment. A small loss of the FMN cofactor or minor protein denaturation during the experiment can however not be totally excluded.

E_m FMN of $_F$Ala^{178} did not vary from that of the WT, whereas in the $_F$Leu^{178} and $_F$Phe^{178} mutants a negative shift of 25 to 40 mV was observed. This decrease can be related to the hydrophobic natures of Leu and Phe : the more hydrophobic the Flavin's environment, the more negative its E_m [250]. The slightly less important shift for $_F$Phe^{178} indicates that the aromatic ring provides a certain degree of (de)stabilization. The side chain methyl group of $_F$Ala^{178} is probably too far away and not hydrophobic enough to induce a variation of E_m FMN. In addition, the space left empty between $_F$Ala^{178} and the FMN (compared to the WT) might be occupied by solvent, "mimicking" an FMN environment similar to that of a $_F$Tyr^{178} in terms of polarity. Taken together, these findings indicate that the mixed nature of $_F$Tyr^{178} (hydrophobic aromatic ring, hydrophilic phenol) is important to stabilize E_m FMN at a functionally optimal value.

In the $_F$Cys^{178} variant, an 80 mV downshift of E_m FMN to -343 mV was observed. It is unclear if this quite significant shift is due to the stabilization of the oxidized state or to the destabilization of the reduced state of FMN. It is possible that the free electron doublets from Cys can stabilize the oxidized FMN in a quinoid state, as proposed in Figure 3.2.3. Such an effect can be seen in the phototropin LOV2 domain[251], which contains an FMN

interacting with a Cys. However, this enzyme is not an oxidase and the Cys faces C_8 and C_9 of the isoalloxazine ring, whereas in the $_F$Cys^{178} variant of Complex I it is on the other side of the ring (i.e. facing C_6, C_{5a} and N_5 - see Figure 1.3.5 for FMN atom numbering). In LOV2 domains from other organisms, a Cys is involved in the redox reaction through the creation of an C_{4a}-Cys adduct, a possibility which might not be excluded here. This adduct has an absorption maximum at 390 nm[252], but unfortunately the FMN from Complex I also absorbs at this wavelength so that no conclusion could be drawn from the titration curves of the $_F$Cys^{178} mutant. Although $_F$Cys^{178} would theoretically be *ca.* 5 Å away from N_5 and the C_2 carbonyl (as judged from the position of $_F$Tyr^{178} in the crystallographic structure[108]), a possibility of hydrogen-bond formation exists if the residue is situated slightly closer to the FMN in the mutants. This might directly affect hydride transfer from NADH (H-bond to N_5) or the stabilization of the oxidized FMN (H-bond to C_2=O). The Cysteine might also undergo deprotonation (typical pKa ≈ 8.3), for example by the neighboring $_F$Glu^{95} if its pKa is high enough or if the pKa of Cys is lowered, which would add a potential lowering negative charge to the FMN binding pocket. In another flavoenzyme, the Xenobiotic Reductase A from *Pseudomonas putida*[253], a Cys is observed in a similar position as in Complex I with respect to FMN (i.e., facing C_6 C_{5a} and N_5). Interestingly, the mutation of this Cys to a Ser resulted in the opposite E_m FMN shift (+82 mV) as seen here. In this study it was shown that the Cys from Xen-A did not deprotonate nor that hydrogen bonds to C_2=O or N_5 were involved during the reaction. It was proposed that the Cys controlled the FMN potential by restraining its planarity, thus modulating the electron structure of the isoalloxazine. The mutation thus affected the equilibrium between the oxidative and the reductive half-reactions rates. Transposed to Complex I, this could mean that the presence of $_F$Cys^{178} slows down the reduction rate of NADH and speeds up its reoxidation rate by the FeS clusters, consistent with a lower E_m FMN. The functional implications of the potential downshift in $_F$Cys^{178} Complex I are clear : the E_m of FMN no longer matches the E_m of NADH (-290 mV at pH 6), slowing down electron transfer to Q and thus diminishing the overall activity of Complex I.

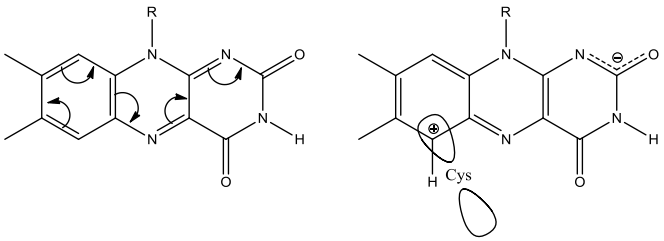

Figure 3.2.3 : Stabilization of oxidized FMN in a quinoid state through interaction with $_F$Cys^{178}

Besides the highest slope for the 2 e^- transition FMN, a smaller shoulder can be seen at lower potentials in δΔ Abs_{450nm} of the WT, the $_F$Leu^{178} and $_F$Phe^{178} variants and, to a smaller extent, in the $_F$Ala^{178} and $_F$Cys^{178} mutants. Most likely, this transition represents the redox reaction of an iron-sulfur cluster with an E_m below -350 mV. As it is influenced by the replacement of $_F$Tyr^{178}, it might belong to the adjacent N3. Another interesting effect of the replacement of $_F$Tyr^{178} can be seen in the profile of the FeS transitions (δΔ Abs_{520nm}) on Figure 3.2.2 : it seems that apparent E_m of some clusters "follows" that of FMN, which is representative of the close equilibrium linking the two. The midpoint potentials situated at the edges of the studied potential range seem to be perturbed : in the $_F$Ala^{178}, $_F$Leu^{178} and $_F$Cys^{178} variants, the lowest transition can be seen at -425 mV, compared to -375 mV for the lowest transition in the WT and the $_F$Phe^{178} mutant. Additional variations can also be seen below -250 mV, which might indicate that electron transfer to or from N1a is affected by the mutations. However, Δ_{Abs} at 520 nm used to estimate the contributions from the iron-sulfur clusters is 3 to 4 times smaller compared to that at 450 nm, thus the signal to noise ratio at 520 nm is lower. Added to the lack of consensus midpoint potential values for the FeS clusters, we thus refrained from over-interpreting the shifts seen here.

3.2.2.3 FTIR difference spectroscopy of the $_F$Ala^{178} and $_F$Cys^{178} variants

The FTIR difference spectra of the $_F$Ala^{178} and $_F$Cys^{178} mutants were measured immediately after the UV-Vis titration by transferring the measure cell in the FTIR spectrometer, with the same samples. As one UV-Vis titration took in general 6 to 9 hours (at 12°C), some samples were not active enough anymore to yield reproducible spectra, and eventually some subunits were lost. The spectra are shown here only to get an idea of how the single $_F$Tyr^{178} mutation might affect the overall redox-induced changes in Complex I and to see if any alteration of the vibrational modes of FMN is visible. A more detailed study including the Phe and Leu mutants is underway.

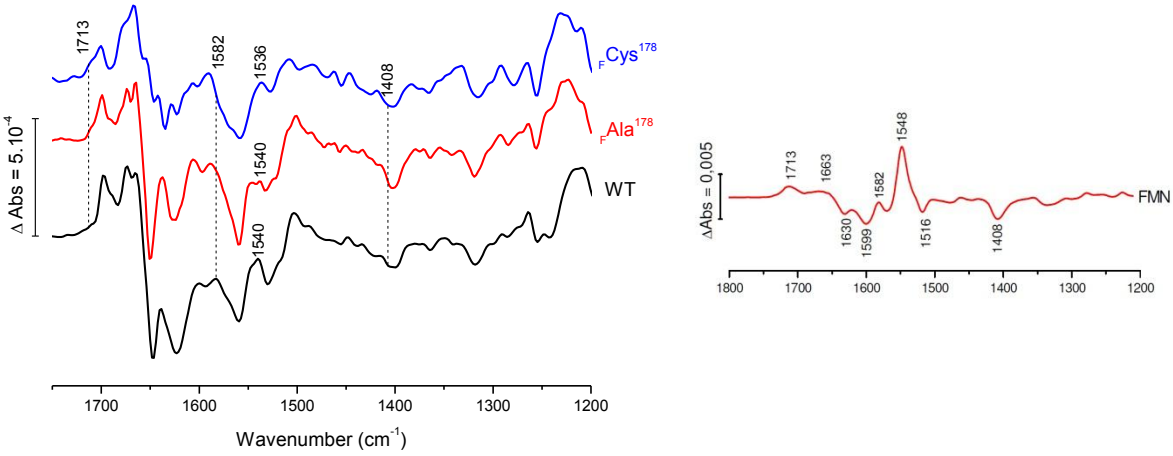

Figure 3.2.4 : Electrochemically induced FTIR difference spectra of Complex I and the $_F$Tyr^{178} mutants and of FMN. The left panel shows the fully oxidized *minus* fully reduced spectra of Complex I and its mutants and the right panel shows that of the isolated FMN recorded under the same conditions (adapted from ref[197]).

The general shape of the oxidized *minus* reduced spectrum of $_F$Ala^{178} was similar to that of the WT Complex I. The data for $_F$Cys^{178} was more altered, especially in the amide I region (1700-1600 cm^{-1}), representing a perturbation of the conformational movements associated to the redox reaction of the enzyme. The positions of the most prominent modes of FMN[192] are indicated on the spectra in Figure 3.2.4. The mode with the highest molar extinction coefficient, ν(C=C) is located at 1540 cm^{-1} in the WT. Upon replacement of $_F$Tyr^{178} by Ala, this signal is slightly diminished ; when a Cys was introduced, it was diminished and shifted by 4 cm^{-1} to lower wavenumbers. This is consistent with the measured kinetic parameters and E_m FMN, further pointing to a restriction of the isoalloxazine's planarity by a Cysteine in this particular position. At 1582 cm^{-1}, the ν(C=N) mode from the flavin might be seen. In the Ala mutant this signal is almost unchanged, whereas it seems not to be present (or shifted) in the Cys mutant. The ν(C=O) mode at 1713 cm^{-1} did apparently not vary but its overlap with other carbonyl vibrations makes its assessment prone to errors. The same observation can be made for the isoalloxazine ring mode at 1408 cm^{-1} (overlap with $\nu_s(COO^-)$ modes). As tyrosine are strong IR absorbers ($\varepsilon_{\nu(C=C)} \approx 250$ and 450 mol^{-1}.cm^{-1} for Tyr-OH and Tyr-O$^-$, respectively) slight changes around 1500 cm^{-1} might also be due to the replacement of $_F$Tyr^{178}.

3.2.3 NADH-OH inhibition

The H_2O_2 production of the NADH-OH inhibited Complex I was measured at 50 and 90 % inhibition and compared to that of the uninhibited enzyme. The results are summarized in Table 3.2.3.

[NADH-OH] (µM)	Inhbition %	% H_2O_2 / NADH consumed
0	0	1.9 ± 0.3
0.5	50	7.0 ± 0.3
3	90	22 ± 1

Table 3.2.3 : ROS production in the NADH-OH inhibited Complex I. K_i NADH-OH = $1.2.10^{-8}$ M[150]. The measurements were made by M. Schulte.

The ROS production per consumed NADH increased by a factor 3 to 4 when Complex I was inhibited at 50 % by NADH-OH and by more than 10 times at an inhibition of 90 %. It is unclear by which mechanism H_2O_2 is generated here : in the inhibited enzyme, no electron transfer from NADH to the enzyme is in principle possible since the binding pocket is already occupied by the inhibitor. Apparently no electron transfer to the iron sulfur clusters takes place upon NADH-OH binding so that it is unknown if and how NADH-OH itself can be oxidized by Complex I[150]. It is possible that the otherwise highly unstable $NAD(H)^{\bullet}$ and $FMN(H)^{\bullet}$ radicals can be generated with NADH-OH, which might then react with oxygen. This would yield $O_2^{\bullet-}$, which can form the detected H_2O_2 through superoxide dismutation. As this reaction requires two superoxides, it would be favored if the first $O_2^{\bullet-}$ remains in the vicinity of the NADH-OH - FMN interaction site, while the second $O_2^{\bullet-}$ is formed. Another possibility is that NADH-OH is effectively oxidized to NAD^+-OH and that the resulting $FMNH^-$ is stabilized by the nucleotide, opening the way for the creation of hydroperoxyflavin, the presumed precursor of hydrogen peroxide[254, 255]. However, this would require that oxygen can access the reduced flavin, which seems precluded by the bound nucleotide. In both proposed processes, the alcohols from the NADH-OH nicotinamide ring might play a role in stabilization of reactive intermediates or might even be involved in the redox reaction. As NADH-OH also absorbs at 340 nm (wavelength used to estimate NADH consumption), the percentage of ROS produced per consumed NADH might include NADH-OH that was oxidized during the reaction.

The UV-Vis titration of E_m FMN of the NADH-OH inhibited enzyme was done the same way as for the $_F$Tyr^{178} mutants. Figure 3.2.5 shows the corresponding difference spectra, $\delta\Delta Abs_{450nm}$ and $\delta\Delta Abs_{520nm}$ used to estimate the midpoint potential. The potential-induced difference spectra were of worse quality than those of the WT and of the $_F$Tyr^{178} mutants. This might be due to a lowering of the FMN's ε_{450nm} in presence of NADH-OH (as described in ref[150]), yielding less intense transitions and thus a lower signal to noise ratio. However, the results were reproducible, only the error was higher : ± 25 mV out of four experiments.

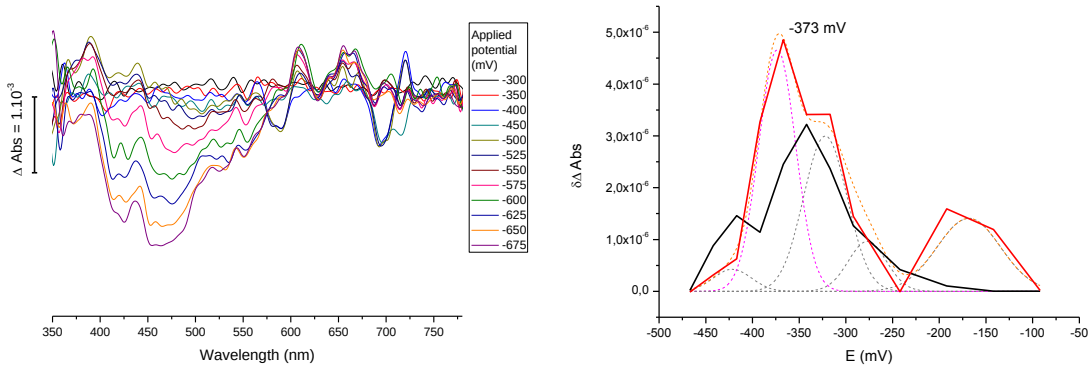

Figure 3.2.5 : Estimation of Em FMN and of the FeS clusters in the NADH-OH inhibited Complex I. Curves are colored as in Figure 3.2.1.

E_m FMN upon inhibition was estimated at -373 mV. This represents a 110 mV downshift from the uninhibited Complex I, indicating a strong perturbation of the FMN's electronic structure by NADH-OH. The best fit was obtained by a n = 2 curve, indicating that no particular stabilization of the flavin radical is induced by NADH-OH. $\lambda_{Abs\ max}$ was 10 to 20 nm redshifted. Taken together, this shows that NADH-OH forms a very stable adduct with FMN. The transitions of the FeS clusters also seem to be affected by the presence of the inhibitor (as judged by $\delta\Delta Abs_{520nm}$) but for the same reasons as for the $_F$Tyr^{178} mutants, this will not be further discussed here.

The effect of NADH-OH was also probed through electrochemically induced spectroscopy, by the same method as for the $_F$Tyr^{178} mutants. However, no meaningful results were produced in these experiments. The spectra showed very poor red-ox/ox-red

reversibility in the range where the Complex I signals are expected (i.e. 1750 cm^{-1} to 1200 cm^{-1}) and as the redox cycles progressed, even pointed to progressive denaturation of the protein. After increase of the equilibration times and lowering of the applied potential to -750 mV vs Ag/AgCl (instead of -700 mV in other experiments) to tentatively match the lower E_m FMN seen in the UV-Vis titration, the situation did not improve. As the (reversible) signals from the MES buffer were still seen, it is unlikely that the experimental setup itself was not correctly working. The lack of the usual Complex I signals might simply indicate that no electron transfer can take place in the NADH-OH inhibited enzyme, even if FMN can be electrochemically reduced. Thus, the usual conformational movements, cofactor and residue reactions that shape the redox induced FTIR spectrum of Complex I do not take place here, yielding an almost inert enzyme.

3.2.4 Conclusion

The results from this chapter clearly demonstrate the central role of $_F$Tyr^{178} in NADH binding, hydride and subsequent electron transfers and the prevention of ROS production. The variations of K_m NADH in the $_F$Tyr^{178} mutants are less than expected for a direct interaction with the substrate, excepted for the $_F$Phe^{178} variant. This could be due to occupation of the space left empty by a solvent molecule that hydrogen bonds to $_F$Glu^{95}, which is not possible when the bulky Phe is present. Hydrophobic repulsion of the neutral nicotamide group of NADH is probably also involved in the lower K_m of $_F$Phe^{178}. The π-electron system from the Tyrosine's aromatic ring seems to be important for hydride- or electron- transfer to the FeS centers (or for both), as demonstrated by the lower impact of the $_F$Phe^{178} mutation on V_{max} despite its lower K_m NADH and E_m FMN. The spatial proximity of these electrons to the isoalloxazine ring can fine-tune its HOMO and LUMO in function of the oxidation state, as shown by the movement of the Tyr side chain in the oxidized and reduced X-ray structures of Complex I[108]. If no aromatic system is present, one of these steps (H^- or e^- transfer) might become rate limiting. Regarding ROS production, $_F$Tyr^{178} acts as antioxidant : the hydrophilic phenol could simply act as a repellant for the hydrophobic O_2. When $_F$Tyr^{178} is replaced by the hydrophobic Phe or Leu, this repelling is lost. In the (slightly) more polar Ala and Cys variants, a small repulsion of O_2 might be present but can be counterbalanced by the reduced steric hindrance of these residues, allowing O_2 to "sneak

past" to the FMN. In addition, the formation of a tyrosil radical is also possible. Another factor not studied here might also increase the production of ROS : the K_i of NAD^+. If it is higher for the mutants than for the WT, NAD^+ would dissociate faster and the reduced flavin would be exposed to O_2 for a longer period of time.

In the context of Leigh-like syndrome, the probable cause of the symptoms (i.e. disturbance of oxidative phosphorylation) is the substantial lowering of E_m FMN when ${}_F\text{Tyr}^{178}$ is replaced by a cysteine, slowing down electron transfer to Q and subsequent proton pumping. As Complex I generates 40 % of the proton gradient used by mitochondria to generate ATP, a diminishment of its activity by ca. 65 % (as judged from V_{max}) can significantly affect the oxidative phosphorylation process. The higher production rate of ROS might also contribute to the Leigh-like condition, however Complex I is responsible for less than 5 % of the total cellular ROS production[139] so that even the 3- to 5-fold increase of ROS production seen in ${}_F\text{Cys}^{178}$ might still be handled at cellular level. In addition, the reduced catalytic rate would take the ROS production almost back to normal.

To further clarify the role of ${}_F\text{Tyr}^{178}$ and the effect of its substitution, additional investigation is required. The measure of K_i NAD^+ in the different mutants might help to shed light on otherwise unexplained features, as the reduced V_{max} of the ${}_F\text{Ala}^{178}$ and ${}_F\text{Leu}^{178}$ while their K_m NADH and E_m FMN did not or only slightly vary. The study of the complete series of mutants by vibrational spectroscopy, especially by Resonance Raman spectroscopy as done for the WT Complex I[114], could further elucidate the contribution of the amino acid in position ${}_F178$ to the electronic and atomic configuration of FMN. Concerning ROS production, insight in the importance of ${}_F\text{Tyr}^{178}$ in prevention of their formation could be gained from measures of direct superoxide production[111, 116] known to represent 20 % of the ROS produced by *E. coli* Complex I[116] and to compare the ratio of $O_2^{\bullet -}$ / H_2O_2 produced in the ${}_F\text{Tyr}^{178}$ variants to the WT. This might also be useful to further understand how ROS are produced in the NADH-OH inhibited enzyme. Finally, the creation of additional mutants could also be of interest to probe the role of the phenyl alcohol (${}_F\text{Ser}^{178}$) and of the sulfur atom (${}_F\text{Met}^{178}$).

Our understanding of the effect of the $_{F}Tyr^{178}$ substitution on the flavin's planarity and of the NADH-OH inhibition mode would also greatly benefit from X-ray crystal structures at improved resolution. This might be achieved by introducing the mutations in the NuoEF subcomplex from *Aquifex Aeolicus* previously crystallized in the T. Friedrich group (M. Vranas, E. Gnandt, K. Morina, personal communication) and by co-crystallization of the same subcomplex in presence of NADH-OH. This would open the way for molecular modeling to calculate electron tunneling rates from FMN to N1a (and back) in order to clarify the mechanism by which the electron pair from NADH is split and sequentially transferred to Q, and which role $_{F}Tyr^{178}$ plays in this process.

3.3 Interaction of Complex I with Phospholipids

3.3.1 Introduction

In this part, the effects of the three major phospholipids comprised in the *E. coli* membrane (PE, PG and CL - see chapter 1.4) on a lipid-depleted Complex I sample are studied. The preparation of this sample is described in chapter 2.1.2. To get a first idea of the effect of lipids on the delipidated Complex I samples, their catalytic NADH:DQ activities during progressive lipid re-addition were measured by Ina Psarjow (U. Freiburg). The resulting curves (Figure 3.3.1) show that the enzymatic activity of the lipid-depleted Complex I is restored when the lipid to protein w/w ratio reaches ~0.05 to ~0.1 (i.e. less than 50 moles of lipids per mole of Complex I), although slight variations in the shapes of the curves and the maximal activity were observed depending on the nature of the lipid added, suggesting the presence of specific binding sites.

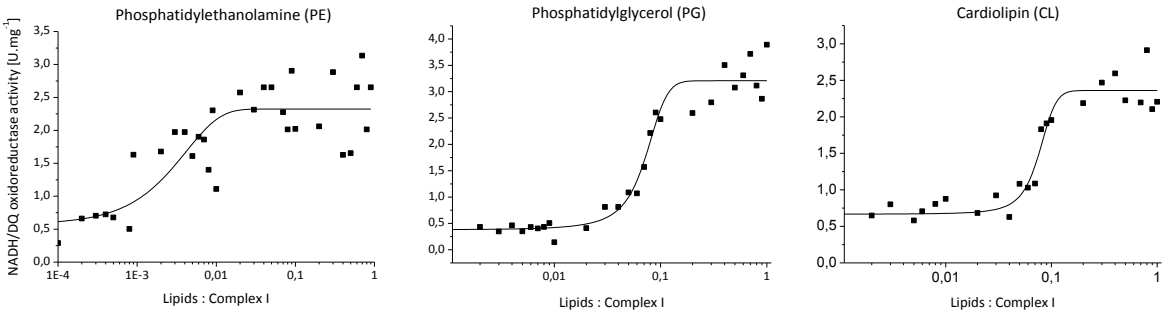

Figure 3.3.1 : Evolution of Complex I NADH/DQ oxidoreductase activity in function of the addition of phospholipids. The x axis corresponds to the lipids:protein w/w ratio. Measurements made by I. Psarjow.

To get a clearer idea of the influence of the lipid nature on Complex I function, each lipid was studied separately *via* a combination of two methods : electrochemically-induced FTIR difference spectroscopy was used to obtain a better understanding of the changes occurring upon oxidation or reduction with and without lipids, and ^{2}H-^{1}H exchange dynamics were done to study the effect of the lipids on the solvent accessibility i.e. on the tertiary and quaternary structures of the enzyme.

3.3.2 FTIR difference spectroscopy of Complex I in the presence of lipids

3.3.2.1 Difference between regular and delipidated Wild Type Complex I

To collect information about the general effect of lipids on Complex I, electrochemically induced FTIR difference spectroscopy was conducted on two Complex I samples : one was not specially treated, i.e. lipids were present, while the other was lipid-depleted. Figure 3.3.2 shows the fully oxidized (+200 mV) minus fully reduced (-700 mV) FTIR spectra in the range from 1800 to 1200 cm^{-1} of both samples. The spectral features for this redox step involve large changes in the amide I and II regions (from 1700 to 1610 cm^{-1} and from 1570 to 1500 cm^{-1} respectively), contributions from the FMN (1716 cm^{-1} (shoulder) and positive peak at 1540 cm^{-1}) and contributions from side chains, mainly Asp, Glu and Tyr. Ubiquinone also contributes to the specrum (1601, 1266 and 1256 cm^{-1}). These features are well described[174, 192] and the tentative attributions for each peak are summarized in Appendix 5.

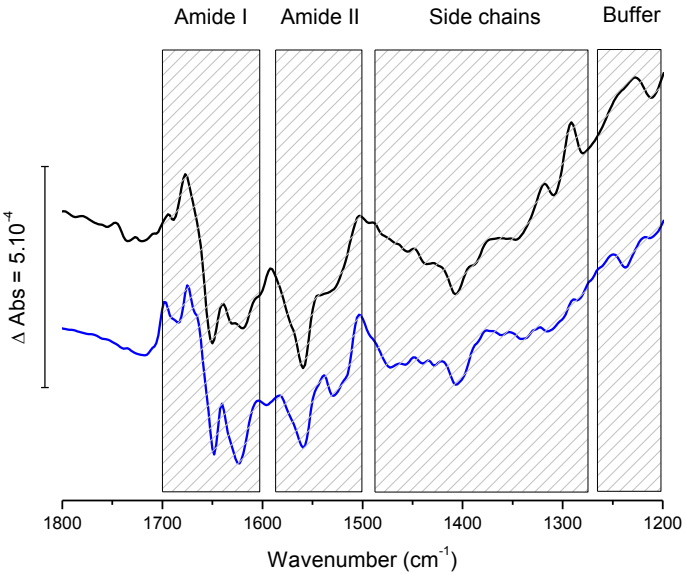

Figure 3.3.2 : Oxidized *minus* reduced FTIR spectra of Complex I with (black line) and without (blue line) lipids.Both spectra correspond to the fully oxidized (+200 mV vs. Ag/AgCl 3 M KCl) minus fully reduced step (-700 mV vs. Ag/AgCl 3 M KCl).

In order to highlight the spectral changes produced by the lipids, a double difference spectrum was calculated by interactive subtraction with Opus 6.5 software (Figure 3.3.3).

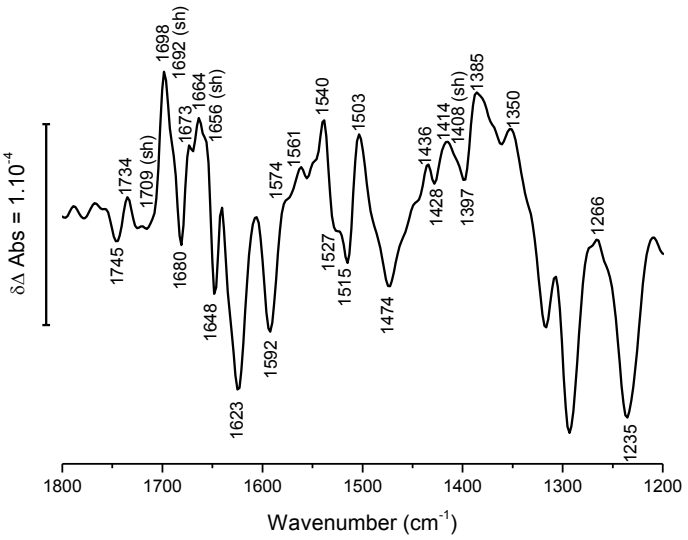

Figure 3.3.3 : Double difference spectrum of delipidated Complex I *minus* WT Complex I.The spectrum was obtained by interactive subtraction of the two oxidized minus reduced spectra shown on Figure 3.3.2.

A first observation on the changes induced by the removal of the lipids concern the amide I and II bands. Both are perturbed by the withdrawal of lipids, as seen by the peaks at 1698(+), 1664(+), 1648(-),1623(-) cm^{-1} (Amide I) and 1592(-), 1561(+), and 1540(+) cm^{-1} (Amide II). This indicates that the conformational movements associated with the functioning of the enzyme are altered. Based on their position, the peaks within the amide I signal can be attributed to different types of secondary structure variations[198, 203]. The band at 1680 (+) cm^{-1} corresponds to fluctuations in the organization of β-turns, the signals at 1664(+) and 1656(+) cm^{-1} reflect changes in α-helical components and the peak at 1648(-) cm^{-1} corresponds to randomly organized structures. Structural variations of β-sheets can be seen at 1698(+)/1692(sh) and 1623 cm^{-1}. As all types of structures undergo modifications, it can be concluded that the presence of lipids alters redox-induced structural changes at the level of the whole enzyme and not only on the predominantly α-helical membrane part, which is consistent with the observations about NADH/DQ oxidoreductase activity.

Interestingly, the positions were bands of quinones (coenzyme Q) are expected (1612, 1601 and 1266 cm^{-1} principally) almost zero out in the double difference spectrum, which could have different meanings : either quinones are equally present in both samples but not affected by the presence of lipids, which is unlikely since the rest of the electron transfer chain is altered and lipids are suspected to play a role in the presentation of the substrate to the quinone binding site[256], or the supplementary purification reduces the quinone content of the samples and the readdition of lipids enhance the ubiquinone reductase activity so that only small changes appear in the double difference spectrum. A third hypothesis where no quinones are present in both samples is also unlikely since it shown that they are retained in the *E. coli* enzyme after purification[172, 257].

A further consequence of the effects of lipids on the activity of Complex I can be seen in the variation of the vibrational modes from certain types of side chains. Even if the coupling mechanism of the electron transfer and the proton pumping is still open to debate, it is now clear that it involves a chain of charged residues running from the quinone binding site to the distal part of the membrane domain along the central axis of the domain[89]. These residues are principally composed of Glu, Lys and His, with a few Tyr and Arg being involved as well. Fortunately, the ν(C=O) vibrations of protonated Asp and Glu appear above 1710 cm^{-1}, which is clear of signals from the protein backbone and other amino acid side chains[201]. The peaks at 1745(-) and 1734(+) cm^{-1} thus stem, at least partially, from the alteration by lipids of the functioning of this charged chain. Modifications in the vicinity of bound lipids could also contribute in this region ($\nu(C=O)_{ester\ phospholipids}$ = 1739-1740 cm^{-1} in dry samples - see Appendix 6), especially since the frequency of the carbonyl vibration is sensitive to hydrogen bonding and polarity changes[258]. Another indicator of modifications around the lipid headgroup region is the signal at 1235(-) cm^{-1}, which can be partially attributed to the $\nu_{as}(PO_2^-)$ vibration of the lipid phosphate group. However, this region is affected by signals from the inorganic phosphate buffer and it is thus not possible to attribute this band unambiguously to the lipids.

In Complex I as well as in other redox-active proton translocating enzymes, the redox-induced protonation of Asp or Glu is linked to the disappearance of signals arising from the deprotonated carboxylate groups, and vice-versa[206, 211]. These signals are usually found

around 1570-1560 ($\nu_{as}(COO^-)_{asp,glu}$) and 1400 cm^{-1} ($\nu_s(COO^-)_{asp,glu}$). In the case of Complex I, they appear at 1574, 1561 and 1407 cm^{-1}, but other groups also contribute in these regions (Amide II, FMN) so that the signals at these positions cannot be attributed to Asp or Glu with certainty. Nevertheless, the small but present signals in the double differential spectrum are indicators that these negatively charged residues are also affected. Experiments in deuterated buffer in chapter 3.3.2.2 will help to clarify the attributions.

As mentioned before, Lys residues are also involved in proton translocation by Complex I. The modifications affecting the Asp or Glu residues should therefore affect the signals of Lys. Unfortunately, the extinction coefficient of the $\delta_{as}(NH_3^+)$ (1626 cm^{-1}) and $\delta_s(NH_3^+)$ (1527 cm^{-1}) modes are relatively weak and thus difficult to observe in proteins due to overlap with other signals. Since a strong band arising from the modifications of the β-sheet structures is present at 1623(-) cm^{-1}, the hypothetic variation of the $\delta_{as}(NH_3^+)$ vibration is not observable here. However, the small shoulder at 1527(-) cm^{-1} can be tentatively attributed to variations of the $\delta_s(NH_3^+)$ mode.

The resolution of the crystal structures of the hydrophilic arm in the oxidized and reduced state[108] highlighted redox-induced changes in the vicinity of the iron-sulfur clusters involving Cys residues. The variations of the cysteine's $\delta(CH_2)$ mode, which is influenced by the proximity and ionization state of the sulfur atom, contributes to the peaks observed at 1436(+) and 1428(-) cm^{-1}. $\delta(CH_2)$ modes from other amino acids and from lipid acyl chains are found at higher wavenumbers. In the present case, small variations of these modes are seen but they can't be assigned to any particular type of residue.

Further implications of other amino acids are seen as well, they will be discussed in chapter 3.3.2.2. The general impression from this first part about the Complex I - lipid interaction is that their presence affects the enzyme at every level, from the electron transfer chain to the proton translocation. In order to identify specific interaction with particular types of lipids, the three main phospholipids from the *E. coli* membrane were studied.

3.3.2.2 Influence of the type of lipid added

The three major phospholipids of the *E. coli* inner membrane - PE, PG and CL - were added to delipidated Complex I at a 50:1 lipid:protein mol/mol ratio in order to avoid partial effects due to insufficient quantities of lipids. The electrochemically induced FTIR difference spectrum was then recorded and compared to the one of delipidated Complex I *via* calculation of the double difference spectrum. Figure 3.3.4 shows the spectra corresponding to the delipidated Complex I *minus* delipidated Complex I with PE, PG or CL.

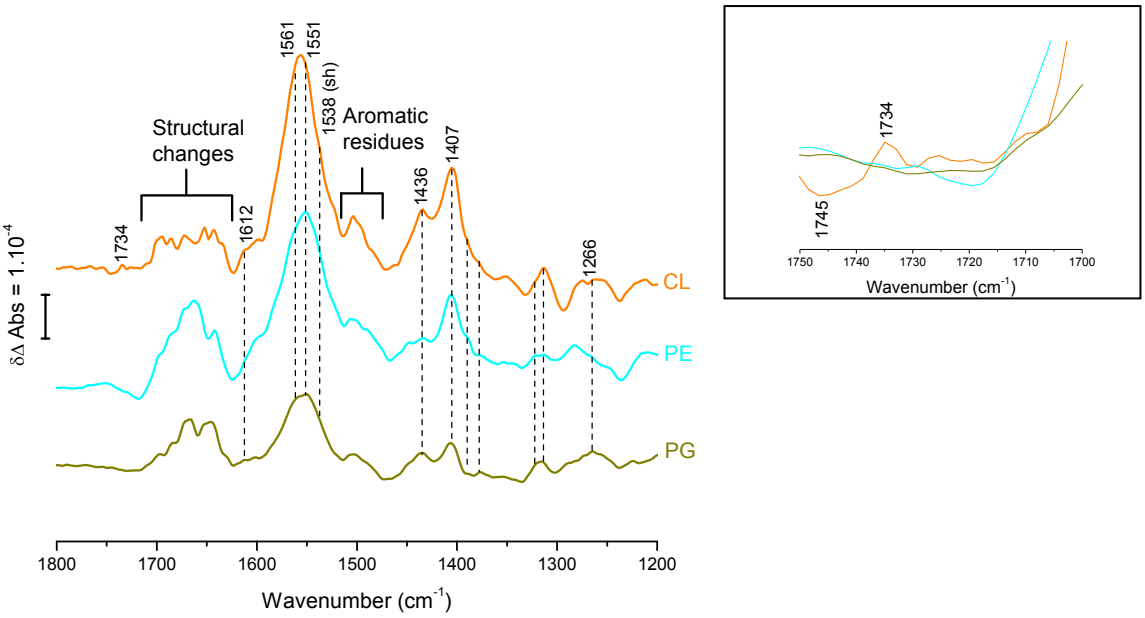

Figure 3.3.4 : Double difference spectra of delipidated Complex I *minus* Complex I in the presence of PG, CL and PE. Each spectrum corresponds to the interactively calculated double difference between the individual fully oxidized *minus* fully reduced spectra. The inset shows a zoom on the region from 1750 to 1700 cm^{-1}. The original single difference spectra from which the double difference spectra were calculated are shown in Appendix 7.

As for the delipidated WT *minus* regular WT, numerous changes in the signature of the Amide I and II bands can be observed. The positions of the individual signals composing these bands remain almost unchanged, but their intensities vary. A general effect for each of the three added lipids is that the components corresponding to the α-helices, the β-hairpins and the randomly oriented elements are more affected than those corresponding to the β-sheets. Another common feature of the presence of lipids is the alteration of the signals

corresponding to protonated and deprotonated Asp and Glu side-chains. The $\nu_{as}(COO^-)_{asp,glu}$ and $\nu_s(COO^-)_{asp,glu}$ modes (at 1574 (Glu), 1561 (Asp) and 1407 cm^{-1}, respectively) are especially perturbed. This could indicate that the proton pumping is particularly affected. A concomitant increase in the signals pertaining to protonated Asp or Glu residues (above 1710 cm^{-1}) can be observed as well. Signals belonging to perturbed Lys residues (1626 and 1527 cm^{-1}) can be seen as well, more or less clearly depending on the overlap of other bands. Finally, no quinone signals seem to be present here.

Altogether, these findings indicate that while each lipid taken individually contributes to global changes during the turnover of the enzyme, they mainly impact the membrane domain and thus may be crucial to proton pumping. For optimal activity resulting in the spectral changes observed in chapter 3.3.2.1, the combined presence of PE, PG and CL is required. This circumstance is illustrated by the spectra presented in Figure 3.3.5 : the re-addition to previously delipidated Complex I of *E. coli* lipid extract, which is constituted of the three major phospholipids at the physiological ratio, results in almost the same spectrum as for the non-lipid-depleted Complex I. On the other hand, the sum of the spectra of PE, PG and CL added individually shows some common features with the other two spectra, but the signals in the Amide II and $\nu_s(COO^-)_{asp,glu}$ area (1510 to 1580 cm^{-1}) and the $\nu_s(C=O)$ (1400's cm^{-1}) region have higher intensities, overlapping the other bands in these areas. Also, changes in α-helical structures are exacerbated in this spectrum. These features are a probable consequence of the non-specific binding of lipids. Indeed, the excess of lipids present might bind to general lipid-binding motifs, which control primarily the proton-pumping function. This is supported by the similarities between the PE, PG and CL spectra in Figure 3.3.4.

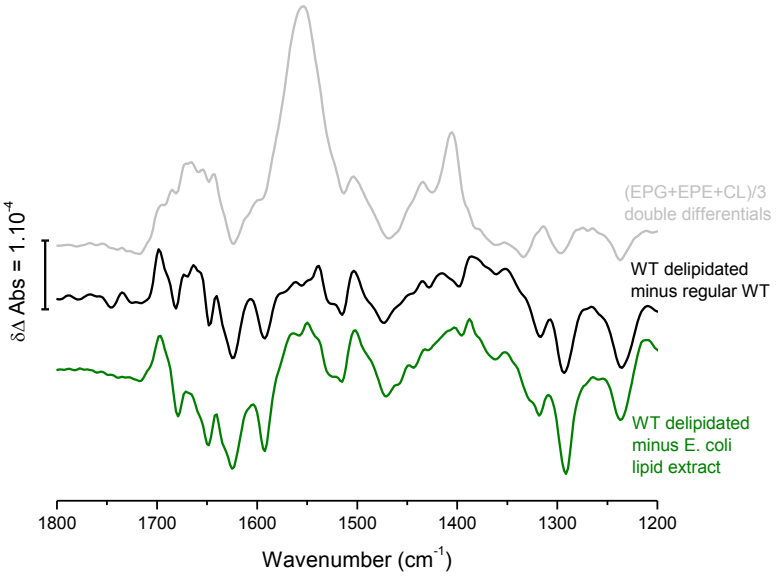

Figure 3.3.5 : Comparison between the effect of native lipids, added *E. coli* lipid extract and PE, PG and CL added individually. The original single difference spectra from which the double difference spectra were calculated are shown in Appendix 7.

The similarities observed for PE, PG and CL point to the presence of several non-specific lipid binding sites on the membrane domain of Complex I, especially for PE and PG. However, the presence of CL induces changes that are not observed for the other two lipids : the ν(C=O) vibrational mode at 1734(+) and 1745(-), which are also observed in the non-depleted Complex I, stem from the interaction of CL with the enzyme (inset in Figure 3.3.5). These signals could arise from the perturbation of Asp and Glu residues or from the perturbation of the ester carboxyls on the CL. Since they are not present in the spectra of PE and PG, which both affect the activity of the enzyme, the latter case is more likely. When compared to the general shape of the PE and PG spectra, the signals in common between the three phospholipids are the most intense in CL. Altogether, this indicates that one or more CL specific binding sites are present on Complex I. Due to the structural similarities between the lipids, it is possible that CL also binds to the less specific sites occupied by PE or PG *in vivo*, which accounts for the intensity of the observed signals. Due to the particularity of the CL structure, i.e. the quadruple acyl chains and the dual interfacial region, it is unlikely that PE or PG can bind to the CL-specific site.

To confirm the specificity of CL binding and to tentatively attribute certain signals to the perturbation of precise types of residues, the re-addition of lipids was conducted in deuterated buffer. The spectra depicted on Figure 3.3.6 conserve the main features already seen in the $^{1}H_2O$ buffer, with the expected isotopic shifts partially taking place. Since the exchange to deuterated solvent is done after the purification of the enzyme, only solvent accessible parts of the protein, i.e. the outer shell and channels or interfacial regions, are subject to ^{1}H-^{2}H exchange. *Ca.* 40 to 50 % of the residues are buried away from the solvent and are thus not affected by the exchange, hence the overlap of signals stemming from vibrational modes in the presence of ^{1}H and ^{2}H. This circumstance, while representing a drawback for the attribution of specific vibrational modes, permits the discrimination between residues accessible and non-accessible to the solvent. Further details about the Hydrogen-Deuterium exchange proportions and kinetics can be found in chapter 3.3.3.

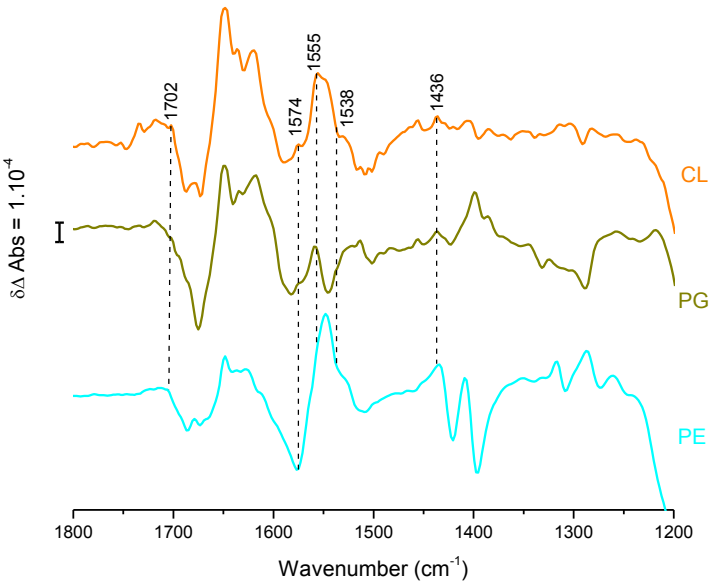

Figure 3.3.6 : Double difference spectra of delipidated Complex I *minus* delipidated Complex I in the presence of PE, PG and CL in $^{2}H_2O$ buffer. The original single difference spectra from which the double difference spectra were calculated are shown in Appendix 7.

In addition to the variations in the percentage of ^{1}H-^{2}H exchange, protein samples from different purification batches were used to make the measures in deuterated buffer. In spite of our precautions to keep the purification procedure strictly identical, a small quantity

of lipids still present on the enzyme might have influenced the spectra. This may give rise to additional differences when the spectra are compared between each other and with the spectra in $^{1}H_2O$ buffer, especially for the double difference spectrum of PE in $^{2}H_2O$.

Upon ^{1}H-^{2}H exchange, the positions, polarities and intensities of the signals composing the Amide I mode vary considerably. The precise analysis of the shifts of each single band in this region would be prone to error due to the factors described above. The sole conclusion that can be drawn from this spectral area is again that all types of structures are affected by the presence of lipids, with a more intense effect on the α-helical, the β-turn and the randomly organized structures than on the β-sheets. The isotope replacement also induces changes in the Amide II mode, whose two main components (δ(N-H) and ν(C-N)) split into two bands : below 1070 cm^{-1} for δ(N-^{2}H) and from 1490 to 1430 cm^{-1} for ν(C-N) (Amide II'). The ^{1}H-Amide II mode loses the major part of its intensity in the $^{2}H_2O$ spectra concomitantly with the appearance of signals below 1070 cm^{-1} (not shown), especially for PG.

The perturbations tentatively attributed to the δ(CH_2) mode of Cys residues are seen in both $^{1}H_2O$ and $^{2}H_2O$, without any noticeable shift. The absence of shift upon ^{1}H-^{2}H exchange is expected since alkyls are not able to make hydrogen bonds. Concomitant small variations of the ν(S-H) mode in the region around 2550 cm^{-1} for ν(S-^{1}H) and 1850 cm^{-1} for ν(S-^{2}H) were also seen (not shown).

The diminution of the Amide II intensity in deuterated buffer reveals the presence of two peaks at 1574 and 1555 cm^{-1} that can now be attributed to the $\nu_{as}(COO^{-})$ modes of Asp and Glu, respectively. Surprisingly, the strong $\nu_{s}(COO^{-})$ mode seen at 1407 cm^{-1} in $^{1}H_2O$ buffer is not clearly present in $^{2}H_2O$. Instead, many more or less intense signals can be seen in the region from 1390 to 1420 cm^{-1}. This might be the result of certain modes being shifted, depending on the nature of the residue (Asp and Glu absorb in this area) and their solvent accessibility. No signals that could be identified as Lys vibration modes can be found in deuterated buffer, which is a probable consequence of the downshift of their $\delta_{s,as}(NH_3^{+})$ modes. In addition to the small molar extinction coefficients of these vibrations, this makes their observation not possible here.

The spectrum of CL presents the same ν(C=O) modes at 1734 and 1745 cm^{-1} as in ^1H_2O. These modes are absent in PE and minor in PG. It is possible that the remaining signals in PG are due to differences in the purification, i.e. some CL might have been retained. Alternatively, PG could partially bind to CL binding sites, but no evidence of this is seen in the spectrum in ^1H_2O. The absence of shift upon ^1H-^2H exchange could have two explanations : either these signals belong to carboxylic residues that are not affected by the exchange, or they originate from variations in the proximity of the bound CL ester carboxyls. Since the proposed variations of Asp or Glu involved in the proton pumping process are solvent accessible and should thus be much more affected by ^1H-^2H, it is more probable that the observed signals pertain to modifications in the vicinity of the CL esters.

As positively charged groups are thought to engage in the salt bond formation to the phospholipid headgroups, their signature was sought after in the present spectra. Small signals of Lys residues have already been identified in the ^1H_2O spectra, but since they are also involved in the proton pumping mechanism a distinction between these different signal origins can't be made. His residues exposed to solvent at pH 7 (at which the measures were made) are predominantly neutral, and besides their vibrational modes are hardly identifiable in proteins. This leaves Arg residues as potential candidates for salt-bridge formation with the phosphate. Arg modes are characterized by two strong signals at 1673 ($\nu_{as}(CN_3H_5^+)$) and 1633 cm^{-1} ($\nu_s(CN_3H_5^+)$) in ^1H_2O and respectively 1608 and 1586 cm^{-1} in ^2H_2O. The clear presence of these peaks in the double difference spectra in ^1H_2O and the apparition of shoulders in the ^2H_2O spectra show that Arg residues are effectively influenced by the presence of lipids, especially with the negatively charged CL and PG and moderately with the zwitterionic PE.

Hydrophobic interactions between the acyl chains and non-polar residues are observable in the spectral region from 1430 to 1480 cm^{-1}, but it is not possible to assign signals to specific residues. However, interactions with aromatic residues can be seen around 1500 cm^{-1} (ν(C=C) and δ(C-H)) and be more specifically assigned. The peaks at 1513, 1503 and 1493 cm^{-1} are present in all the spectra. The first can be attributed to the perturbations of TyrOH residues, the second arises from modifications in the behavior of $TyrO^-$ principally and Phe and the third comes from perturbations of Trp residues. Their

intensities vary : they are stronger in CL than in PG and PE. Since several tyrosines are known to be involved both in the electron transfer and the proton pumping mechanism, the two bands at 1513 and 1503 cm^{-1} mostly represent the perturbations of these functions. Tryptophanes on the other hand are not known to be involved in these mechanisms and their alteration upon lipid binding makes them good candidates for being part of lipid-binding sites[259]. In addition, a negative signal at 1334 cm^{-1} can also be attributed to variations in the ring modes of Trp residues.

3.3.3 Hydrogen-Deuterium Exchange kinetics in the presence of lipids

To estimate the part of the protein bound to lipids and their effect on solvent accessibility, ^{1}H-^{2}H exchange kinetic experiments were conducted on samples of delipidated Complex I with and without re-added lipids. As explained in chapters 1.6.3 and 2.3, the samples were dried on an ATR crystal, rehydrated and deuterated buffer was perfused to replace the $^{1}H_2O$ buffer. Since the positions within the Amide I mode shift only a few wavenumbers and the Amide II mode splits in two bands at completely different frequencies, the ratio of their integrals is representative of the protein backbone fraction that underwent ^{1}H-^{2}H exchange. By fitting a three term exponential to the curve of the integrals ratio against time, it is possible to estimate the fraction of fast, intermediate and slow exchange representative of the readily solvent accessible surface, the channels and interfacial domains, and the hydrophobic core of the protein, respectively. Due to the constant flow of buffer, non-specifically bound annular lipids are washed away and do not bias the results. The obtained curves are shown in Figure 3.3.7 and the results are summarized in Table 3.3.1.

The ^{1}H-^{2}H exchange was also carried out in presence of CL and *E. coli* lipid extract, but in both cases the enzyme did not remain attached to the surface of ATR crystal.

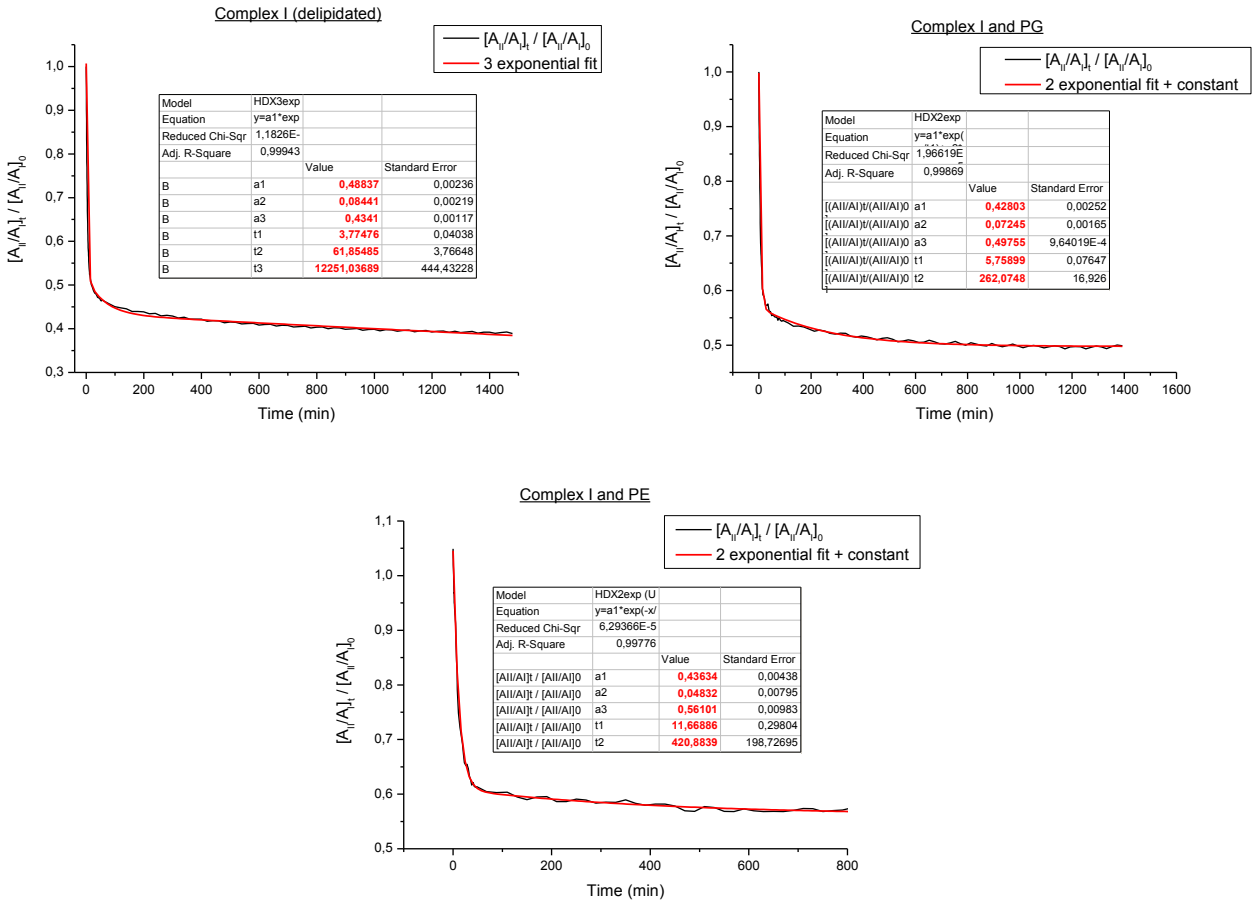

Figure 3.3.7 : ^{1}H-^{2}H exchange kinetic curves of delipidated Complex I alone and in the presence of PE and PG. The black lines correspond to the experimental curves and the red lines to the curves fitted as described in chapter 2.3.2. The calculated exchange parameters are shown in the tables on each graph and are summarized in Table 3.3.1.

	Complex I (delipidated)	Complex I + PE	Complex I + PG
a1 (fast - surface)	49 %	43 %	43 %
a2 (intermediate - channels and interfacial parts)	8 %	6 %	7 %
a3 (slow - hydrophobic core)	43 %	51 %	49%
T1 (min)	4	12	6
T2 (min)	62	420	262
T3 (min)	constant	constant	constant

Table 3.3.1 : ^{1}H-^{2}H exchange rates and times for delipidated Complex I alone and in the presence of PE and PG.

Both PE and PG presented here induce a 6 % diminution of the readily-solvent accessible surface concomitant with a 8 % (PE) to 6 % (PG) increase of the hydrophobic core. The intermediate part diminishes by 2 to 1 %, which is almost negligible. However, the time constant calculated for the intermediate part increases dramatically from around 1 to more than 4 hours. Since the time constants for the fast part do not vary significantly, this means that the major part of the intermediate section can be considered non solvent accessible. Hence, an increase of the hydrophobic core area in the presence of lipids of ca. 10 % is more realistic. The reason for the decrease of the intermediate part together with the augmentation of its time constant is that the lipid binding sites are often located at the interface of two or more subunits[171, 260], meaning that once the lipid is bound it shields the interior of the crevice from the solvent. Eventually, the solvent will still penetrate deeper in the hydrophobic core but it takes much longer. A small percentage of the intermediate area also represents the proton translocation pathways, whose accessibility should not be affected by the presence of lipids in the resting state. The decrease of the fast part reflects lipids bound directly on the solvent exposed surface. These variations are in good agreement with previous experiments done in our group on the non-lipid-depleted Complex I[242].

To estimate the number of bound lipids, the solvent exposed area of the entire enzyme and of individual lipids were calculated *via* PyMol. The solvent accessible surface of the whole protein (PDB ID : 4HEA) was hereby estimated to *ca.* 150 000 Å² and that of PE and PG to *ca.* 1500 Å² per phospholipid. As the area of the protein covered by one lipid is around half of its surface, an effective coverage of 750 Å² was used. A 10 % variation of the protein's hydrophobic core thus corresponds to a variation of 15 000 Å², which would mean that 20 ±10 lipids are bound to each enzyme. This value, while in agreement with the results from other groups on the mitochondrial enzyme[176, 177], has to be handled with caution since it is only a rough estimation : the margin of error was estimated to ±10 lipids. PG, which has a slightly more important solvent-accessible area and a slightly less intense effect on the hydrophobic core than PE, is probably present in a little less quantity, reflecting its lower distribution among the lipids composing the *E. coli* inner membrane : *ca.* 7:2 of PE:PG.

3.3.4 Conclusion

Lipids have an effect on every level of Complex I function : the electron transfer chain, the proton translocation mechanism and the conformational movements linking the two are perturbed. Lipids are therefore responsible for the regulation of the catalytic activity of Complex I. The three major components of the *E. coli* inner membrane share these common effects. CL induces the strongest perturbations, which points to the particular role that this lipid plays for Complex I and the respiratory chain in general[66, 261]. Regulation pathways linking the levels of CL synthesis to the strength of the proton gradient created by the respiratory enzymes have been uncovered in mitochondria[159]. When CL synthesis is impaired, for example in Barth Syndrom, the number of enzymes present is diminished[262]. Since Complex I is responsible for the generation of *ca.* 40 % of the proton gradient[78, 129], the regulation of the enzyme's proton pumping activity especially by CL is not surprising. Due to the chemical properties of its headgroup, CL also plays the role of a proton trap[263], restricting pumped protons within its headgroup domain and therefore limiting pH changes in the bulk phase. In addition, its bridging capacities between two adjacent protein domains are central for the lateral organization of the proteins in the membrane[264], resulting in the formation of respiratory complexes rafts and supercomplexes[265]. Studies on yeast lacking CL expression showed that while this phospholipid was not essential for cell-survival, its absence reduced the yeast's life-span[67, 266]. This might be attributed to a lack of regulation and organization of the respiratory chain, in turn leading to lower mitochondrial activity and higher production of reactive oxygen species (ROS).

CL not being vital signifies that to some extent, other phospholipids assume parts of its role. However, the optimal activity of Complex I is only reached when a combination of all three major phospholipids is present[267]. This is in line with our results and is illustrated in Figure 3.3.5 by the fact that the addition of *E. coli* lipid extract results in the same spectrum as for non-lipid-depleted Complex I whereas the sum of the spectra of each lipid added separately leads to a more altered spectrum.

To tentatively locate the lipid binding site on the surface of the membrane domain from Complex I, the localizations of the residues within this domain suggested to be

disturbed by the presence of lipids in chapter 3.3.2 are shown on Figure 3.3.8. Since the full structure of this domain is available only for the Complex I from *T. thermophilus*, we chose to represent it here. For comparison, the structure of the membrane domain from *E. coli* (lacking NuoH) is represented with the same residues highlighted in Appendix 8. Slight changes can be seen in the repartition of the labeled residues, but the observations made hereafter hold true for both enzymes. As both bacteria are gram-negative, the major phospholipids composing their inner membranes are similar.

A first observation that can be made about the repartition of the highlighted residues on the surface is that two rims are formed along the alleged positions of the lipids headgroups. The cytoplasmic (mitochondrial matrix) facing side presents most of the positively charged residues, which was already indicated by the calculated charge distribution map on Figure 1.4.3. The asymmetry reflects the natural lipid repartition dissymmetry between the two leaflets of the lipid bilayer[268], indicating that the anionic PG and CL are more abundant in the side facing the intermembrane space, which is consistent with the inside positive rule[269]. Secondly, Trp residues are mostly located within a few (ca. 5 to 15) Angströms of a charged residue. Trp is a prime candidate for interactions with the interfacial region of the lipid due to the almost apolar nature of its indole cycle combined with its capacity to form hydrogen bonds[259]. The distance between the charged residues and the Trp residues matches the spacing between the charged lipid headgroup and its ester group (interfacial region), thus creating a high affinity binding motif for phospholipids. Each motif identified on the surface of the membrane domain is shown on Figure 3.3.8 (dashed circles). These motives are just one of the possibilities for lipid binding. Other domains[166], not detected by this method, are most likely present on the surface of the membrane domain from Complex I. However, their composition is related to that of putative lipid binding sites (principally CL) in another respiratory chain complex, the Cytochrome *c* oxidase[170]. Further implications of this detail of utmost importance will be discussed together with the proton pumping mechanism in chapter 3.5.

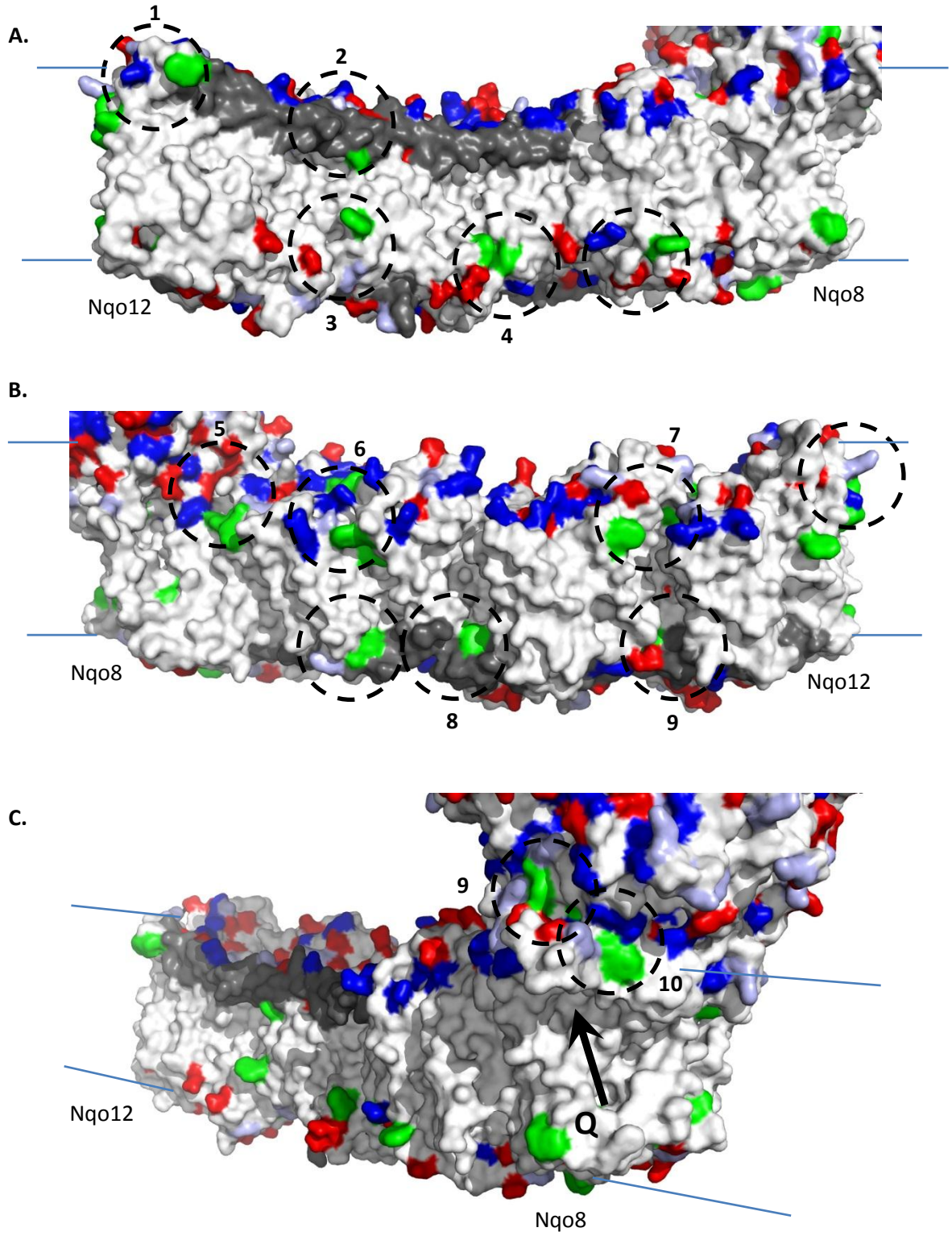

Figure 3.3.8 : Representations of the membrane domain of Complex I. PDB ID : 4HEA. The approximate position of the membrane is shown by the blue lines. Arg residues are colored in blue, Lys in lightblue, Asp and Glu in red and Trp in green. The elements transducing conformational changes across the membrane domain (helix HL and βH) are shown in dark grey.Putative lipid binding sites are indicated by dashed circles. **A.** and **B.** correspond to the side views rotated by 180°, **C.** shows an enlarged back view focusing on the quinone binding pocket indicated by an arrow.

From the 14 lipid binding sites identified by this method, 2 are located close to the α-HL helix (Figure 3.3.8 A. 1 and 2) and 2 more next to the βH elements (Figure 3.3.8 B. 7 and 8). As these elements transduce conformational changes across the membrane domain upon electron transfer, their interaction with bound lipids could explain how the latter influence the conformational movements associated with the proton translocation across the membrane. The residues interacting with the lipids thus move or react in a different fashion than when no lipids are present, explaining the additional signals seen in the FTIR double difference spectra from chapter 3.3.2. Among the binding motives, many are also located in crevices or at the interface between two subunits (Figure 3.3.8 A. and B. 2 to 9) ; thus lipids bound there may also contribute to the propagation of conformational changes along the membrane domain. CL has been shown to present a preference for these interstitial spaces[264], which explains why its presence or absence induces the strongest perturbations of the Complex I FTIR difference spectrum (Figure 3.3.4 and Figure 3.3.6).

Finally, Figure 3.3.8 C. shows the presence of at least one lipid-binding site in the proximity of the entry to the quinone reaction chamber recently revealed by the X-ray structure of the full Complex I[89]. The binding of specific lipids in this region might regulate the access of the quinone to the chamber, resulting in a further control of the oxidoreductase activity of the enzyme.

In order to confirm the suggestions made in this chapter, electrochemically induced FTIR difference spectroscopy of Complex I and lipids in the presence of quinone would help to clarify the role played by phospholipids. $^{1}H_2O$-$^{2}H_2O$ exchange experiments on the reduced enzyme (by addition of NADH) and with quinones in the presence of different lipids can also contribute to the extension of our knowledge about their interactions with the enzyme. Furthermore, the insertion of the protein into a lipid bilayer rather than the addition of isolated lipids can also provide valuable information about the function of Complex I in a biomimetic environment. In chapter 3.1, this insertion was probed *via* SEIRAS. Finally, a different approach proposed by Lensink *et al.*[270] using molecular dynamics simulations to locate specific lipid binding sites would be of interest.

3.4 Zn^{2+} inhibition of Complex I

3.4.1 Introduction

In chapter 1.5, the effects of Zn2+ on the respiratory chain in general and on the mitochondrial Complex I were described. The bacterial enzyme also showed to be inhibited by Zinc and displayed the same progressive inhibition during turnover as the mitochondrial enzyme (Marius Schulte, manuscript in preparation). In addition, the presence of at least three uncompetitive binding sites with different affinities was suggested. One low affinity site (K_i > 700 µM) was shown to alter NADH oxidation, and two higher affinity sites (K_i ≈ 50 to 80 µM) to affect Quinone reduction and proton translocation. The pH dependency of these higher affinity sites suggested that carboxylic acid residues are involved in Zn^{2+} binding at these sites. To gather more information about the interaction of Zn^{2+} ions and Complex I, electrochemically-induced FTIR difference spectroscopy was conducted here. Since Zn^{2+} is known to have a strong affinity to polyhistidine moieties, both the *nuoF* His-tagged Complex I and the wild type enzyme were prepared and probed. To be certain that the enzyme was inhibited, the samples were incubated with a hundred-fold excess of Zinc (in the form of $ZnSO_4$) for three hour prior to the experiments. Differential FTIR spectroscopy is a potent method for the detection of specific interactions of certain amino acids with metals, the most common Zn^{2+} binding residues being His, Cys, Asp/Glu and Tyr, followed by Arg, Lys, Met and Gln/Asn[271].

3.4.2 FTIR Difference spectroscopy of Complex I in the presence and absence of Zn^{2+}

Figure 3.4.1 shows the oxidized *minus* reduced FTIR difference spectra of wild type Complex I with and without Zinc in the spectral region from 1800 to 1000 cm^{-1}. The attributions of each signal were already discussed in the previous chapter and are summarized in Appendix 5. The difference spectra of $nuoF_{HIS}$ Complex I with and without Zinc are almost identical to those of the wild type and are thus not shown here. Slight variations between the two preparations might arise from the differences of the lipid

content still present in the samples, which is higher in the *nuoF*$_{HIS}$ Complex I, as there are less purification steps.

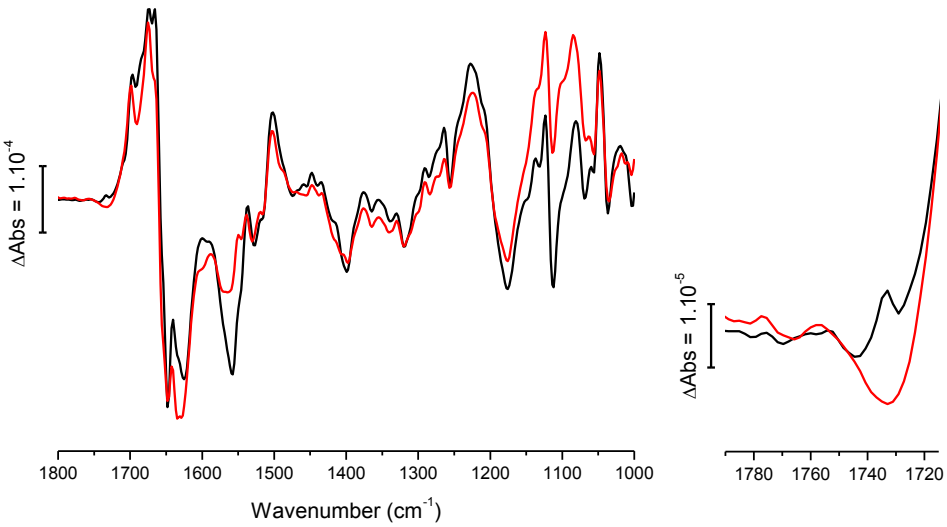

Figure 3.4.1 : Oxidized *minus* reduced FTIR difference spectra of Complex I with (red line) and without Zn^{2+} (black line). Left : spectral region from 1800 to 1000 cm^{-1} ; Right : Extended view of the spectral region from 1770 to 1715 cm^{-1}. The two spectra were recorded on samples from the same preparation.

The presence of Zinc induces small changes in the difference spectrum of Complex I, the most striking shift being the decrease of the signals in the Amide II region (1580 to 1520 cm^{-1}). Modifications in the signatures of protonable residues (Asp and Glu) are also seen. To highlight the Zinc induced changes the double difference spectrum of Complex I *minus* Complex I and Zn^{2+} was calculated *via* interactive subtraction and is shown both for *nuoF*$_{HIS}$ and wild type Complex I (Figure 3.4.2 A)). The experiments on *nuoF*$_{HIS}$ Complex I were also carried out in $^{2}H_2O$, and the result is shown on Figure 3.4.2 B).

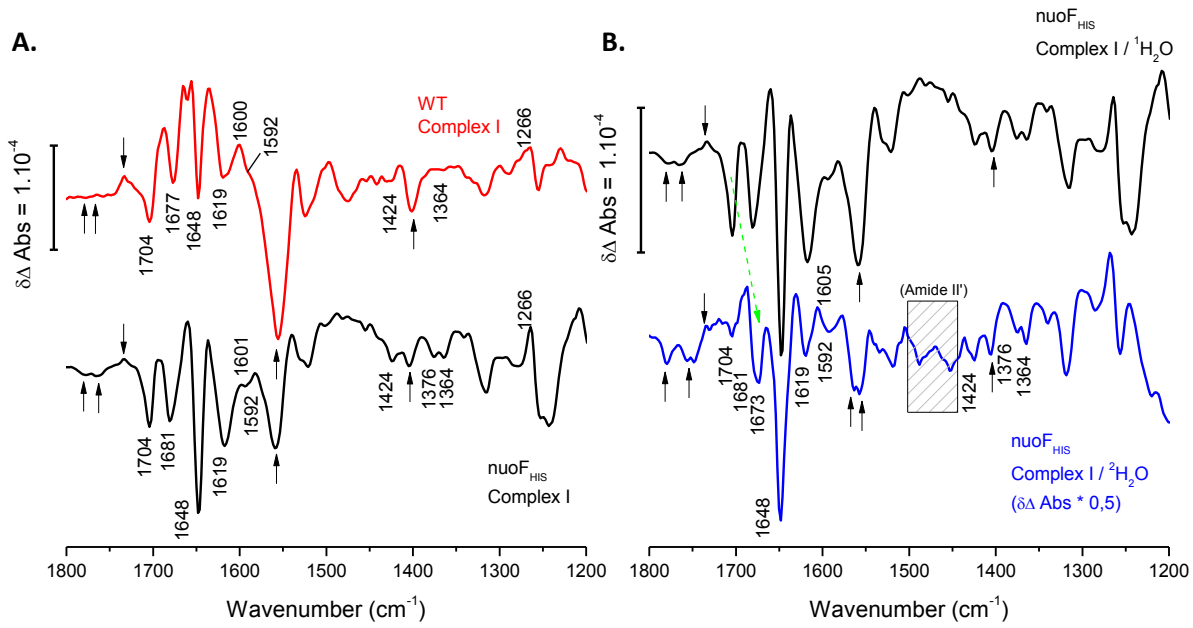

Figure 3.4.2 : Double-difference spectra of Complex I *minus* Complex I with Zn^{2+} in the spectral region from 1800 to 1200 cm^{-1}.A. : Wild type Complex I (red line) ; *nuoF*$_{HIS}$ Complex I (black line). **B.** : *nuoF*$_{HIS}$ Complex I in $^{1}H_2O$ (black line - same as in A.); *nuoF*$_{HIS}$ Complex I in $^{2}H_2O$ (blue line). The arrows on both panels indicate signals attributed to acidic residues affected by the presence of Zinc. The original single difference spectra from which the double difference spectra were calculated are an average of the spectra shown in Figure 3.4.3 and Figure 3.4.5.

The double difference spectra include changes in the Amide I and Amide II modes in the region from 1700 to 1500 cm^{-1}, by changes in the vibrational modes of the side chains and quinones from 1500 to 1200 cm^{-1} and by contributions from the buffer below 1200 cm^{-1} (not shown). As judged by the peaks in the Amide I region all types of substructures seem to be perturbed. The negative peaks could correspond to alterations of randomly organized residues (1648 cm^{-1}) and of beta type structures (hairpins, 1681 cm^{-1}). The positive signals would in turn reflect the perturbation of α-helixes (1656 and 1665 cm^{-1}) and β-sheets (1636 and 1686 cm^{-1}). However, only very small shifts are observed in the $^{2}H_2O$ spectrum, which is inconsistent with attributions to the protein backbone. Hence, it is uncertain if these signals are linked to conformational changes at all, as will be discussed on page 147. The same observation holds for the Amide II and Amide II' bands, which potentially contribute to the

signals at 1556(-) (WT) / 1559(-) cm^{-1} (*nuoF*$_{HIS}$) and 1488(-) / 1453(-) cm^{-1}, respectively. The attributions discussed hereafter are summarized in Table 3.4.1.

Position (cm^{-1})			Tentative Attribution
WT	*nuoF*$_{HIS}$ ^1H_2O	*nuoF*$_{HIS}$ ^2H_2O	
1781(-)	1781(-)	1779(-)	$\nu(C=O)_{COOH}$, no H-bond, $H^+(H_2O)_n$
1756(-)	1756(-)	1754(-)	$\nu(C=O)_{COOH}$, single H-bond, $H^+(H_2O)_n$
1734(+)	1734(+)	1733(+)	$\nu(C=O)_{protonated\ Asp,\ Glu}$ proton pump
1704(-)	1704(-)	1704(-)	$\nu(C=O)_{Asn,\ Gln}$ in hydrophobic environment
1694/1686(+)	1694/1690(+)	1694/1686(+)	$\nu(C=O)_{Asn,\ Gln}$, Amide I β-sheets
1677(-)	1681(-)	1681(-)	$\nu(C=O)_{Asn,\ Gln}$, ν(C=O) SQ, *$\nu_{as}(CN_3H_5^+)_{Arg}$, Amide I β-turns*
		1673(-)	$\nu(C=O)_{Asn,\ Gln}$
1665/1666(+)	1659(+)	1665(+)	$\nu_{as}(CN_3H_5^+)_{Arg}$, *Amide I α-helices*
1648(-)	1648(-)	1648(-)	$\nu(C=O)_{Asn,\ Gln}$ bound to Zn^{2+}, ν(C=O) Q or SQ, *Amide I random*
1635(+)	1636(+)	1631(+)	$\nu_s(CN_3H_5^+)_{Arg}$, $\delta(NH_3^+)_{Lys}$, *Amide I β-sheets*
1619(-)	1619(-)	1619(-)	$\delta(NH_2)_{Asn,\ Gln}$, ν(C=C) Q or SQ
1600(+)	1601(+)	1605(+)	$\nu(C\text{-}N \text{ and } C\text{-}C)_{HisH+}$
1592(-)	1592(-)	1592(-)	$\nu_{as}(COO^-)_{Asp,\ Glu}$ bound to Zn^{2+}, monodentate
1555(-)	1558(-)	1563/1557(-)	$\nu_{as}(COO^-)_{Asp,\ Glu}$, *Amide II*
1523(-)	1521(-)	1519(-)	$\nu(C=C)_{TyrOH}$
1505(-)	1505(-)	1505(-)	$\nu(C=C)_{TyrO-}$ Zinc chelated
1424(-)	1424(-)	1424(-)	$\nu_s(COO^-)_{Asp,\ Glu}$ bound to Zn^{2+}, monodentate
1401(-)	1405(-)	1405(-)	$\nu_{as}(COO^-)_{Asp,\ Glu}$
1376(-)	1376(-)	1376(-)	$\nu_s(COO^-)_{Asp,\ Glu}$ bound to Zn^{2+}, monodentate
1364(-)	1364(-)	1364(-)	$\nu_s(COO^-)_{Asp,\ Glu}$ bound to Zn^{2+}, bidentate
1266(+)	1266(+)	1268(+)	$\delta(C\text{-}OCH_3)_{UQ}$, $\nu(S=O)_{MES}$

Table 3.4.1 : Tentative assignments for the peaks from Figure 3.4.2. Alternative, less probable attributions are given in italic.

Signals pertaining to quinones are expected in both spectra : the shoulder at 1613 cm^{-1} might represent the ν(C=C) mode of neutral oxidized ubiquinones, as well as the signal at 1266 cm-1 corresponding to the $\delta(C\text{-}OCH_3)$ mode of the methoxy side chain. The MES buffer used for these experiments unfortunately also has a signal at this position (see Appendix 9), thus it can't be unambiguously attributed to the quinone. The ν(C=O) mode of ubiquinone is located around 1650 cm^{-1} and could be responsible for the sharp negative signal at 1648 cm^{-1}. As will be discussed in chapter 3.5, Zn^{2+} inhibition might result in the stabilization of an anionic semiquinone (SQ) which could be at the origin of this peak, together with the peak at 1681 cm^{-1} reflecting an upshifted signal of the quinone's second carbonyl group[48,

[272]. The ν(C=C) mode of such a SQ could result in another negative peak at 1619 cm^{-1}. The invariance of these signals upon ^{1}H-^{2}H further point towards their attribution to quinones. Additional modes corresponding to the ring reorganization upon reduction are expected between 1380 and 1480 cm^{-1} [248], but here they overlap with signals from the side chains. As the measures for the wild type and for the *nuoF*$_{His}$ Complex I were made in the same conditions and on samples from the same batch respectively, the difference in the intensity of the peaks tentatively attributed to quinones could reflect the variation of the quinone content of the samples. More quinones are retained during the purification of *nuoF*$_{His}$ Complex I, which requires less column chromatography steps, probably explaining why the signals are more intense for these samples than for the untagged WT. Alternatively, the variation of these signals could also be due to a stronger inhibition by Zn^{2+}.

As suggested in the introduction to this chapter, the proton translocation machinery appears to be especially perturbed by the presence of Zinc. This is reflected by the alteration of the vibrational modes from the acidic residues Asp and Glu. In Figure 3.4.2, the ν(C=O), $\nu_{as}(COO^-)$ and $\nu_{s}(COO^-)$ modes of protonated and deprotonated Asp and Glu residues are indicated by arrows. A quite uncommon feature in proteins is the presence of signals above 1730 cm^{-1}, seen here at 1756 and 1781 cm^{-1} in $^{1}H_2O$. These peaks can be associated to the ν(C=O) modes of protonated acidic residues in increasingly hydrophobic environments : weaker hydrogen bonds to the Oxygen atoms of the carboxylic group result in higher frequencies of the C=O vibration. The presence of two peaks are representative of two populations of protonated acidic residues : without hydrogen bonds and with a single hydrogen bond. In other terms, protonated acidic residues where the hydrogen is not shared with any other residue exist in the Zinc inhibited Complex I. While single hydrogen bonded acidic residues (i.e., the band around 1760 cm^{-1}) have been reported previously in other proton translocating enzymes such as Bacteriorhodopsin[273] and Cytochrome *bd*[206], the presence of non- or almost non-bounded protonated acidic residues resulting in the signal at 1781 cm^{-1} constitutes a novelty in proteins. Both Acetic and Propanoic acid in vapor phase show peaks above 1780 cm^{-1} representative of this particular mode[274], meaning that the slightly downshifted peak observed in the Zinc inhibited Complex I at 1781 cm^{-1} is probably not totally un-bounded. Upon ^{1}H-^{2}H exchange (Figure 3.4.2 B.), these peaks present a 2 cm^{-1}

downshift of the peak center and a very light broadening of both bands. The signal seen at 1733 cm^{-1} previously attributed to the protonation of one or more aspartic or glutamic acid residues[192] in the non-inhibited Complex I disappears. Variations in the signatures of deprotonated species, that is the $\nu_{as}(COO^-)$ and $\nu_s(COO^-)$ modes of Asp and Glu, can also be seen and are discussed in further details on page 143.

When comparing the spectra of WT and of *nuoF*$_{HIS}$ Complex I on Figure 3.4.2 A), both peaks at 1781 and 1756 cm^{-1} are less intense in the wild type. Nonetheless, they are present as seen in the single difference spectrum on Figure 3.4.1 (right panel). The reason for this variation in intensity with respect to the Zn-inhibited *nuoF*$_{HIS}$ Complex I might be found in the differences of the samples' lipid content. In chapter 3.1, the presence of lipids (in particular Cardiolipin) was shown to promote proton pumping, as judged by the signal at 1733 cm^{-1}. In the more purified, less lipid rich wild type Complex I, the proton pumping activity is limited and the signals are thus diminished. Also, as the presence of lipids increases the volume of the non-solvent accessible hydrophobic core of the protein (^1H_2O-^2H_2O exchange experiments from chapter 3.3.3), the additional sealing they provide might prevent reprotonation of residues in the vicinity of those producing the signals at 1781 and 1756 cm^{-1}. Even between samples prepared by the same method (but not from the same batch), differences in the intensity of these signals are seen, as for the *nuoF*$_{His}$ double difference spectra in ^1H_2O and ^2H_2O in Figure 3.4.2 B).

It is generally accepted that under certain conditions Complex I can function in reverse regime to transfer electrons to NAD^+[140] but little is known about the reversibility of the proton pumping. While the reversibility of the mechanism leading to proton translocation is one of the requisites in the coupling models allowing reverse electron transfer, this does not necessary imply that protons are indeed translocated in the opposite direction. In other proton pumps, a gating mechanism is often present to prevent backslipping of protons to the bulk[275] or backleak to the reaction center[276]. It is probable that such a mechanism is also present in Complex I. In the proton transferring Bacteriorhodopsin, a signal at 1704 cm^{-1} was attributed to a weakly H-bonded Asn residue located in the proton channel[277]. Interestingly, a strong negative peak appears at the same frequency in the double difference

spectra of the Zinc inhibited Complex I. This peak can thus be tentatively associated to the perturbation of the ν(C=O) mode from gating Asn (or Gln) residues upon Zn^{2+} binding. The ν(C=O) mode of carboxamides shows strong sensitivity towards deuteration due to coupling with the $\delta(NH_2)$ vibration[201], explaining the *ca.* 30 cm^{-1} downshift of the major part from the 1704 cm^{-1} signal in ^2H_2O to 1673 cm^{-1} (green dashed arrow in Figure 3.4.2). The ν(C=O) mode of Asn and Gln residues is also sensitive to H-bonding not coupled to the $\delta(NH_2)$ vibration[278], thus another intense negative signal at 1681 cm^{-1} was attributed to stronger H-bonded Asn or Gln residues. The apparent absence of shift of this vibration upon ^1H-^2H exchange might indicate that these residues are not accessible to the solvent during turnover. These attributions are further confirmed by a negative peak at 1619 cm^{-1} representative of the $\delta(NH_2)$ mode from carboxamide side chains. Upon deuteration, this signal is *ca.* two-fold diminished which might confirm the hypothesis of two Asn/Gln populations, with one being solvent inaccessible, or it might represented a mixed signal to which the Quinone might contribute. The other, deuterated part of the $\delta(NH_2)$ mode can shift several hundreds of cm^{-1} down and can thus not precisely be localized here. Last but not least, the strongest negative band in the double difference spectra is located at 1648 cm^{-1} and can be attributed to the ν(C=O) mode of Zinc chelated Asn or Gln residues, which is supported by the fact that its intensity corresponds approximately to the sum of the signals at 1704 and 1681 cm^{-1}, as judged by the integral of each (not shown). The respective redshift of these peaks, i.e. 56 and 23 cm^{-1}, is in the expected range for chelation by an electrophile. The absence of shift upon ^1H-^2H exchange, as expected for an Asn/Gln - Zinc complex, further confirms this tentative attribution in addition to an eventual SQ species, rather than changes in the amide I mode of randomly organized residues that could also be located at this wavenumber. In the case of the bacterial photosynthetic reaction center, which also transfers protons, a direct interaction of Zn2+ with Gln was also suggested[279], pointing to the general role of side chain amides in proton translocation.

Generally, Zn^{2+} is chelated by three to four protein side chains in a pyramidal shape[271]. To achieve high affinity binding sites, it is unlikely that the rarely Zinc-binding Asn or Gln residues[279] constitute the sole ligands, therefore we looked for perturbed signals from other amino acids. The only other side chains clearly bound to Zinc belong to deprotonated

Asp or Glu residues : monodentate chelation of divalent metals creates two non-equivalent C-O bonds, splitting both the $\nu_{as}(COO^-)$ and $\nu_s(COO^-)$ modes into two bands, one at higher and the other at lower wavenumbers[280]. For the $\nu_s(COO^-)$ vibration, the signal at 1405 cm^{-1} is diminished together with the apparition of two bands at 1424 (free C-O) and 1376 cm^{-1} (Zn^{2+} bound C-O), both not affected by ^1H-^2H exchange. The presence of another signal at 1364 cm^{-1} might also be indicative of bidentate binding. For the $\nu_{as}(COO^-)$ mode around 1560 cm^{-1}, the attribution is less evident due to overlap with the amide II absorption from the protein backbone and modes from other side chains. Nevertheless, the peak at 1592 cm^{-1} was tentatively attributed to the ν_{as}(free C-O) mode of Zinc chelated Asp or Glu residues. Its redshifted counterpart can be attributed to the peak at 1520 cm^{-1}, but it could also belong to strong IR absorptive Tyr residues. One peak that might belong to the most common Zinc chelator, Histidine, is observed here (at 1601 / 1605 cm^{-1}). However, the lack of a peak at 1115 cm^{-1} (not shown) indicating an His-Zinc complex[281] argues against direct binding to His. While this does not eliminate binding to functionally unimportant residues, it seems that no Histidines are involved in the inhibition of the proton pumping mechanism by Zinc. Cys, Tyr, Arg and Lys residues are also common Zn^{2+} chelators in their deprotonated state, but when their high pKa is not controlled, as to be expected for surface exposed residues where Zinc supposedly binds, it is unlikely that they are able to chelate the metal. Some signals where nonetheless attributed to Tyr residues in Table 3.4.1, principally for the peak at 1505 cm^{-1}, which could represent the ν(C=C) mode of Zinc coordinated Tyr. From the multiple signals in the range from 1620 to 1690 cm^{-1}, chelation to Arg disturbing the $\nu_{as}(CN_3H_5^+)$ and $\nu_s(CN_3H_5^+)$ modes can also not be ruled out and would provide further explanation to the peak pattern in this area.

Zinc can inhibit the proton pumping in various ways : by directly blocking the proton intake or their output at the entry or exit of a channel, by affecting the quinone reduction or by hindering the conformational movements linking the two. If four proton translocation pathways exist in Complex I[89], which would be concordant with the recently re-reported proton pumped per electron transferred stoichiometry of two (4 H^+ / 2 e^-)[124], this leaves eight direct binding site options in addition to potential indirect ones. As discussed above, Zinc seems to bind to a gating mechanism involving Asn/Gln and Asp-Glu residues. This

mechanism could be present either at the proton intake, to avoid backflow of captured protons into the bulk, or their output, to avoid protonation by the bulk, or both. To discriminate between these possibilities, a dynamic approach was used.

Each spectrum shown in Figure 3.4.1 is an average of 40 to 80 oxidized *minus* reduced spectra recorded over several hours. The resulting spectra, albeit of high signal to noise ratio, only represent an average state of the studied system. As such averaged spectra were used to calculate the double differentials in Figure 3.4.2, important dynamic features of the Zinc inhibition might have been lost in the data processing. To access this type of information, the oxidized *minus* reduced spectra of Zn^{2+} inhibited Complex I were averaged by smaller groups of 5 or 10, 5 being the lower limit to still have an acceptable quality (S/N ratio). The result is shown on Figure 3.4.3.

The temporal evolution of the Zinc inhibited red-ox spectra clearly shows that certain signals are modified as the number of turnovers increase. The variation trend and tentative attributions for each signal are summarized in Table 3.4.2. To make sure that this was not due to another effect, the same data treatment was done on groups of ox-red spectra of the non-inhibited enzyme (Figure 3.4.5), which only shows global synchronous fluctuations of all signals corresponding to small variations in the amount of active sample and the progressive loss of the MCT detector's sensitivity, especially towards the end of the experiment.

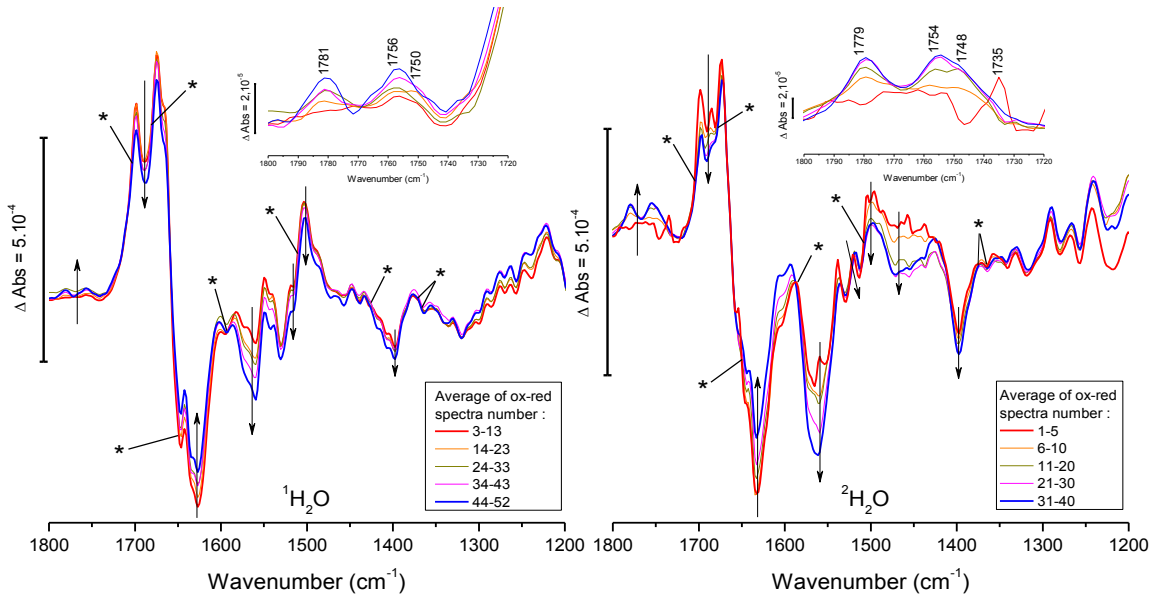

Figure 3.4.3 : Evolution of the oxidized *minus* reduced FTIR spectra of Zn^{2+} inhibited Complex I in function of the number of redox cycles. Spectral region from 1800 to 1200 cm^{-1}. Left panel : in ^1H_2O buffer ; Right panel : in ^2H_2O buffer. Isobestic points tentatively assigned to residues interacting directly with Zinc are marked by stars. The insets show an enlarged view of the spectral region from 1800 to 1720 cm^{-1}.

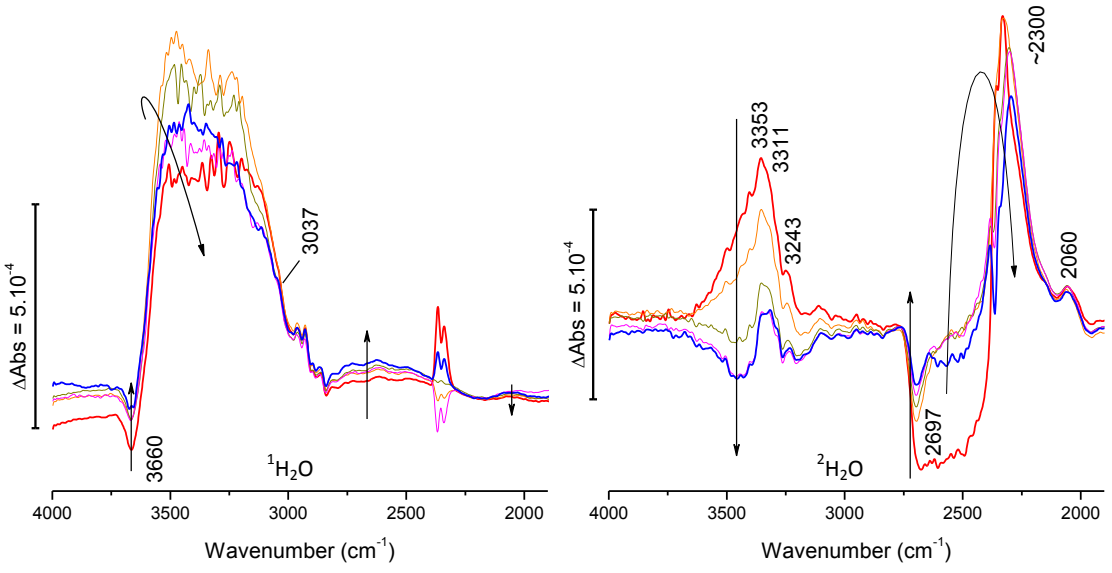

Figure 3.4.4 : Evolution of the oxidized *minus* reduced spectra of Zn^{2+} inhibited Complex I over time. Spectral region from 4000 to 1900 cm^{-1}. Left panel : ^1H_2O ; Right panel : ^2H_2O. The spectra are the same as in Figure 3.4.3, except that a 4 point FFT smoothing was applied.

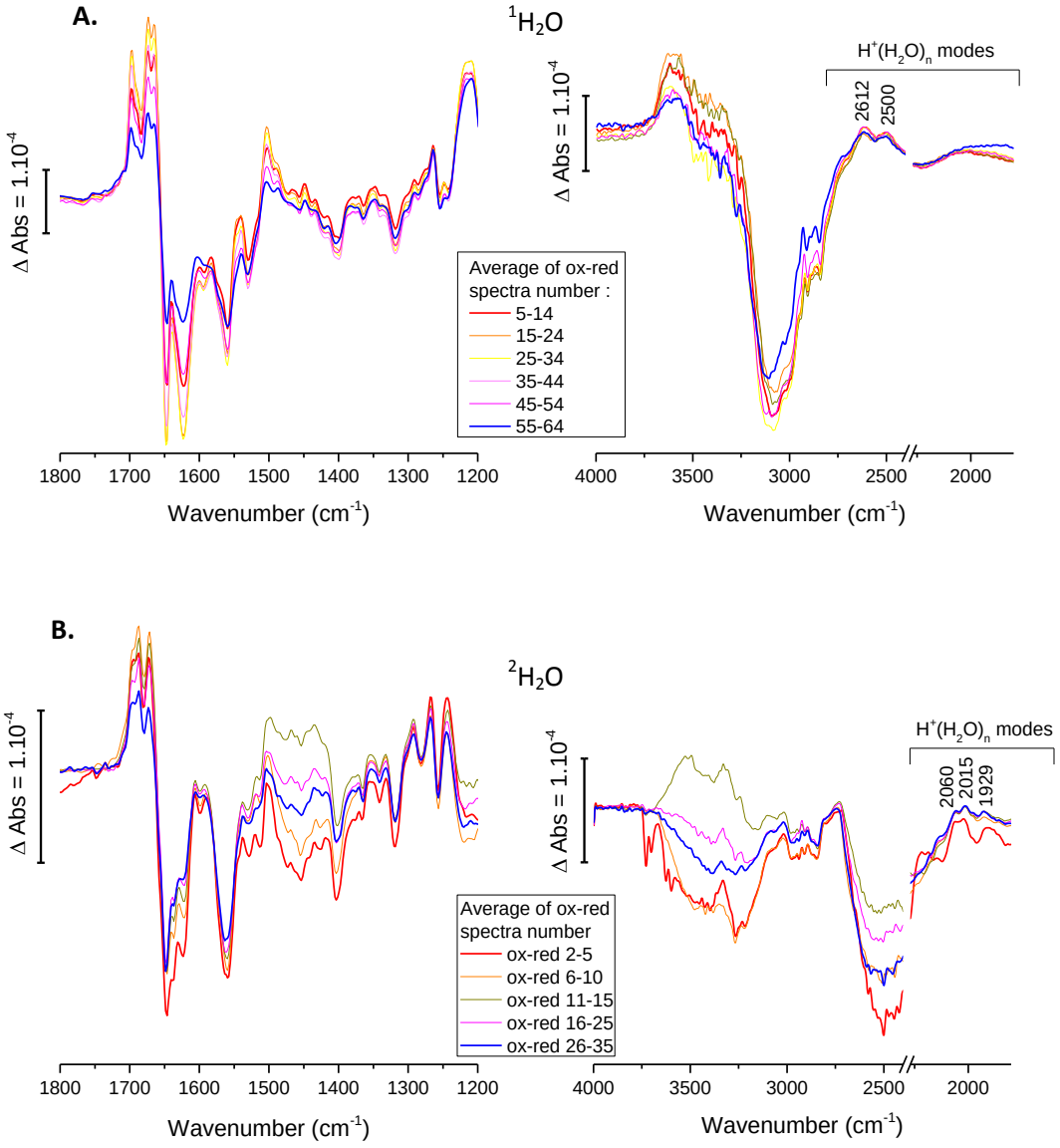

Figure 3.4.5 : Evolution of the oxidized *minus* reduced FTIR spectra of uninhibited Complex I in function of the number of redox cycles. A. : in ^1H_2O buffer ; **B.** : in ^2H_2O buffer. In **B.**, the $H^+(H_2O)_n$ modes can correspond to modes of mixed ^1H and/or ^2H cations.

Position (cm^{-1}) and variation			Tentative Attribution
$nuoF_{HIS}$ ^1H_2O	$nuoF_{HIS}$ ^2H_2O		
1781(+)	1779(+)	↗	$\nu(C=O)_{COOH}$, no H-bond, $H^+(H_2O)_n$
1756(+)	1754(+)	↗	$\nu(C=O)_{COOH}$, single H-bond, $H^+(H_2O)_n$
1750(+)	1748(+)	↗	$\nu(C=O)_{COOH}$
1734(+)	1733(+)	↘	$\nu(C=O)_{protonated\ Asp,\ Glu}$ proton pump
1704	1704	*	$\nu(C=O)_{Asn,\ Gln}$ hydrophobic environment
1698(+)	1698(+)	↘	$\nu(C=O)_{Asn,\ Gln}$, $\nu_{as}(CN_3H_5^+)_{Arg}$, *Amide I β-sheets*
1681	1681	*	$\nu(C=O)_{Asn,\ Gln}$, $\nu(C=O)$ SQ, $\nu_{as}(CN_3H_5^+)_{Arg}$, *Amide I β-turns*
1673(+)	1673(+)	↘	$\nu_{as}(CN_3H_5^+)_{Arg}$
1665(+)(sh)		↘	$\nu_{as}(CN_3H_5^+)_{Arg}$, Amide I α-helices
1648	1648	*	$\nu(C=O)_{Asn,\ Gln}$ bound to Zn^{2+}, $\nu(C=O)$ Q or SQ, *Amide I random*
1640 (broad)	1640 (broad)	↘	$\delta(H_2O)$
1632(-)	1632(-)	↘	$\nu_s(CN_3H_5^+)_{Arg}$, $\delta(NH_3^+)_{Lys}$, *Amide I β-sheets*
1626		↘	$\delta(NH_3^+)_{Lys}$, *Amide I β-sheets*
1619	1619	*	$\delta(NH_2)_{Asn,\ Gln}$
1601	1605	↘	$\nu(C\text{-}N$ and $C\text{-}C)_{HisH+}$
1592	1592	*	$\nu_{as}(COO^-)_{Asp,\ Glu}$ bound to Zn^{2+}, monodentate
1570/1559(-)	1570/1559(-)	↗	**$\nu_{as}(COO^-)_{Asp,\ Glu}$**, *Amide II*
1521(-)	1515(-)	↗	$\nu(C=C)_{TyrOH}$
1505	1505	*	$\nu(C=C)_{TyrO-}$ bound to Zn^{2+}
1501(+)	1501(+)	↘	$\nu(C=C)_{TyrO-}$
1460 (broad)	1460 (broad)	↗	$\delta(^1H\text{-}O\text{-}^2H)$
1424	1424	*	$\nu_s(COO^-)_{Asp,\ Glu}$ bound to Zn^{2+}, monodentate
1397(-)	1397(-)	↗	$\nu_{as}(COO^-)_{Asp,\ Glu}$
1376	1376	*	$\nu_s(COO^-)_{Asp,\ Glu}$ bound to Zn^{2+}, monodentate
1364	1364	*	$\nu_s(COO^-)_{Asp,\ Glu}$ bound to Zn^{2+}, bidentate
1230 (broad)	1230 (broad)	↗	$\delta(^2H_2O)$

Table 3.4.2 : Tentative attributions and direction of variation for the peaks from Figure 3.4.3. ↗ indicates an increase, ↘ a decrease and * an invariance.

A first observation concerns the directly Zn^{2+} bound residues identified previously in Figure 3.4.2 : at the corresponding wavenumbers isobestic points are observed for the majority of the signals in Figure 3.4.3. This means that once bound, the Zn^{2+} ions do not dissociate and no additional Zn^{2+} ions bind to these residues. This is consistent with the irreversible nature of the Zinc inhibition and further confirms our attributions. With this in mind, we can assume that the signals arising over time are not linked to further modifications of the conformational changes of Complex I. As the general shapes of the Amide I and Amide II bands are very close to the one from the uninhibited enzyme, this leads to the conclusion that enzyme still transfers electrons in its regular way, which is also

supported by the good reversibility of the ox-red and red-ox spectra shown in Appendix 10. In other words, the electrochemically induced oxidation state changes lead to the same conformational changes as for the uninhibited Complex I, in turn leading to proton translocation. With the small but utmost important difference that no more protons are actually transferred. From the increase of signals of deprotonated acidic residues as well as the diminution of peaks from protonated His, Lys and Arg residues (see Table 3.4.2), a gradual emptying of the proton channels can be deduced, pointing to an obstruction of the proton intake by Zinc. However, this does not directly explain the rise of the vibrational modes from protonated acidic and phenolic residues in hydrophobic environments, it is therefore also possible that some of the proton channels are blocked at the output level. A third possibility is that instead of disrupting the proton intake itself, the Zinc inhibition rather disables the proposed gating mechanism, enabling backflow of protons from the bowels of the membrane domain to the bulk, up to completely reversed proton pumping.

Another indicator of the progressive emptying of the proton channels is the diminishment of ν(O-H) modes presented in Figure 3.4.4. This is especially clear in the $^{2}H_2O$ spectra, where the broad band centered around 3400 cm^{-1} gradually disappears, leaving only the non-exchanged Amide A (ν(N-H), 3353, 3311 and 3243 cm^{-1}) vibration in this area. Concomitantly, after an initial increase, the intensity of the ν(O-^{2}H) mode centered around 2300 cm^{-1} is also lowered. This frequency of this mode is relatively low compared to a bulk solution of $^{2}H_2O$, indicating that the molecules are strongly bound at the interior of the enzyme and showing that at least in the beginning of the inhibition some $^{2}H^{+}$ are able to access to access the enzyme's proton channels. In $^{1}H_2O$, after a first increase the ν(O-^{1}H) mode also diminishes with time. These O-H vibrations can be attributed to alcohols (including phenols), to protonated carboxylic acids or to structural waters, which have been proposed to be present in the proton translocation channels of Complex I[92] and are known to participate in proton transfer from other enzymes[126]. Compared to the spectra of the uninhibited Complex I in Figure 3.4.5, the polarity of these peaks is inverted. The origin of this inversion is unclear. The peaks at 3660 ($^{1}H_2O$) and 2697 ($^{2}H_2O$) cm^{-1} represent free OH groups, which have been attributed to "dangling" (i.e. non-hydrogen bound) hydroxyl groups of water molecules in proton channels[282, 283]. Their decrease over time indicates that less

and less protons are transferred. This is also supported by the variations of the broad signals between 1900 and 2700 cm^{-1}, which reflect the formation or dissociation of $H^+(H_2O)_n$ molecules, i.e. the transfer of protons along internal water clusters through a Grotthuss mechanism[125]. In the uninhibited Complex I (Figure 3.4.5), the peaks at 2612 and 2500 cm^{-1} in ^1H_2O and 2060, 2015 and 1929 cm^{-1} in ^2H_2O were tentatively attributed to $H^+(H_2O)_4$ *Eigen* cations[284] present in the oxidized state. Except for the peak at 2060 cm^{-1}, these peaks are strongly diminished in the Zn^{2+} inhibited enzyme, indicating that these water clusters lost their protons and do not receive any new. As Carbon-^{2}H modes are found at 2060 cm^{-1} [285, 286], a small possibility that this peak indeed represents such a vibration exists, although the mechanism by which such bonds would be created is unknown. The slight increase of the absorption below 2500 in ^1H_2O probably reflects the presence of some trapped protons which form $H^+(H_2O)_3$ *Zundel* cations[287]. $H^+(H_2O)_2$ *Zundel* cations could also contribute to the peaks at 1779 and 1756 cm^{-1}[288, 289], but the width of these peaks is too narrow to represent solely $(H_5O_2)^+$ ions. In ^2H_2O, The variations in the behavior of internal waters are also seen in Figure 3.4.3, where the weakening of the water's bending mode is partially responsible for the diminution of the signals around 1640 cm^{-1} (^{1}H-O-^{1}H bending) and 1460 / 1220 cm^{-1} (^{1}H-O-^{2}H and ^{2}H-O-^{2}H bending, respectively). In the non-inhibited Complex I, the signals described here are either not present or invariant, illustrating the normal functioning of the enzyme (see Figure 3.4.5).

For most of the variable peaks in Figure 3.4.3 and Figure 3.4.4, the maxima or minima are reached after 20 to 30 redox cycles, giving a clue about the length of the proton channels. As this number is too high to represent proton translocation along a single transmembrane helix, a mechanism as proposed by the Sazanov group[89] where parts of the translocation occur along the hydrophilic chain running through the middle of the membrane arm is plausible. This will also be evidenced in the mechanism presented in the next part.

3.4.3 Conclusion

Zinc inhibition of Complex I results in numerous changes of its FTIR difference spectrum. From the results shown here, direct Zn^{2+} binding to acidic residues and to Gln/Asn residues was proposed. The inhibition of the enzyme produces complex changes in its proton translocation machinery, as judged by the modifications in the signals of deeply buried acidic residues and probably other charged residues as well. These changes seem to result from the progressive emptying of the proton channels, driven by the conformational changes that accompany the electron transfer within the enzyme. Taken together, the findings from this chapter point towards Zinc inhibition at the entry of the proton channels. However, a direct effect on the Quinone reduction site which would echo in the absence of proton pumping is not excluded. Indirect inhibition by alteration of the conformational movements can be ruled out. Spectroscopic evidence for internal proton transfer through water cluster chain reorganization was also shown for the first time in Complex I. To clarify the behavior of these internal protons and waters, future work will include experiments in $H_2{}^{18}O$ and turnover by turnover analysis of the FTIR difference spectra. This will require the acquisition of more scans for each step to achieve a better S/N ratio. Time-resolved IR spectroscopy adapted to the time-scale of the proton translocation events (ca. 10 µs to 1 ms) could also be applied to Complex I to solve mechanistic details.

3.5 Proton pumping and coupling with UQ reduction - A model for the function of Complex I

In this chapter, the coupling mechanism between Quinone reduction and proton translocation will be discussed on the basis of the results gathered through FTIR spectroscopy and the recently revealed X-ray structure of the entire Complex I[89]. A model at molecular level will be proposed.

3.5.1 Structural analysis of the coupling elements

With the Zinc binding residues identified in the previous chapter and the presumption that the inhibition sites are located at the proton intake level, we proceeded to the localization of the putative binding sites with the help of sequence alignments from 30 species (already available in refs[89, 92]) and the X-ray structures of the entire Complex I from *T. thermophilus* (PDB ID 4HEA) and the membrane arm from *E. coli* (PDB ID : 3RKO - lacking NuoH). In the aligned sequences from all core subunits of the membrane domain, conserved surface exposed Gln, Asn, Asp and/or Glu residues close enough from each other (< 7 Å) to form the Zinc pocket were found. In the first part here, the *E. coli* nomenclature was used for naming of the subunits and numbering of the residues, for the correspondence with other organisms see Figure 1.3.2.

On the periplasmic side of subunit NuoL, the well-conserved $_{L}Asn^{135}$ is located directly next to the reasonably conserved $_{L}Asp^{134}$ in the loop between TM-helices 4 and 5, but no counterparts were identified in other subunits that could point to Zn^{2+} binding at the proton output level. In subunits NuoL and M, a sequence meeting our requirements was found in the cytoplasmic loop between TM-helices 9 and 10 (Table 3.5.1). The well-conserved Gln (301 in NuoL, 308 in NuoM) is separated from a well-to-strictly conserved Asp (303 / 310) by a Thr or an Ile. In NuoN, the well-conserved Gln^{291} is still found in the same loop but an acidic residue is rarely present in position 293, which is mostly occupied by Asn, Gln or Lys. However, in the crystallographic structure shown on Figure 3.5.1, the C-terminal Gly of NuoK is seen next to $_{N}Gln^{291}$, which is also the case in *T. thermophilus* (Appendix 11). As C-terminal

amino acids bear a free carboxylic acid group, they can replace the lacking acid in position 293 from NuoN. $_{K}Gly^{C\text{-}term}$ is also reasonably well conserved, supporting this idea.

Organism	TM9 / TM10 cytoplasmic loop			TM7 / TM8
	NuoL/Nqo12/ND5	NuoM/Nqo13/ND4	NuoN/Nqo14/ND2	NuoH/Nqo8/ND1
E. coli	ALVQTDIKR	AFAQTDIKR	ALSQTNIKR	RASLPRPRYDQV
T. thermophilus	AFGQTDIKK	AFAAKDFKT	ALAQKEAKR	RATWFRLRYDQL
H. sapiens	ALTQNDIKK	CLRQTDLKS	GLNQTQLRK	RTAYPRFRYDQL

Table 3.5.1 : Residue conservation in cytoplasmic loops of interest for different organisms.

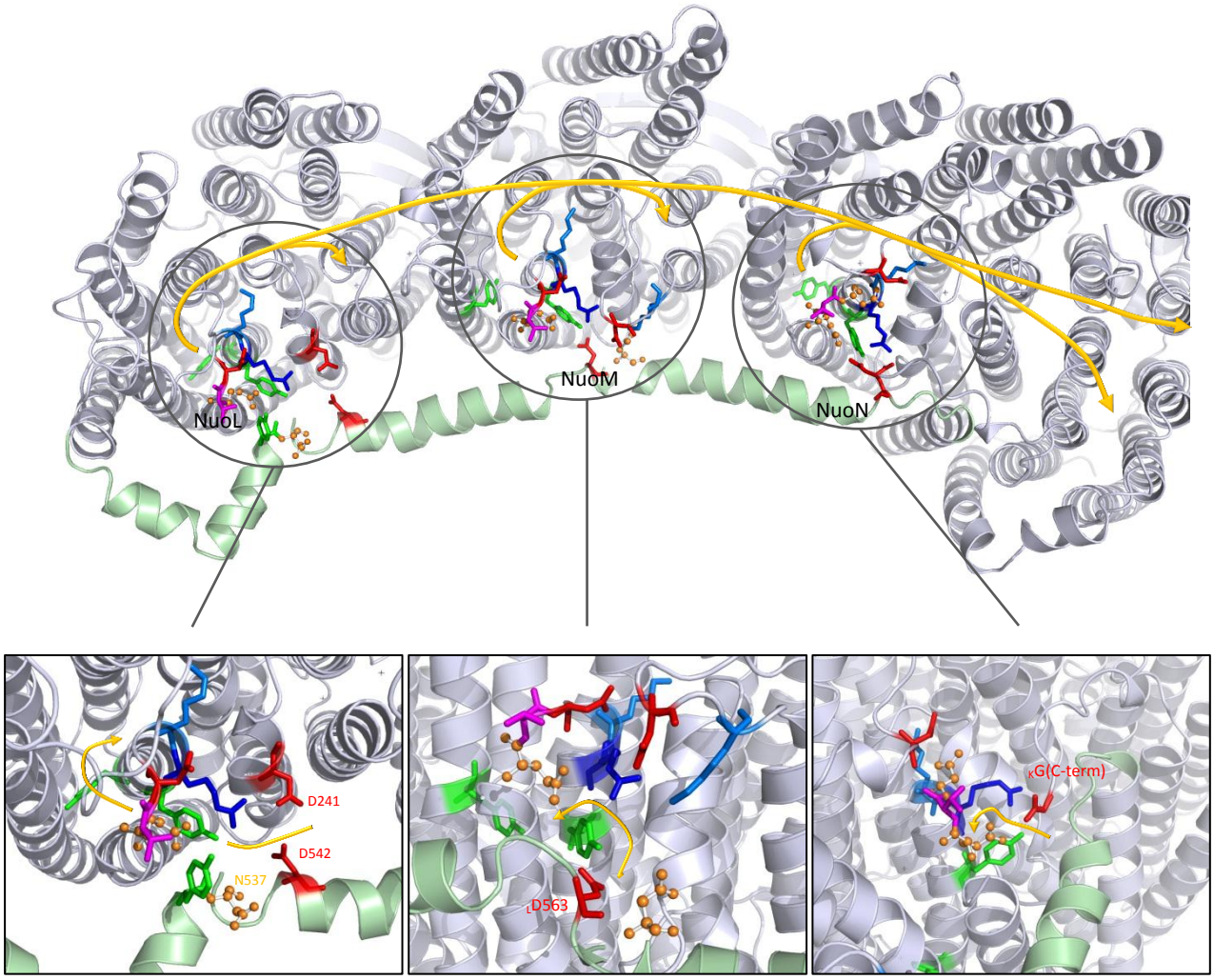

Figure 3.5.1 : Localization of the putative Zinc binding sites in the membrane domain of Complex I from *E. coli*. Top view of the membrane arm, PDB ID : 3RKO. The circles indicate conserved residues in NuoL, M and N (left to right). In each detailed view, the residues are colored as follows : Gln, Asn - Orange (balls and sticks) ; Asp, Glu, $_{K}Gly^{C\text{-}term}$ - Red ; Arg - Deep Blue ; Lys - Light Blue ; Tyr - Green ; Thr - Magenta. Helix HL is colored in Pale Green. The Orange arrows roughly indicate potential proton pathways combined with the central hydrophilic axis (see text for further details).

The conserved Asp residues located two residues away from $Gln^{LoopTM9/10}$ in each subunit are too far away (>7 Å) to simultaneously bind to Zinc. However, all three potential Zinc binding sites are adjacent to the membrane-domain spanning NuoL HL helix. In NuoM, $_{L\text{-}HL}Asp^{563}$, which was shown to be involved in proton transfer[99], is located within 5.6 Å of $_{M}Gln^{308}$, close enough to fit a Zn^{2+} ion between the two. In NuoL, $_{L\text{-}HL}Asp^{542}$ is separated from $_{L}Gln^{301}$ by $_{L}Asn^{537}$, indicating that the mechanism here is somewhat different, as supported by the unchanged H^+/e^- stoichiometry for the $_{L}$D542N mutation in refs[99, 290]. As the reasonably conserved $_{L}Asp^{241}$ is adjacent to $_{L}Asp^{542}$, it could be possible that Zinc binding occurs between $_{L}Asp^{241}$ and Asn rather than Gln, explaining the two different populations of Zinc bound Asn/Gln residues observed in Figure 3.4.2. In NuoN, no acidic residue on the HL-helix is close enough to $_{N}Gln^{291}$ for Zinc to bind the two. It is probable that the metal binds to $_{N}Gln^{291}$ and $_{K}Gly^{C\text{-}term}$ instead, indicating that the proton uptake / gating mechanism here does not directly involve the amphipatic HL helix. This is backed by the H^+/e^- stoichiometry of 2 in ΔNuoL mutants[99]. In the *T. thermophilus* structure show in Appendix 11, the picture changes slightly, with the NuoN (Nqo14) site remaining the same, but in NuoM (Nqo13) the Gln is replaced by an Ala and in NuoL (Nqo12) the Asn from helix HL is replaced by a Glu.

With these three presumed sites identified on the surface of the membrane arm, the topology and conservation of the residues located around them was explored to see if they are candidates for proton intake. Interestingly, the upper part of TM10 situated directly below/next to the key Gln residues is almost entirely strictly conserved in each antiporter-like subunit. When mapping only the highly conserved hydrophilic residues in TM10 and its surrounding helices (TM 7 to 13), a pattern emerges : Gln is in proximity of a surfacing Asp and Arg tandem and this cluster is sitting on top of an almost entirely buried Tyr. Other conserved hydrophilic residues seem to create a vortex-shaped connection to the central hydrophilic axis through the upper (cytoplasmic facing) part bundle of TM helices 13-12-11-10-9, which would be suitable for proton intake. As it is probable that proton intake also involves a network of water molecules, the presence of one structural H_2O in the proposed input from NuoN in the *E. coli* structure shown here backs our postulate, together with the calculated positions of waters from ref[89]. Moreover, the presence of conserved residues on the top of TM10 could be part of the channels' opening mechanism. On the other hand, it

was not possible to identify which would be the first proton acceptor in these channels and a different mechanism remains as plausible. As proposed by other groups, the channels are presumed to be closed in the oxidized state, making their exact localization difficult. Nevertheless, for additional reasons that will be discussed on page 160, we suggest that the TM9 to 13 bundle is involved in H^+ intake (see also Figure 3.5.6).

The alleged entry of these channel is located above the strictly conserved kink in TM7, which harbors a His in NuoM and N and a Gln in NuoL on the HL helix facing part, followed by an intermediate Pro responsible for structural rigidity and a Trp stabilizing the kink on one side and protruding in the central hydrophilic axis on the other. All the residues in these kinks show a high degree of conservation, with Trp ($_L^{238}$, $_M^{226}$, $_N^{243}$) being strictly conserved. It turns out that the acidic residues from HL helix $_L$Asp^{542}, $_L$Asp^{563} and $_L$Glu^{587} are within H-bond distance of His or Gln in the kinks. A conformational shift of HL-helix would thus drive an opposite shift of the Trp and His residues as indicated in Figure 3.5.2, moving the bulky Trp residues along the central hydrophilic axis (indicated by a dashed orange line). Additional more or less conserved polar residues present on the upper part of TM7 can assist this movement. Moreover, on the kink-like flexible π-bulk in the middle of TM8, conserved bulky hydrophobic residues (Leu, Ile or Val) face the Trp from TM7 and constitute the second part of these gates. The high conservation and apparent rigidity (due to two Pro residues) of the cytoplasmic loop connecting TM7 and TM8 indicates that the conformational shifts induced by HL helix in TM7 can be transferred to TM8, leading to almost synchronous opening of the two door panels. The “back” of TM8 can also be moved by the helix bundle tied together through the periplasmic β-elements (Figure 3.5.6).

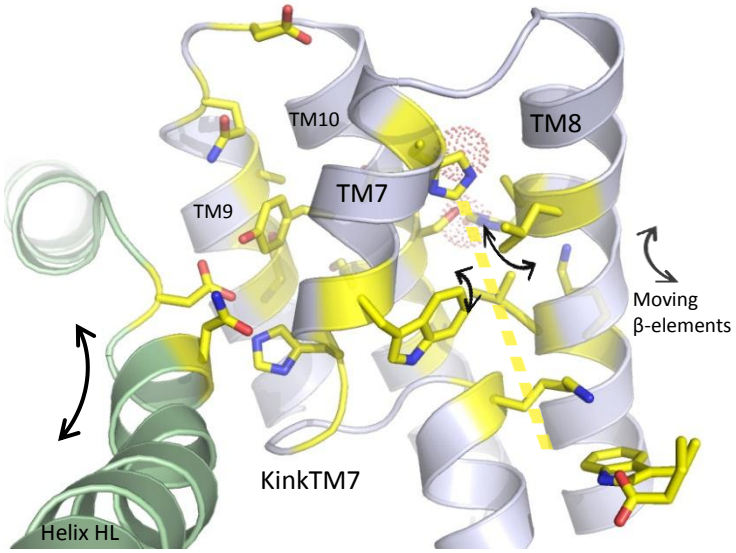

Figure 3.5.2 : HL helix and β-element induced internal proton flow regulating mechanism.

The protonable residues located on either side of these gates (Lys and His) would then be able to drive a proton through them, by direct contact or over an intermediate water molecule. From the available crystallographic structure, it appears that the proposed gates are in the closed state when the enzyme is oxidized. Instead of - or in supplement to - controlling proton uptake itself, the HL helix thus controls their flow along the central hydrophilic axis, in a sort of proton peristalsis. As Zn^{2+} was proposed to bind between $_{L}Asp^{563}$ and Gln (NuoM) or $_{L}Asp^{542}$ and Asn (NuoL), an inhibition of this internal gating mechanism is consistent with the signals observed in chapter 3.4.2 : the residues situated upstream of the gates retain their protons while those located downstream gradually expulse their protons, both through the regular mechanism. In NuoN, the circumstances are different : $_{L}Glu^{587}$ is not solvent accessible and can thus not be part of the Zinc binding site. As proposed previously, Zn^{2+} probably binds to $_{K}Gly^{C\text{-}term}$ here, which could be responsible for the blocking of H^+ intake and lead to complete emptying of protons from this channel, explaining why some signals still evolve after more than 30 turnovers.

In the *T. thermophilus* structure, the situation is somewhat different, as the separation created by the proposed gates is less apparent, excepted for Nqo12. Especially in Nqo13 (equivalent to NuoM), the gates seem to be open and TM8 is distorted as expected, bringing the two Lysines closer together. These diversities could be owed to a slightly different mechanism, or the dissociation of the antiporter modules from NuoH and the soluble domain in the *E. coli* structure might reflect a non-functional, “relaxed” state of the enzyme. As from now the general mechanism of Complex I will be discussed, the nomenclature of *T. thermophilus* was used in the next part of this chapter.

The proposed H^+ inputs are not, as in other models, found in the proximal - hydrophilic arm facing - part of the antiporter modules. Their distal localization might however be the key of the coupling mechanism between Q reduction and proton pumping, together with an electrostatic attraction or repulsion effect. As shown in bacterial[291] and in mitochondrial Complex I[75, 76], semiquinone species are involved in the coupling mechanism. These species can be charged negatively ($SQ^{\bullet -}$), and upon reduction by a second electron result in Q^{2-} or QH^- if a single protonation occurs. These pathways together with the potentials and pKa of

these transitions for UQ are shown in Figure 3.5.3. Evolutionary analysis of this reaction suggested that the most probable pathway goes through Q^{2-} [49].

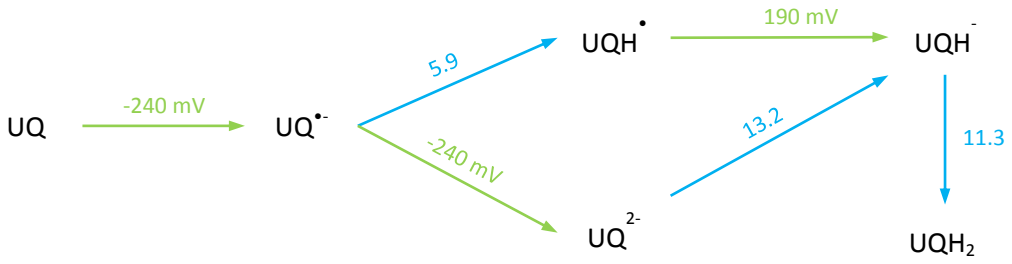

Figure 3.5.3 : Ubiquinone oxidoreduction reactions with intermediate species. Green arrows represent reductions with corresponding E_{m7}, blue arrows protonations with corresponding pKa. Values are given for UQ in 80 % EtOH and taken from ref[49]. Physiologically irrelevant transitions are not shown.

To exist long enough to induce changes in the rest of the enzyme, these anions need a strict control over protonation, i.e. the reaction site has to be shielded from the solvent and a mechanism that delivers the last proton(s) only when the anionic Q has finished exerting its effect has to be present. The sealing of the quinone reaction chamber was evidenced in the structure of the entire Complex I from *T. thermophilus*[89]. When looking for potential Zinc binding sites in Nqo8 (NuoH in the *E. coli* nomenclature), a highly conserved motif resembling those suggested for proton intake in the antiporter-like subunits was found in the cytoplasmic loop between TM7 and TM8 (Table 3.5.1). To our surprise, the mapping of the conserved hydrophilic residues underneath/around this loop formed not only the putative H^+ channel proposed previously[89] but also lead up to the quinone binding $_4$His^{38} (Figure 3.5.4). This channel could be a remnant from a former vectorial H^+ channel whose function would have shifted to control over the $_4$His^{38} protonation state, or a mechanism allowing both vectorial proton pumping through the E-channel and $_4$His^{38} protonation control could be present. The channel entry is gated as suggested by the presence of $_8$Gln^{304}, and a leucine situated in the middle of the channel and attached to the tip of the moving helix bundle $_4$HB4 could provide further gating[108], together with $_8$Gln^{226}. Mutations of key residues here drastically affect the enzyme's ability to reduce quinones[292-294]. If this channel

really controls the existence of the Q anion, a mechanism fired only once the anion has prompted distal H^+ pumping should exist. As shown in Figure 3.5.4, a bifurcation of the central hydrophilic axis is present at the junction between Nqo7, 8 and 10. The main branch continues towards the distal antiporter modules whereas $_7Asp^{72}$ is situated at the direct opposite of $_7Glu^{74}$ on $_7TM2$. Facing $_7Glu^{74}$ on the kinked $_8TM8$, $_8Pro^{315}$ and $_8Trp^{310}$ are within its interaction range, especially considered that a cavity which might be filled with water molecules is formed between the three key residues. A shift of $_7Glu^{74}$ could thus be transmitted to the flexible upper part of $_8TM8$, in turn resulting in the opening of the $_4His^{38}$ H^+ channel located just above. All these residues are strictly conserved and some of them have been addressed by directed mutagenesis, revealing dramatic decreases of the Q reductase activity in the mutants[295], thus strongly supporting this theory.

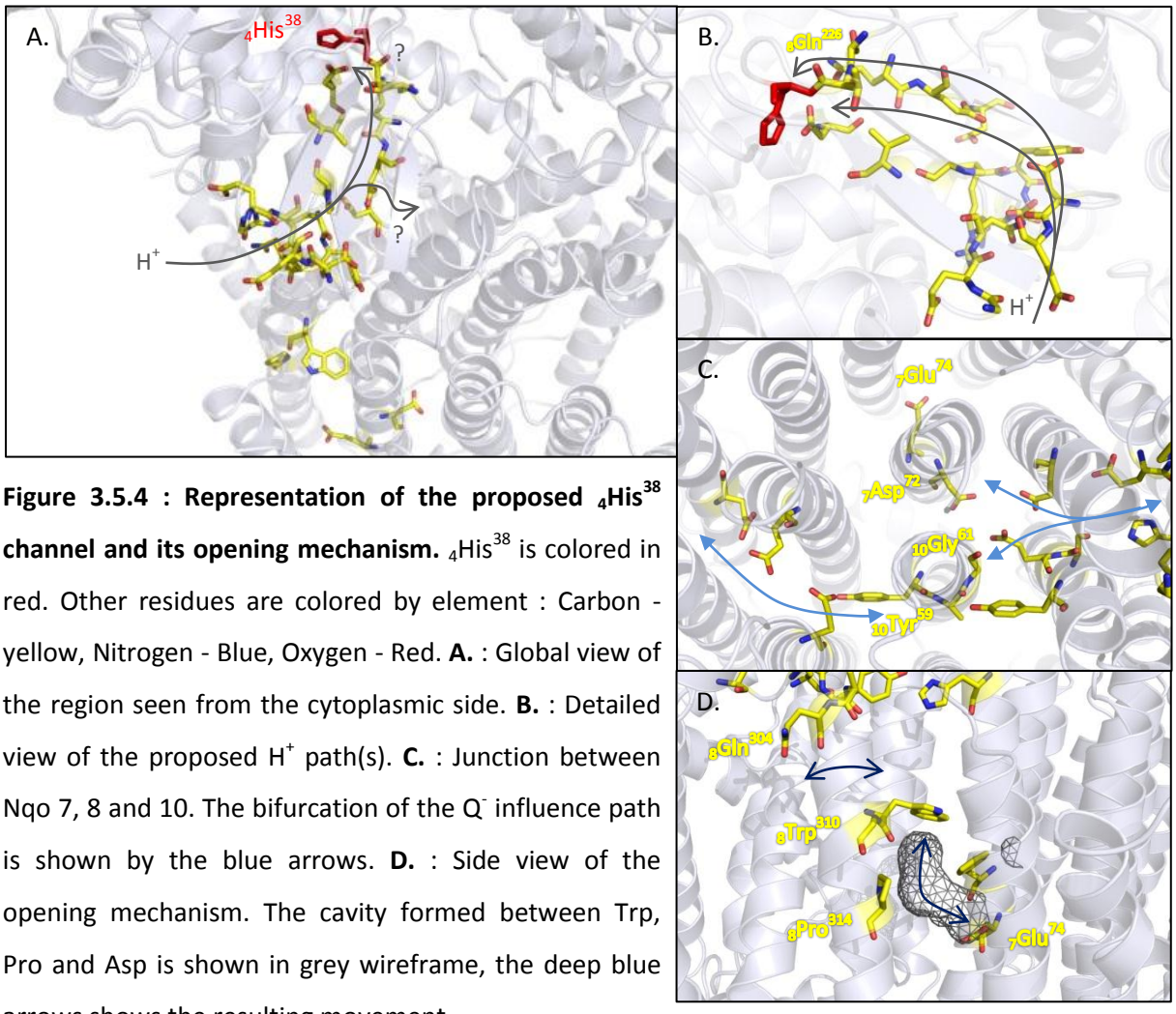

Figure 3.5.4 : Representation of the proposed $_4His^{38}$ channel and its opening mechanism. $_4His^{38}$ is colored in red. Other residues are colored by element : Carbon - yellow, Nitrogen - Blue, Oxygen - Red. **A.** : Global view of the region seen from the cytoplasmic side. **B.** : Detailed view of the proposed H^+ path(s). **C.** : Junction between Nqo 7, 8 and 10. The bifurcation of the Q^- influence path is shown by the blue arrows. **D.** : Side view of the opening mechanism. The cavity formed between Trp, Pro and Asp is shown in grey wireframe, the deep blue arrows shows the resulting movement.

The suggested Q protonation cycle is relatively short, so that the lifetime of the intermediate anionic Q species is limited to the strict minimum to avoid damage to its environment or production of ROS. Henceforth, a Zn^{2+} inhibition of proton uptake by this channel would have catastrophic consequences, leading to deterioration of the enzyme's interior. The increase of signals from COO^- entities in Figure 3.4.3 could reflect this reductive destruction, as more and more electrons escape from the trapped Q to the E channel or elsewhere. This is also consistent with the irreversible and progressive nature of the Zn^{2+} inhibition, as these damages would persist even after removal of the Zinc ion.

As it is more and more evident that the trapped Q anion is effectively the driving force of the distal proton pumping, a mechanism linking the two can be proposed with the elements in our possession. While it is not exactly limpid how the electrostatic force is transferred through Nqo8, its propagation from the interface of Nqo8 to the first antiporter module Nqo14 and beyond starts to untangle. In the bifurcation shown on Figure 3.5.4, the alteration of $_8Glu^{130}$ and $_8Glu^{163}$ is transmitted to $_7Asp^{72}$ in one direction and to $_{10}Gly^{61}$ in the other. As $_{10}Gly^{61}$ is situated in the kink of TM, its backbone carbonyl is not involved in helical hydrogen bonding and can thus be moved by the neighboring $_8Glu$. This displaces $_{10}Tyr^{59}$, resulting in a cascade of Glu movements or water molecule migration through Nqo11 to the interfacial $_{14}Glu^{112}$. From there starts the same motif repeated in each antiporter : the interfacial Glu, two Lys separated by the Trp gates, a His, a cluster of Tyr and a Gly located in the kink of the distal discontinuous helix. This loop can be operated by the movement of the β-elements presented in Figure 3.5.6. Additional, less conserved polar residues enhance this scaffold. The incoming perturbation of the proximal Glu is then proposed to initiate proton migration along these residues as described on Figure 3.5.5.

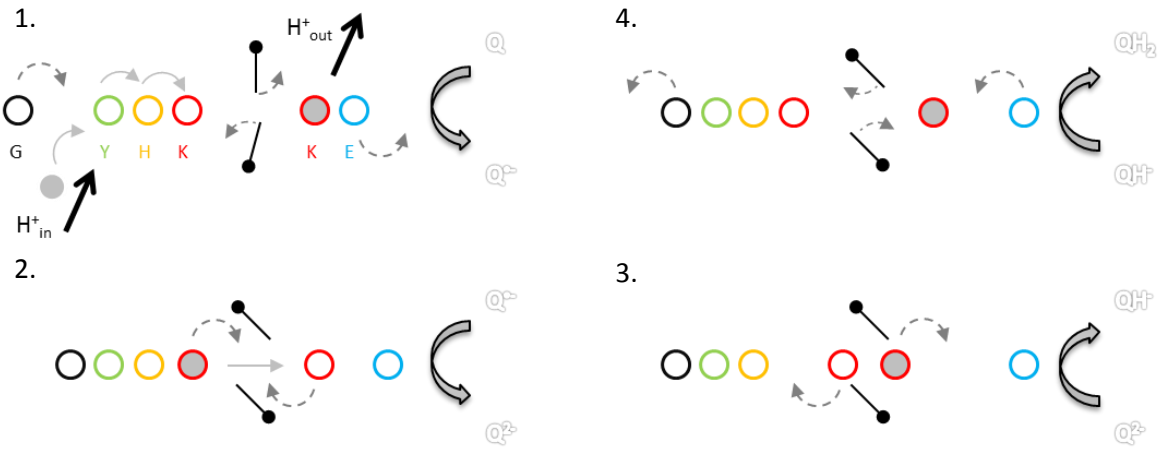

Figure 3.5.5 : Directional proton transfer mechanism in the antiporter modules. Each circle represents a key residue. Protonated residues are represented by the grey filled circles. The Trp gates are represented by the two lines between the Lysines, with the upper line representing the bulky hydrophobic residues and the lower line representing the Trp residues. The direction of Q in its different states is indicated. Dashed arrows represent residue or gate movements and full arrows represent proton transfer.

The exact sequence and nature of the events presented on Figure 3.5.5 might be slightly different, but the general principle would explain directional proton transfer. The protons could also be pumped in or out at step 4, upon return of the enzyme to its resting state. The number of protons initially present in the mechanism (one) was arbitrary chosen, but the mechanisms would work with two or even more if H^+ can be stored on water molecules. It would even be more efficient with more protons, as the positive charge would be delocalized, reducing the energetic cost of importing an H^+ from the bulk[127]. The de- or re-protonation of the interfacial Glu is also possible but not necessary, as its main role is the modification of the pKa from the adjacent Lys. The moving Trp can also alter the pKa of the Lys residues through π-cation interactions[296]. It should be noted that Tyr was proposed as a protonable residue for the sake of simplification, but the orientation of the aromatic rings and the positions of water molecules could mean that this Tyr cluster actually stabilizes $H^+(H_2O)_n$ ions, also through π-cation interactions. This is supported by the previously attributed signals of *Zundel* and *Eigen* cations and the variation of signals from Tyr residues during Zn^{2+} inhibition (chapter 3.4.2). Finally, this mechanism is supported by the previously

mentioned apparent “open” position of the Nqo13 subunit in the structure of the entire Complex I together with the calculated pKa from the central hydrophilic residues within the same reference[89] : in Nqo14 and 12, the pKa of the proximal Lys is 7 and 8, indicating that it is able to store a proton, whereas in Nqo13 it is 5.3, representing a more transient state.

A more simplistic view of the global Q reduction - H^+ translocation coupling mechanism is that the HL helix and the β-elements opens the Trp valves and prepares key residues for proton transfer, followed by a Q^- induced pushing or pulling of the water molecule river to establish a transient proton pathway. This brings us to the key issue of how the protons are effectively pumped in and out of this stream. The continuity of the central hydrophilic all the way to the distal end of Nqo12 and the local structure at this terminus suggest that the Q^- induced water/proton migration can move the lower end of $_{12}$TM15 through $_{12}Gly^{375}$ together with polar residues present towards the periplasmic side of $_{12}$TM15. The latter were proposed to act as H^+ output channel, but this is not consistent with the model proposed here. Moreover, in the *E. coli* structure the proton exit would be located in the hydrophobic part of the lipid bilayer and in the *T. thermophilus* structure hydrophobic residues deliver shielding from the solvent. The effects of lipids on Q reductase activity could find an explanation here, as they would be essential for providing an additional sealing at the end of this H_2O river. When observing the pattern of β sheets/turns and C-term domains parallel to the membrane surface, it appears that the movement of $_{12}$TM15 can induce the movement described in Figure 3.5.6 C., which then propagates back to the proximal part of the membrane domain via the highlighted helices and structures (Figure 3.5.6 A.). Alternatively, the movement of the β-elements could also originate from the movement of the Nqo7 loop, through $_7$TM1 (Figure 3.5.6 A. and B.) as will be described later. In both cases they would induce a shift of the cytoplasmic loops between TM13 and 14 inducing a barrel roll of the small α-helical structure from the loop between TM11 and 12 that could open the entry of the proton gateway (Figure 3.5.6 D. and E.). By doing so, the loop between TM9 and 10 is also moved, linking the movements of the β-elements to that of the HL helix and vice-versa.

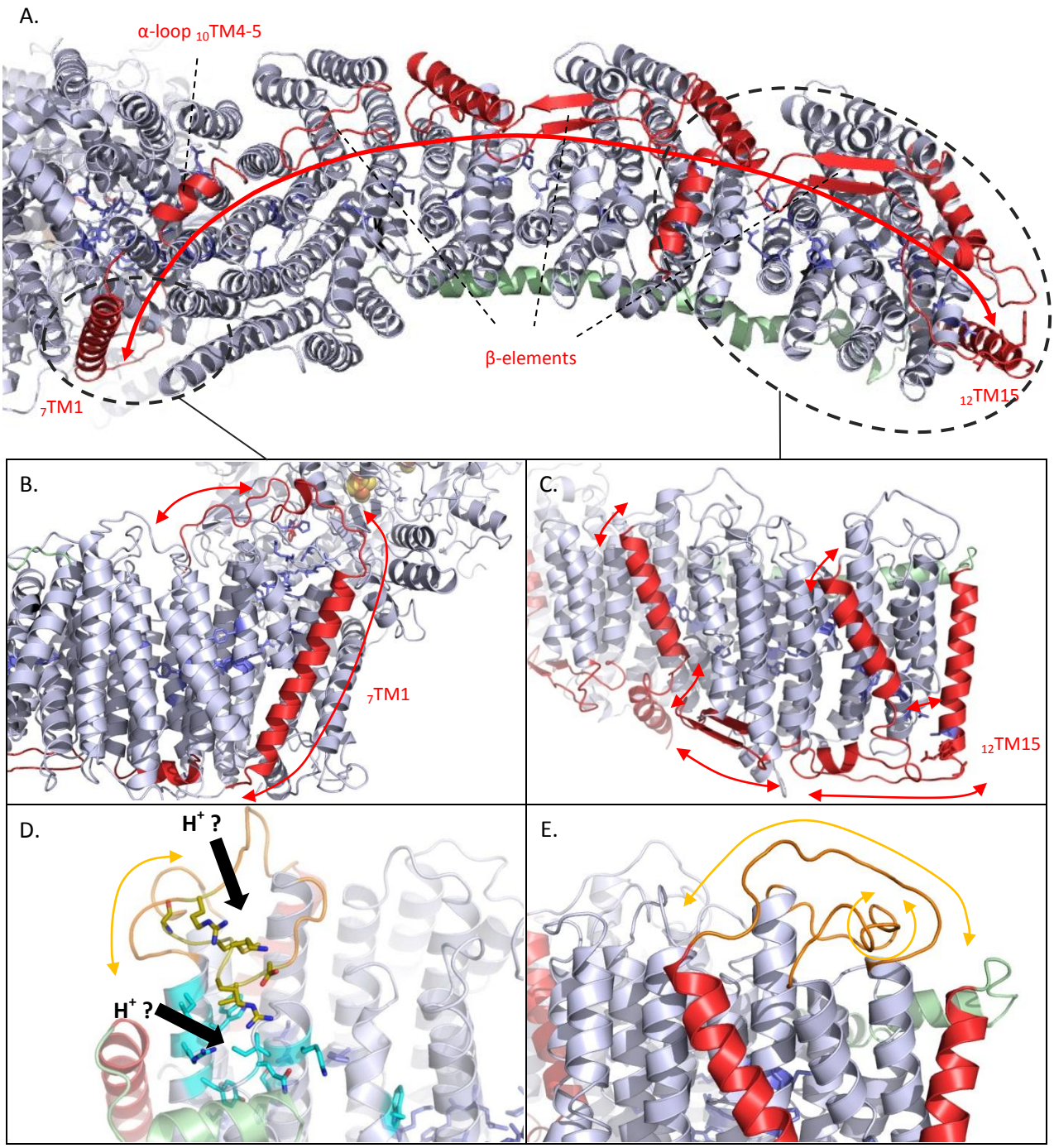

Figure 3.5.6 : Conformational movements inducing distal proton intake. The proposed movements are shown by red ($_7$TM1-2 loop and β- and C-terminal- elements tied to TM helices) or orange (TM11-12 and 13-14 loops) arrows. Helix HL is colored in pale green. Residues from the central hydrophilic axis are shown as blue sticks. **A.** : View of the membrane domain from the periplasmic side. **B.** : Detailed side view of Nqo7 TM1 and the loop. $_4$His^{34} and cluster N2 can be seen in the background. **C.** : Detailed view of the distal Nqo13 and 12 subunits and how parts of the β-elements interact with the kinks harboring the distal Gly. **D.** : Shifts of the TM11-12 and 13-14 loops proposed to initiate proton intake, together with two potential proton channels. **E.** : Same as D. but viewed from the other side.

Although these cytoplasmic loops are not especially well conserved, they build a structure which is remarkably maintained in each antiporter module and in the two available X-ray structures, except for NuoN in *E. coli* where the protein backbone suffered apparent damage prior or during crystallization. Underneath these loops large cavities facilitating their movements are present. This can result in the creation of a transient H^+ intake pathway leading through the Tyr vortex to the central hydrophilic channel. The charge defect created by the Q^- induced "proton peristalsis" is the driving force to attract protons in the entry of the channels. The localizations of putative Cardiolipin binding sites from chapter 3.1 also argue for the proposed positions of these channels, as the proton trap effect of CL[263] would allow capture of the rare ([c] ≈ 10^{-7} M at pH 7) and highly mobile (0.93 $Å^2.ps^{-1}$) [127, 297] protons and keep them ready for intake, as recently shown on Complex IV[170].

On the opposite side of the membrane, the exact position of the output half-channels could neither be determined on the basis of the positions of conserved hydrophilic residues embedded in the membrane domain nor on the basis of cavities and the proposed mechanism. It is probable that they are also closed in the oxidized state, thereby completely sealing the central hydrophilic axis from the solvent so that Q^- can play its role. As the modules within the antiporters are linked by an internal symmetry where TM helices 9 to 13 are rotated 180° around the membrane axis to form TM helices 4 to 8[92], a 180° rotated counterpart to the input mechanism might control the output half-channels. While the cytoplasmic side of the membrane domain shows a structural repetition in each antiporter module, the periplasmic side spots some differences. Added to the variances present in the central hydrophilic axis at the interface between each antiporter subunit, this raises the question of the proton output similarity. The most striking dissimilarity is seen at the interface between Nqo14 and 11, where no kink is formed in $_{11}$TM3 and the Gly otherwise responsible for transmission of the water molecule movements without H^+ transfer is completely integrated in the α-helix here. Instead, protonable Glu residues continue the axis to the interface between Nqo11 and 10, where a well-defined channel of hydrophilic residues leads to the periplasm. This channel was previously proposed as exit for a pumped proton from Nqo8[89], but the transmission of the Q^- effect through the backbone of $_{10}$TM3 and the lining of this helix by two hydrophobic "walls" blocking potential proton transfer

through water strongly argue against this hypothesis. The quite impressive length of the resulting channel might again be correlated to the evolution of COO^- and COOH species during Zn^{2+} inhbition from chapter 3.4.2 over 20 or more redox cycles.

Before proposing a global coupling mechanism, the most important part remains to be clarified : how is the energy gained from Q reduction turned into conformational changes in HL helix and β elements and how is Q protonation and release controlled. During electron transfer from NADH to Q, a part of the energy gained through this process is released when the terminal cluster N2 gets reduced[108]. However, this fraction seems too small to induce at a time the conformational shifts seen in the lower hydrophilic domain AND the numerous conformational changes attributed to the HL-helix / β-elements displacement. Thus, they have to be displaced upon Q reduction, favoring the theory of a pseudo two-stroke mechanism, with strict control of Q reduction and protonation state. By following a trail of highly conserved polar residues through the upper, cytoplasmic facing parts of Nqo4, 7, 8 and 11, a potential push/pull mechanism linking the Q-binding cavity to the C-terminal part of Nqo11 was identified (Figure 3.5.7). Towards Q, a highly conserved cluster from Nqo7 forms a loop in which invariant $_7Glu^{45}$ (essential for activity[295]), $_7Ser^{46}$ (replaced by Cys in some organisms and ligated in the deactive form mitochondrial enzyme[298, 299]) and $_7Tyr^{44}$ (Phe in some organisms) contact $_4His^{34}$, located in the Q binding pocket and also essential for activity[292, 300]. The backbone oxygen and nitrogen atoms from Glu and Ser form an imbricated hydrogen bonding motif with the strictly conserved $_7Gly^{47}$, suggesting that an event occurring at $_4His^{34}$, for example Q binding or (de)protonation, will lead to a conformational shift of this part. This shift is then transduced through the whole Nqo7 loop (as judged by the presence of additional Gly and Pro residues) in turn moving the C-terminal part of Nqo11 which is tightly bound to helix HL. Unfortunately, the 25 first residues of the Nqo4 N-terminal part are missing in the model, but it is likely that they contribute to this mechanism, perhaps by closing the gap between the cytoplasmic loops from Nqo 7 and Nqo11. Additionally, the movement of the Nqo7 loop would also move $_7$TM1, resulting in the displacement of the β-elements, creating an antiparallel movement of the periplasmic and the cytoplasmic loops. The junction of the central hydrophilic axis is in the middle of this system, thus this movement could partially operate it. As shown in ref[108], the helix bundle

$_4$HB4 moves upon N2 reduction, probably assisting the whole process in a way that needs further clarification.

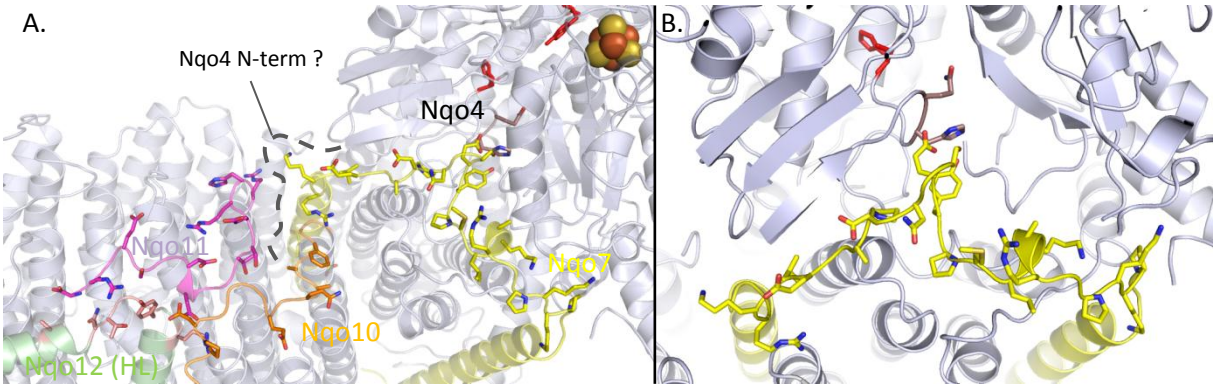

Figure 3.5.7 : Nqo7 loop and proposed transmission to HL helix and β-elements. N2 is shown as spheres. Key residues are shown as sticks. The Q binding $_4$His^{38} and $_4$Tyr^{87} are colored in red. Other residues are colored according to their composition, with Oxygen in red and Nitrogen in blue. Carbons are colored depending on their subunits as marked on the picture. **A.** : Global view of the region. The putative position of the C-terminal residues from Nqo4 are shown as a dashed grey line. **B.** : Detailed view of the Nqo7 loop and its connection to the Q binding site.

As mentioned above, $_4$His^{34} is located in the Q binding pocket, but while it is essential for activity it does apparently not bind to the quinone moiety. Instead, it faces the first or second isoprenoid unit from the hydrophobic tail (the bound Quinone was not included in the PDB entry 4HEA). However, it is preceded by the conserved $_4$Gln^{33} (Asn in *E. coli*)[300] which is within interaction distance with one of the Q carbonyls (4 to 5 Å - see Figure 3.5.8 for further detail). As the amide of the side chain from Gln or Asn is hardly deprotonable (pKa above 15 for the OCN-H / OCN$^+$ couple), it is probable that its role is to stabilize the negative semiquinone through a hydrogen bond. In the oxidoreduction reactions of UQ presented in Figure 3.5.3, it appears that the pKa of UQ$^{\bullet-}$ is *ca.* 6. Thus, to acquire a proton a residue with a neighboring pKa should be present in the proposed binding site. The pKa of these residues were calculated with the help of Propka3[301], showing that $_4$His^{38} and $_4$Tyr^{87} have a pKa of 8.9 and 13.4 respectively, which in both cases is insufficient to protonate UQ$^{\bullet-}$. The charge created could however attract $_4$Gln^{33}, pulling $_4$His^{34} and displacing the Nqo7 loop, thereby triggering the movements of the β-elements and the HL helix. The next step would

be the second reduction of $UQ^{\bullet-}$ to UQ^{2-}, which has a pKa of about 13, thus deprotonating $_4$His^{38} and leading to the events in the E-channel to which it is connected through $_4$Asp^{139} and $_8$Gln^{226}. As the pKa of UQH^- (about 11) is too low to deprotonate $_4$Tyr^{87}, the last H^+ has to be provided elsewhere. No other deprotonable residues are present in the upper part of the binding pocket, thus the only way to achieve the reaction would be a strictly controlled undocking of UQH^- and its migration to more deprotonable horizons. The first residue that could play this role is $_4$His^{34}, but from its calculated pKa (5.7) it is probably in the deprotonated state. In addition, it has to be considered that the enzyme can work in reverse mode, a His would thus not be basic enough to deprotonate QH_2. Further away the residues at the entrance of the E-channel, mainly Arg and Glu residues, are found. Arginines would be good candidates to provide the last H^+ as their pKa is generally between 10 and 13, so that in the forward reaction a protonated Arg with a pKa slightly below 11 could protonate UQH^-, while in the reverse reaction its pKa should be slightly upshifted and no proton present in order to deprotonate QH_2. The structural complexity of this region did however not allow us to favor one residue over another, but the presence of polar residues on the other side of the binding pocket (Figure 3.5.8) support our theory, as they might stabilize UQH^- there until it undergoes its final protonation. We suggest that this site is the target of acetogenin inhibition[154]. The energy liberated by this last protonation would then be used to shift the whole system back to its initial position.

This Q reduction mechanism is supported by a few observation : first, the role of $_4$Tyr^{87} here would not be to provide a proton for Q^- as suggested previously[108], but rather to stabilize the Quinone during its reduction, in addition to its potential role as electron transfer relay. The activity of some semi-conservative $_4$Tyr^{87} ($_{49kDa}$Tyr^{144} in *Yarrowia lipolytica*) mutants from ref[302] with Q_1 and Q_2 but not DQ (*n*-decylubiquinone) indicates that the presence of a (de)protonable Tyr residue is not mandatory, as the proton is provided elsewhere. Nonetheless, the presence of an aromatic group is mandatory for electron transfer. This means that the enzyme controls exactly the orientation of the isoprenoid chain, and that this is enough to stabilize Q_n (with n isoprenoid units) in tunneling distance to N2. $_4$Thr^{135} also stabilizes the Quinone there (Figure 3.5.8), as judged from the almost normal activity of the Ser192Ile (= $_4$Thr^{135} in 49 kDa subunit from *Y. lipolytica*) mutant in presence of

Q_2 compared to no activity with DQ[292]. Second, the proposed migration can be assisted by the two Gln ($_4Gln^{33}$ and $_8Gln^{226}$) paving the upper part of the binding pocket. The inhibition of this mechanism by the presence of Zinc could be at the origin of the two negative peaks at 1704 and 1781 cm^{-1} seen in the double difference spectra of the Zn^{2+} inhibited Complex I (Figure 3.4.2), from which one is accessible to ^2H_2O exchange ($_8Gln^{226}$ in our model). The absence of conformational movements of the randomly organized loops underlying this process might also explain the large negative peak at 1648 cm^{-1} and explain its absence of shift in ^2H_2O, since the major part of these loops is solvent inaccessible. Third, two SQ species have been detected in EPR spectroscopy of Complex I, namely SQ_{Nf} (fast relaxing) and SQ_{Ns}.(slow relaxing) (see ref[303] for review). The $\Delta\mu_{H+}$ poised SQ_{Nf} was estimated to be within 8-12 Å of cluster N2, which agrees with its attribution to the first semiquinone intermediate, $SQ^{\bullet-}$, at the $_4Tyr^{87}$ binding site. Fourth, the structure of the Nqo7 loop is closely related to those of the TM11-12 loops suggested to control H^+ intake in the antiporter modules (Figure 3.5.6 B.), possibly representing the reminiscence of a scalar proton channel which would corroborate the H^+ intake channel localization and opening mechanism in the antiporter modules. Fifth and last, Figure 3.5.8 shows that the Q binding pocket presents a few outgrowths, which might represent the proposed proton channels or at least free space for residues to form transient channels. One is directed to $_4His^{38}$, the other to $_4His^{34}$ and/or the E-channel. Additional protuberances might provide a putative fourth proton channel as discussed in the conclusion of this chapter.

Finally, once the Q radical is annealed through the successive protonations, the vanishing of the electrostatic force combined with conformational rearrangements triggered by these protonations probably shift the helices at the entry of the Q binding pocket back to an open state, allowing QH_2 to leave the pocket and to join the Q pool in the membrane. Additional readjustments in the pocket interior might help this process.

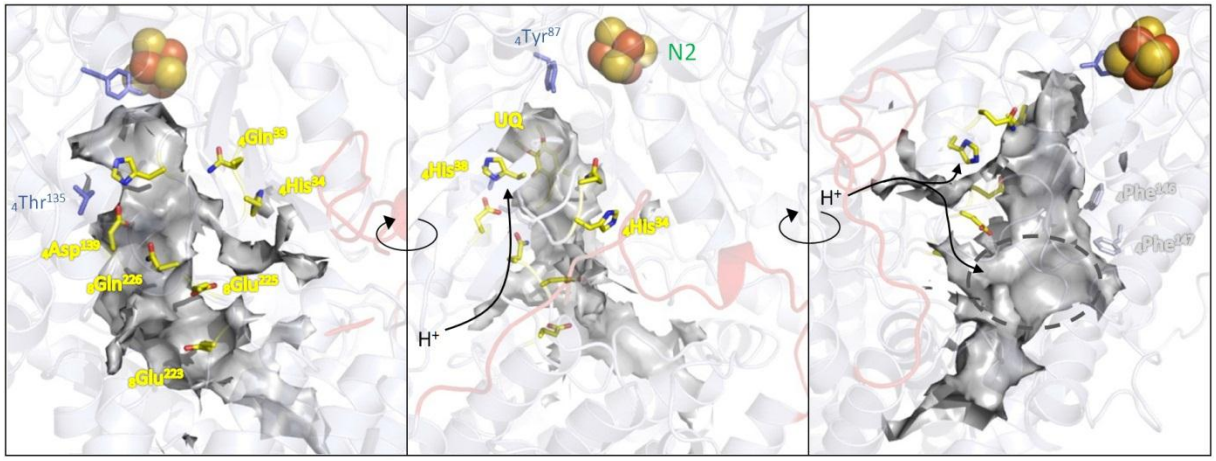

Figure 3.5.8 : Representation of the Q binding cavity. Each view is rotated by 90° around the vertical axis. N2 is shown as spheres, key residues are shown as sticks and are colored according to their composition with oxygen in red, nitrogen in blue, carbon in yellow except for $_4$Tyr^{87} and $_4$Thr^{135} where it is in slate blue. In the middle panel Ubiquinone was positioned manually inside the binding pocket, shown as a transparent grey surface. Protonation pathways are shown by black arrows and correspond to the $_4$His^{38} path in the middle panel and the $_4$His^{34} / E-channel path in the right panel. The dashed circle in the right panel indicates the putative localization of QH^-.

A last point that supporting the overall mechanism is the Debye-Waller factor map of the X-ray structure shown in Appendix 12 : each element that was proposed to move in this chapter presents a relatively high b-factor, indicating its respective flexibility. Especially the loop from Nqo4 harbouring the key Histidines and the Nqo7 loop between TM1 and 2 are very mobile. Surprisingly, most of the HL helix presents a lower b-factor, with three more mobile regions facing the alleged proton intakes. This favors a transmission of the conformational shifts through $_7$TM1, the β-elements and the TM13-14 loops to the regions facing the helix, rather than a Nqo7-10-11 induced shift of the whole helix, consigning its role to simple subunit cohesion. Yet there might be more than meets the eye, as suggested by the putative cardiolipin binding sites from chapter 3.3 : the empty space between the helix and the membrane domain might be occupied by these phospholipids important for H^+ intake.

3.5.2 Coupling mechanism between electron transfer and proton pumping

The elements discussed until now allow us to complete the picture of how Q reduction is linked to proton translocation and a general Complex I mechanism is proposed hereafter and summarized in Figure 3.3.4.1.

1 - Oxidation of NADH, transfer of the electrons through FMN and the FeS chain to N2. Q binding. Reduction of N2 resulting in small conformational rearrangements (e.g. sealing of the Q pocket) to prepare Q reduction and subsequent proton pumping.

2 - Reduction of Q to $Q^{\bullet-}$ inducing conformational movements of the β- and C-terminal-elements and the HL helix through $_4Gln^{33}$ and $_4His^{34}$ and the Nqo7 loop. Opening of the Trp gates, modulation of pKa from key amino acids located in the central hydrophilic axis. *Proton intake / output.*

3 - Second reduction of N2 and $Q^{\bullet-}$ to form Q^{2-}. Deprotonation of $_4His^{38}$ and transmission of this event through the E-channel to the junction between Nqo7, 8 and 10. Split to induce $_4His^{38}$ reprotonation and QH^- undocking on the one hand and trigger directional proton / water migration in the antiporter modules on the other.

4 - QH^- migration to $_4His^{34}$ or further away (entry of the E-channel) to undergo its final protonation. Conversion of the released energy into a backshift of the system to its initial position and opening of the Q binding pocket. QH_2 release. *Proton intake / output.*

As discussed earlier, the proton intake and output is most likely to be done at step 2, but a variant where it is split between steps 2 and 4 cannot be totally excluded, principally because of the reversibility of the mechanism.

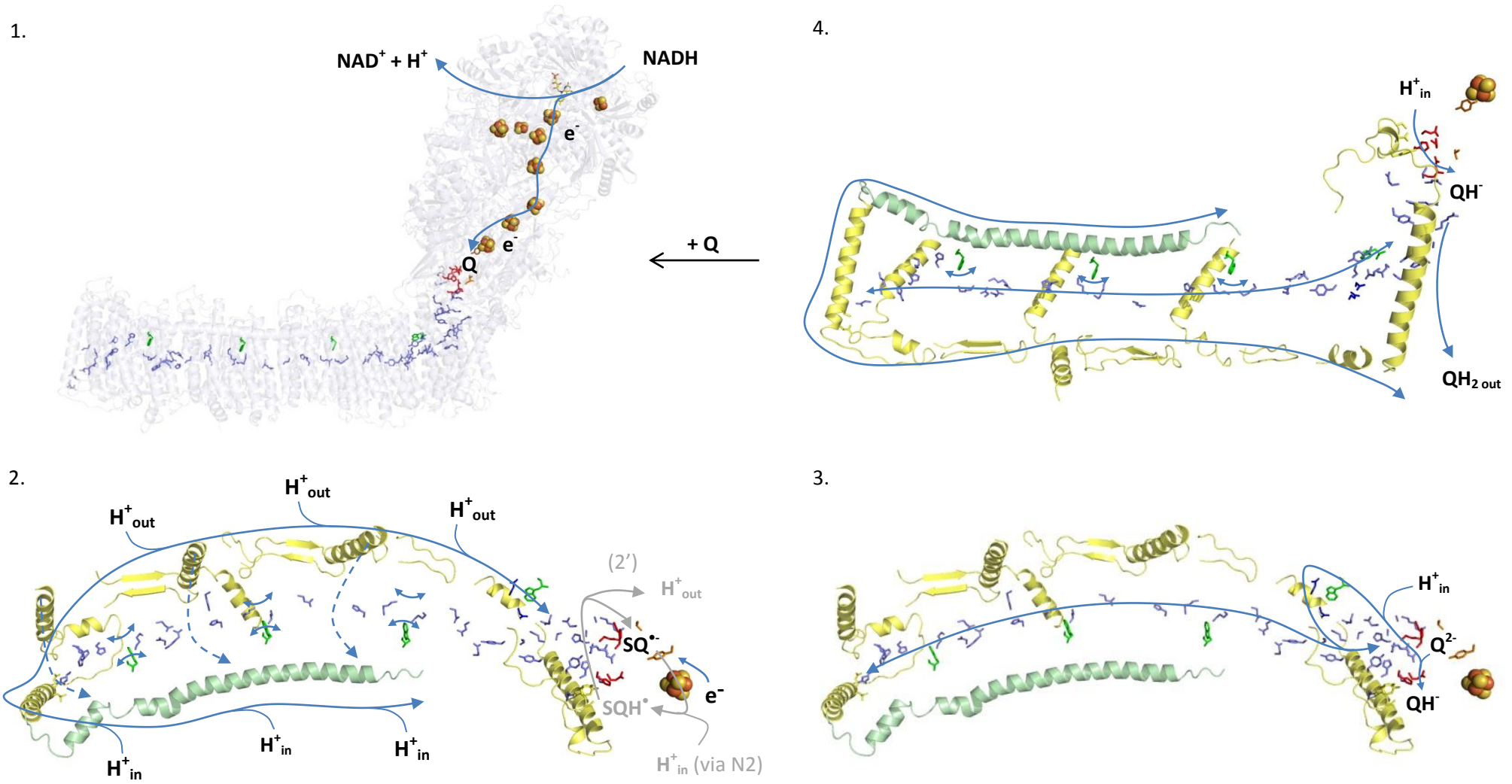

Figure 3.5.9 : Proposed coupling mechanism of Complex I. The steps correspond to those described in the text. The explicit position of Q is shown in Figure 3.5.10, together with step 2' which accounts for an optional fourth translocated H^+. The FeS clusters are shown as spheres (only N2 is shown in steps 2, 3 and 4). The central hydrophilic residues are shown in blue, those of the Nqo7-8-10 junction in deep blue, those of the $_4His^{34}$ and $_4His^{38}$ channels in red and the Q binding residues in orange. Trp from the gates are shown in green. The Nqo7 loop connected to the β- and C-terminal- elements are colored in yellow and the HL helix in pale green. Blue arrows indicate conformational, substrate, H^+ or e^- movements. The dashed blue lines in step 2 represent the cytosolic loops between TM12-12 and 13-14 proposed to mediate proton intake in the antiporter modules. Note that the overall mechanism operates close to equilibrium and is thus reversible (Δp driven reduction of NAD^+ by QH_2).

To some extent, the mechanism presented here is related to that proposed by Treberg and Brand[132]. A combination of the two is conceivable to explain translocation of a fourth proton : within the Q binding pocket, a third proton might be transferred through N2 and its disconnectable tandem cysteines to $SQ^{\bullet -}$, then transferring it to $_4His^{34}$ by a relatively small shuttle movement (6 Å or less, depending on where $_4His^{34}$ is positioned at this step). To get its second electron, $SQ^{\bullet -}$ would have to return to the $_4Tyr^{87}$ binding site and the rest of the mechanism would be the same, except that a fourth proton would be pumped through the membrane. This would explain the second EPR SQ signal (SQ_{Ns}) which was recently attributed to $QH^{\bullet}$ [291] but not its position estimated to be more than 30 Å away from N2[303]. The disconnection of the N2-binding tandem Cys when reduced might play a role in the acquisition of the proton in the first place : it was shown that the pKa of N2 (i.e., of one of the Cys) was > 8.5 in the reduced form and < 6 in the oxidized form[304]. As the first Cys to disconnect[108] ($_6Cys^{45}$) is facing Q, it may take up an H^+ from $_4His^{169}$ [79] and after transfer of its electron to form $SQ^{\bullet -}$ (pKa 5.9) donate it to the quinone. This proton would be provided by a channel through $_6Glu^{49}$ [212] and polar residues from Nqo4 (mainly), 6 and 9. Upon second reduction of N2, $_6Cys^{46}$ disconnects but as it is not facing Q and no protonable residues are located in its vicinity, no H^+ is transferred. This possibility was included into our mechanism as step 2' (Figure 3.5.9 and Figure 3.5.10 A. B.).

Also, due to the antiporter-like fold of Nqo8, an additional fourth vectorial proton translocation pathway in Nqo8 more similar to those from the antiporter modules cannot be excluded[89]. However, the absence of a second antiporter-like fold for H^+ intake/output as in the distal proton pumping modules is puzzling. The Sazanov group proposed the bundle of helices between Nqo10 and 11 to serve as exit module, but in our mechanism this is inconsistent with direction of proton pumping. In addition and as mentioned before, the interface between Nqo8 and 10 seems to form a hydrophobic barrier through which proton transfer is unlikely, thus the Nqo10-11 helix bundle is more likely to represent the exit of the Nqo14 H^+ channel. If a fourth proton channel is present here, its mechanism has to be sensibly different from the other three, which would be the case in our adapted Treberg model. A consensus value for the number of protons translocated by Complex I is still needed to orient further research[79].

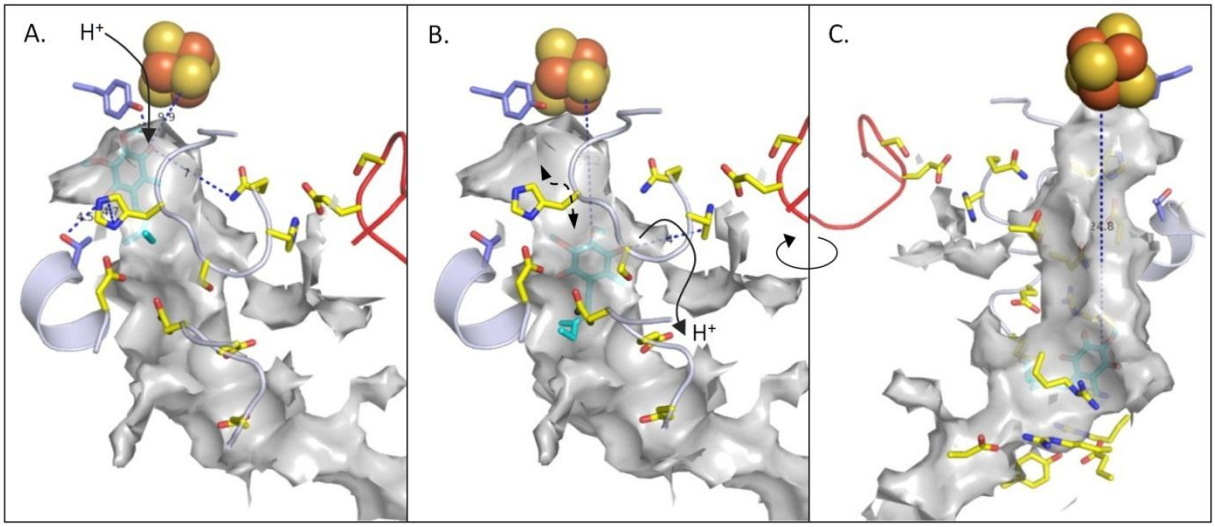

Figure 3.5.10 : Different positions of Ubiquinone in its binding pocket. N2 and key residues are displayed and colored as in Figure 3.5.8. Ubiquinone shown in light blue sticks was positioned manually inside the binding pocket, shown as a transparent grey surface. Important loops are shown as cartoon, with the Nqo7 loop colored in red. **A.** : UQ bound to $_4$Tyr^{87}, $_4$Thr^{135} and $_4$His^{38} (as in ref[89]), at *ca.* 10 Å from N2. Proton intake through N2 is shown by a black arrow **B.** : UQ in its alleged temporary binding site near $_4$His^{34} and $_8$Gln^{226}, at *ca.* 10 Å from N2, probably in its QH$^{\bullet}$ state. The dashed black arrow represents the shuttling movement UQ would have to undergo to deliver a proton from N2 to $_4$His^{34} in step 2' of our mechanism, the proton delivery is shown as a full arrow. **C.** : UQ in its terminal binding site, near the entry of the E-channel, at *ca.* 25 Å from N2. The view was rotated by 180° along the vertical axis compared to A. and B.. Additional polar residues from Nqo6 and 8 lining the bottom and opposite of the Q chamber are shown.

The antiporter-like fold of Nqo8 probably represents a remnant of its ancestors, with an H^+ channel evolved to control Q protonation : when Q reduction was attached to proton pumping[49], the pumping module was probably represented by Nqo8 (H^+ in) and Nqo10-11 (H^+ out). During evolution, a second antiporter was attached and the mechanism linking the two became more and more efficient, together with the recruitment of the third and fourth antiporters. At one point, proton translocation in the proximal pump was sacrificed on the altar of Q reduction control and overall enzymatic activity, with the scaffold of the proton pump evolving into the fascinating molecular machine that is Complex I.

In the context of Zinc inhibition, the most likely hypothesis is that the Zinc ions hinder conformational movements of the Nqo7 loop, either by locking some of the H^+ channels in the antiporter modules in an always open or always closed state as (or a combination of both), or by direct interaction with this loop. The diminution of the signals from protonated His, Lys and Tyr residues militate for the progressive emptying of proton channels, pointing to an obstruction of the opening mechanism. The intense negative peak at 1648 cm^{-1} would be a combination of ν(C=O) modes from the trapped Q and the solvent inaccessible random loops located in the vicinity of the Q binding pocket, rather than from Zn^{2+} bound Gln or Asn residues. As one of the potential Zn^{2+} binding sites seems to be accessible only in a certain state of the enzyme (chapter 3.4.1), resulting in the progressive inhibition represented by the apparition or evolution of vibrational modes from deeply buried COOH and COO^- after a few turnovers. It is likely that this site is located in the vicinity of the $_4His^{38}$ or the $_4His^{34}$ / E-channel reprotonation channels, thus extending the lifetime of high-energy Q intermediates which might result in oxidative damage of the enzyme's reduction mechanism consistent with the irreversible nature of the inhibition. As shortly mentioned previously, the Nqo7 loop harbors a conserved Ser/Cys which is chemically modified in the deactive state of the mammalian enzyme, restoring ancestral Na^+/H^+ antiporter activity[298, 305]. It might be worth to look into this kind of activity in the Zn^{2+} inhibited Complex I to confirm a potential Nqo7 loop binding site. If the mechanism involves the proposed 2' step, Zn^{2+} might also block the entrance of the channel delivering a proton to N2 and $Q^{\bullet-}$. Thus it would be interesting to measure ROS production by the Zinc inhibited Complex I at the Q site to confirm this adapted mechanism.

A few details remain to be clarified in our mechanism : the precise location (and implicitly, number) of H^+ output channels, the explicit opening mechanism of the intake channels and when exactly both are triggered. Also, the direction in which all the mobile elements are pushed or pulled and where the QH^- species moves. Time-resolved FTIR spectroscopy at the submillisecond scale as done for Bacteriorhodopsin[126, 282, 306] would be a prime choice to elucidate the last points. Turnover by turnover analysis of the Zn^{2+} inhibited enzyme could further reveal key features but would require collecting more scans to achieve good spectral quality. A better resolved, complete and intact* (see next page) X-ray of the entire Complex I would also solve many remaining issues. If our model is correct

and the radical/anionic Q drives most of the mechanism, it is doubtful that the enzyme will ever be crystallized in the reduced state, unless a method to generate precise Q intermediates *in situ* in the crystals is found. To confirm the localization of the Zn^{2+} inhibited proton input sites, EXAFS or could be used on the Zn^{2+} inhibited enzyme[186, 279], provided that not to many unspecific Zinc binding sites are present. EPR spectroscopy specifically aimed at the detection of SQ species on the Zn^{2+} inhibited enzyme taken after a few turnovers would also be of great interest. Bioinformatics to locate Cardiolipin binding sites could further confirm putative H^+ channels[170]. Of course these studies would have to be accompanied by directed mutagenesis and classical biochemical characterizations of these mutants.

The model presented here might also shed a new light on the ongoing discussion of how many quinones are bound to Complex I and if one is tightly bound. Numerous studies show at least one bound Quinone[176] and some even an over-stoichiometric quantity in purified samples from various organisms[77, 135, 291]. In particular, the *E. coli* Complex I sample from ref[291] on which EPR signals of SQ species were observed for the first time on the isolated bacterial enzyme reportedly contained two Quinones. However, the purification method used in this study was very gentle and no measure of the sample's lipid content was made. An allosteric Q_n binding site might be present at the outside of the membrane domain, modulating certain steps of the mechanism, or lipids could play this role and the additional Q was simply solubilized in the remaining lipids[177]. The question of a binding site for a second Q within the Q pocket was raised[135], but the authors of the entire *T thermophilus* X-ray structure argued that this pocket appears to be too small to fit two quinones, at least at e^- tunneling distance to N2. In addition, the $_4Tyr^{87}$ binding site seemed accessible to DQ and the inhibitor Piericidin A, but the 3.3 Å resolution is insufficient to make a clear distinction between the two (10 carbon *vs.* 13 carbon isoprenoid-like tail). It is however enough to see that no long chain quinone (as the $Menaquinone_8$ mainly used by *T. thermophilus*) and thus to exclude a non-exchangeable Q. Moreover, the transfer of electrons to a second Q would have been complicated and required a rather improbable mechanism to function. One of the main arguments for a two Q mechanism was the calculated position of the SQ_{Ns} EPR signal 25 to 30 Å away from N2[303]. In our adapted model (Figure 3.5.10), $QH^\bullet$ would shuttle a little more than 15 Å away from N2, explaining the slower relaxation constant as it would not

anymore be able to undergo spin-spin coupling with N2. Finally, the only remaining option would be the presence of an additional redox cofactor[191] introduced by co- or post-translational modifications[307]. For example, it might be possible that $_4$His^{34} is covalently linked to the neighbouring $_7$Tyr^{44}, allowing the formation of a tyrosyl radical as in the active site of Cytochrome *c* oxidase[41, 308]. This might provide an explanation for the position of the SQ_{NS} EPR signal, as $_7$Tyr^{44} is located ca. 23 Å away from N2. However, in some organisms such as in *E. coli*, this tyrosine is replaced by a phenylalanine, which would imply the formation of an aryl radical. Although this is rather improbable, this option can't be discarded totally since IR absorption bands that might represent carbon-^{2}H vibrations were present in the IR difference spectra of both Zn^{2+} inhibited and uninhibited Complex I (see page 149).

Another possibility for an additional cofactor is present in Nqo6, where five residues from this subunit situated on a loop within the Q binding pocket are missing in the structure of the entire Complex I (sequence : ^{65}SEVFR^{69}). It is unknown if the residues are present but heavily disordered, if they were enzymatically removed during assembly or if they were replaced by this putative cofactor. Analysis of the sequences from *T. thermophilus* Nqo6 and its homologues from *E. coli*, *H sapiens* and *B. taurus* revealed that this missing part is enclosed between two conserved motives (Figure 3.5.11) but no specific know recognition motifs for deletion, post-trans modifications or cofactor insertion were identified therein. A recent study revealed that post-translational hydroxylation of an arginine residue located in this area occurred in mammalian Complex I but not in the *E. coli* enzyme[123].

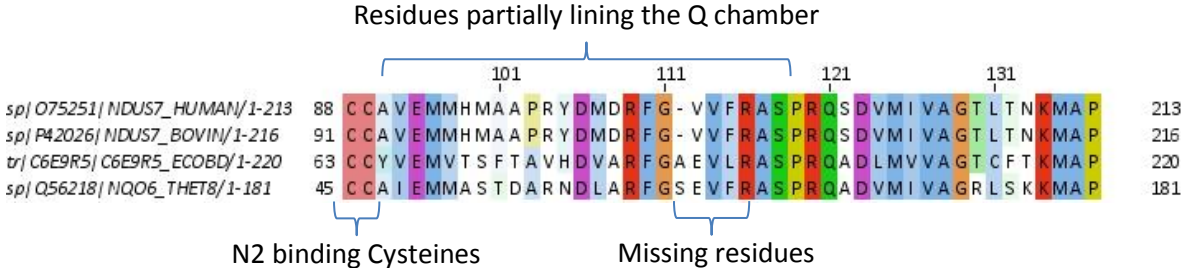

Figure 3.5.11 : Sequence alignment for Nqo6 homologues from different organisms. The following sequences were used (with Uniparc accession numbers in Brackets) : *H. sapiens* NDUFS7 (O75251), *B.*

taurus PSST (P42026), *E. coli* NuoB (C6E9R5), *T. thermophilus* Nqo6 (Q56128). Residues are colored using clustalx color scheme and residue conservation. The alignment was realized in ClustalX2.

In a crosslinking study on Complex I it appeared that subunits Nqo4 and 6 underwent covalent crosslinking even without chemical agents[141]. This was shown to be O_2 dependent and embodied oxidative damage. Thus, it is easy to imagine that the Nqo6 rupture seen in the X-ray structure was caused by ROS and that the missing segment was simply proteolysed. Its proximity to $_4His^{34}$ further confirms our adapted mechanism in which $SQH^{\bullet}$ shuttles a proton to $_4His^{34}$, which would then be able to transfer it to the E-channel or to another yet to be defined fourth channel. Moreover, the pKa of $_4His^{34}$ without the influence of the artificially created amine group from $_6Ala^{70}$ (Pymol considers it as an N-terminal residue) would be 6.9 (Propka calculations) and thus almost ideal for proton translocation, slightly too low to be already protonated but basic enough to deprotonated $SQH^{\bullet}$ with its pKa of 5.9.

4 Summary

In this work, Complex I was studied through different approaches. First, the enzyme was adsorbed in a biomimetic fashion on a modified gold surface and characterized by SEIRAS in the differential mode and by CV. The adsorbed enzyme catalyzed inhibitor sensitive reversible quinone reduction, as seen from the CVs. However, no direct signals of the redox cofactors were seen, indicating that the electron transfer from the electrode to the FMN was probably rate-limiting or that the surface coverage of the enzyme was too low. The SEIRAS experiments showed signals that could be attributed to subcomplexes of Complex I (NuoEF and NDF), however further experiments are needed to make specific assignments. With the combined SEIRAS/CV experimental setup created in this work, other redox enzymes can and will be studied in the future.

In the second part, the role of $_{F}Tyr^{178}$ in the modulation of the FMN and NADH binding was studied. It was shown that this residue was essential for NADH binding, subsequent electron transfer to the proximal iron sulfur-clusters and for the prevention of ROS production by Complex I. The replacement of $_{F}Tyr^{178}$ by a Cysteine, as seen in cases of Leigh-like syndrome, produced a 80 mV downshift of the FMN's midpoint potential, indicating that the resulting diminished NADH:DQ activity of Complex I was mainly due to slower electron transfer from NADH to FMN. Increased ROS production was also seen in this mutant. NADH-OH inhibition of Complex I at the NADH binding site was also studied, showing that it resulted in a >100 mV downshift of the FMN's midpoint potential and hampered electron transfer to the other redox cofactors.

The importance of phospholipids for the functioning of Complex I was studied in the third part. The lipid-depleted enzyme responded differently to the addition of PE, PG and CL ; while all three restored NADH:DQ activity and influenced conformational changes in the active enzyme, CL seemed to have an additional effect on the proton pumping activity of the enzyme. Additional perturbations of certain types of amino acids (mainly Arg, Lys and Trp) were seen in the FTIR spectra, which allowed to propose a map of putative lipid binding sites

on the membrane domain. Hydrogen-Deuterium exchange kinetics allowed to conclude that ca. 20 PE or PG remain tightly bound to interstices in the Complex I membrane domain.

In the last experimental part, the effect of Zn^{2+} inhibition on Complex I was studied. It was shown that the Zinc ions bind to acidic residues probably located at the entrance of the proton channels. Signals attributed to Asn and/or Gln residues were perturbed, indicating that they play an essential role in proton translocation, probably in some sort of gating mechanism. An effect on the conformational movements of Complex I and on putative bound quinones was also seen, although this could not be confirmed with certainty. For the first time in Complex I, experimental evidence that water chain clusters underlie the proton transfer mechanism was produced ; signals tentatively attributed to Zundel or Eigen cations were seen in the FTIR difference spectra of the uninhibited enzyme. These signals were diminished or shifted upon Zn^{2+} inhibition and additional signals of dangling OH bonds appeared. Moreover, the bands of internal waters, alcohols and acidic residues were strongly shifted in the Zn^{2+} inhibited Complex I. This was even clearer when experiments in $^{2}H_2O$ were made. The dynamic analysis of the signals from the inhibited enzyme indicated that a progressive emptying of the proton channels occurred as the number of turnovers increased.

The detailed analysis of the crystal structure, the conservation of amino acids and mutagenic studies from the literature allowed further exploration of the Complex I mechanism. Coupled to our results about the interactions of Complex I with lipids and Zinc ions, this led to the proposition of key elements responsible for the coupling between electron transfer and proton transfer. Alternative localizations of the proton channels were suggested, together with a channel opening- and a directional proton transfer- mechanism based on chemical and mechanic gates situated in each antiporter module. The free energy liberated upon quinone reduction is transformed into conformational movements and electrostatic energy which control and drive the distal proton pumps, mainly through a cytosolic loop in Nqo7, a series of β- and C-terminal elements and the central hydrophilic axis. Finally, a complete coupling mechanism was proposed.

In conclusion, the aspects of Complex I studied in this work took our understanding of its functioning a step further towards the complete picture of how more than 75000 atoms transform almost the entire energy of two electrons into the translocation of four protons across the membrane. In each section, additional experiments or methods were suggested to complete this picture, with the hope that one day this knowledge will drive medical and therapeutic innovation to cure Complex I-linked diseases.

5 Appendix

5.1 Experimental procedures appendix

5.1.1 *nuoF*$_{HIS}$ Complex I preparation

The preparation of *nuoF*$_{HIS}$ Complex I was done according to a well-established protocol in Pr. Friedrich's laboratory, as described in 2.1.1. After the collection of the cytoplasmic membranes through ultracentrifugation, the proteins embedded in these membranes were solubilized through detergent extraction, maintaining 83 % of the initial NADH/[$K_3Fe(CN)_6$] oxidoreductase activity (Appendix 3). The extract was then applied to a Fractogel EMD anion exchange chromatography column. As shown on Appendix 1, a first set of unbound proteins, lipids and detergents was simply washed away with binding buffer (50 mM NaCl content). Weakly bound proteins were subsequently eluted by increasing the NaCl concentration to 150 mM. More strongly bound proteins (including Complex I) were then eluted by a NaCl concentration gradient ranging from 150 mM to 350 mM.

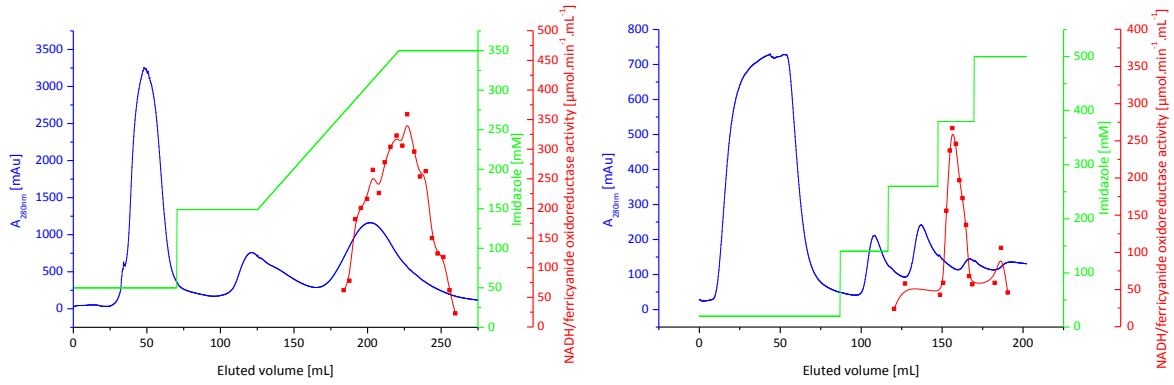

Appendix 1 : Elution profiles of the Fractogel EMD anion exchange (left) and the Ni^{2+}IDA affinity (right) columns.

The fractions presenting a NADH/ferrycianide oxidoreductase activity higher than 150 µmol.min^{-1}.mg^{-1} were pooled together and transferred to a Probond Ni^{2+}-IDA affinity chromatography column after addition of 20 mM imidazole. A similar strategy to the one used for the elution from the anion exchange was used here, i.e. unbound protein was

washed away with binding buffer, weakly bound protein was eluted at an imidazole concentration of 140 mM and finally Complex I was eluted at 380 mM imidazole (Appendix 1). The presence of a small NADH/ferricyanide oxidoreductase activity in other fractions (peaks of A_{280} around 125 mL and 170 mL) than the one containing Complex I (around 140 mL) are indicative of the fact that fragments or aggregates of Complex I were also eluted.

To ensure the integrity and to probe the purity of the purified enzyme, a SDS-PAGE gel of the final sample was run. Appendix 2 shows the typical pattern of the 14 subunits constituting Complex I. No significant contamination could be observed through this technique.

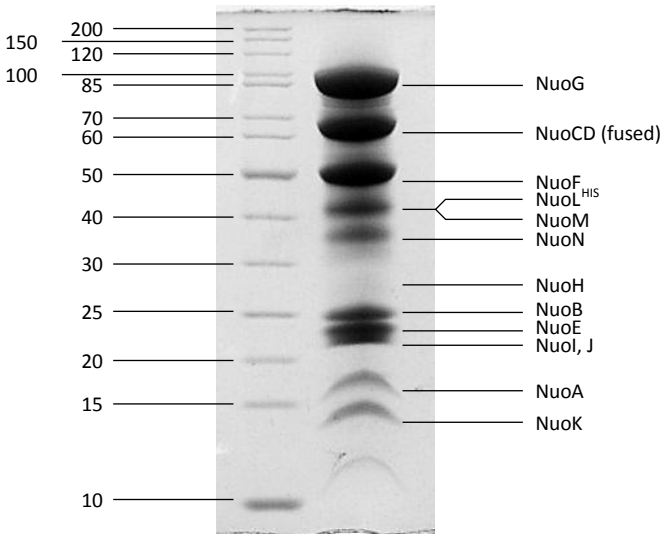

Appendix 2 : SDS-PAGE of purified *nuoF*$_{His}$-Complex I.Left lane : Molecular marker, weight in kDa. Right lane : Complex I subunits marked in correspondence to their molecular weight.

The evolution of Complex I content during the different steps of the purification was followed by Biuret reaction together with NADH/ferricyanide activity measurements. These results are shown in Appendix 3. In terms of purification fold, the Probond Ni^{2+}-IDA column is the most important phase, which clearly supports the use of the His-tag when compared to previous purifications[107].

Fraction	Volume	Protein	NADH/ferricyanide oxidoreductase activity		Fold purification	Yield
			Total	Specific		
	[mL]	[mg]	[µmol.min^{-1}]	[µmol.min^{-1}.mg^{-1}]	[x]	[%]
Membranes	17.8	1094	6581	6.0	1	100
Detergent extract	56	1061	5437	5.1	0.85	83
Fractogel EMD	54	269	2866	10.7	1.8	44
ProBond Ni^{2+}-IDA	0.6	6.8	1452	213.5	35.6	22

Appendix 3 : Isolation of Complex I from 35 g of BW25113Δnuo/pBAD*nuo*/*nuoF*$_{HIS}$ *E. coli* cells.

This method yielded an average (15 purifications) of 6 mg Complex I for 30 to 40 g of *E. coli* cells which is, for a membrane protein of this size and complexity, a decent yield. This corresponded to our needs in terms of protein quantity while keeping the amount of time spent on preparations at a reasonable level (1 day per purification).

5.1.2 Preparation of *nuoF*$_{HIS}$ Complex I with reduced lipid content

To remove a higher amount of phospholipids during the purification of Complex I, a soft method involving a longer washing step during the Probond Ni^{2+}-IDA affinity column chromatography was chosen here. Other common methods to delipidate protein samples, as for example the treatment with phospholipase A[207] were not considered here due to the highly sensitive nature of the enzyme. Appendix 4 shows the modified elution profile of the affinity column, where approx. 150 mL of binding buffer were washed over the column after the first decrease of A_{280}. Since phospholipids absorb light at 280 nm, the small but steady decrease of A_{280} during this step indicates that they are being washed away.

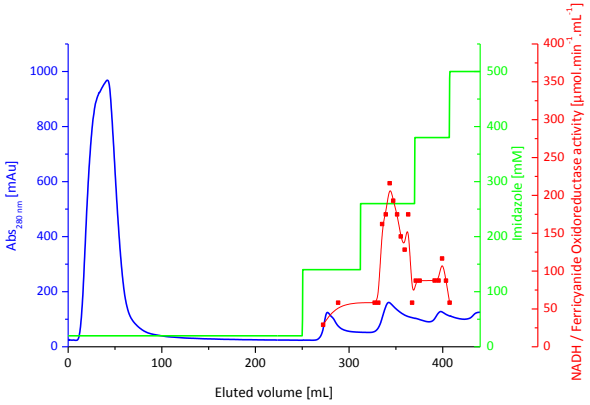

Appendix 4 : Elution profile of Ni^{2+} IDA column for reduced lipid content Complex I.

The other parts of the purification remaining unchanged compared to the classic procedure for Complex I, no significant changes in the results (as probed by Biuret reaction and SDS-PAGE) were observed (data not shown).

5.1.3 Preparations of Complex I *nuoF*$_{HIS}$ Tyr^{178} mutants

The λ-Red mediated mutagenesis of the $_{F}$Tyr^{178} mutants was done by Emmanuel Gnandt and Klaudia Morina in the laboratory of Pr. Friedrich. This method was first published by Pohl *et al*.[97] and leads to high expression levels of the modified Complex I in *E. coli* cells.

The restriction analysis showed that the mutations were well incorporated. Only slight differences were observed in the cell growth of the transformed *E. coli* cultures (E. Gnandt, unpublished data). The purifications of all mutants were identical to that of wild type *nuoF*$_{HIS}$ Complex I and the SDS-PAGE showed the same subunit pattern.

5.1.4 Preparations of wild type Complex I, NDF and *nuoEF* fragment

The preparation of these three subcomplexes is well documented[96, 237, 238] and their detailed description is beyond the scope of this thesis.

5.2 Results and discussion appendix

Wild-type	Wild-type *nuoF*$_{HIS}$	Tentative attributions
1742(-)	1743(-)	$\nu(C=O)_{asp,glu}$
1730(+)	1730(+)	$\nu(C=O)_{asp,glu}$
	1713(s)	$\nu(C=O)_{FMN}$
1693(+)	1697(+)	$\nu(C=O)_{FMN}$, amide I
1684(-)	1680(-)	amide I, β-loops
1671(+)	1673(+)	amide I, $\nu(C=O)_{UQ}$, $\nu_{as}(CN_3H_5^+)_{arg}$
1644(-)	1647(-)	amide I, α-helix, $\nu(C=O)_{asn,gln}$
1638(+)	1639(+)	
1624(-)	1630(-)	amide I, β-sheet, $\nu_s(CN_3H_5^+)_{arg}$
	1601(+)	$\nu(C=C)_{UQ}$
	1583(+)	$\nu(C=N)_{FMN}$, amide II
1560(-)	1562(-)	amide II
1540(+)	1535(+)	$\nu(C=C)_{FMN}$, $\nu_{as}(COO^-)_{asp,glu}$
1528(-)		amide II
1516(+)	1514(+)	ring-OH_{tyr}
1500(+)		
	1498(-)	$\nu(CC)ring_{tyr\text{-}O^-}$
	1485(+)	
	1406(-)	$\nu_s(COO^-)_{asp,glu}$, $ring_{FMN}$isoalloxazine
1318(-)		
	1275(-)	
1266(+)		$\delta(C\text{-}OCH_3)_{UQ}$, $\nu_{7'a}(CO)_{tyr}$
1256(-)		$\delta(C\text{-}OCH_3)_{UQ}$
1224(+)	1221(+)	$\nu(S=O)_{MES}$, $ring_{FMN}$isoalloxazine
	1184(+)	$\delta(OH)_{MES}$
1174(-)		
	1147(-)	$\nu(C\text{-}O)_{MES}$
1124(+)		
1084(+)	1107(+)	
1060(-)	1080(-)	
1048(+)	1066(+)	$\nu(C\text{-}N)_{MES}$
1036(-)		$\nu(C\text{-}N)_{MES}$
1022(+)		

Appendix 5 : Tentative assignments for the electrochemically induced FTIR difference spectra of Complex I from *E. coli.*

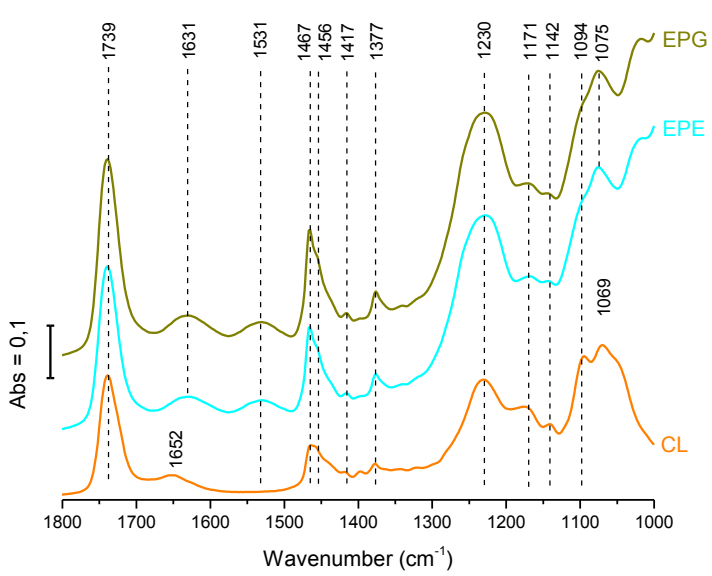

Wavenumber (cm^{-1})	Attribution
1739	$\nu(C=O)_{ester}$
1631 / 1652	NH3 / OH
1531	NH3 / OH
1467	δCH_2
1456	δCH_2
1417	δCH_2
1377	δCH_3
1230	$\nu_{as}(P=O)$
1171	$\nu(C\text{-}O)_{ester}$
1142	$\nu(C\text{-}C)$
1094	$\nu_{as}(P=O)$
1075 / 1069	R-O-P-O-R'

Appendix 6 : ATR-FTIR absorption spectra of dry phospholipid films and tentative assignments. The films were prepared by the deposition of a 2µL drop of lipids solubilized in 50 mM KPi, 50 mM NaCl, pH 7 buffer on the ATR-Crystal followed by drying with an Argon flux for 1 hour.

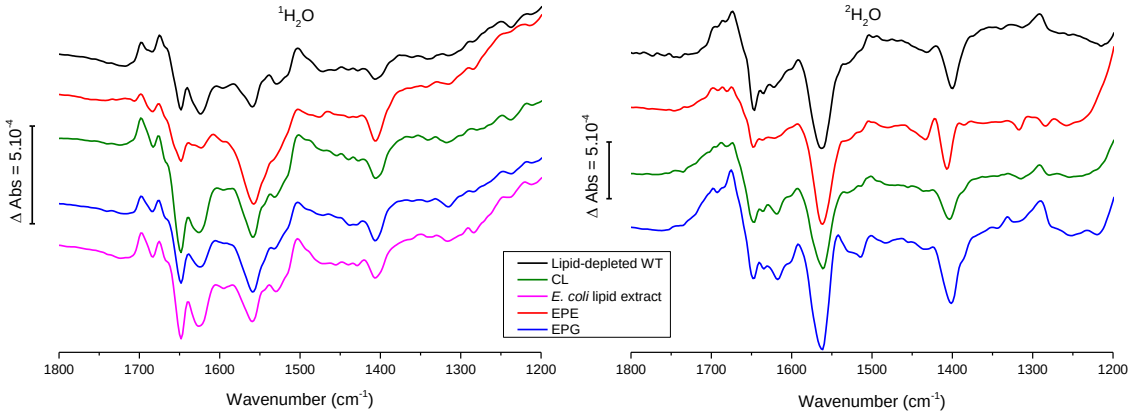

Appendix 7 : Fully oxidized *minus* fully reduced FTIR difference spectra of lipid-depleted Complex I in the absence and presence of different types of lipids. Lipid-depleted Complex I samples were used, to which 50:1 mol/mol of the corresponding lipids were added. Left panel : spectra in $^{1}H_2O$ KPi buffer ; Right panel : spectra in $^{2}H_2O$ KPi buffer.

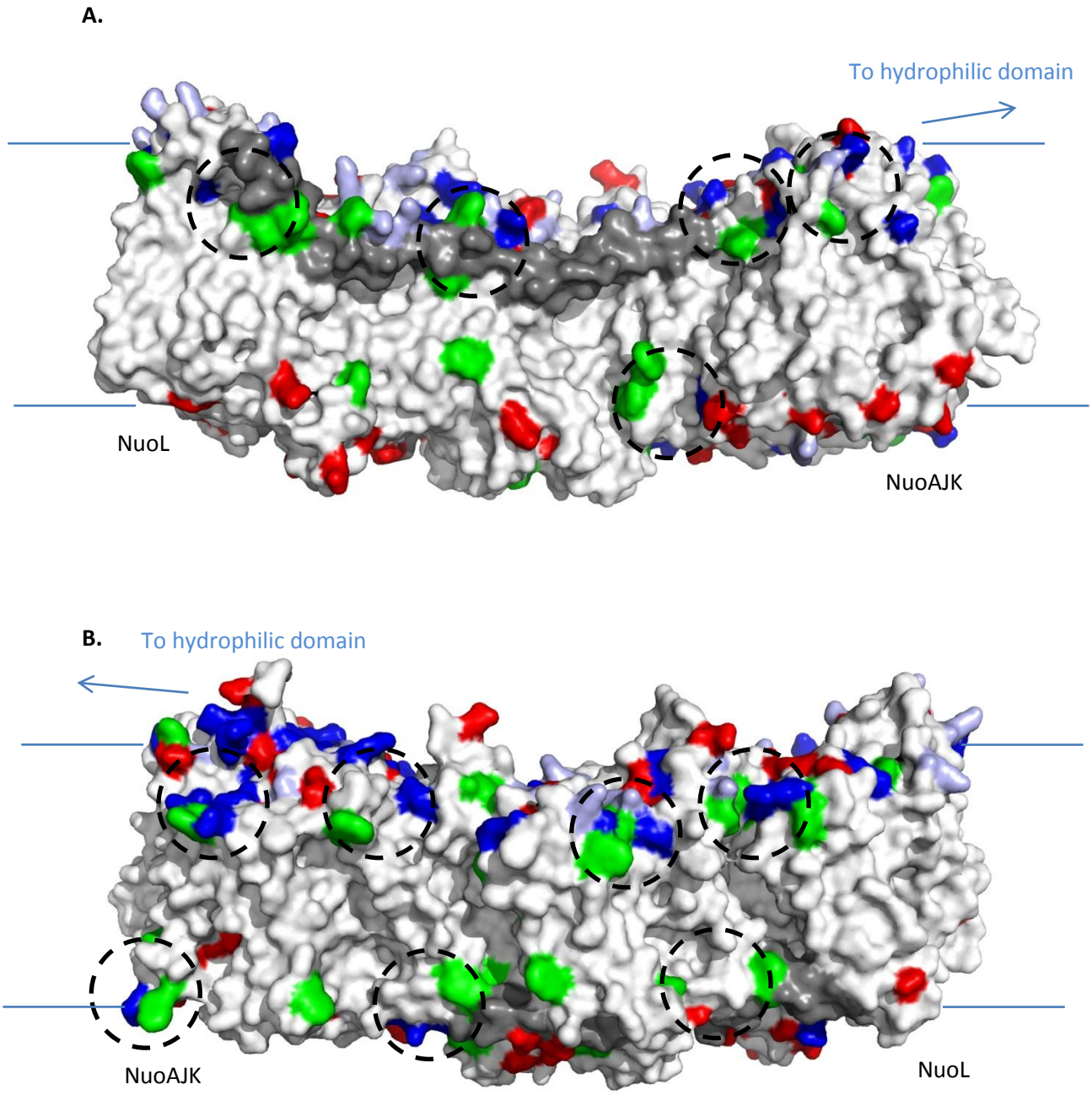

Appendix 8 : Putative specific lipid binding sites of the *E. coli* Complex I membrane domain. PDB ID : 3RKO. The approximate position of the membrane is shown by the blue lines. Arg residues are colored in blue, Lys in lightblue, Asp and Glu in red and Trp in green. The elements transducing conformational changes across the membrane domain (helix HL and βH) are shown in dark grey.Putative lipid binding sites are indicated by dashed circles. **A.** and **B.** correspond to the side views rotated by 180°.

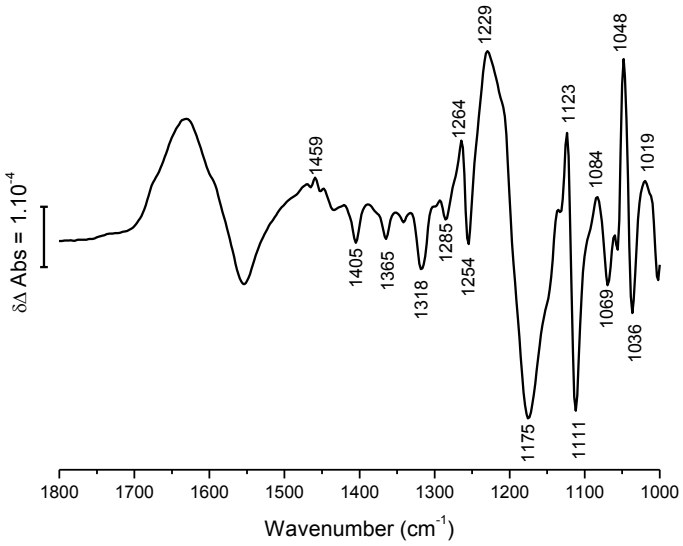

Appendix 9 : Oxidized *minus* reduced FTIR difference spectrum of MES buffer.Composition : MES 50 mM, NaCl 50 mM, DDM 0.01 %, pH 6.3.

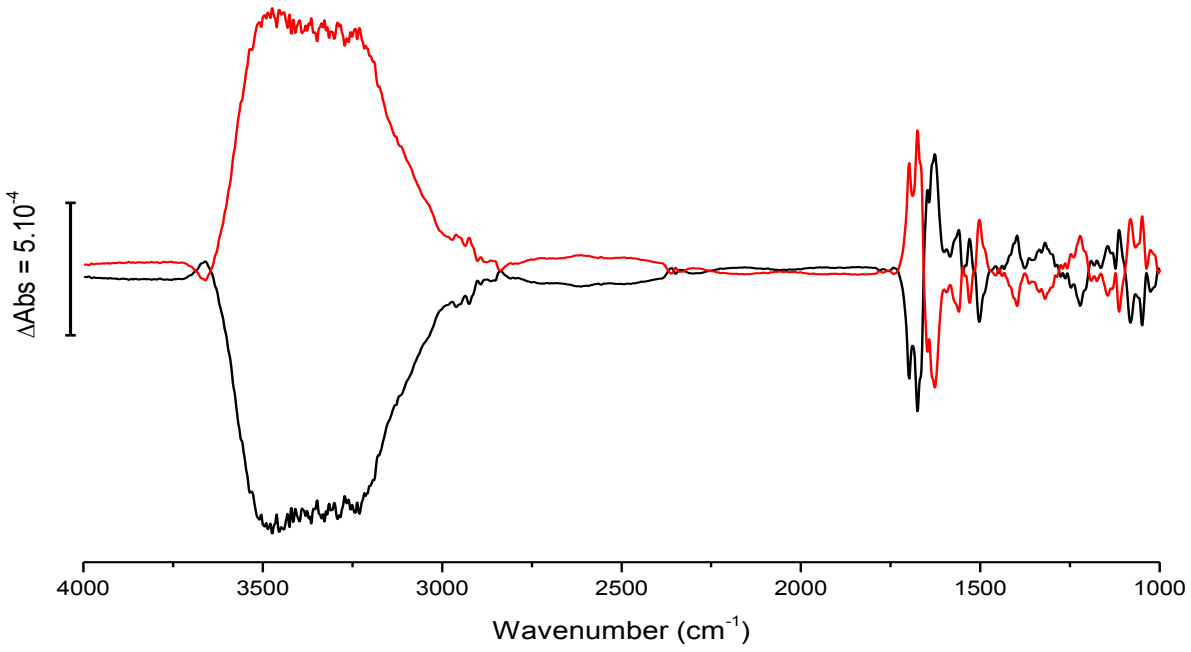

Appendix 10 : Oxidized minus reduced (red) and reduced minus oxidized (black) spectra of Zn^{2+} inhibited Complex I.

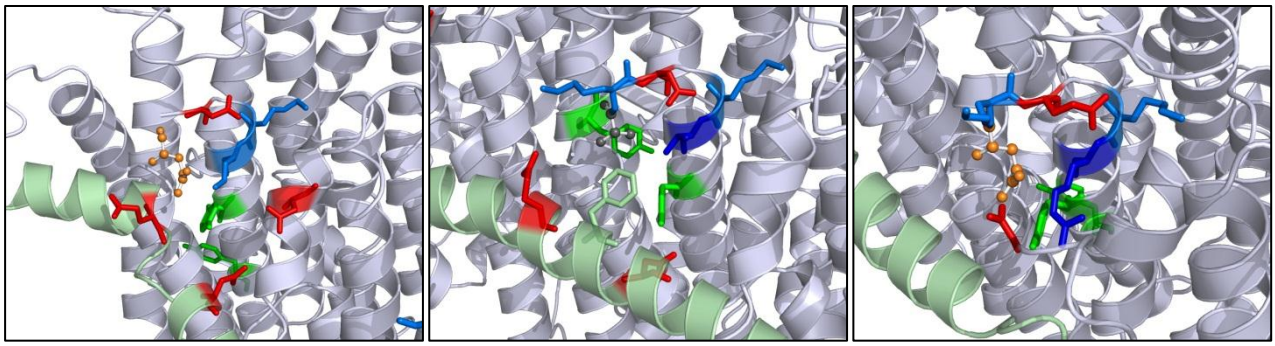

Appendix 11 : Representation of the putative Zn^{2+} binding sites on the membrane domain of Complex I from *T. thermophilus*. PDB ID : 4HEA.From left to right : Nqo12, 13 and 14. Residues are colored as follows : Gln, Asn - Orange (balls and sticks) ; Ala - Black (balls and sticks) ; Asp, Glu, $_{K}Gly^{C\text{-}term}$ - Red ; Arg - Deep Blue ; Lys - Light Blue ; Tyr - Green ; Thr - Magenta. Helix HL is colored in Pale Green.

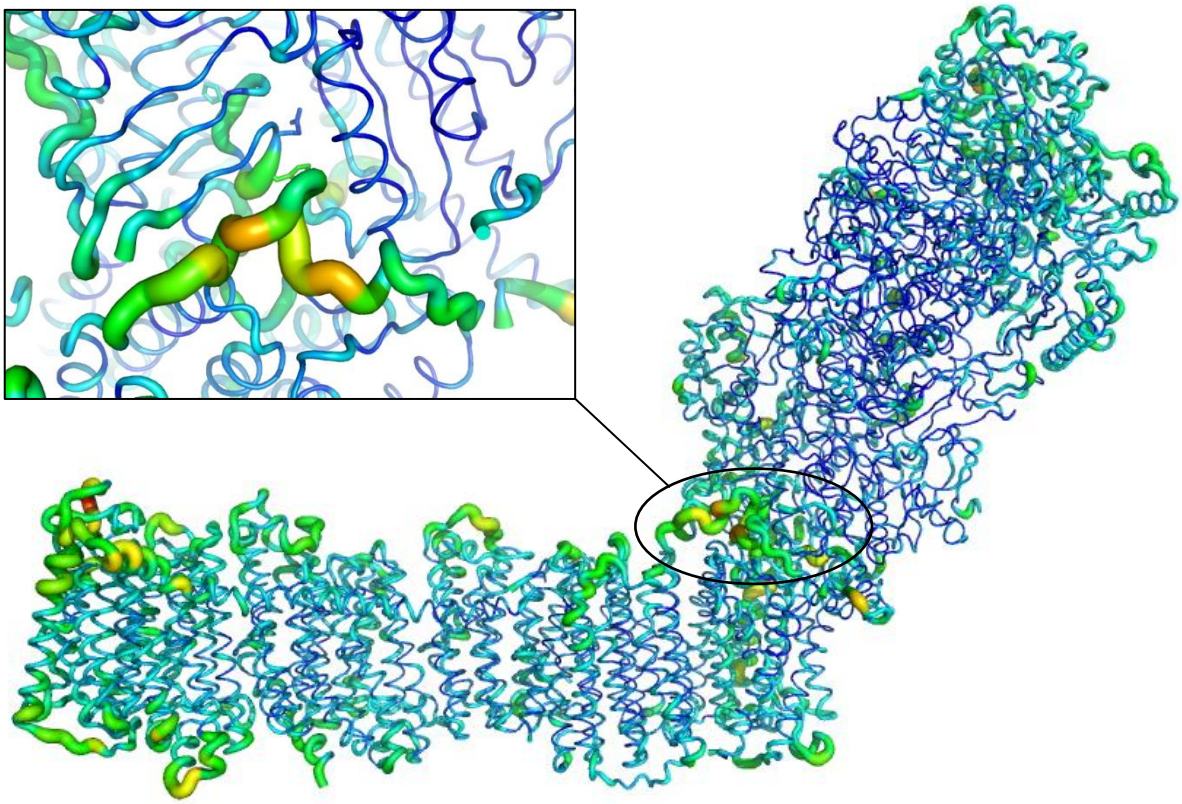

Appendix 12 : B-factor map of the 4HEA PDB entry (entire Complex I). The protein backbone is shown as a cartoon of variable thickness and color : from thin and blue (low b-factor) to thick and green (high b-factor). The inset shows the Q binding region, with $_{4}His^{34}$, $_{4}Gln^{33}$ and $_{4}His^{38}$ shown as sticks.

References

1. Amunts, A., Drory, O., and Nelson, N. (2007) The structure of a plant photosystem I supercomplex at 3.4 Å resolution, *Nature 447*, 58-63.

2. Chitnis, P. R. (2001) PHOTOSYSTEM I: Function and Physiology, *Annu Rev Plant Physiol Plant Mol Biol 52*, 593-626.

3. Umena, Y., Kawakami, K., Shen, J.-R., and Kamiya, N. (2011) Crystal structure of oxygen-evolving photosystem II at a resolution of 1.9 Å, *Nature 473*, 55-60.

4. Vinyard, D. J., Ananyev, G. M., and Charles Dismukes, G. (2013) Photosystem II: The Reaction Center of Oxygenic Photosynthesis*, *Annual Review of Biochemistry 82*, 577-606.

5. Stroebel, D., Choquet, Y., Popot, J. L., and Picot, D. (2003) An atypical haem in the cytochrome b(6)f complex, *Nature 426*, 413-418.

6. Abrahams, J. P., Leslie, A. G. W., Lutter, R., and Walker, J. E. (1994) Structure at 2.8 A resolution of F1-ATPase from bovine heart mitochondria, *Nature 370*, 621-628.

7. Junge, W., Sielaff, H., and Engelbrecht, S. (2009) Torque generation and elastic power transmission in the rotary FOF1-ATPase, *Nature 459*, 364-370.

8. Noji, H., Yasuda, R., Yoshida, M., and Kinosita, K., Jr. (1997) Direct observation of the rotation of F1-ATPase, *Nature 386*, 299-302.

9. von Ballmoos, C., Wiedenmann, A., and Dimroth, P. (2009) Essentials for ATP Synthesis by F1F0ATP Synthases, *Annual Review of Biochemistry 78*, 649-672.

10. Walker, John E. (2013) The ATP synthase: the understood, the uncertain and the unknown, *Biochemical Society Transactions 41*, 1-16.

11. Karplus, P. A., Daniels, M. J., and Herriott. (1991) Atomic structure of ferredoxin-NADP+ reductase: prototype for a structurally novel flavoenzyme family, *Science 251*, 60-66.

12. Calvin, M. (1961) Nobel Lecture: The Path of Carbon in Photosynthesis". Nobelprize.org. Nobel Media AB 2013. Web. 25 Aug 2013.

13. Brooker, R. J., Widmaier, E. P., Graham, L. E., and Stiling, P. D. (2011) *Biology - 2nd Edition*.

14. Krebs, H. A. (1953) Nobel Lecture: The Citric Acid Cycle. Nobelprize.org. Nobel Media AB 2013. Web. 24 Aug 2013. .

15. Enger, E. D., Ross, F. C., and Bailey, D. B. (2012) *Concepts in biology - 14th Edition*.

16. Rich, P. R. (2003) The molecular machinery of Keilin's respiratory chain, *Biochem Soc Trans 31*, 1095-1105.

17. Keilin, D. (1925) On Cytochrome, a Respiratory Pigment, Common to Animals, Yeast, and Higher Plants, *Proceedings of the Royal Society of London. Series B, Containing Papers of a Biological Character 98*, 312-339.

18. Warburg, O. (1928) Über die Rolle des Eisens in der Atmung des Seeigeleis nebst Bemerkungen über einige durch Eisen beschleunigte Oxydationen, In *Über die Katalytischen Wirkungen der Lebendigen Substanz* (Warburg, O., Ed.), pp 47-66, Springer Berlin Heidelberg.

19. Wieland, H. (1912) Über Hydrierung und Dehydrierung, *Berichte der deutschen chemischen Gesellschaft 45*, 484-493.

20. Slater, E. C. (1953) Mechanism of Phosphorylation in the Respiratory Chain, *Nature 172*, 975-978.

21. Mitchell, P. (1961) Coupling of phosphorylation to electron and hydrogen transfer by a chemi-osmotic type of mechanism, *Nature 191*, 144-148.

22. Mitchell, P. (2011) Chemiosmotic coupling in oxidative and photosynthetic phosphorylation, *Biochimica et Biophysica Acta (BBA) - Bioenergetics 1807*, 1507-1538.

23. Mitchell, P. (1978) Nobel Lecture: David Keilin´s Respiratory Chain Concept and Its Chemiosmotic Consequences. Nobelprize.org. Nobel Media AB 2013. Web. 24 Aug 2013. .

24. Abramson, J., Riistama, S., Larsson, G., Jasaitis, A., Svensson-Ek, M., Laakkonen, L., Puustinen, A., Iwata, S., and Wikstrom, M. (2000) The structure of the ubiquinol oxidase from Escherichia coli and its ubiquinone binding site, *Nat Struct Biol 7*, 910-917.

25. Unden, G., and Bongaerts, J. (1997) Alternative respiratory pathways of Escherichia coli: energetics and transcriptional regulation in response to electron acceptors., *Biochimica et biophysica acta 1320*, 217-234.

26. BotRejectsInc. (2007) Mitochondria and Cellular respiration - an example of a metabolic pathway, BotRejectsInc.

27. Cecchini, G. (2003) Function and structure of Complex II of the respiratory chain, *Annual Review of Biochemistry 72*, 77-109.

28. Iverson, T. M. (2013) Catalytic mechanisms of complex II enzymes: A structural perspective, *Biochimica et Biophysica Acta (BBA) - Bioenergetics 1827*, 648-657.

29. Wheeler, R. (2006) http://en.wikipedia.org/wiki/Succinate_dehydrogenase.

30. Maklashina, E., Cecchini, G., and Dikanov, S. A. (2013) Defining a direction: Electron transfer and catalysis in Escherichia coli complex II enzymes, *Biochimica et Biophysica Acta (BBA) - Bioenergetics 1827*, 668-678.

31. Crofts, A. R. (2004) The Cytochrome bc1 Complex: Function in the Context of Structure, *Annual Review of Physiology 66*, 689-733.

32. Covian, R., and Trumpower, B. L. (2008) Regulatory interactions in the dimeric cytochrome bc1 complex: The advantages of being a twin, *Biochimica et Biophysica Acta (BBA) - Bioenergetics 1777*, 1079-1091.

33. Cramer, W. A., Hasan, S. S., and Yamashita, E. (2011) The Q cycle of cytochrome bc complexes: A structure perspective, *Biochimica et Biophysica Acta (BBA) - Bioenergetics 1807*, 788-802.

34. Mitchell, P. (1975) Protonmotive redox mechanism of the cytochrome b-c1 complex in the respiratory chain: Protonmotive ubiquinone cycle, *FEBS Letters 56*, 1-6.

35. Crofts, A. R. (2004) http://www.life.illinois.edu/crofts/bc-complex_site/.

36. Zhang, Z., Huang, L., Shulmeister, V. M., Chi, Y. I., Kim, K. K., Hung, L. W., Crofts, A. R., Berry, E. A., and Kim, S. H. (1998) Electron transfer by domain movement in cytochrome bc1, *Nature 392*, 677-684.

37. Michel, H., Behr, J., Harrenga, A., and Kannt, A. (1998) Cytochrome c oxidase: Structure and Spectroscopy, *Annual Review of Biophysics and Biomolecular Structure 27*, 329-356.

38. Yoshikawa, S., Muramoto, K., and Shinzawa-Itoh, K. (2011) Proton-Pumping Mechanism of Cytochrome c Oxidase, *Annual Review of Biophysics 40*, 205-223.

39. Tsukihara, T., Aoyama, H., Yamashita, E., Tomizaki, T., Yamaguchi, H., Shinzawa-Itoh, K., Nakashima, R., Yaono, R., and Yoshikawa, S. (1996) The Whole Structure of the 13-Subunit Oxidized Cytochrome c Oxidase at 2.8 Å, *Science 272*, 1136-1144.

40. Lee, S. J., Yamashita, E., Abe, T., Fukumoto, Y., Tsukihara, T., Shinzawa-Itoh, K., Ueda, H., and Yoshikawa, S. (2001) Intermonomer interactions in dimer of bovine heart cytochrome c oxidase, *Acta Crystallographica Section D 57*, 941-947.

41. Yoshikawa, S., Shinzawa-Itoh, K., Nakashima, R., Yaono, R., Yamashita, E., Inoue, N., Yao, M., Fei, M. J., Libeu, C. P., Mizushima, T., Yamaguchi, H., Tomizaki, T., and Tsukihara, T. (1998) Redox-Coupled Crystal Structural

Changes in Bovine Heart Cytochrome c Oxidase, *Science 280*, 1723-1729.

42. Nyquist, R. M., Heitbrink, D., Bolwien, C., Gennis, R. B., and Heberle, J. (2003) Direct observation of protonation reactions during the catalytic cycle of cytochrome c oxidase, *Proceedings of the National Academy of Sciences 100*, 8715-8720.

43. Lodish, H. (2008) *Molecular cell biology, 6th edition*, W.H. Freeman and Company.

44. Moser, C. C., Farid, T. A., Chobot, S. E., and Dutton, P. L. (2006) Electron tunneling chains of mitochondria, *Biochimica et Biophysica Acta (BBA) - Bioenergetics 1757*, 1096-1109.

45. Hayashi, T., and Stuchebrukhov, A. A. (2011) First principles studies of electron tunneling in proteins, *Comput Theor Chem 975*, 61-68.

46. Wolf, D. E., Hoffman, C. H., Trenner, N. R., Arison, B. H., Shunk, C. H., Linn, B. O., McPherson, J. F., and Folkers, K. (1958) COENZYME Q. I. STRUCTURE STUDIES ON THE COENZYME Q GROUP, *Journal of the American Chemical Society 80*, 4752-4752.

47. Urban, P. F., and Klingenberg, M. (1969) On the Redox Potentials of Ubiquinone and Cytochrome b in the Respiratory Chain, *European Journal of Biochemistry 9*, 519-525.

48. Berthomieu, C., Nabedryk, E., Mantele, W., and Breton, J. (1990) Characterization by FTIR spectroscopy of the photoreduction of the primary quinone acceptor QA in photosystem II, *FEBS Lett 269*, 363-367.

49. Efremov, R. G., and Sazanov, L. A. (2012) The coupling mechanism of respiratory complex I — A structural and evolutionary perspective, *Biochimica et Biophysica Acta (BBA) - Bioenergetics 1817*, 1785-1795.

50. Guin, P. S., Das, S., and Mandal, P. C. (2011) Electrochemical Reduction of Quinones in Different Media: A Review, *International Journal of Electrochemistry 2011*, 1-22.

51. Ragan, C. I., and Reed, J. S. (1986) Regulation of electron transfer by the quinone pool, *J Bioenerg Biomembr 18*, 403-418.

52. Lapuente-Brun, E., Moreno-Loshuertos, R., Acin-Perez, R., Latorre-Pellicer, A., Colas, C., Balsa, E., Perales-Clemente, E., Quiros, P. M., Calvo, E., Rodriguez-Hernandez, M. A., Navas, P., Cruz, R., Carracedo, A., Lopez-Otin, C., Perez-Martos, A., Fernandez-Silva, P., Fernandez-Vizarra, E., and Enriquez, J. A. (2013) Supercomplex Assembly Determines Electron Flux in the Mitochondrial Electron Transport Chain, *Science 340*, 1567-1570.

53. Fisher, N., and Rich, P. R. (2000) A motif for quinone binding sites in respiratory and photosynthetic systems, *Journal of Molecular Biology 296*, 1153-1162.

54. Bushnell, G. W., Louie, G. V., and Brayer, G. D. (1990) High-resolution three-dimensional structure of horse heart cytochrome c, *Journal of Molecular Biology 214*, 585-595.

55. Vanderkooi, J. M., Maniara, G., and Erecinska, M. (1985) Mobility of fluorescent derivatives of cytochrome c in mitochondria, *The Journal of Cell Biology 100*, 435-441.

56. Solmaz, S. R. N., and Hunte, C. (2008) Structure of Complex III with Bound Cytochrome c in Reduced State and Definition of a Minimal Core Interface for Electron Transfer, *Journal of Biological Chemistry 283*, 17542-17549.

57. Jiang, X., and Wang, X. (2004) Cytochrome c-mediated apoptosis, *Annual Review of Biochemistry 73*, 87-106.

58. Orrenius, S., Gogvadze, V., and Zhivotovsky, B. (2007) Mitochondrial Oxidative Stress: Implications for Cell Death, *Annual Review of Pharmacology and Toxicology 47*, 143-183.

59. Bayir, H., Fadeel, B., Palladino, M. J., Witasp, E., Kurnikov, I. V., Tyurina, Y. Y., Tyurin, V. A., Amoscato, A. A., Jiang, J., Kochanek, P. M., DeKosky, S. T., Greenberger, J. S., Shvedova, A. A., and Kagan, V. E. (2006) Apoptotic interactions of cytochrome c: Redox flirting

with anionic phospholipids within and outside of mitochondria, *Biochimica et Biophysica Acta (BBA) - Bioenergetics 1757*, 648-659.

60. Hanske, J., Toffey, J. R., Morenz, A. M., Bonilla, A. J., Schiavoni, K. H., and Pletneva, E. V. (2012) Conformational properties of cardiolipin-bound cytochrome c, *Proc Natl Acad Sci U S A 109*, 125-130.

61. Davies, K. M., Anselmi, C., Wittig, I., Faraldo-Gomez, J. D., and Kuhlbrandt, W. (2012) Structure of the yeast F1Fo-ATP synthase dimer and its role in shaping the mitochondrial cristae, *Proc Natl Acad Sci U S A 109*, 13602-13607.

62. Davies, K. M., Strauss, M., Daum, B., Kief, J. H., Osiewacz, H. D., Rycovska, A., Zickermann, V., and Kuhlbrandt, W. (2011) Macromolecular organization of ATP synthase and complex I in whole mitochondria, *Proc Natl Acad Sci U S A 108*, 14121-14126.

63. Medvedev, E. S., and Stuchebrukhov, A. A. (2011) Proton diffusion along biological membranes, *Journal of Physics: Condensed Matter 23*, 234103.

64. Chance, B., and Williams, G. R. (1955) A Method for the Localization of Sites for Oxidative Phosphorylation, *Nature 176*, 250-254.

65. Vartak, R., Porras, C. A.-M., and Bai, Y. (2013) Respiratory supercomplexes: structure, function and assembly, *Protein & Cell 4*, 582-590.

66. Arias-Cartin, R., Grimaldi, S., Arnoux, P., Guigliarelli, B., and Magalon, A. (2012) Cardiolipin binding in bacterial respiratory complexes: Structural and functional implications, *Biochimica et Biophysica Acta (BBA) - Bioenergetics 1817*, 1937-1949.

67. Böttinger, L., Horvath, S. E., Kleinschroth, T., Hunte, C., Daum, G., Pfanner, N., and Becker, T. (2012) Phosphatidylethanolamine and Cardiolipin Differentially Affect the Stability of Mitochondrial Respiratory Chain Supercomplexes, *Journal of Molecular Biology 423*, 677-686.

68. Bultema, J. B., Braun, H.-P., Boekema, E. J., and Kouřil, R. (2009) Megacomplex organization of the oxidative phosphorylation system by structural analysis of respiratory supercomplexes from potato, *Biochimica et Biophysica Acta (BBA) - Bioenergetics 1787*, 60-67.

69. Sousa, P. M. F., Silva, S. T. N., Hood, B. L., Charro, N., Carita, J. N., Vaz, F., Penque, D., Conrads, T. P., and Melo, A. M. P. (2011) Supramolecular organizations in the aerobic respiratory chain of Escherichia coli, *Biochimie 93*, 418-425.

70. Voet, D., and Voet, J. G. (2011) *Biochemistry - 4th edition*, Wiley.

71. Watt, I. N., Montgomery, M. G., Runswick, M. J., Leslie, A. G. W., and Walker, J. E. (2010) Bioenergetic cost of making an adenosine triphosphate molecule in animal mitochondria, *Proceedings of the National Academy of Sciences*.

72. Hinkle, P. C. (2005) P/O ratios of mitochondrial oxidative phosphorylation, *Biochimica et Biophysica Acta (BBA) - Bioenergetics 1706*, 1-11.

73. Wilson, D. F. (1994) Factors affecting the rate and energetics of mitochondrial oxidative phosphorylation, *Med Sci Sports Exerc 26*, 37-43.

74. Nicholls, D., and Ferguson, S. (2002) *Bioenergetics 3rd edition*, Elsevier.

75. Magnitsky, S., Toulokhonova, L., Yano, T., Sled, V. D., Hagerhall, C., Grivennikova, V. G., Burbaev, D. S., Vinogradov, A. D., and Ohnishi, T. (2002) EPR characterization of ubisemiquinones and iron-sulfur cluster N2, central components of the energy coupling in the NADH-ubiquinone oxidoreductase (complex I) in situ, *J Bioenerg Biomembr 34*, 193-208.

76. Vinogradov, A. D., Sled, V. D., Burbaev, D. S., Grivennikova, V. G., Moroz, I. A., and Ohnishi,

T. (1995) Energy-dependent Complex I-associated ubisemiquinones in submitochondrial particles, *FEBS Lett 370*, 83-87.

77. Hatefi, Y., Haavik, A. G., and Griffiths, D. E. (1962) Studies on the electron transfer system. XL. Preparation and properties of mitochondrial DPNH-coenzyme Q reductase, *The Journal of biological chemistry 237*, 1676-1680.

78. Brandt, U. (2006) Energy converting NADH:quinone oxidoreductase (complex I), *Annu Rev Biochem 75*, 69-92.

79. Hirst, J. (2013) Mitochondrial Complex I, *Annual Review of Biochemistry 82*, 551-575.

80. Verkhovskaya, M., and Bloch, D. A. (2013) Energy-converting respiratory Complex I: On the way to the molecular mechanism of the proton pump, *The International Journal of Biochemistry & Cell Biology 45*, 491-511.

81. Walker, J. E. (1992) The NADH:ubiquinone oxidoreductase (complex I) of respiratory chains, *Quarterly Reviews of Biophysics 25*, 253-324.

82. Klodmann, J., Sunderhaus, S., Nimtz, M., Jansch, L., and Braun, H. P. (2010) Internal Architecture of Mitochondrial Complex I from Arabidopsis thaliana, *The Plant Cell 22*, 797-810.

83. Hirst, J. (2011) Why does mitochondrial complex I have so many subunits?, *Biochemical Journal 437*, e1-e3.

84. Wong, L. J. C. (2013) *Mitochondrial Disorders Caused by Nuclear Genes*, Vol. XII.

85. Mimaki, M., Wang, X., McKenzie, M., Thorburn, D. R., and Ryan, M. T. (2012) Understanding mitochondrial complex I assembly in health and disease, *Biochimica et Biophysica Acta (BBA) - Bioenergetics 1817*, 851-862.

86. Perales-Clemente, E., Fernandez-Vizarra, E., Acin-Perez, R., Movilla, N., Bayona-Bafaluy, M. P., Moreno-Loshuertos, R., Perez-Martos, A., Fernandez-Silva, P., and Enriquez, J. A. (2010) Five Entry Points of the Mitochondrially Encoded Subunits in Mammalian Complex I Assembly, *Molecular and Cellular Biology 30*, 3038-3047.

87. Schneider, D., Pohl, T., Walter, J., Dörner, K., Kohlstädt, M., Berger, A., Spehr, V., and Friedrich, T. (2008) Assembly of the Escherichia coli NADH:ubiquinone oxidoreductase (complex I), *Biochimica et Biophysica Acta (BBA) - Bioenergetics 1777*, 735-739.

88. Moreno-Lastres, D., Fontanesi, F., García-Consuegra, I., Martín, Miguel A., Arenas, J., Barrientos, A., and Ugalde, C. (2012) Mitochondrial Complex I Plays an Essential Role in Human Respirasome Assembly, *Cell Metabolism 15*, 324-335.

89. Baradaran, R., Berrisford, J. M., Minhas, G. S., and Sazanov, L. A. (2013) Crystal structure of the entire respiratory complex I, *Nature 494*, 443-448.

90. Efremov, R. G., Baradaran, R., and Sazanov, L. A. (2010) The architecture of respiratory complex I, *Nature 465*, 441-445.

91. Sazanov, L. A. (2006) Structure of the Hydrophilic Domain of Respiratory Complex I from Thermus thermophilus, *Science 311*, 1430-1436.

92. Efremov, R. G., and Sazanov, L. A. (2011) Structure of the membrane domain of respiratory complex I, *Nature 476*, 414-420.

93. Hunte, C., Zickermann, V., and Brandt, U. (2010) Functional Modules and Structural Basis of Conformational Coupling in Mitochondrial Complex I, *Science 329*, 448-451.

94. Ohnishi, T. (1998) Iron–sulfur clusters/semiquinones in Complex I, *Biochimica et Biophysica Acta (BBA) - Bioenergetics 1364*, 186-206.

95. Friedrich, T. (1998) The NADH:ubiquinone oxidoreductase (complex I) from Escherichia

coli, *Biochimica et Biophysica Acta (BBA) - Bioenergetics 1364*, 134-146.

96. Spehr, V., Schlitt, A., Scheide, D., Guénebaut, V., and Friedrich, T. (1999) Overexpression of the Escherichia coli nuo-Operon and Isolation of the Overproduced NADH:Ubiquinone Oxidoreductase (Complex I)†, *Biochemistry 38*, 16261-16267.

97. Pohl, T., Uhlmann, M., Kaufenstein, M., and Friedrich, T. (2007) Lambda Red-Mediated Mutagenesis and Efficient Large Scale Affinity Purification of the Escherichia coli NADH:Ubiquinone Oxidoreductase (Complex I), *Biochemistry 46*, 10694-10702.

98. Morina, K., Schulte, M., Hubrich, F., Dorner, K., Steimle, S., Stolpe, S., and Friedrich, T. (2011) Engineering the respiratory complex I to energy-converting NADPH:ubiquinone oxidoreductase, *J Biol Chem 286*, 34627-34634.

99. Steimle, S., Willistein, M., Hegger, P., Janoschke, M., Erhardt, H., and Friedrich, T. (2012) Asp563 of the horizontal helix of subunit NuoL is involved in proton translocation by the respiratory complex I, *FEBS Letters 586*, 699-704.

100. Moparthi, V. K., and Hägerhäll, C. (2011) The Evolution of Respiratory Chain Complex I from a Smaller Last Common Ancestor Consisting of 11 Protein Subunits, *Journal of Molecular Evolution 72*, 484-497.

101. Mathiesen, C., and Hägerhäll, C. (2003) The 'antiporter module' of respiratory chain Complex I includes the MrpC/NuoK subunit – a revision of the modular evolution scheme, *FEBS Letters 549*, 7-13.

102. Swartz, T., Ikewada, S., Ishikawa, O., Ito, M., and Krulwich, T. (2005) The Mrp system: a giant among monovalent cation/proton antiporters?, *Extremophiles 9*, 345-354.

103. Yip, C. Y., Harbour, M. E., Jayawardena, K., Fearnley, I. M., and Sazanov, L. A. (2011) Evolution of respiratory complex I: "supernumerary" subunits are present in the alpha-proteobacterial enzyme, *J Biol Chem 286*, 5023-5033.

104. Birrell, J. A., and Hirst, J. (2013) Investigation of NADH Binding, Hydride Transfer, and NAD+Dissociation during NADH Oxidation by Mitochondrial Complex I Using Modified Nicotinamide Nucleotides, *Biochemistry 52*, 4048-4055.

105. Johnson, D. C., Dean, D. R., Smith, A. D., and Johnson, M. K. (2005) Structure, function, and formation of biological iron-sulfur clusters, *Annu Rev Biochem 74*, 247-281.

106. Hayashi, T., and Stuchebrukhov, A. A. (2010) Electron tunneling in respiratory complex I, *Proc Natl Acad Sci U S A 107*, 19157-19162.

107. Pohl, T., Bauer, T., Dörner, K., Stolpe, S., Sell, P., Zocher, G., and Friedrich, T. (2007) Iron−Sulfur Cluster N7 of the NADH:Ubiquinone Oxidoreductase (Complex I) Is Essential for Stability but Not Involved in Electron Transfer†, *Biochemistry 46*, 6588-6596.

108. Berrisford, J. M., and Sazanov, L. A. (2009) Structural Basis for the Mechanism of Respiratory Complex I, *Journal of Biological Chemistry 284*, 29773-29783.

109. Bridges, H. R., Bill, E., and Hirst, J. (2012) Mössbauer Spectroscopy on Respiratory Complex I: The Iron–Sulfur Cluster Ensemble in the NADH-Reduced Enzyme Is Partially Oxidized, *Biochemistry 51*, 149-158.

110. Medvedev, E. S., Couch, V. A., and Stuchebrukhov, A. A. (2010) Determination of the intrinsic redox potentials of FeS centers of respiratory complex I from experimental titration curves, *Biochimica et Biophysica Acta (BBA) - Bioenergetics 1797*, 1665-1671.

111. Ohnishi, S. T., Shinzawa-Itoh, K., Ohta, K., Yoshikawa, S., and Ohnishi, T. (2010) New insights into the superoxide generation sites in bovine heart NADH-ubiquinone oxidoreductase (Complex I): The significance of protein-associated ubiquinone and the dynamic shifting of generation sites between

semiflavin and semiquinone radicals, *Biochimica et Biophysica Acta (BBA) - Bioenergetics 1797*, 1901-1909.

112. Vinogradov, A. D. (1998) Catalytic properties of the mitochondrial NADH-ubiquinone oxidoreductase (complex I) and the pseudo-reversible active/inactive enzyme transition, *Biochimica et Biophysica Acta 1364*, 169-185.

113. Pryde, K. R., and Hirst, J. (2011) Superoxide Is Produced by the Reduced Flavin in Mitochondrial Complex I: A SINGLE, UNIFIED MECHANISM THAT APPLIES DURING BOTH FORWARD AND REVERSE ELECTRON TRANSFER, *Journal of Biological Chemistry 286*, 18056-18065.

114. Hikita, M., Shinzawa-Itoh, K., Moriyama, M., Ogura, T., Kihira, K., and Yoshikawa, S. (2013) Resonance Raman Spectral Properties of FMN of Bovine Heart NADH:ubiquinone Oxidoreductase Suggesting a Mechanism for the Prevention of Spontaneous Production of Reactive Oxygen Species, *Biochemistry 52*, 98-104.

115. Mayhew, S. G. (1999) The effects of pH and semiquinone formation on the oxidation–reduction potentials of flavin mononucleotide, *European Journal of Biochemistry 265*, 698-702.

116. Esterházy, D., King, M. S., Yakovlev, G., and Hirst, J. (2008) Production of Reactive Oxygen Species by Complex I (NADH:Ubiquinone Oxidoreductase) from Escherichia coli and Comparison to the Enzyme from Mitochondria†, *Biochemistry 47*, 3964-3971.

117. Sled, V. D., Rudnitzky, N. I., Hatefi, Y., and Ohnishi, T. (1994) Thermodynamic Analysis of Flavin in Mitochondrial NADH:Ubiquinone Oxidoreductase (Complex I), *Biochemistry 33*, 10069-10075.

118. Lostao, a., Gómez-Moreno, C., Mayhew, S. G., and Sancho, J. (1997) Differential stabilization of the three FMN redox forms by tyrosine 94 and tryptophan 57 in flavodoxin from Anabaena and its influence on the redox potentials., *Biochemistry 36*, 14334-14344.

119. Euro, L., Belevich, G., Bloch, D. A., Verkhovsky, M. I., Wikström, M., and Verkhovskaya, M. (2009) The role of the invariant glutamate 95 in the catalytic site of Complex I from Escherichia coli, *Biochimica et Biophysica Acta (BBA) - Bioenergetics 1787*, 68-73.

120. Gostimskaya, I. S., Grivennikova, V. G., Cecchini, G., and Vinogradov, A. D. (2007) Reversible dissociation of flavin mononucleotide from the mammalian membrane-bound NADH:ubiquinone oxidoreductase (complex I), *FEBS Letters 581*, 5803-5806.

121. Bénit, P., Chretien, D., Kadhom, N., de Lonlay-Debeney, P., Cormier-Daire, V., Cabral, a., Peudenier, S., Rustin, P., Munnich, a., and Rötig, a. (2001) Large-scale deletion and point mutations of the nuclear NDUFV1 and NDUFS1 genes in mitochondrial complex I deficiency., *American journal of human genetics 68*, 1344-1352.

122. Pagniez-Mammeri, H., Loublier, S., Legrand, A., Bénit, P., Rustin, P., and Slama, A. (2012) Mitochondrial complex I deficiency of nuclear origin I. Structural genes., *Molecular genetics and metabolism 105*, 163-172.

123. Carroll, J., Ding, S., Fearnley, I. M., and Walker, J. E. (2013) Post-translational Modifications near the Quinone Binding Site of Mammalian Complex I, *Journal of Biological Chemistry 288*, 24799-24808.

124. Ripple, M. O., Kim, N., and Springett, R. (2013) Mammalian Complex I Pumps 4 Protons per 2 Electrons at High and Physiological Proton Motive Force in Living Cells, *Journal of Biological Chemistry 288*, 5374-5380.

125. Agmon, N. (1995) The Grotthuss mechanism, *Chemical Physics Letters 244*, 456-462.

126. Freier, E., Wolf, S., and Gerwert, K. (2011) Proton transfer via a transient linear water-molecule chain in a membrane protein, *Proc Natl Acad Sci U S A 108*, 11435-11439.

127. Wraight, C. A. (2006) Chance and design—Proton transfer in water, channels and

bioenergetic proteins, *Biochimica et Biophysica Acta (BBA) - Bioenergetics 1757*, 886-912.

128. Ohnishi, T. (2010) Structural biology: Piston drives a proton pump, *Nature 465*, 428-429.

129. Efremov, R. G., and Sazanov, L. A. (2011) Respiratory complex I: 'steam engine' of the cell?, *Curr Opin Struct Biol 21*, 532-540.

130. Gonzalez-Halphen, D., Ghelli, A., Iommarini, L., Carelli, V., and Esposti, M. D. (2011) Mitochondrial complex I and cell death: a semi-automatic shotgun model, *Cell Death and Disease 2*, e222.

131. Ohnishi, S. T., Salerno, J. C., and Ohnishi, T. (2010) Possible roles of two quinone molecules in direct and indirect proton pumps of bovine heart NADH-quinone oxidoreductase (complex I), *Biochimica et Biophysica Acta (BBA) - Bioenergetics 1797*, 1891-1893.

132. Treberg, J. R., and Brand, M. D. (2011) A Model of the Proton Translocation Mechanism of Complex I, *Journal of Biological Chemistry 286*, 17579-17584.

133. Brandt, U. (2011) A two-state stabilization-change mechanism for proton-pumping complex I, *Biochimica et Biophysica Acta (BBA) - Bioenergetics 1807*, 1364-1369.

134. Wikstrom, M., and Hummer, G. (2012) Stoichiometry of proton translocation by respiratory complex I and its mechanistic implications, *Proceedings of the National Academy of Sciences 109*, 4431-4436.

135. Verkhovsky, M., Bloch, D. A., and Verkhovskaya, M. (2012) Tightly-bound ubiquinone in the Escherichia coli respiratory Complex I, *Biochimica et Biophysica Acta (BBA) - Bioenergetics 1817*, 1550-1556.

136. Newmeyer, D. D., and Ferguson-Miller, S. (2003) Mitochondria: releasing power for life and unleashing the machineries of death, *Cell 112*, 481-490.

137. Ott, M., Gogvadze, V., Orrenius, S., and Zhivotovsky, B. (2007) Mitochondria, oxidative stress and cell death, *Apoptosis 12*, 913-922.

138. Lin, M. T., and Beal, M. F. (2006) Mitochondrial dysfunction and oxidative stress in neurodegenerative diseases, *Nature 443*, 787-795.

139. Grivennikova, V. G., and Vinogradov, A. D. (2013) Partitioning of superoxide and hydrogen peroxide production by mitochondrial respiratory complex I, *Biochimica et Biophysica Acta (BBA) - Bioenergetics 1827*, 446-454.

140. Treberg, J. R., Quinlan, C. L., and Brand, M. D. (2011) Evidence for Two Sites of Superoxide Production by Mitochondrial NADH-Ubiquinone Oxidoreductase (Complex I), *Journal of Biological Chemistry 286*, 27103-27110.

141. Berrisford, J. M., Thompson, C. J., and Sazanov, L. A. (2008) Chemical and NADH-induced, ROS-dependent, cross-linking between subunits of complex I from Escherichia coli and Thermus thermophilus, *Biochemistry 47*, 10262-10270.

142. Stefanatos, R., and Sanz, A. (2011) Mitochondrial complex I: A central regulator of the aging process, *Cell Cycle 10*, 1528-1532.

143. Distelmaier, F., Koopman, W. J. H., van den Heuvel, L. P., Rodenburg, R. J., Mayatepek, E., Willems, P. H. G. M., and Smeitink, J. A. M. (2008) Mitochondrial complex I deficiency: from organelle dysfunction to clinical disease, *Brain 132*, 833-842.

144. Papa, S., and De Rasmo, D. (2013) Complex I deficiencies in neurological disorders, *Trends in Molecular Medicine 19*, 61-69.

145. Keeney, P. M. (2006) Parkinson's Disease Brain Mitochondrial Complex I Has Oxidatively Damaged Subunits and Is Functionally Impaired and Misassembled, *Journal of Neuroscience 26*, 5256-5264.

146. He, X., Zhou, A., Lu, H., Chen, Y., Huang, G., Yue, X., Zhao, P., and Wu, Y. (2013) Suppression of mitochondrial complex I

influences cell metastatic properties, *PLoS One 8*, e61677.

147. Iommarini, L., Calvaruso, M. A., Kurelac, I., Gasparre, G., and Porcelli, A. M. (2013) Complex I impairment in mitochondrial diseases and cancer: Parallel roads leading to different outcomes, *The International Journal of Biochemistry & Cell Biology 45*, 47-63.

148. Santidrian, A. F., Matsuno-Yagi, A., Ritland, M., Seo, B. B., LeBoeuf, S. E., Gay, L. J., Yagi, T., and Felding-Habermann, B. (2013) Mitochondrial complex I activity and NAD+/NADH balance regulate breast cancer progression, *Journal of Clinical Investigation 123*, 1068-1081.

149. Sharpley, M. S., and Hirst, J. (2006) The Inhibition of Mitochondrial Complex I (NADH:Ubiquinone Oxidoreductase) by Zn2+, *Journal of Biological Chemistry 281*, 34803-34809.

150. Kotlyar, A. B., Karliner, J. S., and Cecchini, G. (2005) A novel strong competitive inhibitor of complex I, *FEBS Letters 579*, 4861-4866.

151. Yoshida, T., Murai, M., Abe, M., Ichimaru, N., Harada, T., Nishioka, T., and Miyoshi, H. (2007) Crucial structural factors and mode of action of polyene amides as inhibitors for mitochondrial NADH-ubiquinone oxidoreductase (complex I), *Biochemistry 46*, 10365-10372.

152. Morgan, J. B., Mahdi, F., Liu, Y., Coothankandaswamy, V., Jekabsons, M. B., Johnson, T. A., Sashidhara, K. V., Crews, P., Nagle, D. G., and Zhou, Y.-D. (2010) The marine sponge metabolite mycothiazole: A novel prototype mitochondrial complex I inhibitor, *Bioorganic & Medicinal Chemistry 18*, 5988-5994.

153. Fedeles, B. I., Zhu, A. Y., Young, K. S., Hillier, S. M., Proffitt, K. D., Essigmann, J. M., and Croy, R. G. (2011) Chemical Genetics Analysis of an Aniline Mustard Anticancer Agent Reveals Complex I of the Electron Transport Chain as a Target, *Journal of Biological Chemistry 286*, 33910-33920.

154. Nakanishi, S., Abe, M., Yamamoto, S., Murai, M., and Miyoshi, H. (2011) Bis-THF motif of acetogenin binds to the third matrix-side loop of ND1 subunit in mitochondrial NADH-ubiquinone oxidoreductase, *Biochimica et Biophysica Acta (BBA) - Bioenergetics 1807*, 1170-1176.

155. Höfle, G., Gerth, K., Reichenbach, H., Kunze, B., Sasse, F., Forche, E., and Prusov, E. V. (2012) Isolation, Biological Activity Evaluation, Structure Elucidation, and Total Synthesis of Eliamid: A Novel Complex I Inhibitor, *Chemistry - A European Journal 18*, 11362-11370.

156. Schapira, A. H. V. (2010) Complex I: Inhibitors, inhibition and neurodegeneration, *Exp Neurol 224*, 331-335.

157. Singer, S. J., and Nicolson, G. L. (1972) The fluid mosaic model of the structure of cell membranes, *Science 175*, 720-731.

158. Lingwood, D., and Simons, K. (2010) Lipid rafts as a membrane-organizing principle, *Science 327*, 46-50.

159. Gohil, V. M., and Greenberg, M. L. (2009) Mitochondrial membrane biogenesis: phospholipids and proteins go hand in hand, *The Journal of Cell Biology 184*, 469-472.

160. Hunte, C., and Richers, S. (2008) Lipids and membrane protein structures., *Current opinion in structural biology 18*, 406-411.

161. Niemelä, P. S., Miettinen, M. S., Monticelli, L., Hammaren, H., Bjelkmar, P., Murtola, T., Lindahl, E., and Vattulainen, I. (2010) Membrane proteins diffuse as dynamic complexes with lipids., *Journal of the American Chemical Society 132*, 7574-7575.

162. Lee, A. G. (2004) How lipids affect the activities of integral membrane proteins., *Biochimica et biophysica acta 1666*, 62-87.

163. Andersen, O. S., and Koeppe, R. E. (2007) Bilayer thickness and membrane protein function: an energetic perspective., *Annual review of biophysics and biomolecular structure 36*, 107-130.

164. Marsh, D. (2008) Protein modulation of lipids, and vice-versa, in membranes., *Biochimica et biophysica acta 1778*, 1545-1575.

165. Phillips, R., Ursell, T., Wiggins, P., and Sens, P. (2009) Emerging roles for lipids in shaping membrane-protein function., *Nature 459*, 379-385.

166. Adamian, L., Naveed, H., and Liang, J. (2011) Lipid-binding surfaces of membrane proteins: Evidence from evolutionary and structural analysis, *Biochimica et Biophysica Acta (BBA) - Biomembranes 1808*, 1092-1102.

167. Günther, T., Richter, L., and Schmalbeck, J. (1975) Phospholipids of Escherichia coli in magnesium deficiency, *Journal of general microbiology 86*, 191-193.

168. Dowhan, W. (1997) Molecular basis for membrane phospholipid diversity: why are there so many lipids?, *Annu Rev Biochem 66*, 199-232.

169. Bogdanov, M., Heacock, P., Guan, Z., and Dowhan, W. (2010) Plasticity of lipid-protein interactions in the function and topogenesis of the membrane protein lactose permease from Escherichia coli, *Proc Natl Acad Sci U S A 107*, 15057-15062.

170. Arnarez, C., Marrink, S. J., and Periole, X. (2013) Identification of cardiolipin binding sites on cytochrome c oxidase at the entrance of proton channels, *Scientific Reports 3*.

171. Pöyry, S., Cramariuc, O., Postila, P. A., Kaszuba, K., Sarewicz, M., Osyczka, A., Vattulainen, I., and Róg, T. (2013) Atomistic simulations indicate cardiolipin to have an integral role in the structure of the cytochrome bc1 complex, *Biochimica et Biophysica Acta (BBA) - Bioenergetics 1827*, 769-778.

172. Graff, A., Fraysse-Ailhas, C., Palivan, C. G., Grzelakowski, M., Friedrich, T., Vebert, C., Gescheidt, G., and Meier, W. (2010) Amphiphilic Copolymer Membranes Promote NADH:Ubiquinone Oxidoreductase Activity: Towards an Electron-Transfer Nanodevice, *Macromolecular Chemistry and Physics 211*, 229-238.

173. Sazanov, L. A. (2003) A Role for Native Lipids in the Stabilization and Two-dimensional Crystallization of the Escherichia coli NADH-Ubiquinone Oxidoreductase (Complex I), *Journal of Biological Chemistry 278*, 19483-19491.

174. Hielscher, R. (2009) The role of lipids and nucleotides in the catalytic mechanism of proteins from the respiratory chain : an electrochemical and infrared spectroscopic approach, In *Institut de Chimie*, Université de Strasbourg, Strasbourg.

175. Hielscher, R., Wenz, T., Stolpe, S., Hunte, C., Friedrich, T., and Hellwig, P. (2006) Monitoring redox-dependent contribution of lipids in Fourier transform infrared difference spectra of complex I fromEscherichia coli, *Biopolymers 82*, 291-294.

176. Shinzawa-Itoh, K., Seiyama, J., Terada, H., Nakatsubo, R., Naoki, K., Nakashima, Y., and Yoshikawa, S. (2010) Bovine Heart NADH−Ubiquinone Oxidoreductase Contains One Molecule of Ubiquinone with Ten Isoprene Units as One of the Cofactors, *Biochemistry 49*, 487-492.

177. Sharpley, M. S., Shannon, R. J., Draghi, F., and Hirst, J. (2006) Interactions between phospholipids and NADH:ubiquinone oxidoreductase (complex I) from bovine mitochondria, *Biochemistry 45*, 241-248.

178. Frederickson, C. J., Koh, J.-Y., and Bush, A. I. (2005) The neurobiology of zinc in health and disease, *Nature Reviews Neuroscience 6*, 449-462.

179. Vallee, B. L., and Falchuk, K. H. (1993) The biochemical basis of zinc physiology, *Physiol Rev 73*, 79-118.

180. Lee, D.-W., El Khoury, Y., Francia, F., Zambelli, B., Ciurli, S., Venturoli, G., Hellwig, P., and Daldal, F. (2011) Zinc Inhibition of Bacterial Cytochromebc1Reveals the Role of

CytochromebE295 in Proton Release at the QoSite, *Biochemistry 50*, 4263-4272.

181. Link, T. A., and von Jagow, G. (1995) Zinc ions inhibit the QP center of bovine heart mitochondrial bc1 complex by blocking a protonatable group, *J Biol Chem 270*, 25001-25006.

182. Martino, P. L., Capitanio, G., Capitanio, N., and Papa, S. (2011) Inhibition of proton pumping in membrane reconstituted bovine heart cytochrome c oxidase by zinc binding at the inner matrix side, *Biochimica et Biophysica Acta (BBA) - Bioenergetics 1807*, 1075-1082.

183. Mills, D. A., Schmidt, B., Hiser, C., Westley, E., and Ferguson-Miller, S. (2002) Membrane potential-controlled inhibition of cytochrome c oxidase by zinc, *J Biol Chem 277*, 14894-14901.

184. Florianczyk, B., and Trojanowski, T. (2009) Inhibition of respiratory processes by overabundance of zinc in neuronal cells, *Folia Neuropathol 47*, 234-239.

185. Kannt, A., Ostermann, T., Muller, H., and Ruitenberg, M. (2001) Zn(2+) binding to the cytoplasmic side of Paracoccus denitrificans cytochrome c oxidase selectively uncouples electron transfer and proton translocation, *FEBS Lett 503*, 142-146.

186. Giachini, L., Francia, F., Boscherini, F., Pacelli, C., Cocco, T., Papa, S., and Venturoli, G. (2007) EXAFS reveals a structural zinc binding site in the bovine NADH-Q oxidoreductase, *FEBS Letters 581*, 5645-5648.

187. Mackenzie, S. R. (2013) http://mackenzie.chem.ox.ac.uk/teaching/Molecular%20Vibrational%20Spectroscopy.pdf.

188. Beer, A. (1852) Bestimmung der Absorption des rothen Lichts in farbigen Flüssigkeiten, *Annalen der Physik 162*, 78-88.

189. Skoog, A. D., West, D. M., Holler, F. J., and Crouch, S. R. (2004) *Fundamentals of Analytical Chemistry, 8th Ed.*, Thomson.

190. Gill, S. C., and Hippel, P. H. (1989) Calculation of Protein extinction Coefficients from Amino Acid Sequence Data, *Analytical Biochemistry 182*, 319-326.

191. Friedrich, T., Brors, B., Hellwig, P., Kintscher, L., Rasmussen, T., Scheide, D., Schulte, U., Mantele, W., and Weiss, H. (2000) Characterization of two novel redox groups in the respiratory NADH:ubiquinone oxidoreductase (complex I), *Biochim Biophys Acta 1459*, 305-309.

192. Hellwig, P., Scheide, D., Bungert, S., Mantele, W., and Friedrich, T. (2000) FT-IR spectroscopic characterization of NADH:ubiquinone oxidoreductase (complex I) from Escherichia coli: oxidation of FeS cluster N2 is coupled with the protonation of an aspartate or glutamate side chain, *Biochemistry 39*, 10884-10891.

193. Friedrich, T., Hofhaus, G., Ise, W., Nehls, U., Schmitz, B., and Weiss, H. (1989) A small isoform of NADH : ubiquinone oxidoreductase (complex I) without mitochondrially encoded subunits is made in chloramphenicol-treated *Neurospora crassa*, *Eur J Biochem 180*, 173-180.

194. Euro, L., Bloch, D. a., Wikström, M., Verkhovsky, M. I., and Verkhovskaya, M. (2008) Electrostatic interactions between FeS clusters in NADH:ubiquinone oxidoreductase (Complex I) from Escherichia coli., *Biochemistry 47*, 3185-3193.

195. Chalmers, J. M., and Griffiths, P. (2002) *Handbook of vibrational spectroscopy (Vol 1-5)*, Wiley.

196. Stuart, B. (2004) *Infrared Spectroscopy : Fundamentals and Applications*, John Wiley & Sons, Ltd.

197. Neehaul, Y. (2012) Study of protein interactions in the respiratory chain by IR spectroscopy and electrochemistry, In *Institut de Chimie*, Université de Strasbourg, Strasbourg.

198. Barth, A. (2007) Infrared spectroscopy of proteins., *Biochimica et biophysica acta 1767*, 1073-1101.

199. Tamm, L. K., and Tatulian, S. A. (1997) Infrared spectroscopy of proteins and peptides in lipid bilayers, *Q Rev Biophys 30*, 365-429.

200. Barth, A., and Zscherp, C. (2002) What vibrations tell us about proteins, *Q Rev Biophys 35*, 369-430.

201. Barth, A. (2000) The infrared absorption of amino acid side chains., *Progress in biophysics and molecular biology 74*, 141-173.

202. Wolpert, M., and Hellwig, P. (2006) Infrared spectra and molar absorption coefficients of the 20 alpha amino acids in aqueous solutions in the spectral range from 1800 to 500cm−1, *Spectrochimica Acta Part A: Molecular and Biomolecular Spectroscopy 64*, 987-1001.

203. Goormaghtigh, E., Cabiaux, V., and Ruysschaert, J. M. (1990) Secondary structure and dosage of soluble and membrane proteins by attenuated total reflection Fourier-transform infrared spectroscopy on hydrated films., *European journal of biochemistry / FEBS 193*, 409-420.

204. Jackson, M., and Mantsch, H. H. (1995) The use and misuse of FTIR spectroscopy in the determination of protein structure., *Critical reviews in biochemistry and molecular biology 30*, 95-120.

205. Smith, G. D., and Palmer, R. A. (2002) Fast Time-resolved Mid-infrared Spectroscopy Using an Interferometer, In *Time-resolved spectroscopy*, pp 625-640, John Wiley & Sons Ltd.

206. Zhang, J., Oettmeier, W., Gennis, R. B., and Hellwig, P. (2002) FTIR spectroscopic evidence for the involvement of an acidic residue in quinone binding in cytochrome bd from Escherichia coli, *Biochemistry 41*, 4612-4617.

207. Hielscher, R., Wenz, T., Hunte, C., and Hellwig, P. (2009) Monitoring the redox and protonation dependent contributions of cardiolipin in electrochemically induced FTIR difference spectra of the cytochrome bc1 complex from yeast, *Biochimica et Biophysica Acta (BBA) - Bioenergetics 1787*, 617-625.

208. Hellwig, P., Mogi, T., Tomson, F. L., Gennis, R. B., Iwata, J., Miyoshi, H., and Mantele, W. (1999) Vibrational modes of ubiquinone in cytochrome bo(3) from Escherichia coli identified by Fourier transform infrared difference spectroscopy and specific (13)C labeling, *Biochemistry 38*, 14683-14689.

209. El Khoury, Y. (2010) Mid and far infrared spectroelectrochemical studies on the metal–ligand interactions in respiratory chain enzymes, In *Institut de Chimie*, Université de Strasbourg, Strasbourg.

210. Moss, D., Nabedryk, E., Breton, J., and Mantele, W. (1990) Redox-linked conformational changes in proteins detected by a combination of infrared spectroscopy and protein electrochemistry. Evaluation of the technique with cytochrome c, *Eur J Biochem 187*, 565-572.

211. Hellwig, P., Stolpe, S., and Friedrich, T. (2004) Fourier transform infrared spectroscopic study on the conformational reorganization inEscherichia coli complex I due to redox-driven proton translocation, *Biopolymers 74*, 69-72.

212. Friedrich, T., and Hellwig, P. (2010) Redox-induced conformational changes within the Escherichia coli NADH ubiquinone oxidoreductase (complex I): An analysis by mutagenesis and FT-IR spectroscopy, *Biochimica et Biophysica Acta (BBA) - Bioenergetics 1797*, 659-663.

213. Goormaghtigh, E. (1999) Attenuated total reflection infrared spectroscopy of proteins and lipids in biological membranes, *Biochimica et biophysica acta 1422*, 105-185.

214. Marshall, D., Fisher, N., Grigic, L., Zickermann, V., Brandt, U., Shannon, R. J., Hirst, J., Lawrence, R., and Rich, P. R. (2006) ATR-FTIR redox difference spectroscopy of Yarrowia lipolytica and bovine complex I, *Biochemistry 45*, 5458-5467.

215. Pinkerneil, P., Güldenhaupt, J., Gerwert, K., and Kötting, C. (2012) Surface-Attached Polyhistidine-Tag Proteins Characterized by FTIR Difference Spectroscopy, *Chemphyschem 13*, 2649-2653.

216. Schartner, J., Güldenhaupt, J., Mei, B., Rögner, M., Muhler, M., Gerwert, K., and Kötting, C. (2013) Universal Method for Protein Immobilization on Chemically Functionalized Germanium Investigated by ATR-FTIR Difference Spectroscopy, *Journal of the American Chemical Society 135*, 4079-4087.

217. Osawa, M. (2001) Surface-Enhanced Infrared Absorption, In *Near-Field Optics and Surface Plasmon Polaritons* (Kawata, S., Ed.), pp 163-187, Springer Berlin Heidelberg.

218. Ataka, K., Stripp, S. T., and Heberle, J. (2013) Surface-enhanced infrared absorption spectroscopy (SEIRAS) to probe monolayers of membrane proteins, *Biochimica et Biophysica Acta (BBA) - Biomembranes 1828*, 2283-2293.

219. Miyake, H., Ye, S., and Osawa, M. (2002) Electroless deposition of gold thin films on silicon for surface-enhanced infrared spectroelectrochemistry, *Electrochemistry Communications 4*, 973-977.

220. Murgida, D. H., Hildebrandt, P., and Todorovic, S. (2010) Immobilized redox proteins: mimicking basic features of physiological membranes and interfaces, In *Biomimetics, Learning from Nature* (Mukherjee, A., Ed.), p 534, InTech.

221. Naumann, R. L. C., Nowak, C., and Knoll, W. (2011) Proteins in biomimetic membranes: promises and facts, *Soft Matter 7*, 9535.

222. Vigano, C., Smeyers, M., Raussens, V., Scheirlinckx, F., Ruysschaert, J. M., and Goormaghtigh, E. (2004) Hydrogen-deuterium exchange in membrane proteins monitored by IR spectroscopy: A new tool to resolve protein structure and dynamics, *Biopolymers 74*, 19-26.

223. Harvey, D. (2008) *Analytical chemistry 2.0*, McGraw-Hill.

224. Scholtz, F. (2010) *Electroanalytical methods*, Springer.

225. Butt, J. N., and Armstrong, F. A. (2008) Chapter 4 VOLTAMMETRY OF ADSORBED REDOX ENZYMES : MECHANISMS IN THE POTENTIAL DIMENSION, 91-128.

226. Zu, Y., Shannon, R. J., and Hirst, J. (2003) Reversible, electrochemical interconversion of NADH and NAD+ by the catalytic (Ilambda) subcomplex of mitochondrial NADH:ubiquinone oxidoreductase (complex I), *J Am Chem Soc 125*, 6020-6021.

227. Gorton, L. (2007) Electrochemistry of NAD(P)+/NAD(P)H, In *Encyclopedia of electrochemitsry*, Wiley.

228. Ataka, K., and Heberle, J. (2006) Use of surface enhanced infrared absorption spectroscopy (SEIRA) to probe the functionality of a protein monolayer, *Biopolymers 82*, 415-419.

229. Ly, H. K., Sezer, M., Wisitruangsakul, N., Feng, J.-J., Kranich, A., Millo, D., Weidinger, I. M., Zebger, I., Murgida, D. H., and Hildebrandt, P. (2011) Surface-enhanced vibrational spectroscopy for probing transient interactions of proteins with biomimetic interfaces: electric field effects on structure, dynamics and function of cytochrome c., *The FEBS journal 278*, 1382-1390.

230. Jiang, X. U., Ataka, K., and Heberle, J. (2008) Influence of the molecular structure of carboxyl-terminated self-assembled monolayer on the electron transfer of cytochrome c adsorbed on an an electrode: In situ observation by surface-enhanced infrared absorption spectroscopy, *Journal of Physical Chemistry C 112*, 813-819.

231. Murata, K., Kajiya, K., Nukaga, M., Suga, Y., Watanabe, T., Nakamura, N., and Ohno, H. (2010) A Simple Fabrication Method for Three-Dimensional Gold Nanoparticle Electrodes and Their Application to the Study of the Direct Electrochemistry of Cytochrome c, *Electroanalysis 22*, 185-190.

232. Kozuch, J., Steinem, C., Hildebrandt, P., and Millo, D. (2012) Combined electrochemistry and surface-enhanced infrared absorption spectroscopy of gramicidin A incorporated into tethered bilayer lipid membranes., *Angewandte Chemie (International ed. in English) 51*, 8114-8117.

233. Ataka, K., Giess, F., Knoll, W., Naumann, R., Haber-Pohlmeier, S., Richter, B., and Heberle, J. (2004) Oriented attachment and membrane reconstitution of His-tagged cytochrome c oxidase to a gold electrode: in situ monitoring by surface-enhanced infrared absorption spectroscopy, *J Am Chem Soc 126*, 16199-16206.

234. Todorovic, S. (2008) SERR-Spectroelectrochemical Study of a cbb 3 Oxygen Reductase in a Biomimetic Construct, *The journal of physical chemistry. B 112*, 16952-16959.

235. Nowak, C., Schach, D., Gebert, J., Grosserueschkamp, M., Gennis, R. B., Ferguson-Miller, S., Knoll, W., Walz, D., and Naumann, R. L. C. (2010) Oriented immobilization and electron transfer to the cytochrome c oxidase, *Journal of Solid State Electrochemistry 15*, 105-114.

236. Datsenko, K. A., and Wanner, B. L. (2000) One-step inactivation of chromosomal genes in Escherichia coli K-12 using PCR products, *Proceedings of the National Academy of Sciences 97*, 6640-6645.

237. Bungert, S., Krafft, B., Schlesinger, R., and Friedrich, T. (1999) One-step purification of the NADH dehydrogenase fragment of the Escherichia coli complex I by means of Strep-tag affinity chromatography, *FEBS Lett 460*, 207-211.

238. Kohlstadt, M., Dorner, K., Labatzke, R., Koc, C., Hielscher, R., Schiltz, E., Einsle, O., Hellwig, P., and Friedrich, T. (2008) Heterologous Production, Isolation, Characterization and Crystallization of a Soluble Fragment of the NADH:Ubiquinone Oxidoreductase (Complex I) from Aquifex aeolicus, *Biochemistry*.

239. Cohen, S. R., and Plane, R. A. (1957) The Association of Ferrocyanide Ions with Various Cations, *The Journal of Physical Chemistry 61*, 1096-1100.

240. Gornall, A. G., Bardawill, C. J., and David, M. M. (1949) Determination of Serum Proteins by Means of the Biuret Reaction, *J Biol Chem 177*, 751-766.

241. Schägger, H., and von Jagow, G. (1987) Tricine-sodium dodecyl sulfate-polyacrylamide gel electrophoresis for the separation of proteins in the range from 1 to 100 kDa, *Analytical Biochemistry 166*, 368-379.

242. Hielscher, R., Friedrich, T., and Hellwig, P. (2011) Far- and Mid-Infrared Spectroscopic Analysis of the Substrate-Induced Structural Dynamics of Respiratory Complex I, *Chemphyschem 12*, 217-224.

243. Melin, F., Meyer, T., Lankiang, S., Choi, S. K., Gennis, R. B., Blanck, C., Schmutz, M., and Hellwig, P. (2013) Direct electrochemistry of cytochrome bo3 oxidase at a series of gold nanoparticles-modified electrodes, *Electrochemistry Communications 26*, 105-108.

244. Vasan, G., and Erbe, A. (2012) Incidence angle dependence of the enhancement factor in attenuated total reflection surface enhanced infrared absorption spectroscopy studied by numerical solution of the vectorial Maxwell equations., *Physical chemistry chemical physics : PCCP 14*, 14702-14709.

245. Guo, H., Kimura, T., and Furutani, Y. (2013) Distortion of the amide-I and -II bands of an α-helical membrane protein, pharaonis halorhodopsin, depends on thickness of gold films utilized for surface-enhanced infrared absorption spectroscopy, *Chemical Physics 419*, 8-16.

246. Delgado, J. M., Orts, J. M., Perez, J. M., and Rodes, A. (2008) Sputtered thin-film gold electrodes for in situ ATR-SEIRAS and SERS studies, *J Electroanal Chem 617*, 130-140.

247. Garjonyte, R., Malinauskas, A., and Gorton, L. (2003) Investigation of electrochemical

properties of FMN and FAD adsorbed on titanium electrode, *Bioelectrochemistry 61*, 39-49.

248. Mezzetti, A., Leibl, W., Breton, J., and Nabedryk, E. (2003) Photoreduction of the quinone pool in the bacterial photosynthetic membrane: identification of infrared marker bands for quinol formation, *FEBS Lett 537*, 161-165.

249. Zhou, M., Diwu, Z., Panchuk-Voloshina, N., and Haugland, R. P. (1997) A Stable Nonfluorescent Derivative of Resorufin for the Fluorometric Determination of Trace Hydrogen Peroxide: Applications in Detecting the Activity of Phagocyte NADPH Oxidase and Other Oxidases, *Analytical Biochemistry 253*, 162-168.

250. Fraaije, M. W., and Mattevi, A. (2000) Flavoenzymes: diverse catalysts with recurrent features, *Trends in biochemical sciences 25*, 126-132.

251. Alexandre, M. T. A., van Grondelle, R., Hellingwerf, K. J., Robert, B., and Kennis, J. T. M. (2008) Perturbation of the ground-state electronic structure of FMN by the conserved cysteine in phototropin LOV2 domains, *Physical Chemistry Chemical Physics 10*, 6693.

252. Holzer, W., Penzkofer, A., and Hegemann, P. (2005) Absorption and emission spectroscopic characterisation of the LOV2-His domain of phot from Chlamydomonas reinhardtii, *Chemical Physics 308*, 79-91.

253. Spiegelhauer, O., Mende, S., Dickert, F., Knauer, S. H., Ullmann, G. M., and Dobbek, H. (2010) Cysteine as a Modulator Residue in the Active Site of Xenobiotic Reductase A: A Structural, Thermodynamic and Kinetic Study, *Journal of Molecular Biology 398*, 66-82.

254. Ghisla, S., and Massey, V. (1989) Mechanisms of flavoprotein-catalyzed reactions, *European Journal of Biochemistry 181*, 1-17.

255. Chaiyen, P., Fraaije, M. W., and Mattevi, A. (2012) The enigmatic reaction of flavins with oxygen, *Trends in biochemical sciences 37*, 373-380.

256. Arias-Cartin, R., Grimaldi, S., Pommier, J., Lanciano, P., Schaefer, C., Arnoux, P., Giordano, G., Guigliarelli, B., and Magalon, A. (2011) Cardiolipin-based respiratory complex activation in bacteria, *Proc Natl Acad Sci U S A 108*, 7781-7786.

257. Gong, X. (2003) The Ubiquinone-binding Site in NADH:Ubiquinone Oxidoreductase from Escherichia coli, *Journal of Biological Chemistry 278*, 25731-25737.

258. Arrondo, J. L., and Goni, F. M. (1998) Infrared studies of protein-induced perturbation of lipids in lipoproteins and membranes, *Chem Phys Lipids 96*, 53-68.

259. Yau, W. M., Wimley, W. C., Gawrisch, K., and White, S. H. (1998) The preference of tryptophan for membrane interfaces, *Biochemistry 37*, 14713-14718.

260. Palsdottir, H., and Hunte, C. (2004) Lipids in membrane protein structures, *Biochimica et Biophysica Acta (BBA) - Biomembranes 1666*, 2-18.

261. Fry, M., and Green, D. E. (1981) Cardiolipin requirement for electron transfer in complex I and III of the mitochondrial respiratory chain, *J Biol Chem 256*, 1874-1880.

262. Gonzalvez, F., D'Aurelio, M., Boutant, M., Moustapha, A., Puech, J.-P., Landes, T., Arnauné-Pelloquin, L., Vial, G., Taleux, N., Slomianny, C., Wanders, R. J., Houtkooper, R. H., Bellenguer, P., Møller, I. M., Gottlieb, E., Vaz, F. M., Manfredi, G., and Petit, P. X. (2013) Barth syndrome: Cellular compensation of mitochondrial dysfunction and apoptosis inhibition due to changes in cardiolipin remodeling linked to tafazzin (TAZ) gene mutation, *Biochimica et Biophysica Acta (BBA) - Molecular Basis of Disease 1832*, 1194-1206.

263. Haines, T. H., and Dencher, N. A. (2002) Cardiolipin: a proton trap for oxidative phosphorylation, *FEBS Lett 528*, 35-39.

264. Schlame, M., and Ren, M. (2009) The role of cardiolipin in the structural organization of mitochondrial membranes, *Biochimica et Biophysica Acta (BBA) - Biomembranes 1788*, 2080-2083.

265. Althoff, T., Mills, D. J., Popot, J.-L., and Kühlbrandt, W. (2011) Arrangement of electron transport chain components in bovine mitochondrial supercomplex I1III2IV1, *The EMBO Journal 30*, 4652-4664.

266. Zhou, J., Zhong, Q., Li, G., and Greenberg, M. L. (2009) Loss of Cardiolipin Leads to Longevity Defects That Are Alleviated by Alterations in Stress Response Signaling, *Journal of Biological Chemistry 284*, 18106-18114.

267. Drose, S., Zwicker, K., and Brandt, U. (2002) Full recovery of the NADH:ubiquinone activity of complex I (NADH:ubiquinone oxidoreductase) from Yarrowia lipolytica by the addition of phospholipids, *Biochim Biophys Acta 1556*, 65-72.

268. van Meer, G., Voelker, D. R., and Feigenson, G. W. (2008) Membrane lipids: where they are and how they behave, *Nature Reviews Molecular Cell Biology 9*, 112-124.

269. Heijne, G. (1986) The distribution of positively charged residues in bacterial inner membrane proteins correlates with the trans-membrane topology, *EMBO J 5*, 3021-3027.

270. Lensink, M. F., Govaerts, C., and Ruysschaert, J. M. (2010) Identification of Specific Lipid-binding Sites in Integral Membrane Proteins, *Journal of Biological Chemistry 285*, 10519-10526.

271. McCall, K. A., Huang, C., and Fierke, C. A. (2000) Function and mechanism of zinc metalloenzymes, *J Nutr 130*, 1437S-1446S.

272. Burie, J.-R., Boussac, A., Boullais, C., Berger, G., Mattioli, T., Mioskowski, C., Nabedryk, E., and Breton, J. (1995) FTIR Spectroscopy of UV-Generated Quinone Radicals: Evidence for an Intramolecular Hydrogen Atom Transfer in Ubiquinone, Naphthoquinone, and Plastoquinone, *The Journal of Physical Chemistry 99*, 4059-4070.

273. Fahmy, K., Weidlich, O., Engelhard, M., Sigrist, H., and Siebert, F. (1993) Aspartic acid-212 of bacteriorhodopsin is ionized in the M and N photocycle intermediates: an FTIR study on specifically 13C-labeled reconstituted purple membranes, *Biochemistry 32*, 5862-5869.

274. (2013) IR spectra of Acetic and Glutamic Acid in vapor phase, National Institute of Standards and Technology.

275. Ekberg, K., Wielandt, A. G., Buch-Pedersen, M. J., and Palmgren, M. G. (2013) A Conserved Asparagine in a P-type Proton Pump Is Required for Efficient Gating of Protons, *Journal of Biological Chemistry 288*, 9610-9618.

276. Chang, H. Y., Choi, S. K., Vakkasoglu, A. S., Chen, Y., Hemp, J., Fee, J. A., and Gennis, R. B. (2012) Exploring the proton pump and exit pathway for pumped protons in cytochrome ba3 from Thermus thermophilus, *Proceedings of the National Academy of Sciences 109*, 5259-5264.

277. Cao, Y., Varo, G., Klinger, A. L., Czajkowsky, D. M., Braiman, M. S., Needleman, R., and Lanyi, J. K. (1993) Proton transfer from Asp-96 to the bacteriorhodopsin Schiff base is caused by a decrease of the pKa of Asp-96 which follows a protein backbone conformational change, *Biochemistry 32*, 1981-1990.

278. Venyaminov, S. Y., and Kalnin, N. N. (1990) Quantitative IR spectrophotometry of peptide compounds in water (H2O) solutions. I, Spectral parameters of amino acid residue absorption bands, *Biopolymers 30*, 1243-1257.

279. Giachini, L., Francia, F., Mallardi, A., Palazzo, G., Carpene, E., Boscherini, F., and Venturoli, G. (2005) Multiple scattering x-ray absorption studies of Zn2+ binding sites in bacterial photosynthetic reaction centers, *Biophys J 88*, 2038-2046.

280. Nara, M., Tasumi, M., Tanokura, M., Hiraoki, T., Yazawa, M., and Tsutsumi, A. (1994) Infrared

studies of interaction between metal ions and Ca(2+)-binding proteins. Marker bands for identifying the types of coordination of the side-chain COO- groups to metal ions in pike parvalbumin (pI = 4.10), *FEBS Lett 349*, 84-88.

281. Gourion-Arsiquaud, S., Chevance, S., Bouyer, P., Garnier, L., Montillet, J. L., Bondon, A., and Berthomieu, C. (2005) Identification of a Cd2+- and Zn2+-Binding Site in Cytochrome c Using FTIR Coupled to an ATR Microdialysis Setup and NMR Spectroscopy†, *Biochemistry 44*, 8652-8663.

282. Garczarek, F., and Gerwert, K. (2005) Functional waters in intraprotein proton transfer monitored by FTIR difference spectroscopy, *Nature 439*, 109-112.

283. Marechal, A., and Rich, P. R. (2011) Water molecule reorganization in cytochrome c oxidase revealed by FTIR spectroscopy, *Proc Natl Acad Sci U S A 108*, 8634-8638.

284. Headrick, J. M. (2005) Spectral Signatures of Hydrated Proton Vibrations in Water Clusters, *Science 308*, 1765-1769.

285. Suydam, I. T., and Boxer, S. G. (2003) Vibrational Stark Effects Calibrate the Sensitivity of Vibrational Probes for Electric Fields in Proteins†, *Biochemistry 42*, 12050-12055.

286. Zimmermann, J. r., Gundogdu, K., Cremeens, M. E., Bandaria, J. N., Hwang, G. T., Thielges, M. C., Cheatum, C. M., and Romesberg, F. E. (2009) Efforts toward Developing Probes of Protein Dynamics: Vibrational Dephasing and Relaxation of Carbon–Deuterium Stretching Modes in Deuterated Leucine, *The Journal of Physical Chemistry B 113*, 7991-7994.

287. Garczarek, F. (2005) Proton binding within a membrane protein by a protonated water cluster, *Proceedings of the National Academy of Sciences 102*, 3633-3638.

288. Rousseau, R., Kleinschmidt, V., Schmitt, U. W., and Marx, D. (2004) Assigning Protonation Patterns in Water Networks in Bacteriorhodopsin Based on Computed IR Spectra, *Angewandte Chemie International Edition 43*, 4804-4807.

289. Kulig, W., and Agmon, N. (2013) A 'clusters-in-liquid' method for calculating infrared spectra identifies the proton-transfer mode in acidic aqueous solutions, *Nat Chem 5*, 29-35.

290. Belevich, G., Knuuti, J., Verkhovsky, M. I., Wikström, M., and Verkhovskaya, M. (2011) Probing the mechanistic role of the long α-helix in subunit L of respiratory Complex I from Escherichia coli by site-directed mutagenesis, *Mol Microbiol 82*, 1086-1095.

291. Narayanan, M., Gabrieli, D. J., Leung, S. A., Elguindy, M. M., Glaser, C. A., Saju, N., Sinha, S. C., and Nakamaru-Ogiso, E. (2013) Semiquinone and Cluster N6 Signals in His-tagged Proton-translocating NADH:Ubiquinone Oxidoreductase (Complex I) from Escherichia coli, *Journal of Biological Chemistry 288*, 14310-14319.

292. Angerer, H., Nasiri, H. R., Niedergesäß, V., Kerscher, S., Schwalbe, H., and Brandt, U. (2012) Tracing the tail of ubiquinone in mitochondrial complex I, *Biochimica et Biophysica Acta (BBA) - Bioenergetics 1817*, 1776-1784.

293. Kervinen, M. (2006) The MELAS mutations 3946 and 3949 perturb the critical structure in a conserved loop of the ND1 subunit of mitochondrial complex I, *Human Molecular Genetics 15*, 2543-2552.

294. Sinha, P. K., Torres-Bacete, J., Nakamaru-Ogiso, E., Castro-Guerrero, N., Matsuno-Yagi, A., and Yagi, T. (2009) Critical Roles of Subunit NuoH (ND1) in the Assembly of Peripheral Subunits with the Membrane Domain of Escherichia coli NDH-1, *Journal of Biological Chemistry 284*, 9814-9823.

295. Kao, M. C. (2004) Functional Roles of Four Conserved Charged Residues in the Membrane Domain Subunit NuoA of the Proton-translocating NADH-Quinone Oxidoreductase from Escherichia coli, *Journal of Biological Chemistry 279*, 32360-32366.

296. Dougherty, D. A. (1996) Cation-π Interactions in Chemistry and Biology: A New View of Benzene, Phe, Tyr, and Trp, *Science 271*, 163-168.

297. Pines, E., Huppert, D., and Agmon, N. (1988) Geminate recombination in excited-state proton-transfer reactions: Numerical solution of the Debye--Smoluchowski equation with backreaction and comparison with experimental results, *The Journal of Chemical Physics 88*, 5620-5630.

298. Galkin, A., Meyer, B., Wittig, I., Karas, M., Schagger, H., Vinogradov, A., and Brandt, U. (2008) Identification of the Mitochondrial ND3 Subunit as a Structural Component Involved in the Active/Deactive Enzyme Transition of Respiratory Complex I, *Journal of Biological Chemistry 283*, 20907-20913.

299. Chouchani, E. T., Methner, C., Nadtochiy, S. M., Logan, A., Pell, V. R., Ding, S., James, A. M., Cochemé, H. M., Reinhold, J., Lilley, K. S., Partridge, L., Fearnley, I. M., Robinson, A. J., Hartley, R. C., Smith, R. A. J., Krieg, T., Brookes, P. S., and Murphy, M. P. (2013) Cardioprotection by S-nitrosation of a cysteine switch on mitochondrial complex I, *Nature Medicine 19*, 753-759.

300. Grgic, L. (2004) Functional Significance of Conserved Histidines and Arginines in the 49-kDa Subunit of Mitochondrial Complex I, *Journal of Biological Chemistry 279*, 21193-21199.

301. Olsson, M. H. M., Sondergaard, C. R., Rostkowski, M., and Jensen, J. H. (2011) PROPKA3: Consistent Treatment of Internal and Surface Residues in Empirical pK(a) Predictions, *J Chem Theory Comput 7*, 525-537.

302. Tocilescu, M. A., Fendel, U., Zwicker, K., Dröse, S., Kerscher, S., and Brandt, U. (2010) The role of a conserved tyrosine in the 49-kDa subunit of complex I for ubiquinone binding and reduction, *Biochimica et Biophysica Acta (BBA) - Bioenergetics 1797*, 625-632.

303. Ohnishi, T., Ohnishi, S. T., Shinzawa-Itoh, K., Yoshikawa, S., and Weber, R. T. (2012) EPR detection of two protein-associated ubiquinone components (SQNf and SQNs) in the membrane in situ and in proteoliposomes of isolated bovine heart complex I, *Biochimica et Biophysica Acta (BBA) - Bioenergetics 1817*, 1803-1809.

304. Brandt, U. (1997) Proton-translocation by membrane-bound NADH:ubiquinone-oxidoreductase (complex I) through redox-gated ligand conduction, *Biochimica et Biophysica Acta (BBA) - Bioenergetics 1318*, 79-91.

305. Roberts, P. G., and Hirst, J. (2012) The Deactive Form of Respiratory Complex I from Mammalian Mitochondria Is a Na+/H+ Antiporter, *Journal of Biological Chemistry 287*, 34743-34751.

306. Wolf, S., Freier, E., Potschies, M., Hofmann, E., and Gerwert, K. (2010) Directional proton transfer in membrane proteins achieved through protonated protein-bound water molecules: a proton diode, *Angew Chem Int Ed Engl 49*, 6889-6893.

307. Pohl, T. (2008) Lambda-Red vermittelte Mutagenese des nuo-Operons zur Herstellung von Protein-Varianten für die biophysikalische und zellbiologische Charakterisierung der *Escherichia coli* NADH:Ubichinon Oxidoreduktase, In *Fakultät für Chemie, Pharmazie und Geowissenschaften*, Albert-Ludwigs Universität Freiburg, Freiburg i. Br.

308. Hemp, J., Robinson, D. E., Ganesan, K. B., Martinez, T. J., Kelleher, N. L., and Gennis, R. B. (2006) Evolutionary migration of a post-translationally modified active-site residue in the proton-pumping heme-copper oxygen reductases, *Biochemistry 45*, 15405-15410.

Sébastien KRIEGEL

Transformation d'une protéine membranaire de la chaîne respiratoire en une sonde pour l'analyse de substrats, inhibiteurs et lipides

Résumé

Le domaine de la bioénérgétique traîte de la circulation et de la transformation de l'énergie dans et entre des organismes et leur environnement. Dans ce manuscrit de thèse, la respiration cellulaire et plus particulièrement la première enzyme de la chaîne respiratoire, la NADH:ubiquinone oxidoreductase (Complexe I) ont été étudiées, dans l'objectif de clarifier sa fonction et son implication dans certaines maladies. Dans une première partie, la création d'une sonde impliquant l'enzyme immobilisée de façon biomimétique est décrite. La caractérisation de ce système est effectuée *via* spectroscopie infrarouge par exaltation de surface (SEIRAS) couplée à de l'électrochimie. Sa réponse à l'ajout de substrats et d'inhibiteurs est ensuite présentée. Dans une seconde partie, l'interaction du Complexe I avec des lipides et des inhibiteurs (Zn^{2+} et NADH-OH) ainsi que le rôle d'une Tyrosine située au site de fixation du NADH ont été étudiés par spectroscopies IR et UV-Vis différentielles induites par électrochimie. L'exploration des résultats obtenus sous un angle structural a finalement permis de proposer un modèle pour le mécanisme de couplage entre la réduction d'ubiquinone et le pompage de protons par le Complexe I.

Mots-clés : Bioénergétique, chaîne respiratoire, NADH:ubiquinone oxidoreductase, Complexe I, FT-IR, UV-Vis, ATR, SEIRAS, Voltammétrie cyclique, électrochimie, biosenseur.

Abstract

The field of bioenergetics deals with the flow and transformation of energy within and between living organisms and their environment. The work presented in this thesis report focuses on cellular respiration and more specifically on the first enzyme of the respiratory chain, NADH:ubiquinone oxidoreductase (Complex I). This was done to clarify details about its function and its implication in disease. First, the creation of a sensor involving the biomimetically immobilized enzyme is presented and probed through a combination of surface enhanced infrared absorption spectroscopy (SEIRAS) and electrochemistry. This sensor is then tested against different substrates and inhibitors. In a second part, the interaction of Complex I with lipids, inhibitors (Zn^{2+} and NADH-OH) and the role of a Tyrosine residue situated in the NADH binding pocket are investigated through electrochemically induced UV-Vis and FTIR difference spectroscopies. The results gathered through these experiments are then explored under a structural perspective and a coupling mechanism between quinone reduction and proton translocation by Complex I is proposed.

Keywords : Bioenergetics, respiratory chain, NADH:ubiquinone oxidoreductase, Complex I, FT-IR, UV-Vis, ATR, SEIRAS, Cyclic Voltammetry, electrochemistry, biosensor.